HARC

LASER APPLICATIONS RESEARCH CENTER

4802 Research Forest Drive
The Woodlands. Texas 77381
713/363-7920

AD-A218 015

SHORT WAVELENGTH LASER/MATERIALS INTERACTIONS

Final Technical Report

20 December 1989

Leif G. Fredin, David T. Halligan, Brendan D. Krenek,
Terry D. Kunz, Richard F. Menefee, and Michael J. Berry

Laser Applications Research Center, HARC
4802 Research Forest Drive
The Woodlands, TX 77381

Telephone: (713) 363-7970

Prepared for:

Air Force Office of Scientific Research
Electronic and Materials Science Directorate
Bolling AFB, DC 20332-6448

Grant Number AFOSR-85-0365

Distribution: Unlimited

**DTIC
ELECTE
FEB 07 1990
S B D**

90 02 06 123

REPORT DOCUMENTATION PAGE		*Form Approved* *OMB No. 0704-0188*

1a. REPORT SECURITY CLASSIFICATION Unclassified		1b. RESTRICTIVE MARKINGS N/A		
2a. SECURITY CLASSIFICATION AUTHORITY N/A		3. DISTRIBUTION/AVAILABILITY OF REPORT Unlimited		
2b. DECLASSIFICATION/DOWNGRADING SCHEDULE N/A				
4. PERFORMING ORGANIZATION REPORT NUMBER(S) N/A		5. MONITORING ORGANIZATION REPORT NUMBER(S) AFOSR-TR- 90-0049		
6a. NAME OF PERFORMING ORGANIZATION Houston Area Research Center	6b. OFFICE SYMBOL *(If applicable)*	7a. NAME OF MONITORING ORGANIZATION AFOSR		
6c. ADDRESS *(City, State, and ZIP Code)* 4802 Research Forest Drive The Woodlands, TX 77381		7b. ADDRESS *(City, State, and ZIP Code)* Building 410 Bolling AFB, DC 20332-6448		
8a. NAME OF FUNDING/SPONSORING ORGANIZATION AFOSR	8b. OFFICE SYMBOL *(If applicable)* NE	9. PROCUREMENT INSTRUMENT IDENTIFICATION NUMBER AFOSR-85-0365		

8c. ADDRESS *(City, State, and ZIP Code)* Building 410 Bolling AFB, DC 20332-6448	10. SOURCE OF FUNDING NUMBERS			
	PROGRAM ELEMENT NO. 61102F	PROJECT NO. 2306	TASK NO. A2	WORK UNIT ACCESSION NO.

11. TITLE *(Include Security Classification)*

SHORT WAVELENGTH LASER/MATERIALS INTERACTIONS

12. PERSONAL AUTHOR(S)
L. G. Fredin, D. T. Halligan, B. D. Krenek, T. D. Kunz, R. F. Menefee, and M. J. Berry

13a. TYPE OF REPORT Final Technical	13b. TIME COVERED FROM 850901 TO 880930	14. DATE OF REPORT *(Year, Month, Day)* 891220	15. PAGE COUNT 206

16. SUPPLEMENTARY NOTATION

17.	COSATI CODES		18. SUBJECT TERMS *(Continue on reverse if necessary and identify by block number)*
FIELD	GROUP	SUB-GROUP	Laser effects; laser/materials interactions; optical properties; pyrometry, plume spectroscopy; laser hardened materials; spacecraft survivability; high and ultrahigh temperature oxidation resistant materials; ablation.

19. ABSTRACT *(Continue on reverse if necessary and identify by block number)*

This Final Technical Report summarizes work on "Short Wavelength Laser/Materials Interactions" completed by the Houston Area Research Center (HARC) and Rice University (Rice) during the period 1 Sep 85 through 30 Sep 88 under sponsorship by the Air Force Office of Scientific Research on Grant AFOSR-85-0365 [Program Manager: Dr. Liselotte J. Schioler, AFOSR/NE] as part of the Spacecraft Survivability Initiative. The overall objective of the program is to understand the nature of laser interactions with materials, with special emphasis on the phenomenology and effects associated with short wavelength laser interactions with spacecraft materials. HARC/Rice personnel have completed the following projects: 1) development of new diagnostic instrumentation and testing methods for evaluation of laser effects and high temperature performance, 2) fundamental studies of laser/materials interactions, 3) determination of short wavelength laser/materials interaction phenomena and effects, and 4) materials evaluation. The program has led to major advances in science-based understanding of materials performance under extreme conditions for two applications: 1) enhancement of spacecraft survivability, and 2) development of high and ultrahigh temperature oxidation-resistant materials. Keywords

20. DISTRIBUTION/AVAILABILITY OF ABSTRACT [X] UNCLASSIFIED/UNLIMITED ☐ SAME AS RPT. ☐ DTIC USERS	21. ABSTRACT SECURITY CLASSIFICATION Unclassified	
22a. NAME OF RESPONSIBLE INDIVIDUAL Dr. Liselotte J. Schioler	22b. TELEPHONE *(Include Area Code)* (202) 767-4933	22c. OFFICE SYMBOL NE

DD Form 1473, JUN 86   *Previous editions are obsolete.*   SECURITY CLASSIFICATION OF THIS PAGE

SHORT WAVELENGTH LASER/MATERIALS INTERACTIONS
Final Technical Report Contents

SHORT WAVELENGTH LASER/MATERIALS INTERACTIONS
Final Technical Report Contents (continued)

DTIO COPY INSPECTED 5

Accession For

NTIS GRA&I ☑
DTIC TAB ☐
Unannounced ☐
Justification

By
Distribution/
Availability Codes

Dist	Avail and/or Special
A-1	

1.0 INTRODUCTION and SUMMARY

This Final Technical Report summarizes work on "Short Wavelength Laser/Materials Interactions" completed by the Houston Area Research Center (HARC) and Rice University (Rice) during the period 1 Sep 85 through 30 Sep 88 under sponsorship by the Air Force Office of Scientific Research on Grant AFOSR-85-0365 [Program Manager: Dr. Liselotte J. Schioler, AFOSR/NE] as part of the Spacecraft Survivability Initiative. HARC/Rice personnel [Dr. Michael Berry (PI), Dr. Leif Fredin, Dr. David Halligan, Mr. Brendan Krenek, Dr. Terry Kunz, Dr. Leanna Levine, Mr. Richard Menefee, and Dr. Sydney Ulvick] developed new diagnostic instrumentation for evaluation of laser effects, completed fundamental studies of laser/materials interactions, determined short wavelength laser/materials interaction phenomena and effects, and evaluated materials performance at high temperature during laser irradiation. The program has led to major advances in science-based understanding of materials performance under extreme conditions.

The overall primary objective of the AFOSR/HARC/Rice Program is to understand the nature of laser interactions with materials, with special emphasis on the phenomenology and effects associated with short wavelength laser interactions with spacecraft materials. An additional objective of the Program is to develop new instrumentation and test methods for evaluating the performance of both spacecraft and aircraft materials in threat environments. The Air Force requires new spacecraft materials to protect satellites against enemy threats (lasers, *etc.*) and against natural space environment threats (atomic oxygen, *etc.*). Laser directed energy weapons (DEWs) currently operate at relatively long (mid-infrared spectral region) wavelengths; laser countermeasures materials are already available to defeat these current threats. Future laser DEWs [ground-based free electron lasers (GBFELs) and space-based lasers (SBLs)] will operate at much shorter wavelengths (down to $\lambda = 0.4$ μm) than are generated at current laser test facilities (*e.g.*, DF and CO_2 laser test facilities produce $\lambda = 3.8$ μm and 10.6 μm wavelength radiation, respectively). Since coupling coefficients for absorption of laser radiation depend strongly on wavelength, it is essential to obtain wavelength scaling information on these coupling coefficients to evaluate laser effects obtained at currently available laser test facilities and to use these data to predict corresponding effects at actual laser DEW engagement wavelengths.

The Air Force also requires new high temperature and ultrahigh temperature oxidation-resistant materials for turbine engines and for National AeroSpace Plane (NASP) applications. Versatile testing methods are needed to evaluate the performance of these materials under realistic threat environment conditions.

To address the above objectives and requirements, HARC/Rice personnel have carried out the following projects during the period of grant support:

Materials Selection and Characterization

  * Model, state-of-the-art, and developmental materials have been selected and characterized before and after irradiation. The optical properties of both constituent materials and candidate laser hardened materials have been determined to analyze experimental measurements and to assess ablation performance as a function of wavelength and irradiance level.

Instrumentation Development

  * New laser sources and test facilities have been developed and used for materials evaluation.

  * A new multiwavelength optical pyrometer system has been designed, constructed, and used to provide accurate target front surface temperature and spectral emittance measurements.

  * Wavelength scaling diagnostic instrumentation systems have been developed and constructed to obtain time-resolved target front surface coupling coefficients simultaneously at several wavelengths during laser irradiation by a continuous wave (cw) carbon dioxide (CO_2) laser source.

1

Instrumentation Development (continued)

    * Plume diagnostic instrumentation systems have been developed to obtain temporally, spatially, and spectrally resolved optical properties (plume absorption, extinction, and emission spectra) measurements during laser irradiation.

    * Mass spectrometric instrumentation has been used for identification of species present in laser generated plumes.

Laser/Materials Interaction Studies

    * Several types of laser/materials interaction experiments have been performed using continuous wave (cw) and repetitively pulsed (rp) laser irradiation sources at HARC and at the Laser Test Facility at WL/TALE, Kirtland AFB, NM.

    * New instrumentation has been demonstrated and fundamental measurements have been completed during laser/materials interaction experiments.

Short Wavelength Interaction Phenomena and Effects

    * Optical and other properties of candidate spacecraft metals have been reviewed to determine the suitability of metals as protective materials.

    * Wavelength scaling relations have been developed to predict coupling coefficients for short wavelength laser engagements.

    * The fundamental mechanistic basis of short wavelength phenomenology and effects has been developed.

Materials Evaluation

    * The ablation performance of several materials has been evaluated and inter-related with pertinent phenomenology and effects.

    * The oxidation resistance behavior of several materials has been determined.

    This Final Technical Report documents the above and related accomplishments of the AFOSR/HARC/Rice Program and presents recommendations for future research.

2

2.0 PROGRAM OBJECTIVES

Laser effects on materials depend strongly on laser and interaction parameters (wavelength, irradiance, pulse waveform, irradiated spot size, angle of incidence, *etc.*), on material characteristics (composition, optical and thermal properties, pyrolysis kinetics, *etc.*), on plume characteristics (composition, geometric structure, optical properties, *etc.*), and on environmental conditions (pressure, flowfield, acceleration, *etc.*). Figure 1 illustrates some of the physical and chemical phenomena that occur during laser interactions with materials. Of primary interest in this program are: 1) the time resolved value of the wavelength dependent thermal coupling coefficient α_λ during laser ablation and its origins due to optical properties of the target and plume, and 2) the wavelength (λ) dependence of α_λ and its connection with phenomenology occurring on the target front surface and in the ablation plume.
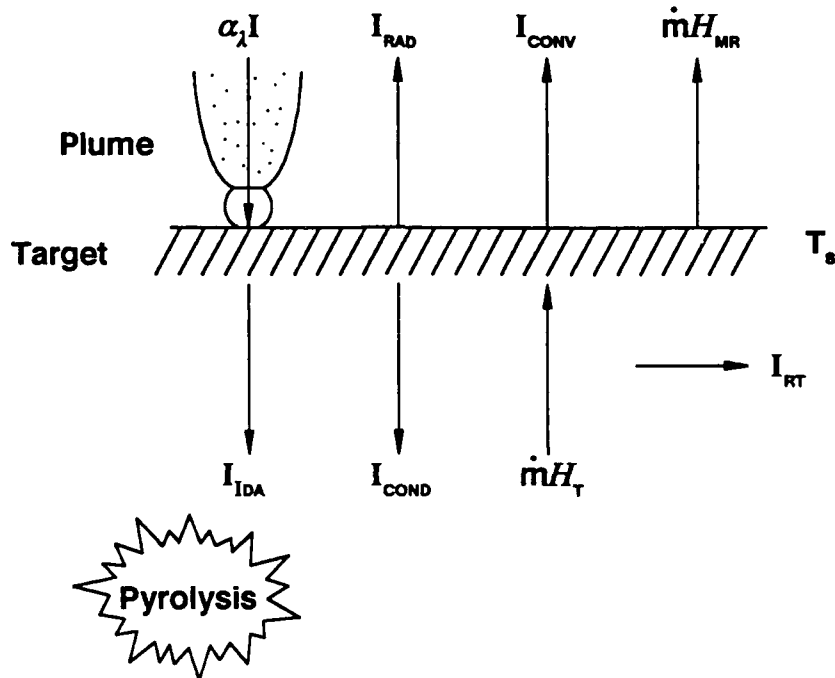

Figure 1. Surface energy (irradiance) balance model for laser/material interactions

Figure 1 shows a one-dimensional (1D) surface energy balance model [Reference 1] that pertains to laser interaction with an ablating material. Energy balances are given in terms of irradiance (energy per unit area per unit time; units: kW/cm^2) balances. The cross-hatched zone is the surface layer of the ablating material; in a 1D model, each surface element has an identical energy balance. In Figure 1, α_λ is the wavelength dependent (and irradiance dependent) thermal coupling coefficient, I is the incident laser irradiance, I_i's are loss irradiances [RAD: radiative, CONV: convective, IDA: in-depth absorption, COND: conductive, RT: radial transport due to two-dimensional losses (scattering, radial conduction, *etc.*)], m is the mass loss rate per unit area [units: $g/(cm^2 \cdot sec)$], H_i's are enthalpies (MR: mass removal, T: solid raised to temperature T_S; units: kJ/g), and T_S is the surface temperature. The wavelength dependent thermal coupling coefficient α_λ is the fraction of the incident laser energy at wavelength λ that is converted into thermal effects in the material. The enthalpy of mass removal H_{MR} is the average enthalpy required to generate ablation products (atoms, molecules, debris, and/or plasma contained in the plume schematically shown in Figure 1) from the material (at its ambient temperature prior to laser irradiation).

3

In-depth absorption produces a loss of energy from the ablation surface, but it may also generate in-depth pyrolysis that is often accompanied by spallation ("chunking") as a mechanism of mass removal. This spallation may decrease H_{MR} significantly from the value it would have for equilibrium thermochemical ablation [Reference 1]. Plume species (atoms, molecules, particles, and/or plasmas) may absorb and/or scatter the incident laser beam; these beam/plume interactions generally decrease α_λ from its transparent plume value. Beam/plume interactions dominate overall radiative transport to the target surface if a dense high opacity plasma is formed within the plume; a dense plasma strongly decouples incident radiation from the target surface.

The simplest ("ideal") case is obtained when all losses (I_i's) are negligible and the ablation plume is transparent; then, the effective enthalpy of ablation Q^* (defined to be the amount of laser energy required to remove a unit mass of material [Reference 2]) is related simply to the two fundamental material parameters α_λ and H_{MR}:

$$Q^* = H_{MR}/\alpha_\lambda. \tag{1}$$

Here, α_λ is just equal to the wavelength dependent material absorptance A_λ which, for an opaque material, is given by [Reference 1]:

$$\alpha_\lambda = A_\lambda = \epsilon_\lambda = 1 - R_\lambda, \tag{2}$$

where ϵ_λ is the spectral emittance and R_λ is the wavelength dependent material reflectance. (Equation [2] assumes that the material does not transmit any laser light, which is true for the classes of materials considered in this program.) This ideal case can be obtained for high irradiance 1D steady-state thermochemical ablation of a surface-absorbing nonconducting material that produces a transparent ablation plume expanding into vacuum. Some materials may exhibit very non-ideal behavior, such as strong beam/plume interactions that alter the thermal coupling coefficient α_λ from its transparent plume value; in such cases, it is essential to measure plume optical properties to develop a proper model that handles target and plume wavelength scaling effects separately.

The overall goal of the AFOSR/HARC/Rice Program is to understand the nature of laser interactions with materials. Toward this end, fundamental measurements of materials' optical properties (leading to a determination of α_λ) and of materials' enthalpies of mass removal (H_{MR}) are required to evaluate the ablation performance (Q^*) of candidate laser hardened materials.

The original specific objectives of the AFOSR/HARC/Rice Program are to:

1) to carry out fundamental studies of continuous wave (cw), repetitively pulsed (rp), and single pulse (sp) laser interactions with model, state-of-the-art, and developmental materials,

2) to measure materials' properties and responses before, during, and after laser irradiation,

3) to determine plume species abundances and energy contents using laser probes and/or mass spectrometric techniques,

4) to evaluate candidate spacecraft materials and hardening concepts that are promising in the context of spacecraft survivability,

5) to compare laser/materials interaction phenomenology and effects as a function of laser parameters, environmental conditions, etc., and

6) to generate mechanistic models for laser/materials interactions that permit the development of new laser hardened materials.

Upon consultation with the original program manager (Major Joseph W. Hager) and the interim program manager (Dr. Alan Rosenstein), an additional objective was added:

7) to transition program emphasis from spacecraft survivability considerations to more general applications such as laser-based instrumentation that is suitable for development and testing of oxidation-resistant coatings for protection of high temperature composite materials.

These objectives have been successfully addressed in the AFOSR/HARC/Rice Program, as detailed in the following sections of the Final Technical Report.

4

3.0 RESULTS

3.1 MATERIALS SELECTION and CHARACTERIZATION

Test materials were selected to provide: a) a survey of model, state-of-the-art, and developmental materials that are pertinent to Air Force program interests, and b) extensive results on one material to demonstrate the utility of target and plume diagnostic instrumentation for measurements of fundamental properties during laser irradiation. Five classes of test materials were included in AFOSR/HARC/Rice Program experiments; code names are used throughout this report to keep the discussion unclassified - M. J. Berry can provide decoding information to authorized government and contractor personnel:

1) structural composites (SCs): materials A101 and A105 [supplied by B. Laub and J. Sullivan (Acurex)], and materials AF1 through AF5 [supplied by Weapons Laboratory (WL) personnel],

2) cured epoxy resins (CERs): materials SR7 and SR8 [supplied by R. Bauer (Shell Development Company)]; SR7 is the same CER used as the resin matrix for materials AF4 and AF5 while SR8 is a highly purified version of SR7,

3) carbon barrier materials (CBMs): graphNOL (G) [supplied by C. M. Stickley (BDM Corporation)], a carbon/carbon composite (C101) [supplied by B. Laub and E. Chu (Acurex)], metal-loaded carbons (MLCs): C102 and C104 [supplied by B. Laub and J. Sullivan (Acurex)] and 101 and C106 [supplied by W. L. Tarasen (Hitco)], reflecting graphite (C105) [supplied by Capt. J. R. Couick (AFWL/TALE)], and metal-coated carbons (MCCs): A200 and Uxx [supplied by R. Tuffias (Ultramet)] and C107 and C108 [supplied by B. Laub and J. Sullivan (Acurex)],

4) metals: aluminum (Al) and titanium (Ti) [purchased from Alfa Products], and

5) ceramics: silicon carbide (SiC) and silicon nitride (Si_3N_4) [supplied by G. Reynolds (MSNW)].

The above materials were fabricated into small coupons (typically, 2-4 mm diameter X 1 mm thickness discs) for laser experimentation at HARC. Larger specimens (at least 12 mm diameter) were used for room temperature reflectance R_λ measurements.

Room temperature total reflectances [$R_\lambda(T_{room})$] were measured at eight wavelengths (λ = 0.351-0.364 μm, 0.458 μm, 0.515 μm, 1.06 μm, 1.5 μm, 2.7 μm, 3.8 μm and 10.6 μm) for both virgin (pre-test, unirradiated) and irradiated materials. Figure 2 shows the reflectance measurement system that was used to obtain $R_\lambda(T_{room})$ measurements. The system includes:

1) an integrating sphere [either a Labsphere Model IS-060-DG integrating sphere (6" diameter, inside coated with a diffuse gold surface) for infrared wavelength measurements or an aluminum integrating sphere (6" diameter, inside coated with Kodak white reflectance paint) for near infrared, visible, and ultraviolet wavelength measurements]; the integrating sphere contains baffles to prevent direct detection of specular reflections,

2) laser sources [a) LineLite Laser Corporation Model 941S cw CO_2 laser for 10.6 μm measurements, b) Amoco Laser Company Model ALC 1064 cw Nd:YAG laser for 1.06 μm measurements, c) Coherent Model Innova 20 Ar$^+$ laser for UV and visible measurements] or thermal light sources [for 2.7 μm and 3.8 μm measurements] for specimen illumination,

3) interference filters to transmit the desired wavelengths,

4) fast response infrared, near infrared, visible, and ultraviolet wavelength detectors (Infrared Associates Model HCT100 HgCdTe detector, PbSe photodiodes, and Si photodiodes),

5) relectance standards [diffuse gold (Labsphere) for infrared and near infrared wavelength reflectance calibration using the manufacturer's listed reflectance values of 0.95 at 10.6 μm, 0.94 at 3.8 and 2.7 μm, and 0.93 at 1.5 and 1.06 μm; hemispherical diffuse reflectance standard for visible wavelength reflectance calibration using NIST measured reflectances of 0.80 at 0.515 μm and 0.77 at 0.458 μm; aluminum specular reflectance standard for 0.35 μm wavelength reflectance calibration using the NIST measured value of 0.91], and
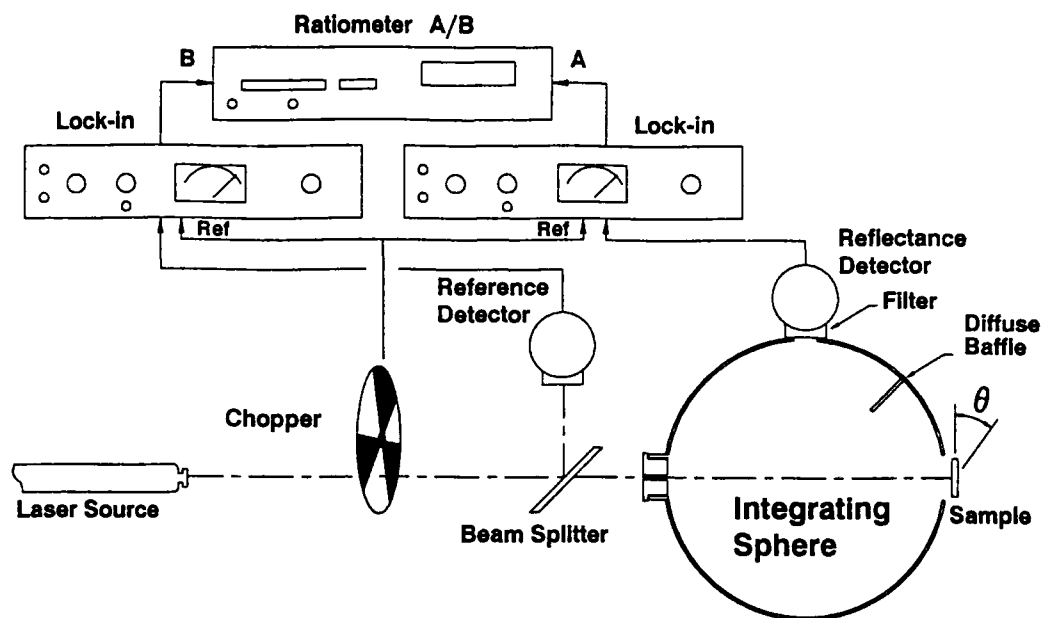
Figure 2. Room Temperature Reflectance Measurement System

6) a phase-lock detection system incorporating a mechanical chopper to modulate the incident beam (typically, at *ca.* 500 Hz), lock-in amplifiers [EG&G Princeton Applied Research (PAR) Model 128] to detect both sample (reflected light) and reference (beam-split incident light) beams, and a ratiometer [EG&G PAR Model 188] to obtain sample/reference beam ratios, thereby reducing noise effects caused by power fluctuation(s) of the beams.

Table 1 presents the measurements; room T reflectances at wavelengths λ (units: μm) are given in columns labelled R_λ. Note that the structural composites (A101 and A105) have very low reflectances in the infrared spectral region compared to all the carbon barrier materials. Material A105 has a slightly larger reflectance at λ = 10.6 μm wavelength than material A101. Materials C105, C106, C107, C108, and A200 all have high room T reflectances at λ = 10.6 μm wavelength; these high reflectances correlate well with fine ablation performance. Some of the samples listed in Table 1 have reflectances that depend on surface preparation; for example, a lightly sanded surface of graphNOL (G) had reflectances of 0.14 at λ = 2.7, 3.8, and 10.6 μm wavelengths compared to higher values of 0.26 - 0.28 at the same wavelengths obtained on a lightly polished surface.

Table 1 also lists ranges of reflectance values (minima and maxima of 48 reflectance values at each wavelength) measured within 16 mm diameter regions distributed over the full front and back surfaces of large panels (*ca.* 15 cm X 10 cm X 0.6 cm thickness) of materials C107 and C108 - the data show that reflectances (and, hence, the coating characteristics) are fairly uniform and occasionally larger than those of corresponding disc samples. Literature values of room temperature reflectances are available for pure single crystal samples of the metal carbides that are coated on materials C107 and C108; the coatings are slightly less (5-10% less) reflective than corresponding single crystals. It is likely that optical properties improvements for the coatings could be achieved through deposition process improvements.

Further discussion of room temperature reflectance measurements is presented in Section 3.5 below.

6

Table 1. Room Temperature Total Reflectance [$R_\lambda(T_{room})$] Measurements*

Material	$R_{0.35}$	$R_{0.458}$	$R_{0.515}$	$R_{1.06}$	$R_{1.5}$	$R_{2.7}$	$R_{3.8}$	$R_{10.6}$
A101	0.09	0.07	0.07	0.10	0.11	0.10	0.10	0.10
A105	0.09	0.07	0.07	0.11	0.12	0.12	0.12	0.18
G(polished)	0.15	0.16	0.16	0.18	0.21	0.27	0.26	0.28
G(sanded)	0.10	0.09	0.09	0.12	0.13	0.14	0.14	0.14
C101	0.14	0.13	0.14	0.20	0.22	0.28	0.29	0.41
C102			0.14	0.19			0.34	0.43
C104			0.17	0.22			0.38	0.45
C105	0.27	0.26	0.27	0.39	0.47	0.49	0.50	0.85
C106	0.17	0.16	0.17	0.22	0.29	0.44	0.45	0.69
C107	0.35	0.37	0.40	0.71	0.75	0.82	0.84	0.90
C107P	0.28-0.35	0.28-0.34	0.30-0.37	0.72-0.78	0.78-0.84	0.85-0.89	0.87-0.90	0.91-0.94
C108	0.24	0.29	0.38	0.76	0.79	0.85	0.87	0.93
C108P	0.26-0.29	0.31-0.38	0.42-0.46	0.78-0.82	0.79-0.83	0.83-0.87	0.85-0.89	0.90-0.92
A200	0.33	0.36	0.37	0.58	0.63	0.69	0.71	0.93

*Uncertainty: ± 0.02; P denotes panel samples

3.2 DEVELOPMENT of NEW INSTRUMENTATION

HARC/Rice personnel developed several new instrument systems in order to provide essential experimental capabilities for the AFOSR/HARC/Rice Program:

1) laser sources - an enhanced cw hydrogen fluoride (HF) chemical laser test facility [Reference 3] as well as new cw carbon dioxide (CO_2), rp HF, and rp excimer laser systems and associated test facilities [References 4-6] have been put into operation in order to study laser effects,

2) multiwavelength optical pyrometer system - a novel six wavelength optical pyrometer system has been designed, constructed, and used to obtain time-resolved target front surface temperature and spectral emittance measurements on materials during laser irradiation,

3) target reflectance diagnostic instrumentation - time-resolved high temperature spectral reflectances of materials during laser ablation have been measured using a versatile instrumentation system,

4) plume diagnostic instrumentation - new diagnostic instrumentation systems have been developed and used to measure temporally, spatially, and spectrally resolved optical properties (absorption, emission, and total extinction) measurements on ablation plumes (and on oxidation products) generated by sp, rp, and cw lasers,

5) mass spectrometric instrumentation - a laser vaporization/quadrupole mass spectrometer system has been used for identification of ablation plume species generated by laser irradiation.

The following Sections 3.2.1 through 3.2.5 give details about the above and related instrumentation developed for the AFOSR/HARC/Rice Program.

3.2.1 Laser Sources

Figure 3 depicts the laser parameter space of primary interest in laser/material interaction experiments. The three laser parameters are the incident laser wavelength λ (units: μm), the irradiance level I (units: W/cm^2), and the waveform parameter [a duty cycle PRF X τ where PRF is the pulse repetition frequency (units: s^{-1}) and τ is the pulse duration (units: s)]. For values of PRF X τ of 0.1 - 1, the waveform is continuous wave (cw) or quasi-cw, leading to an averaging over interaction phenomena. For very small values of PRF X τ of 10^{-7} or less, the waveform is essentially that of a single pulse (sp) in which there are no "memory" effects between pulses. For intermediate values of PRF X τ in the range 10^{-7} - 0.1, the repetitively pulsed (rp) limit, there are variable amounts of "memory" effects such as the interaction of subsequent pulses with a hot and chemically changing material. Figure 3 also shows the pulse fluence level F_p (units: J/cm^2) for the pulse duration ($\tau \approx 200$ ns) pertinent to our rp HF chemical laser experiments.

The incident laser wavelength λ leads to different laser effects on materials for fixed irradiance I and waveform PRF X τ parameters since the wavelength dependent coupling coefficient α_λ varies strongly with wavelength. Photon absorption, reflection, and scattering by the material (and its ablation plume, if present) determine the overall value of α_λ (which may also be time dependent). At a fixed wavelength λ and waveform PRF X τ, the pulse irradiance I may strongly influence phenomenology and effects since the mechanism and kinetics of material removal depend strongly on heating rate. Finally, at a fixed wavelength λ and irradiance I, the phenomenology and effects of laser/materials interactions may depend strongly on waveform PRF X τ; for example, single pulse (sp) laser irradiation typically produces transient effects and ablation on a timescale faster than thermal diffusion while corresponding continuous wave (cw) laser irradiation typically produces "steady state" effects and ablation with considerable thermal damage due to thermal diffusion out of the irradiated spot. [Note, however, that if the cw irradiance level is sufficiently high, it is also possible to reduce thermal damage effects by ablating material faster than the thermal relaxation time out of the irradiated spot.]
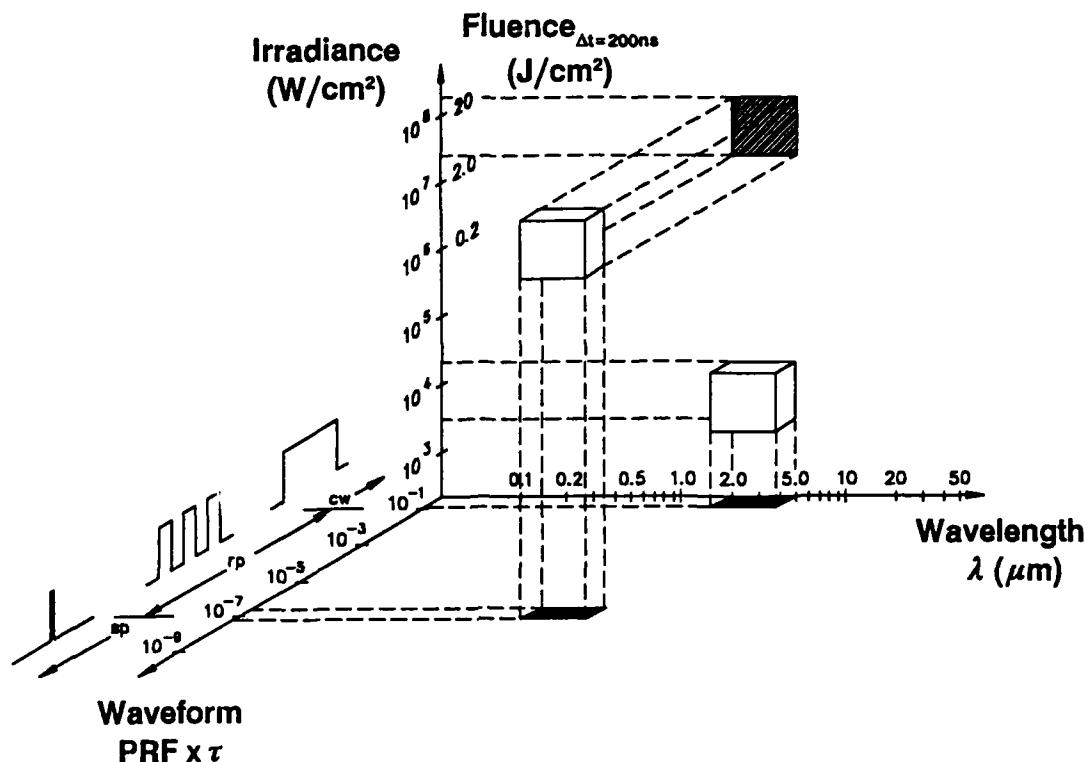
3.2.1 Laser Sources (continued)

Figure 3. Laser Parameter Space (with Typical CW and RP Regimes)

References 3 through 6 (included as Appendix A to this Final Technical Report) present information on the HARC laser sources and test facilities that have been constructed and used to explore the dependence of laser/materials interaction phenomenology and effects on laser parameters.

Larger scale experiments have also been completed using cw CO_2 electric discharge coaxial lasers (EDCLs) at the Weapons Laboratory (WL) Laser Test Facility at Kirtland AFB, NM. A series of materials screening ablation experiments was completed using EDCL 1 (a 15 kW maximum power cw CO_2 laser device) [Reference 1]. More extensive ablation experiments with enhanced target and plume diagnostic instrumentation systems were completed as part of the High Irradiance 2 Program using EDCL 2 (a 40 kW maximum power cw CO_2 laser device) [References 7 and 8], with partial support through the AFOSR/HARC/Rice Program.

9

3.2.2 Multiwavelength Optical Pyrometer System

Figure 4 shows a schematic diagram of the six wavelength (6λ) optical pyrometer system that has been developed to obtain time-resolved target front surface temperature and spectral emittance measurements. The system includes collection optics, fiber optics (transmitter and demultiplexer), six interference filters (9 - 10 nm FWHM bandpass) plus fast silicon photodiode/preamplifier combinations (Silicon Detector Corporation Model SD100-42-22-231, 10 μs risetime) to detect six wavelengths (λ = 481, 530, 632, 760, 870, and 990 nm) simultaneously, transient digitzers (LeCroy Model 6810) to acquire fast signal streams, and a fast 80386 computer (Dell Computer System 310) to store and reduce pyrometer data. All six wavelengths are selected to match plume transmission "windows". As an added precaution, the purge gas used to entrain ablation plumes in High Irradiance 2 Screening Test Series - 2 (STS-2) experiments was N_2 [Reference 8] (rather than air as in Reference 7); STS-2 plume emissions were therefore much less intense than those in STS-1 experiments [References 7-8]. In all tests, the 6λ pyrometer viewed a 1 mm diameter spot in the center of the ablation crater. The two longest wavelength channels (λ = 870 and 990 nm) were calibrated using a tungsten strip lamp spectral radiance standard placed in the target plane. Shorter wavelength channels were calibrated using graphNOL (G) spectral radiances measured during ablation together with independently measured values of spectral emittances [Reference 9]. The principles of operation and the data reduction procedures used to obtain accurate target front surface temperatures and spectral emittances are discussed in detail below. Sample results are discussed in Section 3.3.1.
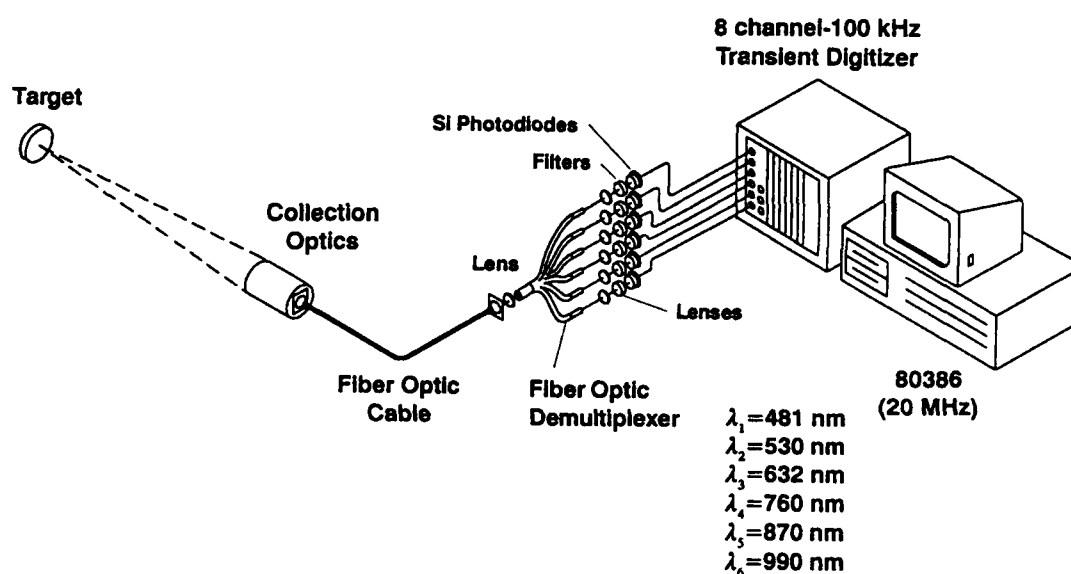

Figure 4. Six Wavelength Optical Pyrometer System

Figure 5 shows blackbody (spectral emittance ϵ_λ = 1 for all wavelengths λ; wavelength units: μm) spectral radiances (N_λ; units: W cm^{-2} μm^{-1} sr^{-1}) for temperatures in the 2500 - 5500 K range, calculated from the Planck distribution [References 10-11]:

$$N_\lambda = \epsilon_\lambda c_1/[\lambda^5(e^Z - 1)], \qquad [3]$$

where

$$Z = c_2/\lambda T, \qquad [4]$$

and c_1 (value: 11910.62 W μm^4 cm^{-2} sr^{-1}) and c_2 (value: 14387.86 μm K) are the first and second radiation constants, respectively.

N_λ (W cm^{-2}μm^{-1} sr^{-1})

$\epsilon_\lambda = 1$

Six-wavelength Pyrometer

.48 .63 .63 .76 .87 .99μm

5500K
5000K
4500K
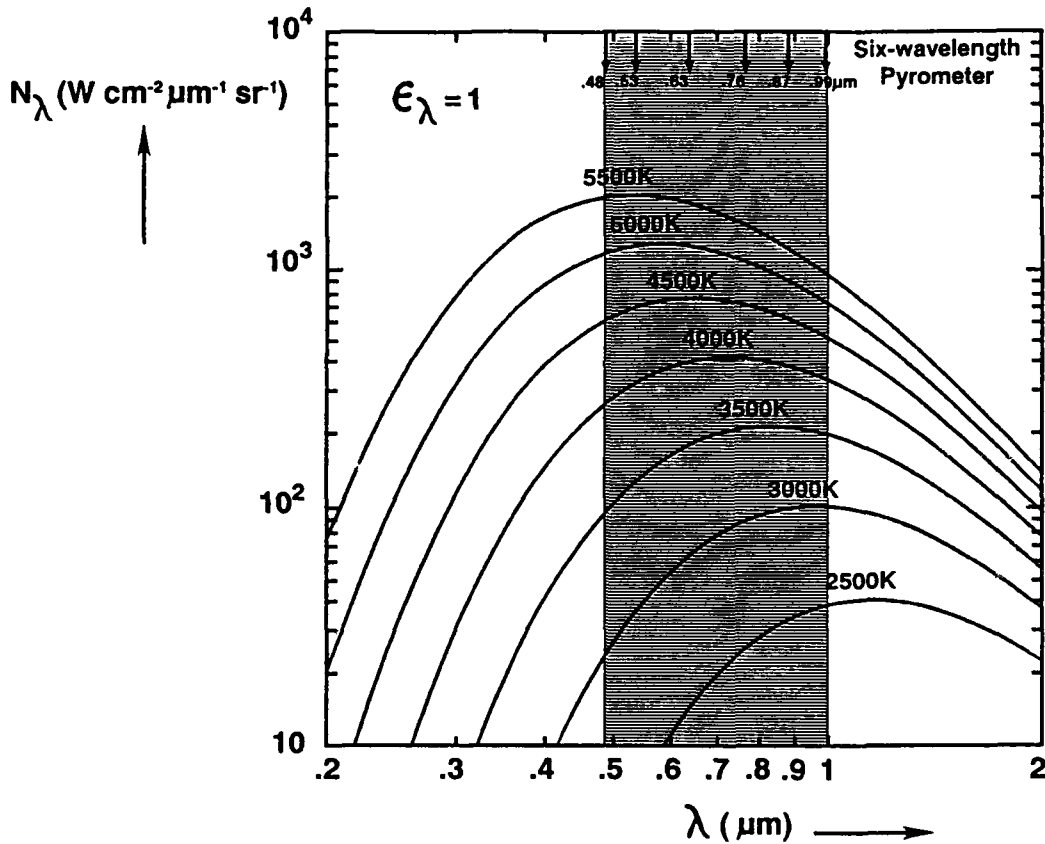4000K
3500K
3000K
2500K

λ (μm) ⟶

Figure 5. Blackbody Spectral Radiances

Figure 6 shows the overall data reduction procedure that was used to determine target front surface temperature from observed 6λ optical pyrometer data. Spectral radiance measurements were calibrated as described above. Plume emission spectra were measured to verify that no plume spectral interferences contaminated target spectral radiance data. The "best fit" target front surface temperature was determined at each observation time period (ca. 10 μs) by nonlinear regression analysis using the Marquardt algorithm [Reference 12] and the relation:

$$\chi^2 = \sum_{i=1}^{k} (N_{\lambda_i} - \tilde{N}_\lambda)^2 / \sigma_i^2,$$ [5]

where χ^2 is a measure of the total weighted variance of the full set of data (which is minimized by proper selection of temperature and spectral emittances),

k is the number of wavelengths λ included in the fit,

N_{λ_i} is the observed spectral radiance (or mean of the observed values if there are multiple measurements) at wavelength λ_i,

σ_i^2 is the variance of the observations at wavelength λ_i (assuming that there are multiple measurements), and

$\tilde{N}_\lambda$ is the trial spectral radiance determined from the Planck function incorporating a linear functional form for the spectral emittance ϵ_λ:

$$\epsilon_\lambda(T) = \epsilon_0(T) + \epsilon_1(T)\lambda.$$ [6]
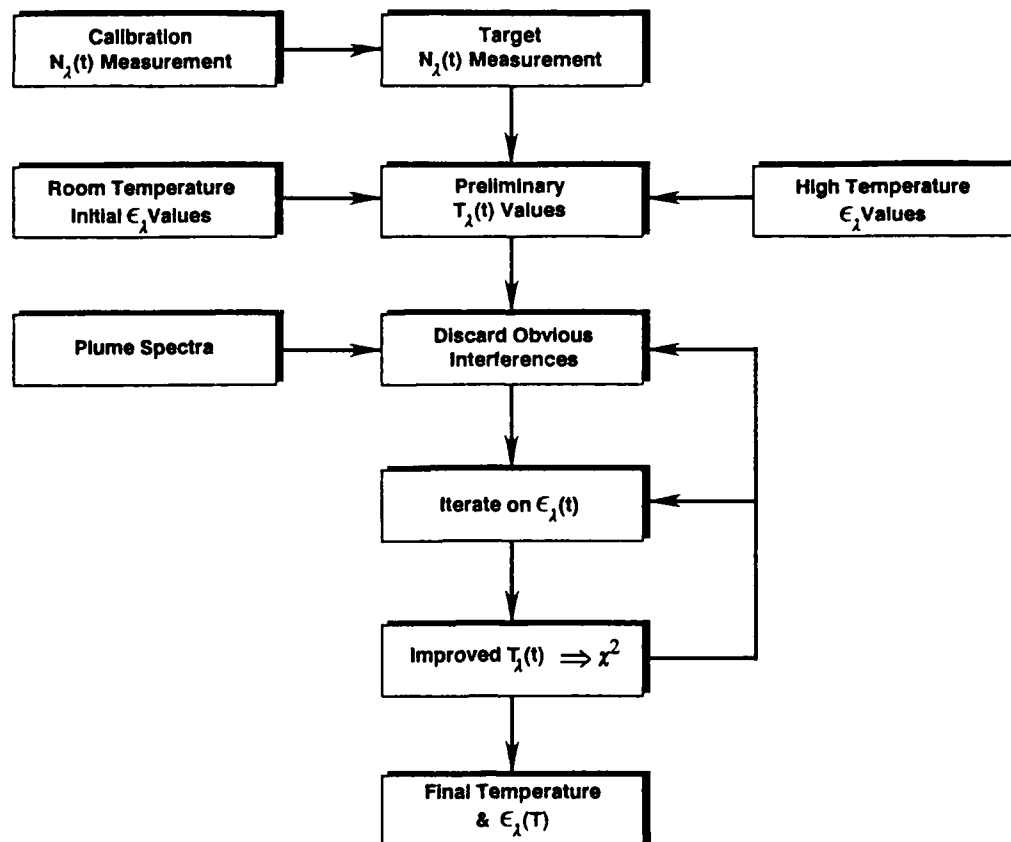
11

Figure 6. Overall Pyrometry Data Reduction Procedure

Figure 7 shows the quality of the nonlinear regression analysis fit using input spectral radiance data for a calibrated tungsten strip lamp spectral radiance secondary standard (Optronic Laboratories, Inc. Model 550, Standard IR-291) traceable to a National Institute of Standards and Technology (NIST) primary standard. The random standard deviation of the temperature fit is small (20 K). The fitted spectral emittance values (ranging from $\epsilon_{0.5} = 0.445$ to $\epsilon_{1.0} = 0.355$) are in fine agreement with literature values [Reference 13]; the mean absolute deviation is 0.012. Part of this small discrepancy may be due to the assumption of a linear spectral emittance (cf. Equation [6]). The fitting procedure can be improved by using measured high temperature values of spectral emittances derived from another method. However, the procedure already converges on fitted values of target spectral emittances that are in good agreement with independently measured values.

Target front surface temperature and spectral emittance measurements obtained with the 6λ optical pyrometer system are presented and discussed in Section 3.3.1 below.
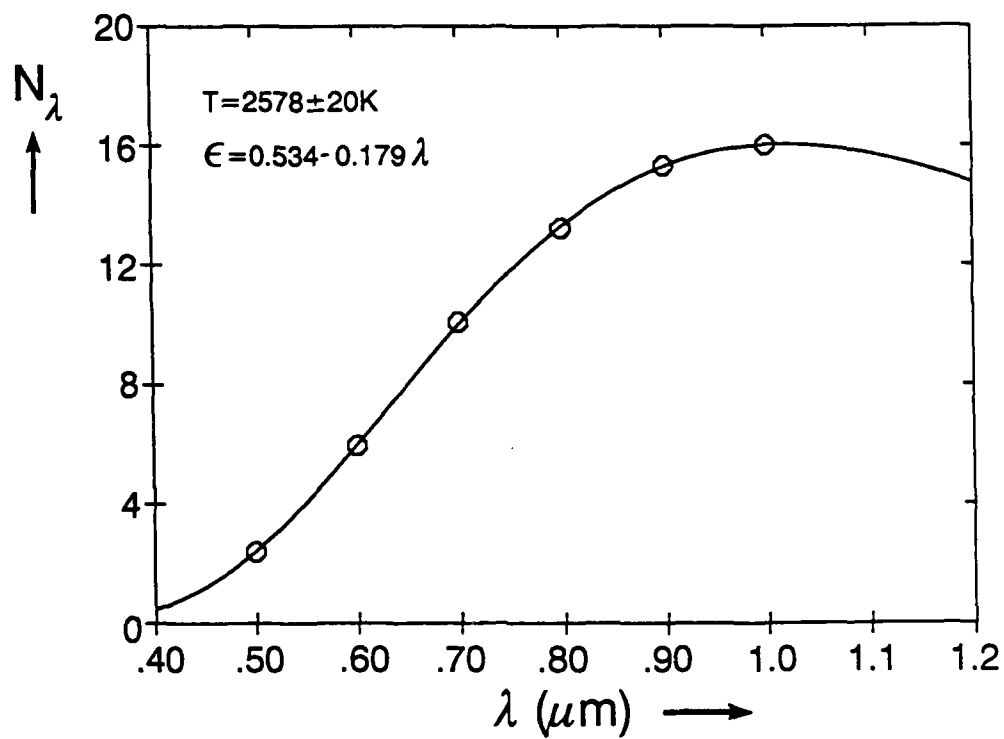
12

$$T = 2578 \pm 20K$$
$$\epsilon = 0.534 - 0.179\,\lambda$$

Figure 7. Nonlinear Regression Analysis Fit to Spectral Radiance Standard Data

13

3.2.3 Target Reflectance Diagnostic Instrumentation

Figures 8 (wavelength scaling diagnostic instrumentation subsystem) and 9 (overall apparatus) show the instrumentation that has been used in the AFOSR/HARC/Rice Program to obtain time-resolved target spectral reflectance measurements during laser ablation. A cw CO_2 laser was used as the damage laser to ablate target samples (*e.g.*, structural composites and carbon barrier materials) positioned tangent to an integrating sphere while time-resolved target front surface spectral reflectances were determined simultaneously at the damage laser wavelength and at additional probe laser wavelengths using multiple detector/filter (D/F) combinations. Key features of the wavelength scaling diagnostic instrumentation system are:

1) the cw CO_2 damage laser is a "workhorse" laser for irradiating target samples with controlled and well-specified beams at $\lambda = 10.6$ μm wavelength using powers up to *ca.* 800 W and peak irradiances between 10 - 200 kW/cm^2,

2) the target chamber provides a vacuum or a variable pressure atmosphere (air, *etc.*) environment, together with convenient access ports to direct probe lasers, view the target front surface, *etc.*; the chamber also includes a sample carousel and accurate positioning controls,

3) probe laser beams at shorter wavelengths ($\lambda = 0.515$ μm, 1.06 μm, and 2.9 μm) are directed onto the irradiated spot, and

4) time resolved target front surface reflectances $R_\lambda(t)$ are measured accurately and simultaneously at several wavelengths during laser ablation using an integrating sphere reflectance measurement system together with several sets of detectors and filters optimized for recording reflected signals from both damage and probe lasers.

Additional diagnostic instrumentation [a plume probe laser plus detector/filter combination, an optical multichannel analyzer (OMA) emission spectroscopy system, optical pyrometers, a burnthrough detector, *etc.*] is used to obtain time resolved measurements of plume attenuations, plume emission spectra, target front and back surface temperatures, burnthrough times, *etc.* Transient digitizers and computer based data acquisition instrumentation systems are used to record, store, and process calibrated signals for quantitative analysis of reflectance and other data. Further description of the overall apparatus capabilities is presented in Reference 4.

The integrating sphere (constructed from sandblasted aluminum) shown in Figures 8 and 9 is important since it "homogenizes" reflected light at all wavelengths to produce signals that are proportional to the total sample reflectances. These signals are accurately calibrated for high reflectances using diffuse reflectance standards [Labsphere gold and NIST white reflectance standards (*cf.* Section 3.1)] that are mounted in the same geometry as target samples. Signals are accurately calibrated for low reflectances using laser ablation of graphNOL targets; graphNOL has been studied extensively during ablation at $\lambda = 3.8$ μm [Reference 2] and at $\lambda = 2.7$ μm [References 14-15]. In addition, supplementary reflectance measurements on graphNOL have been obtained at $\lambda = 0.515$ μm and 1.06 μm wavelengths during cw HF chemical laser ablation. All of these calibration data are useful in providing an *in situ* check of reflectance measurements.

This basic reflectance measurement system has previously been used to measure time resolved target front surface reflectances of numerous carbon barrier materials irradiated by a cw deuterium fluoride (DF) chemical laser [References 1-2 and 16-17]. In the AFOSR/HARC/Rice Program, the system was extended to use a cw CO_2 laser as the primary damage laser and to monitor reflected signals from both the damage laser and from multiple probe lasers (such as cw Ar$^+$ and Nd:YAG lasers). The system works well at high data rates (up to 100 kHz) with modest probe laser powers (down to 100 mW incident on the target surface).

Table 2 lists specific features of the laser/detector/filter combinations used to measure target front surface reflectances at each wavelength during laser irradiation. Laser probe beams were modulated by a mechanical chopper and detected by a lock-in amplifier to improve signal-to-noise (S/N) characteristics of the system.
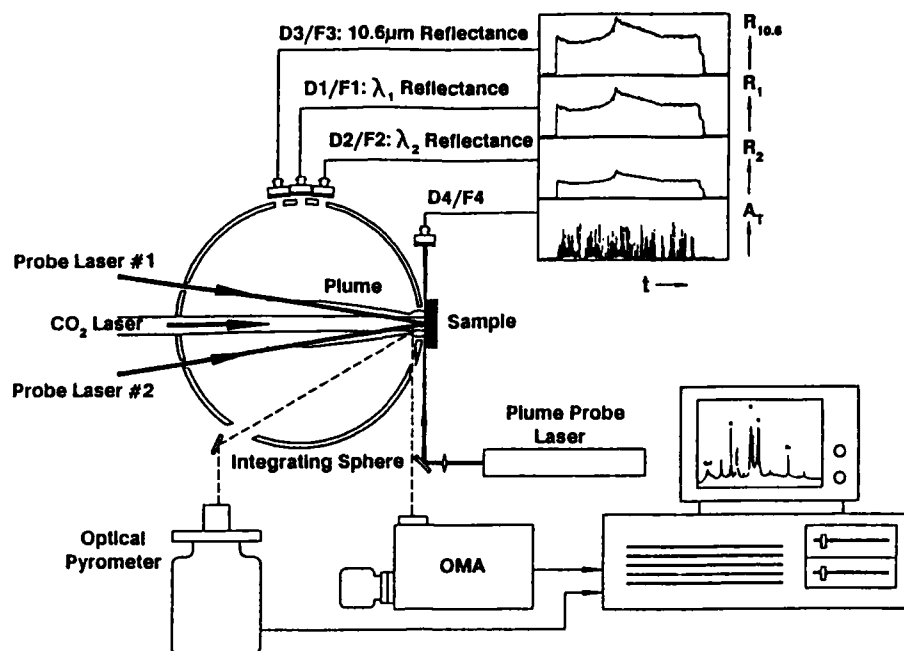
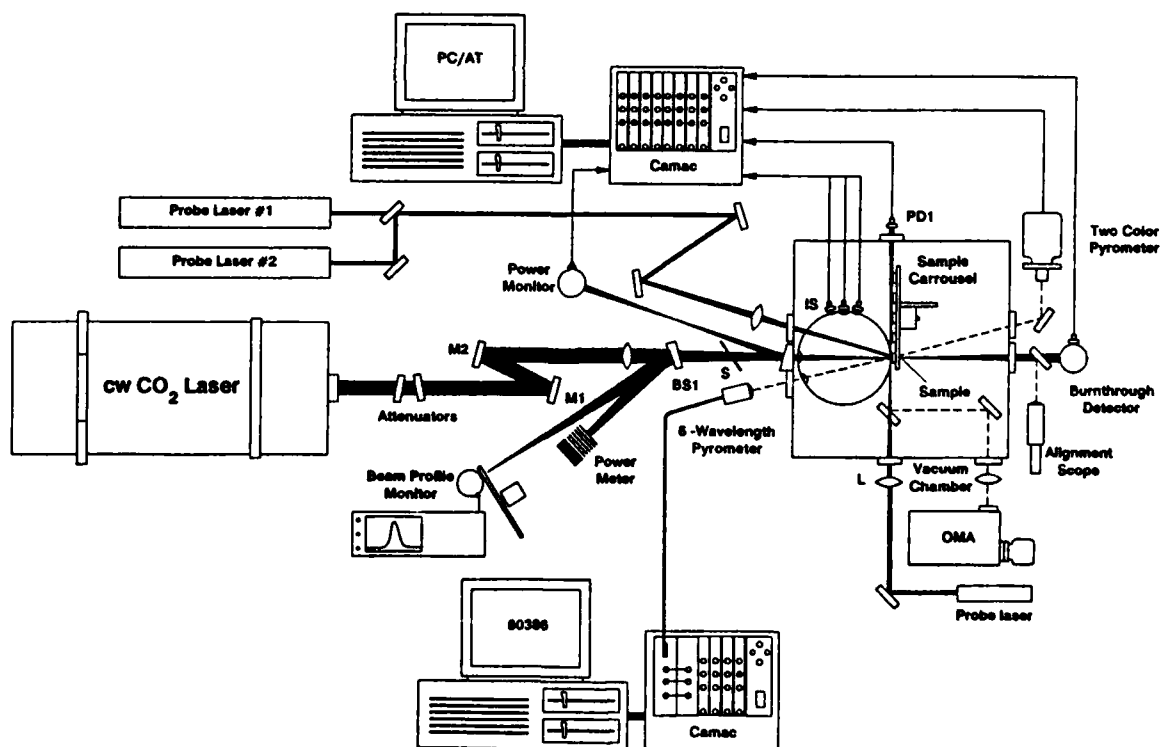Figure 8. Target Front Surface Reflectance/Coupling Coefficient Measurement System

Figure 9. Overall Experimental Apparatus for Coupling Coefficient Measurements

15

3.2.3 Target Reflectance Diagnostic Instrumentation (continued)

Table 2. Components Used to Measure Target Front Surface Reflectances.

Wavelength	Laser Device/Characteristics	Detector/Filter Characteristics
10.6 μm	cw CO_2 damage laser (Laser Corporation of America Model Falcon/800™) - Power on target: *ca.* 400 W, Spot size diameter on target: variable (0.8 - 3.0 mm)	HgCdTe detector (Infrared Associates, Inc. Model HCT-80) operated at 77 K - D^*: 2.3 X 10^{10} cmHz$^{1/2}$W^{-1}; risetime: 5 μs 10.6 μm filter (Spectrogon) - bandwidth: 0.24 μm, blocking: 10^3
2.9 μm	cw HF probe laser (Helios Inc. Model CLI) - Power on target: *ca.* 2 W, Spot size diameter on target: 0.9 mm	PbSe detector (Infrared Industries Model 5055) operated at 300 K - D^*: 2.5 X 10^9 cmHz$^{1/2}$W^{-1}; risetime: 50 μs 2.9 μm filter (Balzers Model V-29) - bandwidth: 0.1 μm; blocking: 10^3
1.06 μm	cw Nd:YAG probe laser (Amoco Laser Model ALC 1064) - Power on target: *ca.* 50 mW, Spot size diameter on target: 0.7 mm	Si detector (Silicon Detector Corp. Model SD100-42-22-231) operated at 300 K - NEP: 1.4 X 10^{-13} W; risetime: 10 μs 1.064 μm filter (Andover 064FS02-25) - bandwidth: 1 nm; blocking: 10^4
0.515 μm	cw Ar$^+$ probe laser (Coherent Inc. Model Innova 20) - Power on target: *ca.* 5 W, Spot size diameter on target: 0.6 mm	Si detector - same as at 1.06 μm 0.5145 μm filter (Corion SP5145-1-2282) - bandwidth: 1 nm; blocking: 10^4

Two cw probe lasers (at λ = 0.413 μm and 10.6 μm wavelengths) were also used to measure plume attenuation. The probe laser beams were positioned approximately 1 mm from initial target surfaces as materials were ablated by the cw CO_2 laser system. Minimum probe beam spot sizes of *ca.* 200 μm were used to provide sensitive detection of particles generated during laser ablation [Reference 18]. A silicon photodiode and a HgCdTe detector were used for λ = 0.413 μm and 10.6 μm probe beam detection, respectively. Both detector responses were monitored by a 125 MHz bandwidth digital oscilloscope (LeCroy Model 9400). No plume attenuation signals were detected during ablation of carbon-based materials (CBMs). However, structural composite materials (A101 and A105) produced significant plume attenuations due to discrete mass removal. Target reflectance measurements may be affected by the presence of plume particles.

Similar time-resolved target spectral reflectance measurements were completed during rp HF chemical laser ablation of graphNOL using the apparatus described in Reference 5. Reflectances (normalized to a gold standard) were measured at λ = 2.9 μm using an indium arsenide (InAs) detector (Judson JQ-5AP-5R00U)/LM733 amplifier/bandpass filter module viewing a miniature integrating sphere/attenuator mounted on the principal integrating sphere that monitored target reflectance. The detector/amplifier system has a bandwidth of 120 MHz and a gain of 10. It is relatively insensitive to RF noise due to its low input impedance. Reflected light waveforms mimiced the incident rp HF chemical laser pulse waveforms. Absolute reflectance for each pulse was determined by normalizing reflected light signals to incident HF laser light signals. Typically, reflectances were recorded for 500 or more pulses during each experiment.

Sample time-resolved cw and rp spectral reflectance measurements are presented and discussed in Section 3.3.2 below.

16

3.2.4 Plume Diagnostic Instrumentation

New plume diagnostic instrumentation systems have been developed in the AFOSR/HARC/Rice Program to provide temporal, spatial, and spectral information on plume species and plume optical properties. The plume diagnostic instrumentation systems schematically shown in Figure 10 include a computer controlled laser absorption spectrometer (CCLAS) system to probe ablation plumes and an optical multichannel analyzer (OMA) system to measure plume emission spectra. Both cw CO_2 and rp HF damage lasers are used to irradiate target samples such as carbon and composite materials with controlled and well-specified beams. The ablation plume expands into vacuum or into air, N_2, or He at specified pressures. The CCLAS system generates a tunable cw dye laser probe beam which is directed through the plume at a fixed, but adjustable, distance (typically, 0.5-4 mm) from the target surface with a small spot size (typically, 0.5 mm diameter) to provide spatial resolution. The transmitted probe beam is detected and ratioed to a reference beam. Transient digitizers and computer based data acquisition instrumentation systems are used to record, store, and process ratioed signals for quantitative spectroscopic analysis of plume species such as atoms, molecules, and ions.
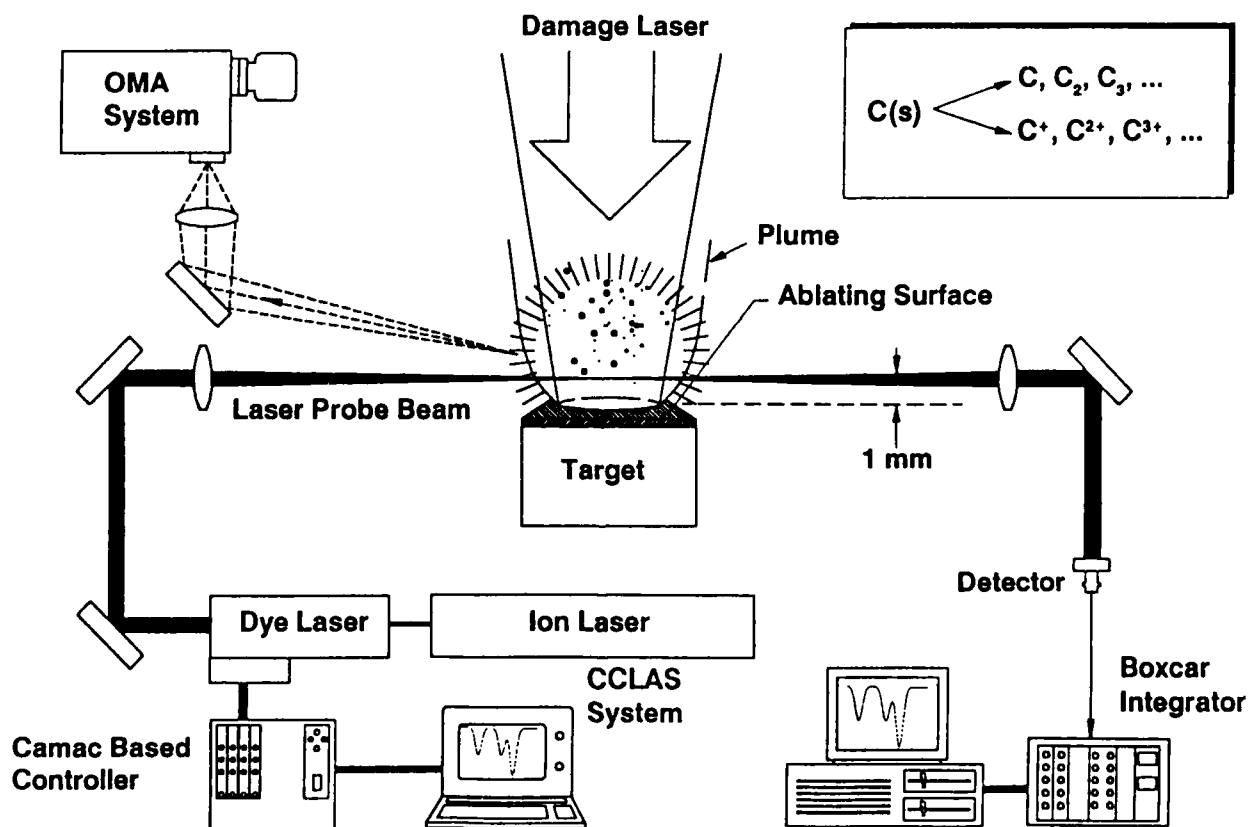

Figure 10. Plume Diagnostic Instrumentation System

Figure 11 schematically shows the Princeton Instruments Optical Multichannel Analyzer (OMA) system that was used to obtain survey plume emission spectra in the $\lambda = 340$-660 nm spectral region during both HARC and WL experiments.
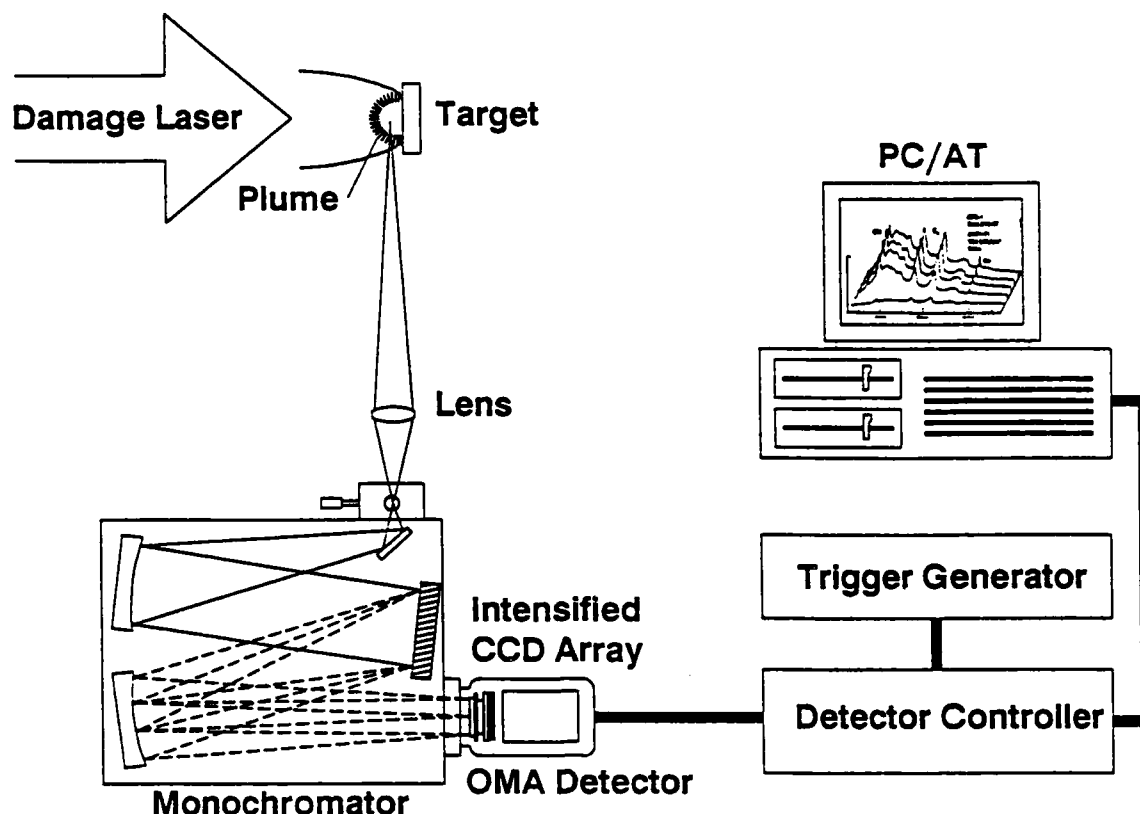
17

Figure 11. Optical Multichannel Analyzer (OMA) Plume Emission Spectroscopy System

The OMA system monochromator (Instruments SA Model HR320 0.32 m monochromator) was ordinarily equipped with a low resolution (150 line/mm) diffraction grating for survey spectroscopy. For selected experiments, the monochromator was equipped with a high resolution (2400 line/mm) diffraction grating to provide high dispersion (ca. 0.07 nm/diode element) spectra. Reference light sources (e.g., Hg lamps) were used to calibrate wavelength scales; for survey spectra, the accuracy is typically 0.2 nm. In all cases, serial gated spectra were recorded with an intensified CCD array mounted on the monochromator exit slit plane. The minimum gatewidth was 10 ns; typical gatewidths were: 100 ns (rp experiments) to 1 μs (cw experiments). Complete spectral scans were recorded (using a PC/AT computer) every 30 ms to yield information on the temporal evolution of plume emissions. Most of the spectra reported in Section 3.3.3 are not corrected for the spectral detection efficiency of the OMA system. A tungsten strip lamp traceable to NIST spectral radiance standards was used to obtain an instrumental correction function [Reference 19] for data processing of selected spectra. Corrected (i.e., true relative emission intensity) spectra are identified in Section 3.3.3.

The above OMA system is a commercially available instrument with significant temporal resolution limitations associated with the serial read-out nature of data recording. In future work, it may be advantageous to design and construct a new OMA system using a 2D detector array to provide rapid (10 μs or faster) parallel detection of plume spectral emission features, together with simultaneous monitoring of several plume spatial locations.

Figure 12 shows principal features of the computer controlled laser absorption spectrometer (CCLAS) system that was used to obtain high resolution plume absorption spectra during damage laser (cw CO_2, rp HF) irradiations. The CCLAS system and experimental techniques are described in detail elsewhere [References 20-21]. Briefly, the CCLAS system provides tunable cw dye laser probe beams with near-Doppler-limited spectral resolution over the entire visible spectral region and a portion of the near infrared spectral region (λ = 400-1000 nm). Frequency doubling crystals are used to upconvert tunable fundamental cw dye laser visible radiation at frequency ω_1 to tunable second harmonic cw laser-like ultraviolet (λ = 200-400 nm) radiation at frequency $2\omega_1$. Typical powers are 10-50 mW in fundamental beams and 1-5 μW in second harmonic beams. Spectral positions are usually measured to an accuracy of 0.04 cm^{-1} in the visible spectral region over a scanning range of 100 cm^{-1}. Most scans were completed in 3-5 cm^{-1} increments at typical spectral scan rates of 1 cm^{-1}/s (cw experiments) or 0.05 cm^{-1}/s (rp experiments) in the vicinity of particular spectral transitions. The spatial resolution of probe beams was 0.5 mm or better. The temporal resolutions of signal detection were typically 1-10 ms and *ca.* 50 ns for cw and rp experiments, respectively. The spectral scan rate as well as the temporal, spatial, and spectral resolution of the CCLAS system can all be upgraded for specific requirements.
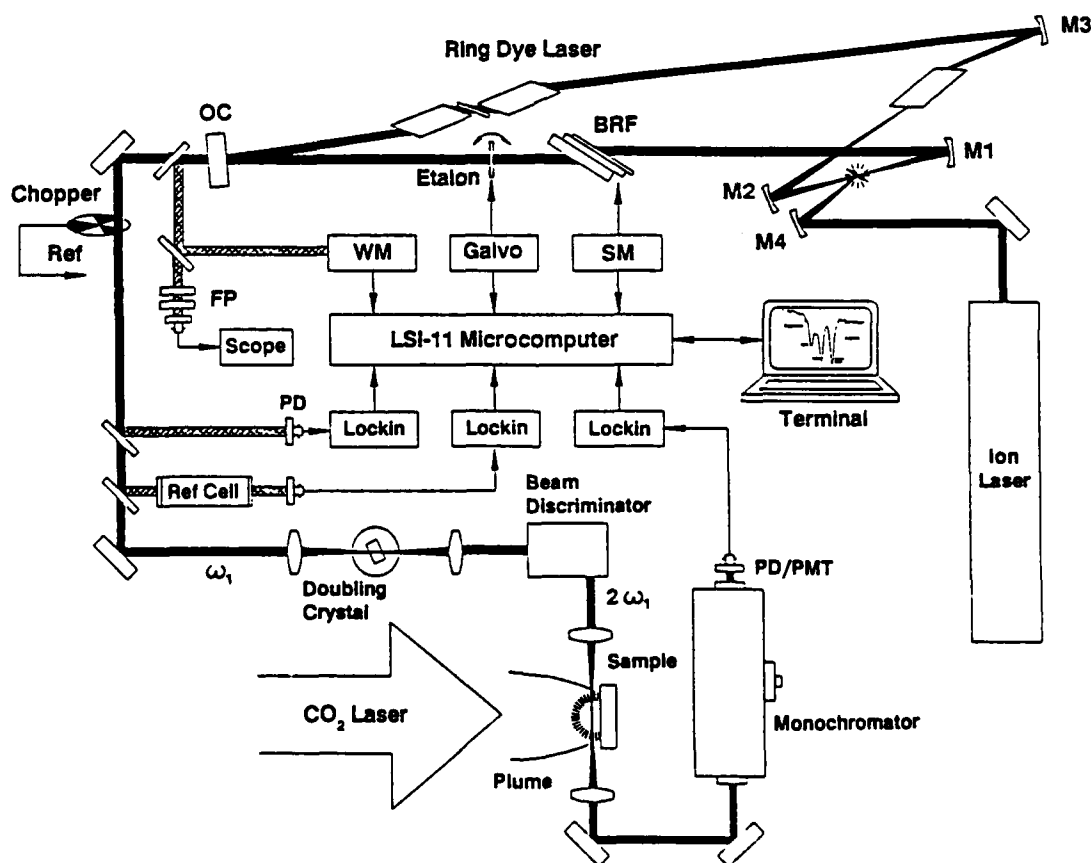

Figure 12. Computer Controlled Laser Absorption Spectrometer (CCLAS) System

19

During the AFOSR/HARC/Rice Program, the CCLAS system has been modified and/or extended in the following ways:

1) tunable ultraviolet (UV) wavelength operation down to $\lambda = 235$ nm has been obtained by using new frequency doubling crystals [β-barium borate (BBO; acquired from CSK Company; 31° and 65° z-cut crystals)] to provide tunable outputs near 235 nm and 308 nm for SiO and Al experiments, respectively,

2) a new fast time-resolved detector (Silicon Detector Corporation Model SD100-42-22-231 Si photodiode; 40 ns risetime), fast amplifier (Comlinear Model 220 amplifier; 190 MHz bandwidth; gain: 50), and fast transient recording systems (a LeCroy Model 9400 digital oscilloscope with 125 MHz bandwidth and a Stanford Research Systems Model SR250 boxcar integrator) have been used to permit plume measurements under sp and rp irradiation conditions,

3) a high speed ratiometer (75 kHz bandwidth; based on Analog Devices Model AD532 Internally Trimmed Integrated Circuit Multiplier) has been constructed and used to obtain ratioed absorption signals with faster temporal resolution, and

4) high stray light (particularly plasma emission) rejection optics consisting of apertures, bandpass filters, and a monochromator (Instruments SA Model H-20V 0.2 m monochromator equipped with a 1200 line/mm diffraction grating) have been developed to reduce interference from non-laser probe signals.

It is worth noting that there is no commercial instrumentation available that can provide the unique combination of broad scanning range, high spectral/temporal/spatial resolution, species sensitivity, and stray light rejection that the present CCLAS system offers. The CCLAS system probes highly luminous plumes to determine species abundances and optical properties, as well as plume temperatures, *etc.* The information content of plume absorption spectra that the CCLAS system obtains is very extensive:

1) both nascent (*i.e.*, directly ablated and/or vaporized) and chemically formed (due to plume species reactions and/or to plume/atmosphere reactions) vapor phase species can be monitored sensitively (to number densities as low as $10^{12}/cm^3$) and measured quantitatively with excellent temporal/spatial/spectral resolution as a function of laser interaction parameters (wavelength, irradiance, waveform, *etc.*) for all irradiated materials (including the most refractory elements and compounds),

2) the kinetics of chemical reactions on the target surface and/or in the plume can be obtained as a function of laser parameters, atmospheric composition, distance from the irradiated surface, material composition, *etc.*, and

3) the abundances, energy contents, and optical properties of plume species as well as plasma parameters (electron density and temperature, plasma opacity, *etc.*) can be determined by measurements on relative absorption intensities and spectral linewidths.

It is essential to use a high spectral brilliance source in order to penetrate the vapor and/or plasma and to permit measurement of quantitative spectral absorption characteristics of atomic, molecular, and plasma species in ablation plumes. Considerable progress has been made in the AFOSR/HARC/Rice Program, as described in Sections 3.3.3 and 3.3.4 below. Additional improvement of plume diagnostic instrumentation can still be accomplished by extending the wavelength coverage to the vacuum ultraviolet spectral region (*cf.* Section 4.0 below).

3.2.5 Mass Spectrometric Instrumentation

No new mass spectrometric instrumentation was constructed since AFOSR funding was not available for required capital equipment. However, HARC/Rice personnel completed initial time-resolved quadrupole mass spectrometric measurements on pyrolysis and ablation products generated by cw CO_2 laser irradiation of cured epoxy resins and structural composite materials. Figure 13 shows a schematic diagram of the existing quadrupole mass spectrometer system [Reference 22] and the laser irradiation geometry that was used for these measurements.
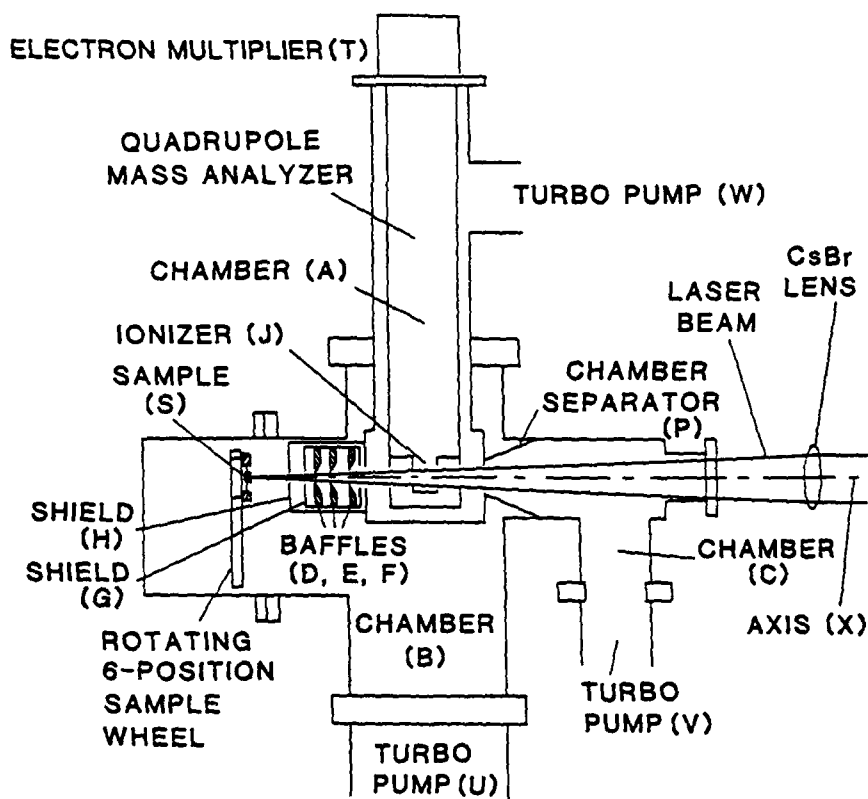

Figure 13. Laser Vaporization/Quadrupole Mass Spectrometer System

The apparatus is described in Reference 22. AFOSR/HARC/Rice Program results are presented and discussed in Section 3.3.5 below.

3.3 LASER/MATERIALS INTERACTION STUDIES

HARC/Rice personnel completed several laser/materials interaction studies on graphNOL and other materials as part of the AFOSR/HARC/Rice Program:

1) time-resolved target front surface temperature and spectral emittance measurements during irradiation by a cw carbon dioxide (CO_2) laser system,

2) time-resolved spectral reflectance measurements during irradiation by cw CO_2, cw HF/DF, and rp HF laser systems,

3) time-resolved laser probe absorption spectroscopy and total extinction measurements and emission spectroscopy measurements on plumes generated by cw and rp laser irradiations, and

4) laser pyrolysis and ablation experiments.

The following Sections 3.3.1 through 3.3.4 present summary results for these AFOSR/HARC/Rice Program studies. More complete discussion is contained in several publications [References 1-2 and 23-24].

GraphNOL results are highlighted in this Final Technical Report. GraphNOL (G) is a fine-grained polycrystalline pure carbon with nearly isotropic and well-known thermal properties that has been used extensively as a baseline material in many laser effects programs [References 7, 8, and 17]. This carbon barrier material is an excellent reference material for studies of laser/materials interactions.

3.3.1 Target Front Surface Temperature/Emittance Measurements

The six wavelength (6λ) optical pyrometer system described in Section 3.2.2 above was used to measure time-resolved target front surface temperatures and spectral emittances during the High Irradiance 2 Program Screening Test Series - 2 (STS-2) experiments completed at the Laser Test Facility, Weapons Laboratory, Kirtland AFB, NM [Reference 8]. Target materials (graphNOL and othre carbon barrier materials - *cf*. Section 3.1) were ablated by the EDCL 2 cw CO_2 laser device at four nominal irradiance levels: 25, 60, 100, and 150 kW/cm². The following sample data are discussed (entries are listed as DDD-xx where DDD is the Julian calendar day and xx is the shot number on that day):

Table 2. Sample Data Selected for Presentation

Material	25 kW/cm²	60 kW/cm²	100 kW/cm²	150 kW/cm²
G	153-11	153-2	156-22	153-18, 156-2
C101		157-21	156-15	157-10
C102		157-4	156-16	156-12, 157-11
C104		157-5	156-17	157-13
C105		143-9	156-24	157-14
C106		157-6	145-7	157-15
C107	144-16	143-14	156-20	142-15
C108		143-15	156-19	142-14

The above selection of tests provides initial experimental data to compare phenomenology and effects over the irradiance range studied in STS-2. Many other data sets are available. The results will be discussed more fully in future publications.

3.3.1.1 GraphNOL Data

Figure 14 shows target front surface temperature and spectral emittance data recorded by the 6λ optical pyrometer system during Run #153-11 [ablation of graphNOL (G) at an irradiance of 25 kW/cm^2]. The top trace displays the time-resolved brightness temperature recorded using a single pyrometer channel at $\lambda = 0.532$ μm wavelength assuming blackbody spectral emittance at 0.532 μm (i.e., $\epsilon_{0.53} = 1$). After an initial temperature rise during the first 100 ms, the target reaches "steady-state" ablation conditions with a constant front surface temperature. The middle trace displays values of the spectral emittance at short ($\lambda = 0.53$ μm) and long ($\lambda = 0.99$ μm) wavelengths calculated by the procedure described in Section 3.2.2. Spectral emittances are smoothed by using Blackman's window [Reference 25] to filter out high frequency data components. The bottom trace displays the true time-resolved temperature calculated from the nonlinear regression fit to all six pyrometer wavelength channels using a linear fit to the spectral emittances at these wavelengths. The calculated true temperature data are always "noisier" than single wavelength pyrometer channels. In addition, there are some negative "spikes" (i.e., rapid temperature decreases) which are probably artifacts from the fitting procedure.
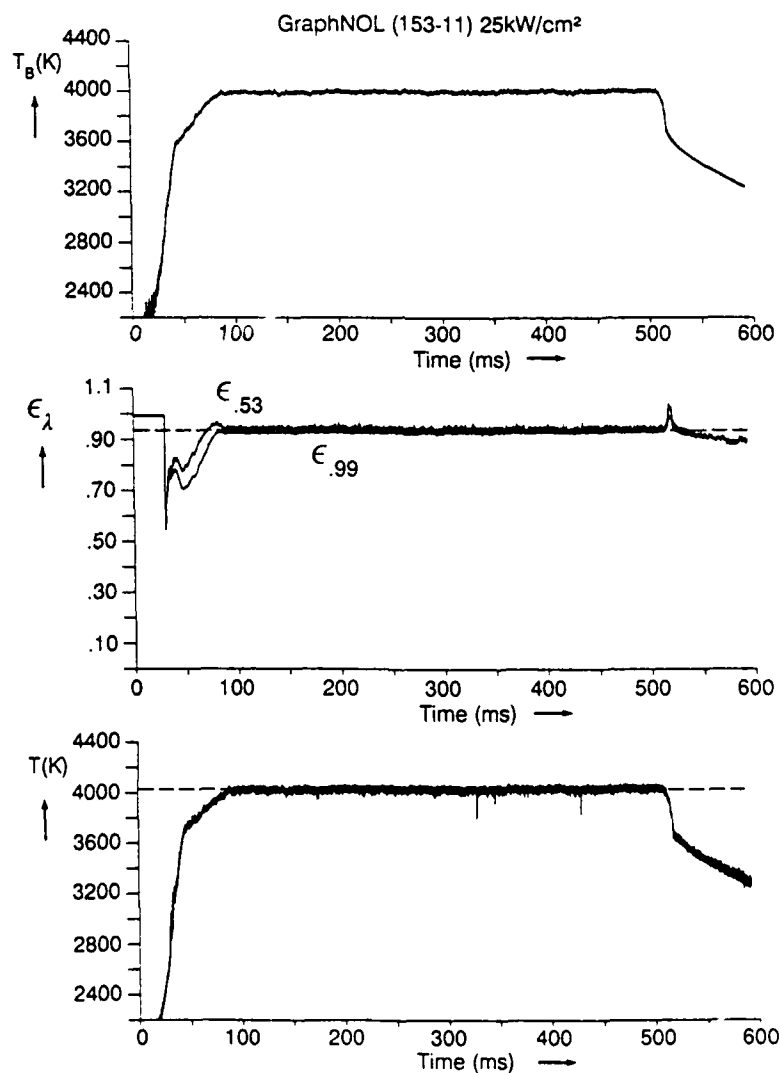

Figure 14. Time-Resolved Front Surface Temperature/Spectral Emittance Data Traces

23

3.3.1.1 GraphNOL Data (continued)

Figure 15 shows the quality of the nonlinear regression analysis fit for a subset (approximately 1000 "steady-state ablation" points) of G (153-11) data. The random standard deviation of the temperature fit is very small (1.7 K). The fitted spectral emittance values (ranging from $\epsilon_{0.48} = 0.95$ to $\epsilon_{0.99} = 0.93$) are in fine agreement with independent high temperature reflectance measurements on G (during cw CO_2 laser ablation at an irradiance of 9 kW/cm^2) which yield spectral emittance values $\epsilon_{0.515} = 0.96 \pm 0.02$ and $\epsilon_{1.06} = 0.94 \pm 0.02$ (cf. Section 3.3.2). It is still possible, however, that there are systematic errors in spectral radiance calibration which can alter the temperature (and spectral emittance) fit shown in Figure 15. Future experiments using a bright spectral radiance standard in the target plane, together with higher collection efficiency multi-wavelength pyrometer optics, are needed to eliminate possible systematic errors in data reduction. The fitted front surface temperature of G in air during 25 kW/cm^2 ablation (T = 4026.3 ± 1.7 K) is in good agreement with the temperature calculated from a realistic model (T = 3963 K using Livermore vapor pressure data or T = 4106 K using JANAF vapor pressure data) of carbon ablation into an atmospheric pressure environment [References 26-27].
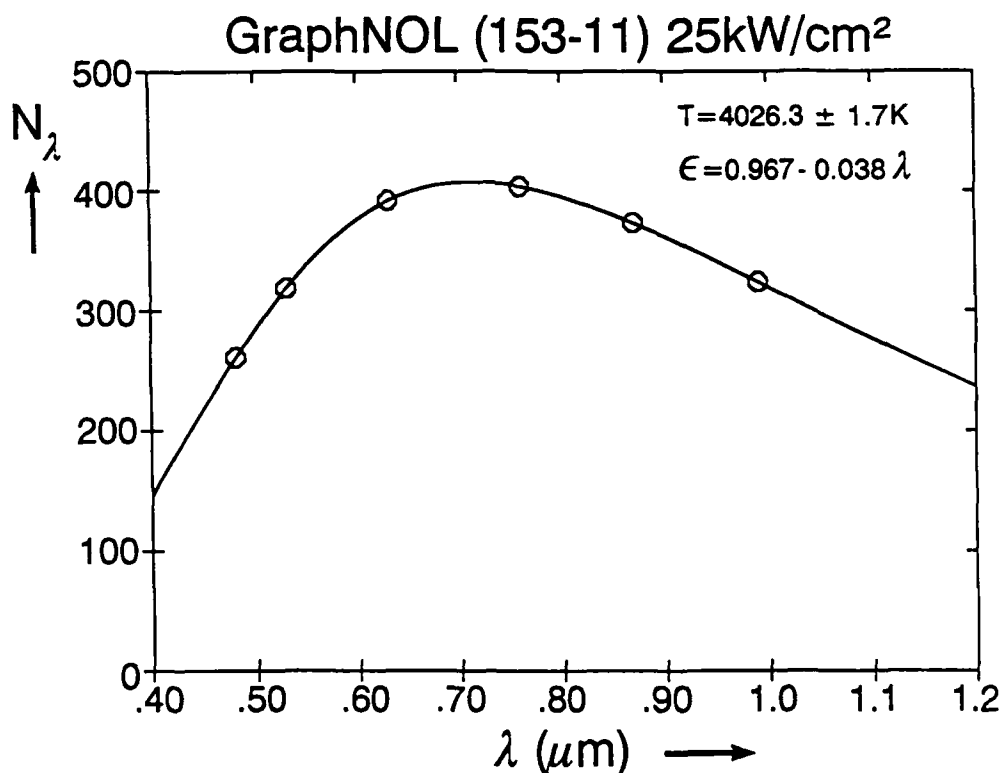

Figure 15. Nonlinear Regression Analysis Fit of G (153-11) Multiwavelength Pyrometer Data

Appendix B collects data traces in the format shown in Figure 14 for all the runs listed in Table 2. Figure 16 collects graphNOL target front surface temperature data traces for all four irradiance levels (using runs #153-11, 153-2, 156-22, and 153-18 for 25, 60, 100, and 150 kW/cm^2, respectively). These data traces show one channel ($\lambda = 0.532$ μm) of the 6λ pyrometer; true temperatures are plotted using the measured spectral radiances and the fitted spectral emittance $\epsilon_{0.53} = 0.95$, which was the same for all irradiance levels.

3.3.1.1 GraphNOL Data (continued)

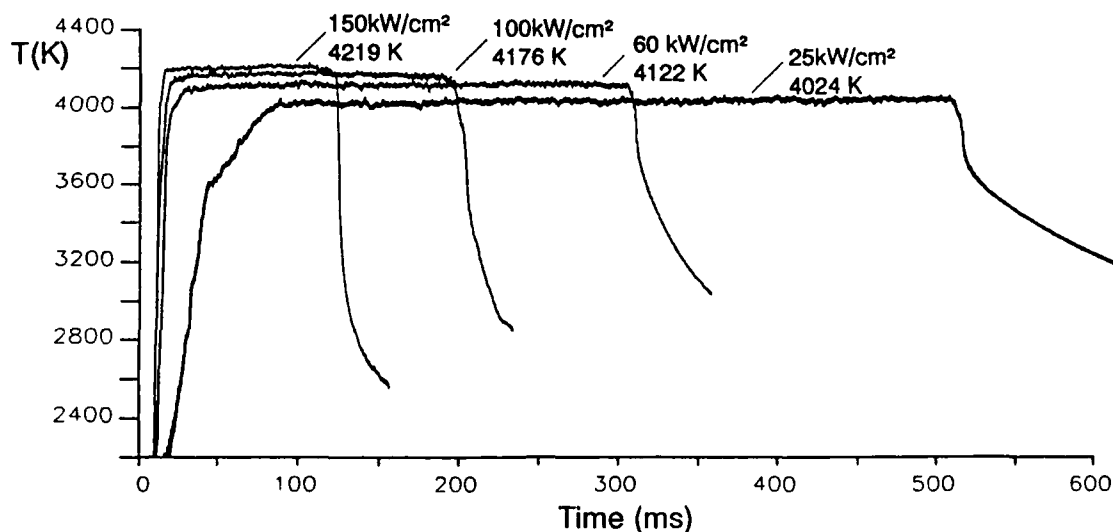Figure 16. Time-Resolved Front Surface Temperature Data Traces for Material G

Note that the target front surface temperature rises from T = 4024 K at the lowest irradiance (I = 25 kW/cm²) through T = 4122 K (I = 60 kW/cm²) and T = 4176 K (I = 100 kW/cm²) to T = 4219 K at the highest irradiance (I = 150 kW/cm²). This increase in the front surface temperature is expected as the mass loss rate (and, hence, ablation pressure) increases as a function of increasing irradiance. The magnitude of the observed increase (ca. 200 K) is not, however, matched by the increase (ca. 100 K) predicted by an ablation model [References 26-27]. It should be possible to achieve complete agreement between experiment and theory for a simple model carbon such as graphNOL and thereby develop confidence in our physical understanding of carbon ablation, but further refinement of the ablation model and better input information on the vapor pressures of carbon vapor species are required.

GraphNOL (G) is a particularly well behaved carbon ablator. As shown by data such as Figure 16 and by filtered HYCAM films [high frame rate (typically, 7000 frames/second) films taken with blue filters and proper exposure levels designed to obtain high contrast target front surface images during laser ablation], G ablates cleanly in an apparent "steady state" manner at a given irradiance level, yielding very stable temperatures and very uniform spectral emittances over the ranges of temperature and wavelength explored. Very little discrete mass removal is observed in G ablation, so the enthalpy of mass removal should be the equilibrium thermochemical ablation value [Reference 23]. In future experiments, graphNOL will be used as an internal standard to calibrate instruments and obtain reproducible data.

3.3.1.2 Material C101 Data

Appendix B contains three sets of time-resolved target front surface temperature and spectral emittance data for material C101 irradiated at 60 kW/cm² (run #157-21), at 100 kW/cm² (run #156-15), and at 150 kW/cm² (run #157-10). These data are presented in the same format as for sample graphNOL (G) data shown in Figure 14 (cf. Section 3.3.1.1). Figure 17 shows one of these data sets (run #157-10 at 150 kW/cm²).
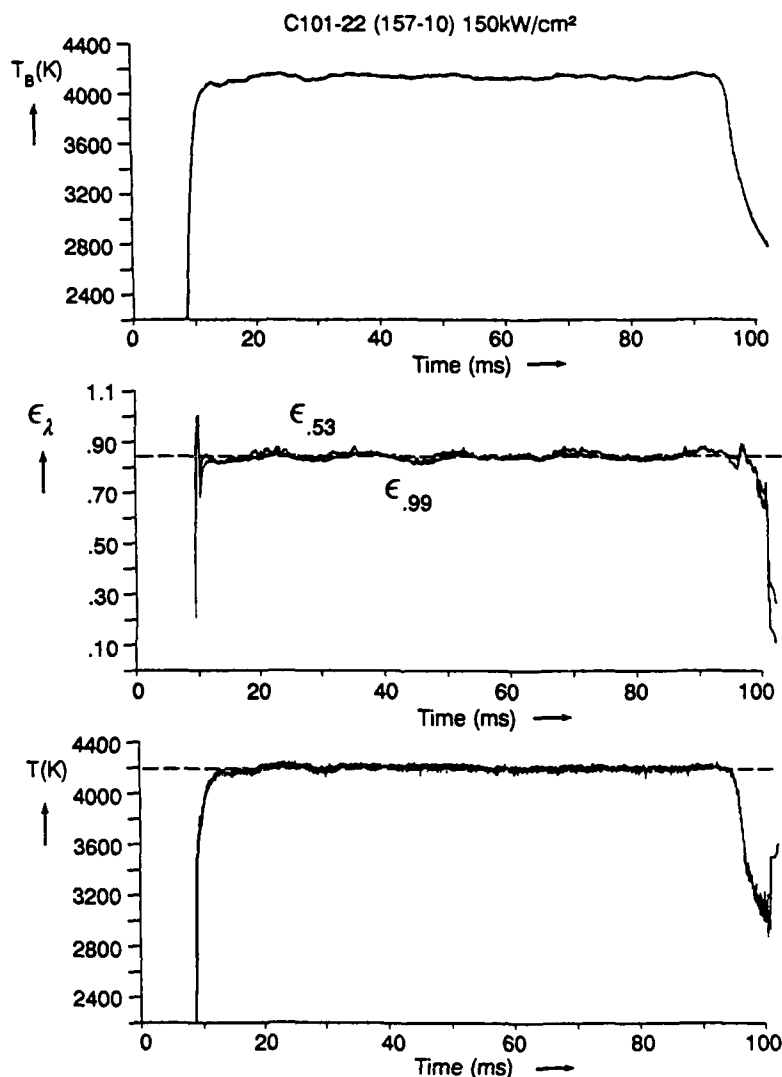

Figure 17. Time-Resolved Front Surface Temperature/Emittance Data Traces for Material C101

Note that the target front surface "steady state" temperature of material C101 ablating at an irradiance of 150 kW/cm² into atmospheric pressure is approximately 4200 K and is very similar to the G steady state temperature under similar conditions (cf. Section 3.3.1.1), but that the spectral emittances of C101 are lower (ca. 0.84 - 0.85) than for G in the λ = 0.53 - 0.99 μm spectral region. Appendix B data for material C101 ablation at lower irradiances (I = 25 - 100 kW/cm²) show target front surface "steady state" temperatures that are very similar to G results under the same conditions. Spectral emittances for material C101 at these lower irradiances are similar (ca. 0.85 - 0.90 in the λ = 0.99 - 0.53 μm spectral region) to the corresponding values at I = 150 kW/cm².

26

3.3.1.2 Material C101 Data (continued)

Direct measurements (*cf.* Section 3.3.2) of target spectral reflectance during irradiation of material C101 at 100 kW/cm^2 yield spectral emittances of 0.88 ± 0.01 and 0.85 ± 0.02 at $\lambda = 0.52$ μm and 1.06 μm, respectively, in close agreement with the fitted values obtained from pyrometry data for material C101 ablated at 100 kW/cm^2 (*cf.* run #156-15 in Appendix B).

Material C101 is another well behaved carbon ablator. As shown by data such as Figure 17 and by filtered HYCAM films, C101 ablates cleanly in an apparent "steady state" manner at a given irradiance level, yielding very stable temperatures and very uniform spectral emittances over the ranges of temperature and wavelength explored. Very little discrete mass removal is observed in C101 ablation, so the enthalpy of mass removal should be the equilibrium thermochemical ablation value [Reference 23]. The differences in laser hardness between materials G and C101 are due solely to differences in optical properties [Reference 9].

3.3.1.3 Material C102 Data

Appendix B contains four sets of time-resolved target front surface temperature and spectral emittance data for material C102 irradiated at 60 kW/cm² (run #157-4), at 100 kW/cm² (run #156-16), and at 150 kW/cm² (runs #156-12 and #157-11). These data are presented in the same format as for sample graphNOL (G) data shown in Figure 14 (cf. Section 3.3.1.1). Figure 18 shows one of these data sets (run #157-11 at 150 kW/cm²).
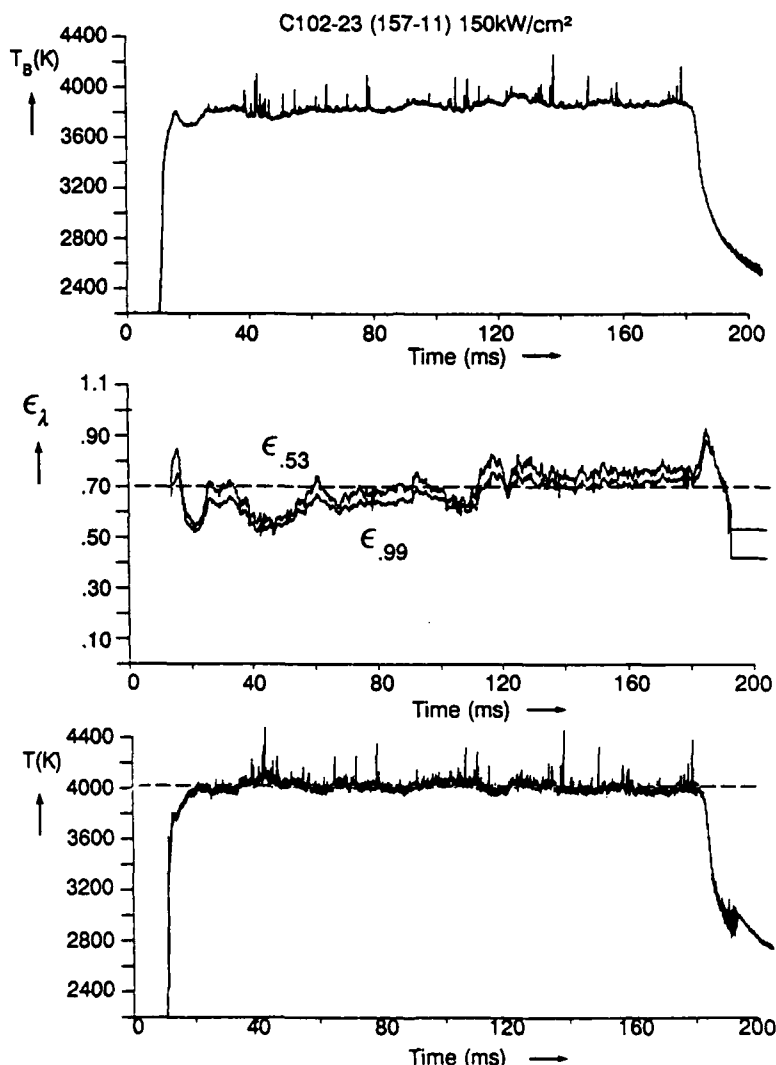

Figure 18. Time-Resolved Front Surface Temperature/Emittance Data Traces for Material C102

Note that the target front surface "steady state" temperature of material C102 ablating at an irradiance of 150 kW/cm² into atmospheric pressure is approximately 4050 K (nearly 150 K less than for materials G and C101 under the same conditions) and that the temperature exhibits large intermittent "spikes" throughout the run. Appendix B data for other runs on material C102 show similar large intermittent temperature "spikes" at all irradiances. Inspection of HYCAM "blue movies" shows that the front surfaces of ablating C102 targets display eruptions of material (resembling small volcanos that sometimes eject particles); these eruptions are probably related to the rapid front surface temperature variations.

28

3.3.1.3 Material C102 Data (continued)

We speculate that the decreased front surface temperature of material C102 relative to materials G and C101 is caused by higher carbon vapor pressure; perhaps the distribution of carbon vapor species has shifted from that characteristic of thermochemical equilibrium ablation. We also note that OMA plume emission spectra show only typical diatomic carbon spectral features (cf. Section 3.3.3); there is no evidence for any new emission features which might correspond to spectral transitions of metal atoms ablated from material C102.

The spectral emittances of material C102 are substantially lower (in the range 0.5 - 0.7 for the first 100 ms of run #157-11; cf. Figure 18) than for either materials G or C101 under the same conditions. There is also a "jump" in the average emittances at later times in run #157-11 and in other runs (cf. Appendix B). Spectral emittances show much more variation during each run than for materials G and C101, suggesting that the front surface composition and optical properties of material C102 are changing rapidly during ablation.

Direct measurements of target spectral reflectance during irradiation of material C102 at 9 kW/cm² (cf. Section 3.3.2) yield spectral emittances of 0.70 ± 0.10 and 0.59 ± 0.07 at $\lambda = 0.52$ μm and 1.06 μm, respectively, in good agreement with the fitted values obtained from pyrometry data for material C102 ablated at 60 - 150 kW/cm². However, similar direct measurements completed during irradiation of material C102 at 100 kW/cm² (cf. Section 3.3.2) yield higher spectral emittances in the range 0.85 - 0.88. A possible explanation for this discrepancy is that different amounts of reflective films are formed in the HARC (microscale) experiments compared to the EDCL 2 (larger scale) experiments.

Material C102 is a "harder" ablator than materials G and C101. Although some discrete mass removal is observed in filtered HYCAM films of the target front surface and the plume, only a small fraction of the total mass is probably ablated in the form of discrete particles. The major increase in hardness of material C102 relative to G is undoubtedly due to differences in optical properties. However, it is also possible that material C102 generates a distribution of carbon vapor species that has a larger enthalpy of mass removal than the value pertinent to thermochemical equilibrium.

29

3.3.1.4 Material C104 Data

Appendix B contains three sets of time-resolved target front surface temperature and spectral emittance data for material C104 irradiated at 60 kW/cm² (run #157-5), at 100 kW/cm² (run #156-17), and at 150 kW/cm² (run #157-13). These data are presented in the same format as for sample graphNOL (G) data shown in Figure 14 (*cf.* Section 3.3.1.1). Figure 19 shows one of these data sets (run #157-13 at 150 kW/cm²).
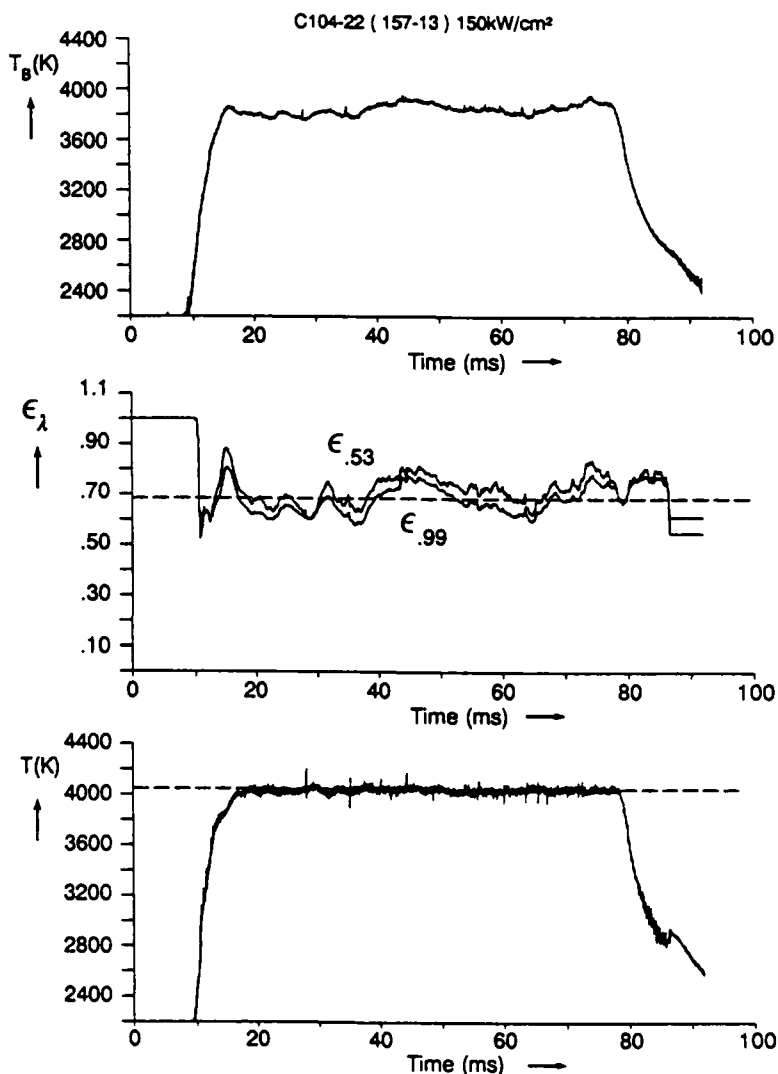

Figure 19. Time-Resolved Front Surface Temperature/Emittance Data Traces for Material C104

Note that the target front surface "steady state" temperature of material C104 ablating at an irradiance of 150 kW/cm² into atmospheric pressure is approximately 4050 K (very similar to that for material C102 but nearly 150 K less than for materials G and C101 under the same conditions) and that the temperature exhibits intermittent "spikes" throughout the run. Appendix B data for other runs on material C104 show similar intermittent temperature "spikes" at all irradiances. Inspection of filtered HYCAM films shows that the front surfaces of ablating C104 targets display eruptions of material (resembling small volcanos that sometimes eject particles); as in the case of material C102, these eruptions are probably related to the rapid front surface temperature variations.

30

3.3.1.4 Material C104 Data (continued)

As in the case of material C102, the decreased front surface temperature of material C104 relative to materials G and C101 may be caused by higher carbon vapor pressure which may indicate that the distribution of carbon vapor species is shifted from that characteristic of thermochemical equilibrium ablation. In addition, OMA plume emission spectra show new emission features which probably correspond to spectral transitions of metal atoms ablated from material C104 (*cf.* Section 3.3.3). Ablation of metal atoms leads to a decrease in the enthalpy of mass removal since carbon is one of the "hardest" ablators [Reference 1].

The spectral emittances of material C104 are substantially lower (in the range 0.6 - 0.8 for run #157-13; *cf.* Figure 19) than for either materials G or C101 under the same conditions. These emittances are slightly higher than those for material C102 under the same conditions. Spectral emittances show large variations during each run compared to materials G and C101, again suggesting (as in the case of material C102) that the front surface composition and optical properties of material C104 are changing rapidly during ablation.

Direct measurements of target spectral reflectance during irradiation of material C104 at 9 kW/cm^2 (*cf.* Section 3.3.2) yield spectral emittances of 0.78 $\pm$ 0.01 and 0.72 $\pm$ 0.01 at λ = 0.52 μm and 1.06 μm, respectively, in reasonable agreement with the fitted values obtained from pyrometry data for material C104 ablated at 60 - 150 kW/cm^2. However, similar direct measurements completed during irradiation of material C104 at 100 kW/cm^2 (*cf.* Section 3.3.2) yield higher spectral emittances in the range 0.88 - 0.89. As in the case of material C102, a possible explanation for this discrepancy is that different amounts of reflective films are formed in the HARC (microscale) experiments compared to the EDCL 2 (larger scale) experiments.

Material C104 is a "harder" ablator than materials G and C101. Although some discrete mass removal is observed in filtered HYCAM films of the target front surface and the plume, only a small fraction of the total mass is probably ablated in the form of discrete particles. The major increase in hardness of material C104 relative to G is undoubtedly due to differences in optical properties. However, it is also possible that material C104 generates a distribution of carbon vapor species that has a larger enthalpy of mass removal than the value pertinent to thermochemical equilibrium. [This effect is offset, in part, by the vaporization of metal atoms.]

3.3.1.5 Material C105 Data

Appendix B contains three sets of time-resolved target front surface temperature and spectral emittance data for material C105 irradiated at 60 kW/cm² (run #143-9), at 100 kW/cm² (run #156-24), and at 150 kW/cm² (run #157-14). These data are presented in the same format as for sample graphNOL (G) data shown in Figure 14 (*cf.* Section 3.3.1.1). Figure 20 shows one of these data sets (run #157-14 at 150 kW/cm²).
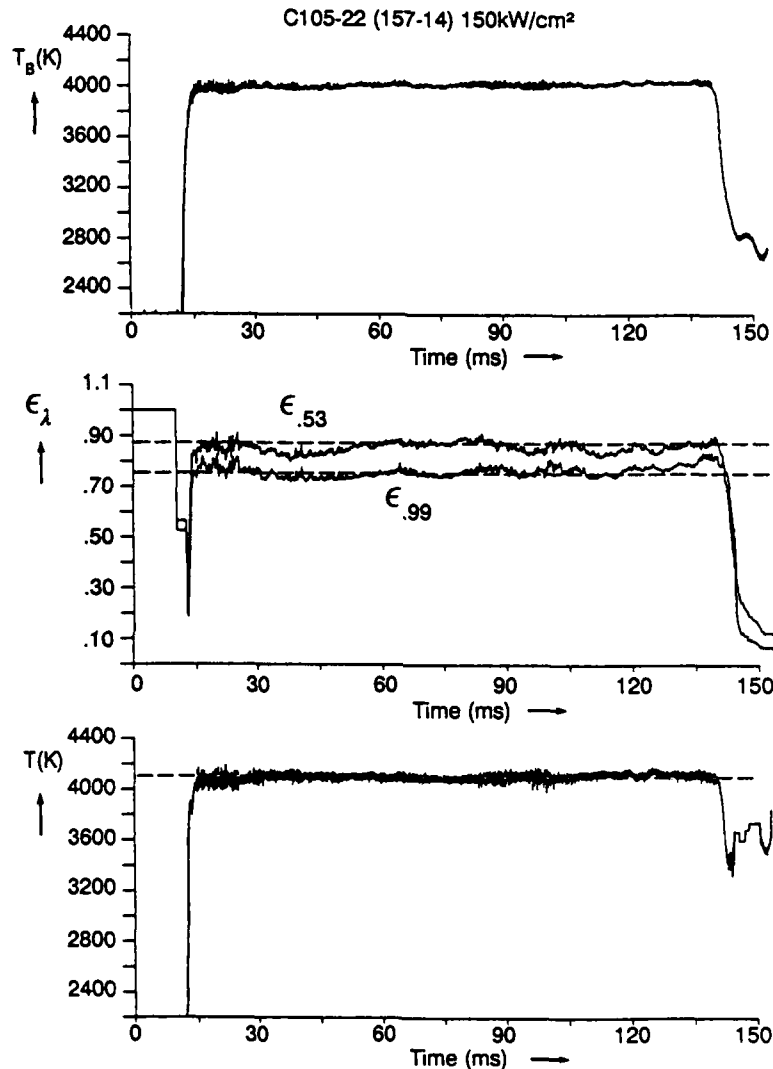

Figure 20. Time-Resolved Front Surface Temperature/Emittance Data Traces for Material C105

Note that the target front surface "steady state" temperature of material C105 ablating at an irradiance of 150 kW/cm² into atmospheric pressure is approximately 4100 K (*ca.* 50 K higher than for materials C102 and C104 but nearly 100 K less than for materials G and C101 under the same conditions) and that the temperature exhibits rapid "spikes" throughout the run. Appendix B data for other runs on material C105 show similar intermittent temperature "spikes" at all irradiances. The amplitudes of these spikes are, however, smaller than those observed in materials C102 and C104. Inspection of filtered HYCAM films shows that the front surfaces of ablating C105 targets "flicker". The origin of these front surface phenomena is not known.

3.3.1.5 Material C105 Data (continued)

As in the case of materials C102 and C104, the decreased front surface temperature of material C105 relative to materials G and C101 may be caused by higher carbon vapor pressure which indicates that the distribution of carbon vapor species may be shifted from that characteristic of thermochemical equilibrium ablation and/or that the vaporization coefficients for carbon vapor species are very different for material C105 compared to G [Reference 28]. OMA plume emission spectra show only typical diatomic carbon spectral features for material C105 (cf. Section 3.3.3); there is no evidence for any new emission features which might correspond to spectral transitions of anything other than carbon ablated from material C105.

The spectral emittances of material C105 are lower (in the range 0.75 - 0.87 for run #157-14; cf. Figure 20) than for either materials G or C101 under the same conditions. These emittances are higher than those for materials C102 and C104 under the same conditions. Spectral emittances show more variation during each run compared to materials G and C101, suggesting that the front surface optical properties of material C105 are changing rapidly during ablation.

Direct measurements of target spectral reflectance during irradiation of material C105 at 9 kW/cm^2 and at 100 kW/cm^2 (cf. Section 3.3.2) yield spectral emittances of 0.87 ± 0.03 and 0.81 ± 0.02 at λ = 0.52 μm and 1.06 μm, respectively, in reasonable agreement with the fitted values obtained from pyrometry data for material C105 ablated at 25 - 150 kW/cm^2.

Material C105 is a "harder" ablator than materials G and C101. Very little discrete mass removal is observed in filtered HYCAM films of the target front surface and the plume, so only a small fraction of the total mass is probably ablated in the form of discrete particles. The major increase in hardness of material C105 relative to G is undoubtedly due to differences in optical properties. It is also possible that material C105 generates a distribution of carbon vapor species that has a larger enthalpy of mass removal than the value pertinent to thermochemical equilibrium (if vaporization coefficients for various carbon vapor species ablated from material C105 are very different from their equilibrium values).

3.3.1.6 Material C106 Data

Appendix B contains three sets of time-resolved target front surface temperature and spectral emittance data for material C106 irradiated at 60 kW/cm² (run #157-6), at 100 kW/cm² (run #145-7), and at 150 kW/cm² (run #157-15). These data are presented in the same format as for sample graphNOL (G) data shown in Figure 14 (cf. Section 3.3.1.1). Figure 21 shows one of these data sets (run #157-15 at 150 kW/cm²).
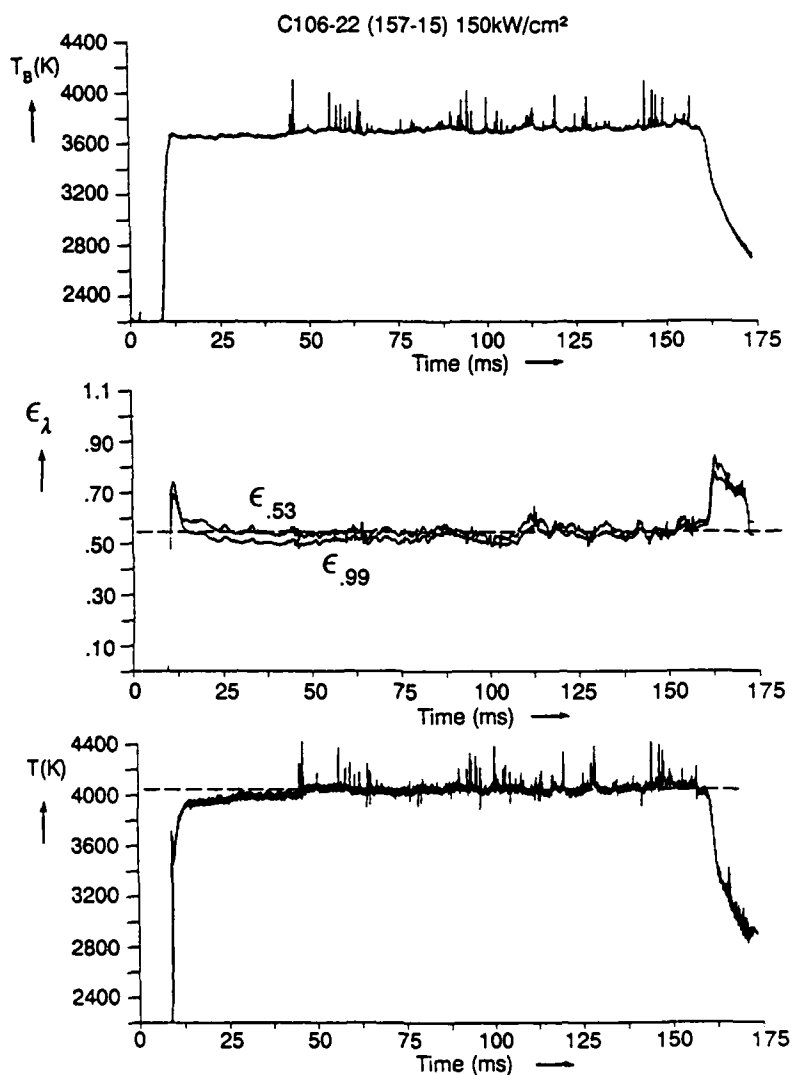

Figure 21. Time-Resolved Front Surface Temperature/Emittance Data Traces for Material C106

Note that the target front surface "steady state" temperature of material C106 ablating at an irradiance of 150 kW/cm² into atmospheric pressure is approximately 4040 K (similar to materials C102 and C104 but ca. 160 K less than for materials G and C101 under the same conditions) and that the temperature exhibits rapid intermittent "spikes" throughout the run. Appendix B data for other runs on material C106 show similar intermittent temperature "spikes" at all irradiances. The amplitudes of these spikes are similar to those observed in material C102. Inspection of filtered HYCAM films shows that the front surfaces of ablating C106 targets display eruptions of material (resembling small volcanos that sometimes eject particles); as in the case of materials C102 and C104, these eruptions are probably related to the rapid front surface temperature variations.

34

3.3.1.6 Material C106 Data (continued)

As in the case of materials C102, C104, and C105, the decreased front surface temperature of material C106 relative to materials G and C101 may be caused by higher carbon vapor pressure which indicates that the distribution of carbon vapor species may be shifted from that characteristic of thermochemical equilibrium ablation. OMA plume emission spectra show only typical diatomic carbon spectral features for material C106 (*cf.* Section 3.3.3); there is no evidence for any new emission features which might correspond to spectral transitions of anything other than carbon ablated from material C106.

The spectral emittances of material C106 are substantially lower (in the range 0.5 - 0.6 for run #157-15; *cf.* Figure 21) than for either materials G or C101 under the same conditions. These emittances are also lower than those for materials C102, C104, and C105 under the same conditions. Spectral emittances show more variation during each run compared to materials G and C101, suggesting that the front surface composition and optical properties of material C106 are changing rapidly during ablation.

Direct measurements of target spectral reflectance during irradiation of material C106 at 9 kW/cm^2 and at 100 kW/cm^2 (*cf.* Section 3.3.2) yield spectral emittances of 0.80 ± 0.05 and 0.73 ± 0.03 at $\lambda = 0.52$ μm and 1.06 μm, respectively, in disagreement with the fitted values obtained from pyrometry data for material C106 ablated at 60 - 150 kW/cm^2. As in the case of materials C102 and C104, a possible explanation for this discrepancy is that different amounts of reflective films are formed in the HARC (microscale) experiments compared to the EDCL 2 (larger scale) experiments.

Material C106 is a "harder" ablator than materials G and C101. Although some discrete mass removal is observed in filtered HYCAM films of the target front surface and the plume, only a small fraction of the total mass is probably ablated in the form of discrete particles. The major increase in hardness of material C106 relative to G is undoubtedly due to differences in optical properties. It is also possible that material C106 generates a distribution of carbon vapor species that has a larger enthalpy of mass removal than the value pertinent to thermochemical equilibrium.

3.3.1.7 Material C107 Data

Appendix B contains four sets of time-resolved target front surface temperature and spectral emittance data for material C107 irradiated at 25 kW/cm² (run #144-16), at 60 kW/cm² (run #143-14), at 100 kW/cm² (run #156-20), and at 150 kW/cm² (run #142-15). These data are presented in the same format as for sample graphNOL (G) data shown in Figure 14 (cf. Section 3.3.1.1). Figure 22 shows one of these data sets (run #156-20 at 100 kW/cm²).
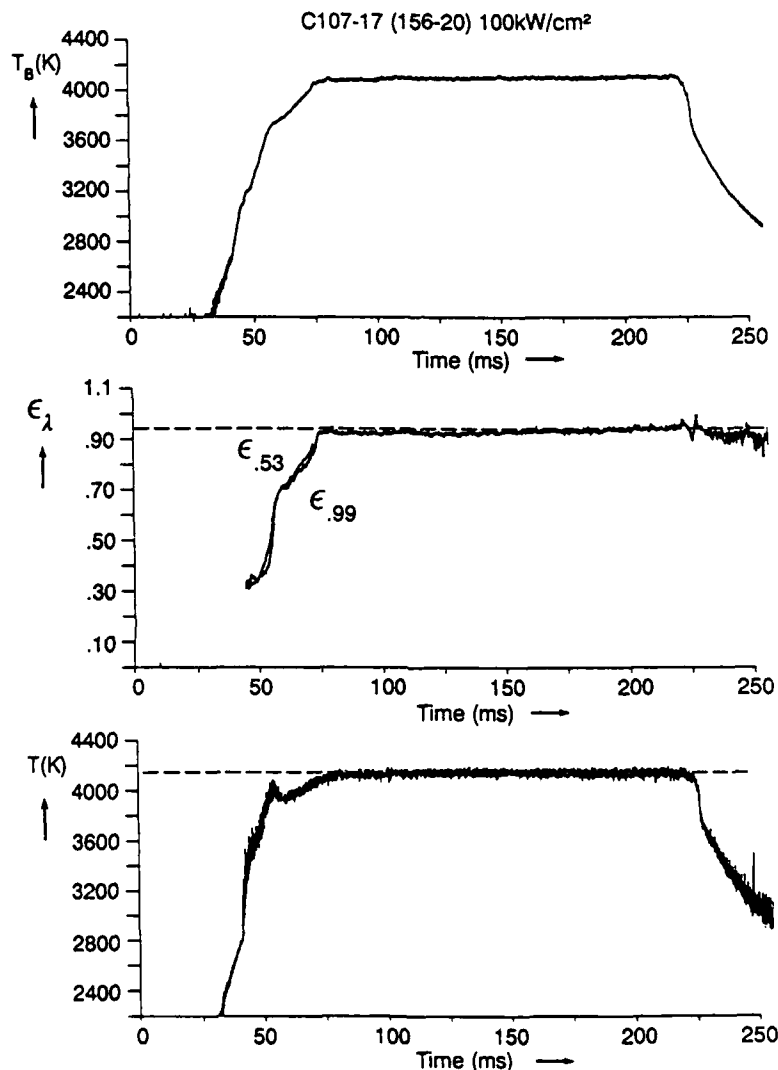

Figure 22. Time-Resolved Front Surface Temperature/Emittance Data Traces for Material C107

Note that the target front surface "steady state" temperature of material C107 ablating at an irradiance of 100 kW/cm² into atmospheric pressure is approximately 4150 K (similar to the "steady state" temperature of materials G and C101 under the same conditions) and that the temperature is very stable following the initial heating curve. Inspection of filtered HYCAM films shows that ablating C107 targets usually display catastrophic failures - specimens often crack relatively early during irradiation due to thermal shock and fracture. On some specimens, front surface coatings are severely damaged during heating and ablation, thereby exposing substrate surfaces.

36

3.3.1.7 Material C107 Data (continued)

The high "steady state" temperature (*ca.* 4150 K) observed in Figure 22 is characteristic of pure carbon ablation, corresponding to exposure of the substrate of material C107 to the EDCL 2 beam. The initial temperature rise (which is much slower than for a pure carbon such as G) prior to *ca.* 70 ms is due to heating of the coating prior to failure. OMA plume emission spectra show only typical diatomic carbon spectral features for material C107 (*cf.* Section 3.3.3); there is no evidence for any new emission features which might correspond to spectral transitions of anything other than carbon ablated from material C107. As revealed by filtered HYCAM films, the refractory coating on material C107 is "peeled back" out of the damage laser beam; it does not fail by vaporization.

The spectral emittances of material C107 at long times (following coating failure) are essentially the same as for material G under the same conditions. The spectral emittances of material C107 at short times are lower (in the range 0.3 - 0.7 for run #156-20; *cf.* Figure 22) than for either materials G or C101 under the same conditions. These emittances are also lower (initially) than those for materials C102, and C104 through C106 under the same conditions. If catastrophic failure can be prevented, spectral emittances of material C107 might be very low.

Direct measurements of target spectral reflectance during irradiation of material C107 at 9 kW/cm^2 and at 100 kW/cm^2 (*cf.* Section 3.3.2) yield spectral emittances of 0.71 ± 0.02 and 0.60 ± 0.03 at λ = 0.52 μm and 1.06 μm, respectively. These values pertain to undamaged coatings and are in general agreement with the fitted values obtained from initial (*i.e.*, short irradiation time, prior to coating failue) pyrometry data for material C107 ablated at 25 - 150 kW/cm^2.

Material C107 is potentially a "harder" ablator than materials G and C101 (if coating failure can be prevented). Little discrete mass removal is observed in filtered HYCAM films of the target front surface and the plume, so only a small fraction of the total mass is probably ablated in the form of discrete particles. The major potential increase in hardness of material C107 relative to G is due to differences in optical properties. It is not known whether material C107 also generates a distribution of carbon vapor species that has a larger enthalpy of mass removal than the value pertinent to thermochemical equilibrium.

3.3.1.8 Material C108 Data

Appendix B contains three sets of time-resolved target front surface temperature and spectral emittance data for material C108 irradiated at 60 kW/cm² (run #143-15), at 100 kW/cm² (run #156-19), and at 150 kW/cm² (run #142-14). These data are presented in the same format as for sample graphNOL (G) data shown in Figure 14 (cf. Section 4.2.3). Figure 23 shows one of these data sets (run #156-19 at 100 kW/cm²).
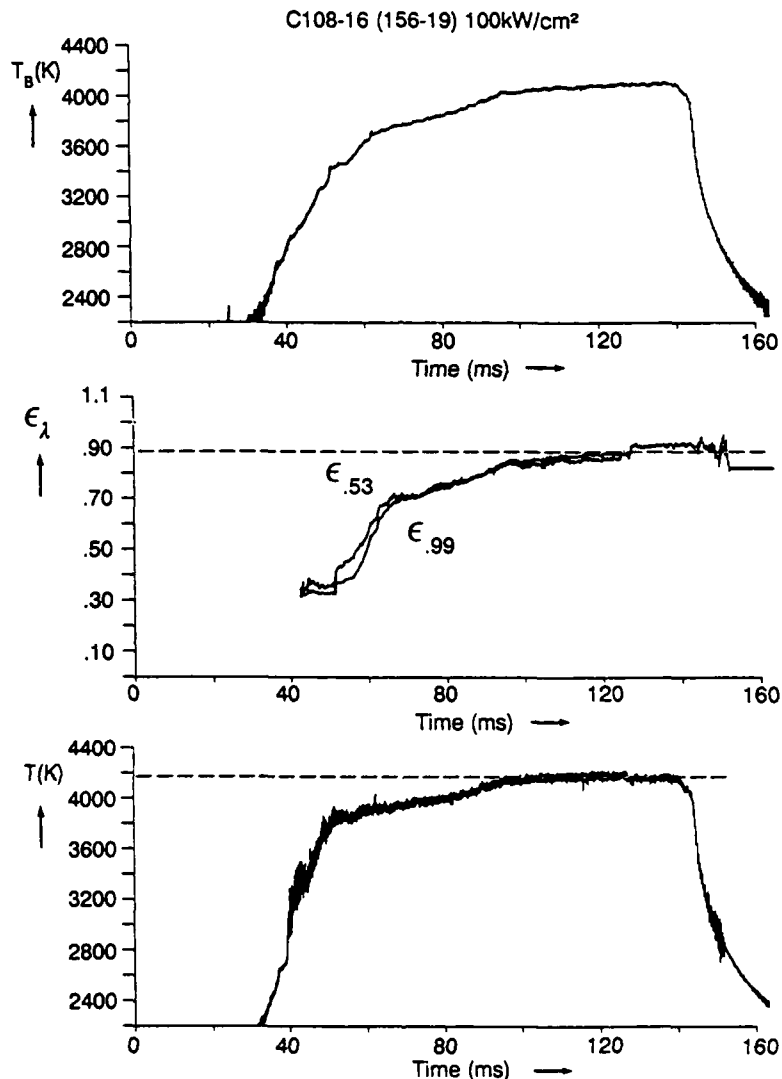

Figure 23. Time-Resolved Front Surface Temperature/Emittance Data Traces for Material C108

Note that the target front surface "steady state" temperature of material C108 ablating at an irradiance of 100 kW/cm² into atmospheric pressure is approximately 4160 K (similar to the "steady state" temperature of materials G and C101 under the same conditions) and that the temperature is very stable following the initial heating curve. Inspection of filtered HYCAM films shows that ablating C108 targets usually display catastrophic failures - specimens often crack due to thermal shock and fracture. On some specimens, front surface coatings are severely damaged during heating and ablation, thereby exposing substrate surfaces.

3.3.1.8 Material C108 Data (continued)

The high "steady state" temperature (*ca.* 4160 K) observed in Figure 23 is characteristic of pure carbon ablation, corresponding to exposure of the substrate of material C108 to the EDCL 2 beam. The initial temperature rise (which is much slower than for a pure carbon such as G) prior to *ca.* 90 ms is due to heating of the coating prior to failure. OMA plume emission spectra show only typical diatomic carbon spectral features for material C108 (*cf.* Section 3.3.3); there is no evidence for any new emission features which might correspond to spectral transitions of anything other than carbon ablated from material C108. As revealed by filtered HYCAM films, the refractory coating on material C108 is "peeled back" out of the damage laser beam; it does not fail by vaporization.

The spectral emittances of material C108 at long times (following coating failure) are essentially the same as for material G under the same conditions. The spectral emittances of material C108 at short times are lower (in the range 0.3 - 0.7 for run #156-21; *cf.* Figure 23) than for either materials G or C101 under the same conditions. These emittances are also lower (initially) than those for materials C102 and C104 through C106 under the same conditions. If catastrophic failure can be prevented, spectral emittances of material C108 might be very low.

Direct measurements of target spectral reflectance during irradiation of material C108 at 9 kW/cm^2 and at 100 kW/cm^2 (*cf.* Section 3.3.2) yield spectral emittances of 0.74 ± 0.02 and 0.63 ± 0.05 at $\lambda = 0.52$ μm and 1.06 μm, respectively. These values pertain to undamaged coatings and are in general agreement with the fitted values obtained from initial (*i.e.*, short irradiation time, prior to coating failue) pyrometry data for material C108 ablated at 60 - 150 kW/cm^2.

Material C108 is potentially a "harder" ablator than materials G and C101 (if coating failure can be prevented). Little discrete mass removal is observed in filtered HYCAM films of the target front surface and the plume, so only a small fraction of the total mass is probably ablated in the form of discrete particles. The major potential increase in hardness of material C108 relative to G is due to differences in optical properties. It is not known whether material C108 also generates a distribution of carbon vapor species that has a larger enthalpy of mass removal than the value pertinent to thermochemical equilibrium. Overall, STS-2 results on material C108 strongly resemble those on material C107. Both coatings are likely to be highly effective if they are deposited on better substrates.

39

3.3.2 Target Spectral Reflectance Measurements

3.3.2.1 CW Laser Ablation

The apparatus described in Section 3.2.3 was used to obtain direct time-resolved target spectral reflectance measurements during laser ablation. Figure 24 shows sample time-resolved reflectance data obtained on graphNOL (G) ablated using a cw CO_2 laser with 9 kW/cm² peak irradiance on target. The top panel shows the front surface temperature measured by a single wavelength (λ = 532 nm) optical pyrometer. The laser shutter opening time and the target burnthrough time (BT) are indicated in the top panel. The remaining four panels show the time-resolved target front surface reflectances at four detection wavelengths obtained using the component laser/filter/detector combinations described in Section 3.2.3 above. Average reflectances during ablation ($\bar{R}$ values) are given in the upper right hand corner of each panel; for graphNOL, these values are the averages between the time the front surface temperature reaches 3000 K and the burnthrough time.
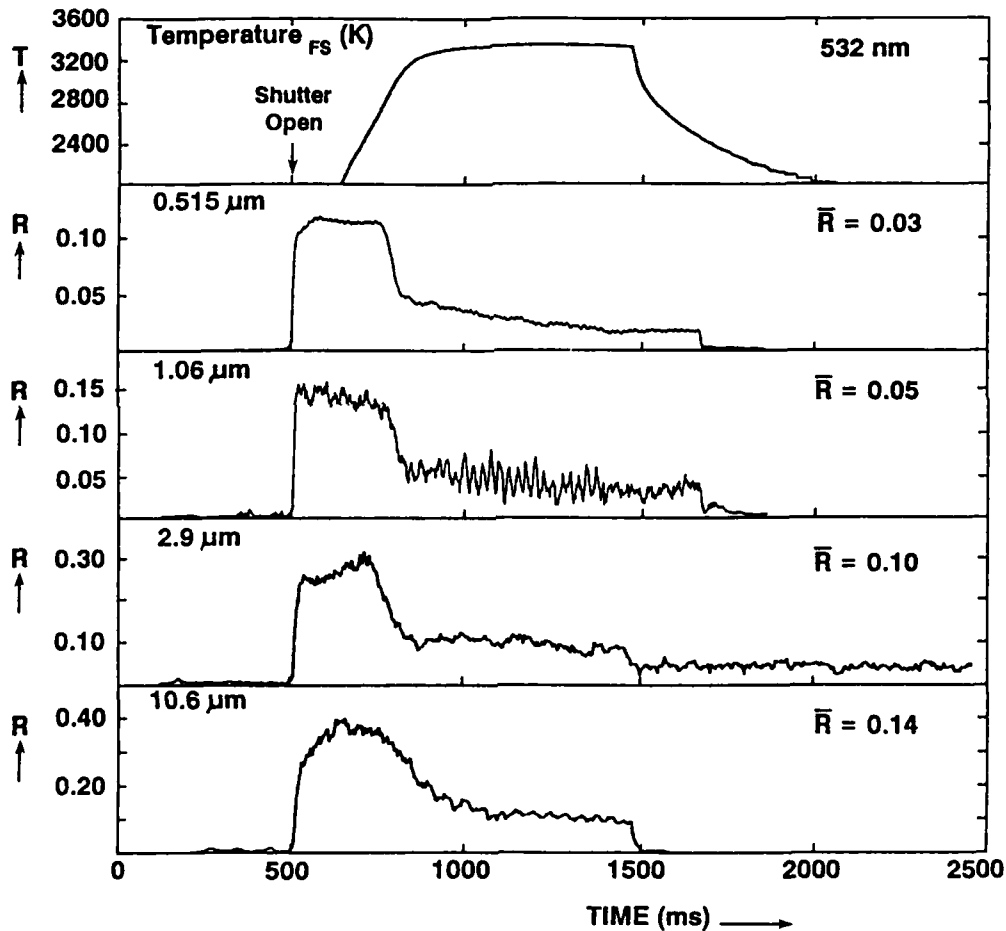
Figure 24. GraphNOL Time-Resolved Reflectances at I_{peak} = 9 kW/cm²

Note that initial reflectances (between the time the shutter opens and the sample reaches a front surface temperature of *ca.* 3000 K) are very similar to the room temperature values (*cf.* Table 1 - polished G data). Then, as graphNOL ablates (and its surface roughens), time-resolved reflectances drop to lower "steady state ablation" values.

40

3.3.2.1 CW Laser Ablation (continued)

Figure 25 shows corresponding time-resolved reflectance data obtained on graphNOL (G) ablated using a cw CO_2 laser with 100 kW/cm² peak irradiance on target. The format is the same as in Figure 24. Again, "steady state ablation" values of the spectral reflectances are lower than room temperature values for the virgin material. Average reflectance measurements at $\lambda = 2.9$ μm wavelength ($\bar{R} = 0.15$) using 100 kW/cm² peak irradiance are in good agreement with previous average reflectance values ($\bar{R} = 0.15 \pm 0.01$ for twelve experiments) obtained using a cw HF chemical laser to ablate specimens directly with peak irradiances in the 10 - 18 kW/cm² range [Reference 15]. There is a small discrepancy between the present data at lower irradiance (cf. Figure 24; $\bar{R} = 0.10$) and previous data [Reference 15] which may be due to a small systematic error. GraphNOL generally yields very reproducible results, with standard deviations of multiple reflectance measurements in the 0.01 - 0.02 range. Other materials exhibit much larger variations in time-resolved reflectances due to complex changes in surface structure and chemistry during ablation. Appendix C contains figures showing sample time-resolved reflectance data for all materials tested at peak irradiances of 9 and 100 kW/cm². Table 3 collects $\bar{R}_\lambda$ values for all the high temperature reflectance measurements completed on core carbon barrier materials (CBMs).
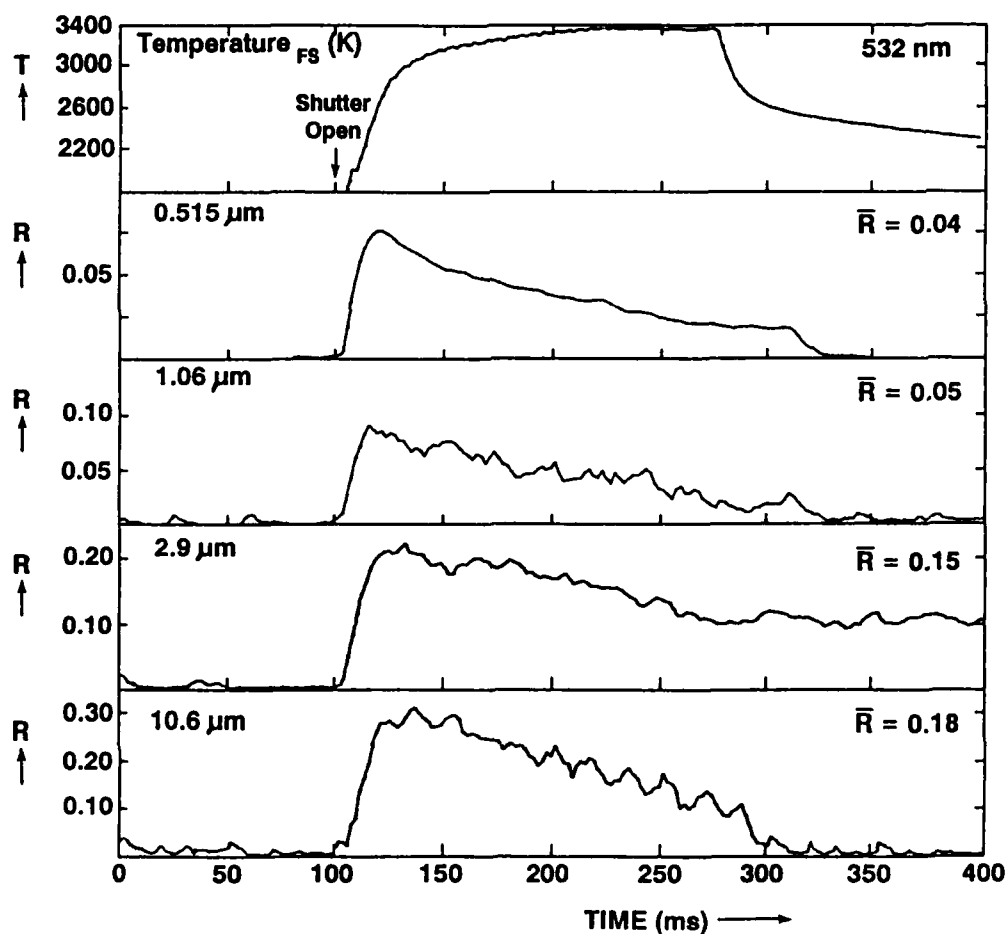

Figure 25. GraphNOL Time-Resolved Reflectances at I_{peak} = 100 kW/cm²

Table 3. Total Average Reflectances $\bar{R}_\lambda$ During Laser Ablation

$\boxed{I_{peak} = 9 \text{ kW/cm}^2}$

Material	$\bar{R}_{0.515}$	$\bar{R}_{1.06}$	$\bar{R}_{2.9}$	$\bar{R}_{10.6}$
G	.04 ± .01	.06 ± .02	.10 ± .01	.15 ± .01
C101	.10 ± .05	.10 ± .02	.44 ± .05	.45 ± .02
C102	.30 ± .10	.41 ± .07	.61 ± .20	.46 ± .08
C104	.22 ± .01	.28 ± .01	.74 ± .16	.46 ± .01
C105	(.15 ± .01)*	(.20 ± .01)*	(.64 ± .10)*	(.77 ± .03)*
C106	.15 ± .03	.25 ± .01	.27 ± .03	.31 ± .02
C107	(.29 ± .02)*	(.41 ± .02)*	(.44 ± .03)*	(.83 ± .03)*
C108	(.27 ± .01)*	(.41 ± .01)*	(.51 ± .06)*	(.74 ± .01)*

*No burnthrough

$\boxed{I_{peak} = 100 \text{ kW/cm}^2}$

Material	$\bar{R}_{0.515}$	$\bar{R}_{1.06}$	$\bar{R}_{2.9}$	$\bar{R}_{10.6}$
G	.04 ± .01	.05 ± .01	.17 ± .02	.19 ± .01
C101	.12 ± .01	.15 ± .02	(.74 ± .04)*	.41 ± .03
C102	.12 ± .02	.15 ± .02	.60 ± .10	.59 ± .05
C104	.10 ± .01	.11 ± .03	(.64 ± .10)*	.47 ± .06
C105	.11 ± .01	.18 ± .01	.35 ± .02	.55 ± .03
C106	.24 ± .01	.28 ± .01	(.79 ± .05)*	.54 ± .01
C107	.29 ± .01	.39 ± .01	.46 ± .14	.63 ± .10
C108	.25 ± .01	.32 ± .01	.47 ± .03	.82 ± .03

*Contaminated by specular reflections

The $\lambda = 1.06$ μm data are often "noisier" than data at other wavelengths due to the relatively low power (50 mW) of the cw Nd:YAG probe laser. A few data points are contaminated by specular reflections from shiny droplets and/or plys formed by certain materials. In addition, data for materials C105 and C108 at $I_{peak} = 9$ kW/cm² pertain to high temperature reflectances of targets that did not ablate completely (i.e., burn through). Higher irradiance data are influenced by the "keyhole" effect since ablation craters can produce trapping of reflected light. All of the data could be improved by using a higher power damage laser to generate larger spots and by using higher power probe lasers to examine reflectances within these larger spots.

Analysis and assessment of these time-resolved reflectance measurements is presented in Section 3.5 below.

42

3.3.2.1 CW Laser Ablation (continued)

As discussed in Section 2.0 above, the wavelength-dependent coupling coefficient α_λ of an opaque material with a transparent plume is just equal to the wavelength-dependent absorptance (*i.e.*, the spectral absorptance) A_λ which is also equal to the spectral emittance ϵ_λ (*cf.* equation [2]). It is desirable to compare spectral absorptances (determined from spectral reflectance measurements) with spectral emittances (determined as described in Sections 3.2.2 and 3.3.1 above) for wavelengths (*viz.*, $\lambda = ca.$ 0.5 μm and 1.0 μm) at which both sets of determinations were made.

Table 4 lists the average spectral absorptances $\bar{A}_\lambda$ calculated from average spectral reflectance $\bar{R}_\lambda$ data in Table 3 using equation [2]. Plume probing experiments on CBMs have demonstrated that the plumes are transparent at the wavelengths of interest [*cf.* Section 3.3.3 below], so the average spectral absorptances $\bar{A}_\lambda$ are equal to the average wavelength-dependent coupling coefficients $\bar{\alpha}_\lambda$ and the average spectral emittances $\bar{\epsilon}_\lambda$. Note that the values listed in Table 4 are temporal averages over the entire time of ablation. The beginning of the "time of ablation" is imprecise but is estimated from the target front surface temperature measurements to be the time at which the sample reaches a "steady state" high temperature. The end of the "time of ablation" is more precise; it corresponds to the burnthrough time on most targets. [Due to the "keyhole" effect, it may be better to use only "early ablation time" data since the steep-walled ablation craters formed in microscale targets can trap reflected light.]

Table 5 lists the average spectral emittances $\bar{\epsilon}_\lambda$ at $\lambda = 0.53$ μm and 0.99 μm wavelengths determined from nonlinear regression fits to 6λ optical pyrometer experimental data collected in Section 3.3.1 and Appendix B. Intercomparison of entries in Tables 4 and 5 shows that spectral absorptances and emittances of some materials (G, C101, and C105) match very well. For example, graphNOL (material G) has a spectral absorptance A_λ of 0.96 ± 0.01 at $\lambda = 0.52$ μm wavelength at both I = 9 and 100 kW/cm^2 irradiances and G has spectral emittances ϵ_λ of 0.95 ± 0.01 and 0.96 ± 0.02 at $\lambda = 0.53$ μm for I = 25 and 150 kW/cm^2 irradiance STS-2 experiments, respectively. However, three other materials (C102, C104, and C106) exhibit discrepancies between spectral absorptance and emittance measurements; spectral absorptance measurements in microscale (HARC) experiments are systematically larger than corresponding spectral emittance determinations made *via* EDCL 2 scale experiments. We speculate that reflective coatings do not form as readily in microscale experiments; perhaps there is not enough molten material to form a liquid film on the HARC scale (which involves penetration of a maximum thickness of 0.5 mm of material, in contrast to the EDCL 2 scale of experiment which typically penetrates 1 - 2.5 mm thickness of material). We recommend that reflectance measurements be completed using larger targets and damage lasers.

Within very broad ranges, materials C107 and C108 also have matching values of spectral absorptance and spectral emittance. Interesting, the spectral absorptance values of these materials at $\lambda = 10.6$ μm are very low (*cf.* Table 4), suggesting that they have considerable hardening potential. Coatings of the type used on materials C107 and C108 should be applied to better substrates.

Spectral absorptances are used to predict ablation performance in Section 3.5 below.

3.3.2.1 CW Laser Ablation (continued)

Table 4. Average Spectral Absorptances $\overline{A}_\lambda$ During Laser Ablation.

$$\boxed{I_{peak} = 9 \text{ kW/cm}^2}$$

Material	$\overline{A}_{0.515}$	$\overline{A}_{1.06}$	$\overline{A}_{2.9}$	$\overline{A}_{10.6}$
G	.96 ± .01	.94 ± .02	.90 ± .01	.85 ± .01
C101	.90 ± .05	.90 ± .02	.56 ± .05	.55 ± .02
C102	.70 ± .10	.59 ± .07	.39 ± .20	.54 ± .08
C104	.78 ± .01	.72 ± .01	.26 ± .16	.54 ± .01
C105	(.85 ± .01)*	(.80 ± .01)*	(.36 ± .10)*	(.23 ± .03)*
C106	.85 ± .03	.75 ± .01	.73 ± .03	.69 ± .02
C107	(.71 ± .02)*	(.59 ± .02)*	(.56 ± .03)*	(.17 ± .03)*
C108	(.73 ± .01)*	(.59 ± .01)*	(.49 ± .06)*	(.26 ± .01)*

*No burnthrough

$$\boxed{I_{peak} = 100 \text{ kW/cm}^2}$$

Material	$\overline{A}_{0.515}$	$\overline{A}_{1.06}$	$\overline{A}_{2.9}$	$\overline{A}_{10.6}$
G	.96 ± .01	.95 ± .01	.83 ± .02	.81 ± .01
C101	.88 ± .01	.85 ± .02	(.26 ± .04)*	.59 ± .03
C102	.88 ± .02	.85 ± .02	.40 ± .10	.41 ± .05
C104	.90 ± .01	.89 ± .03	(.36 ± .10)*	.53 ± .06
C105	.89 ± .01	.82 ± .01	.65 ± .02	.45 ± .03
C106	.76 ± .01	.72 ± .01	(.21 ± .05)*	.46 ± .01
C107	.71 ± .01	.61 ± .01	.54 ± .14	.37 ± .10
C108	.75 ± .01	.68 ± .01	.53 ± .03	.18 ± .03

*Contaminated by specular reflections

44

3.3.2.1 CW Laser Ablation (continued)

Table 5. Average Spectral Emittances $\bar{\epsilon}_\lambda$ During Laser Ablation

Irradiance								
Material	25 kW/cm²		60 kW/cm²		100 kW/cm²		150 kW/cm²	
	$\bar{\epsilon}_{0.53}$	$\bar{\epsilon}_{0.99}$	$\bar{\epsilon}_{0.53}$	$\bar{\epsilon}_{0.99}$	$\bar{\epsilon}_{0.53}$	$\bar{\epsilon}_{0.99}$	$\bar{\epsilon}_{0.53}$	$\bar{\epsilon}_{0.99}$
G	.95 ± .01	.93 ± .01	.91 ± .02	.91 ± .02	.94 ± .02	.94 ± .02	.95 ± .02	.93 ± .02
C101			.87 ± .02	.84 ± .02	.89 ± .02	.84 ± .02	.85 ± .02	.84 ± .02
C102			.63 ± .07	.58 ± .07	.60 ± .07	.57 ± .07	.67 ± .10	.60 ± .07
C104			.65 ± .08	.59 ± .08	.66 ± .08	.61 ± .08	.73 ± .08	.67 ± .08
C105			.82 ± .06	.74 ± .06	.85 ± .03	.78 ± .03	.85 ± .03	.76 ± .03
C106			.55 ± .04	.51 ± .04	.53 ± .03	.50 ± .04	.55 ± .03	.53 ± .03
C107	(.3 - .7)*	(.3 - .7)*	(.3 - .8)*	(.3 - .8)*	(.4 - .8)*	(.4 - .8)*	(.4 - .8)*	(.4 - .8)*
C108			(.3 - .7)*	(.3 - .7)*	(.4 - .8)*	(.4 - .8)*	(.4 - .8)*	(.4 - .8)*

*Varies rapidly during coating heating and damage

3.3.2.2 RP Laser Ablation

All of the above data pertain to continuous wave (cw) laser ablation of CBMs. Initial time-resolved target reflectance measurements were also completed for repetitively pulsed (rp) laser ablation of graphNOL using the apparatus described in Reference 5. Figure 26 shows sample data (reflectance vs. pulse number at average fluences of 2.75, 5.5, 20, and 40 J/cm²; since the incident rp HF chemical laser beam had "hot spots" with a peak to average fluence ratio of ca. 3 to 1, these average fluences correspond to peak fluences of ca. 8.1 - 120 J/cm²) for graphNOL irradiated with a rp HF chemical laser in vacuum [Reference 29]. Note that graphNOL reflectances measured at low fluences (2.75 and 5.5 J/cm²) are comparable to those recorded at $\lambda = 2.9~\mu m$ wavelength under cw laser irradiation conditions (cf. Table 3), but reflectances at higher fluences drop to lower values. This drop is due to a new phenomenon, plasma absorption [References 24 and 30], that is not observed under cw conditions for the irradiance levels typically used. The existence of carbon vapor plasma (i.e., ionized vapor with high electron and ion densities) is confirmed by OMA plume emission spectroscopy (cf. Section 3.3.3) - at peak fluences above 45 J/cm², characteristic carbon vapor plasma emissions are identified in plume emission spectra of graphNOL and other CBMs.

Dense carbon vapor plasma de-couples the incident rp HF chemical laser radiation from the target surface, leading to a marked increase in the effective enthalpy of ablation Q^* (cf. Section 3.3.4 below).

45
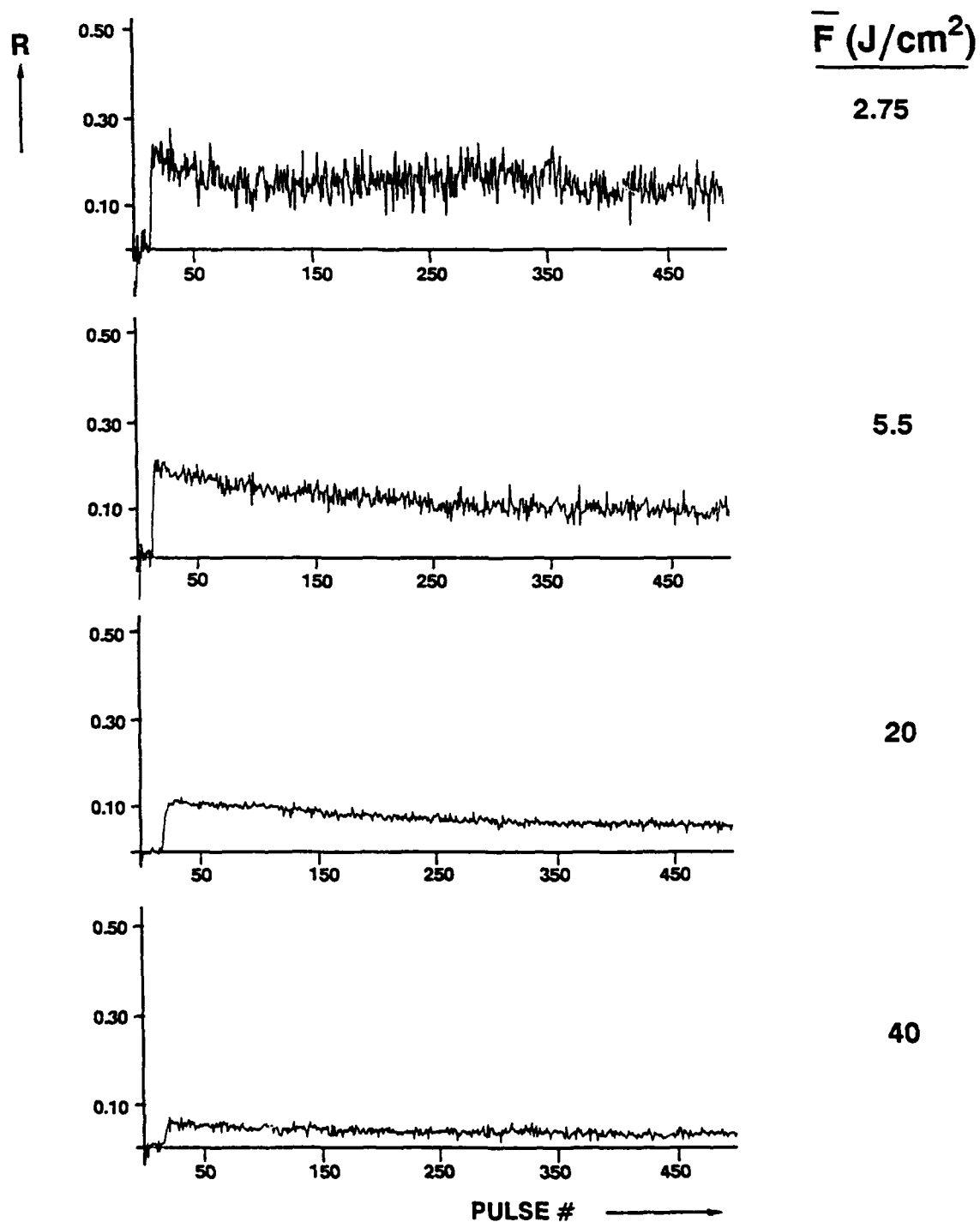
3.3.2.2 <u>RP Laser Ablation</u> (continued)

Figure 26. GraphNOL Time-Resolved Reflectances During RP HF Chemical Laser Ablation

3.3.3 Plume Absorption/Emission/Extinction Measurements

The apparatus systems described in Section 3.2.4 above and in References 3-5, 7-8, 24, and 30-31 were used to obtain time-resolved plume absorption and emission spectroscopy measurements and total extinction measurements during laser ablation. Sections 3.3.3.1 through 3.3.3.3 below present sample experimental data. Section 3.3.3.4 presents analyses of spectroscopic observations.

3.3.3.1 CW Carbon Dioxide Laser/Materials Experiments

The small scale HARC cw CO_2 Laser Test Resource [Reference 4] and the larger scale EDCL 2 cw CO_2 Laser Test Facility at WL/TALE, Kirtland AFB, NM [References 7-8] have both been used to obtain survey plume emission spectra. The top panel of Figure 27 shows a plume emission spectrum recorded by the optical multichannel analyzer (OMA) system (cf. Section 3.2.4) during Run #225-03 (irradiation of graphNOL at 100 kW/cm²) of STS-1/1A experiments [Reference 7]. For comparison, the bottom panel of this figure shows a similar plume emission spectrum recorded at HARC on the same material at about the same irradiance; this spectrum also shows assignments of prominent emission features to various CN and C_2 bands (cf. Section 3.3.3.4). It is clear that the prominent features of both EDCL 2 and HARC spectra are due to these diatomic emissions.
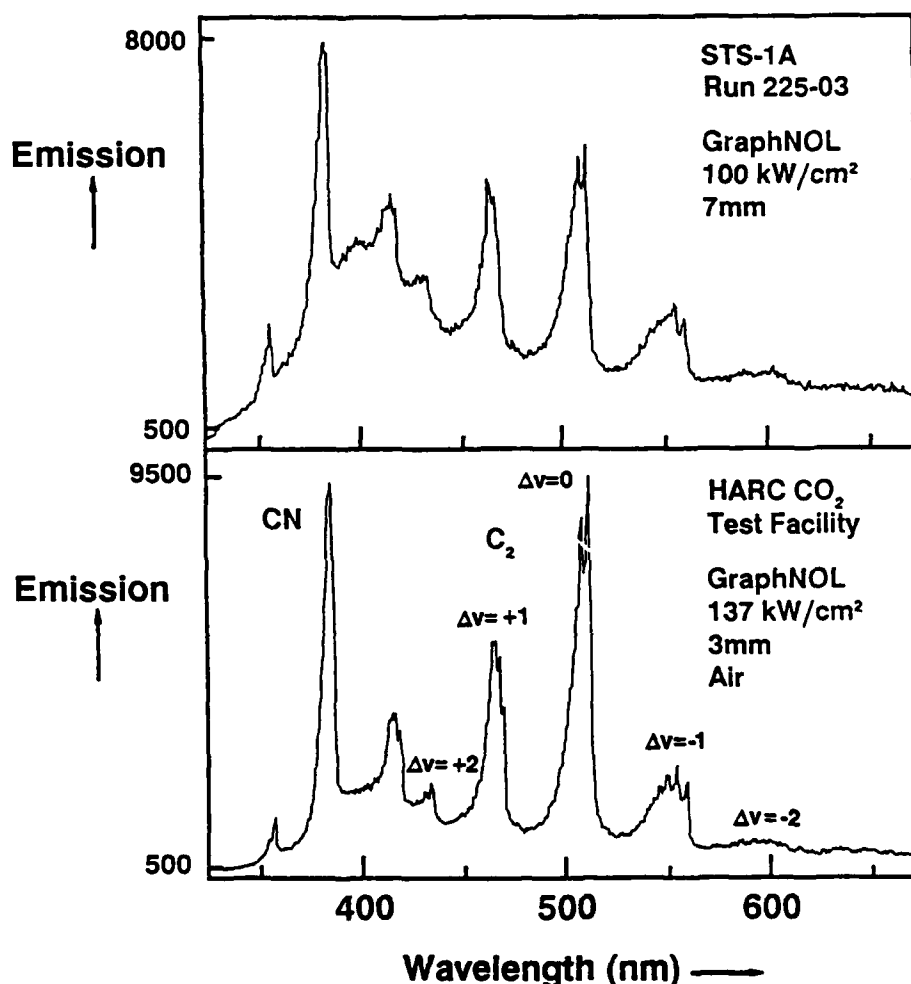
Figure 27. Plume Emission Spectra Recorded at WL (top) and at HARC (bottom)

47

3.3.3.1 CW Carbon Dioxide Laser/Materials Experiments (continued)

Figure 28 shows sample OMA plume emission spectra recorded at HARC during graphNOL (G) ablation using a peak cw CO_2 laser irradiance of *ca.* 100 kW/cm^2 in different environments (top panel - air, middle panel - N_2, bottom panel - He). Emission spectra are corrected for the spectral response function of the optical system using a tungsten strip lamp reference source. Again, prominent band features in the top panel are due to C_2, CN, and (possibly) C_3 electronic emissions superimposed on a continuous background spectrum due to scattered front surface and/or particulate emissions (*cf.* Section 3.3.3.4).
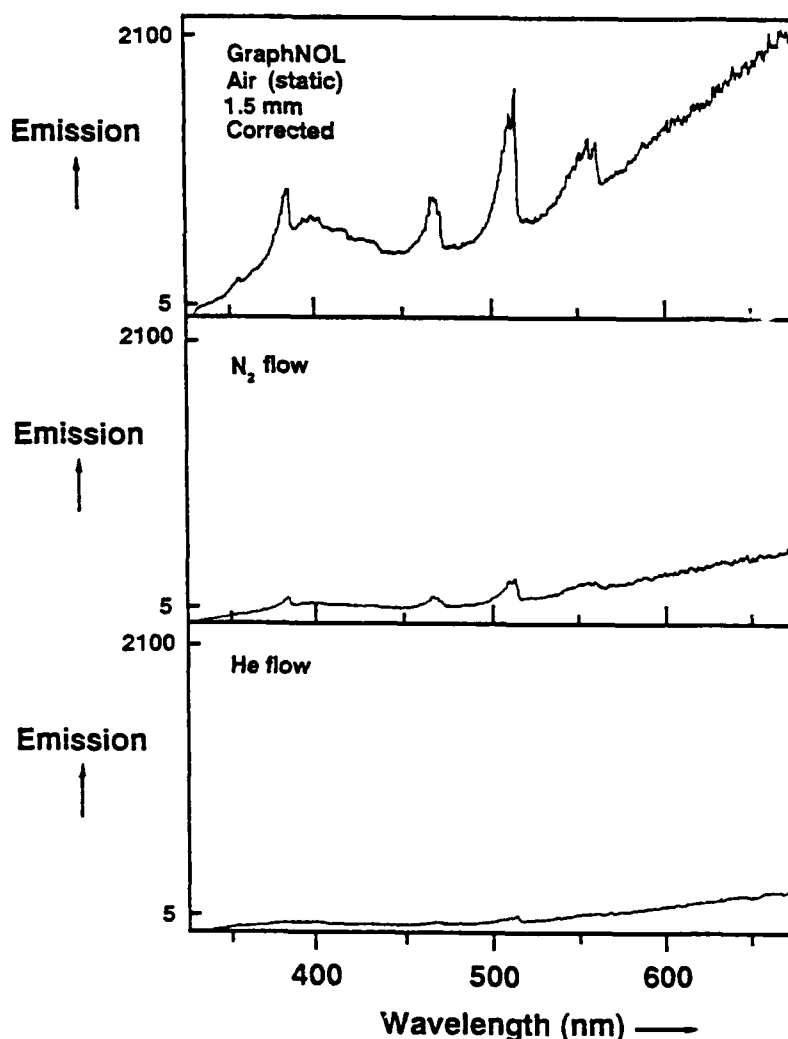
Figure 28. Survey Plume Emission Spectra Observed During cw GraphNOL Ablation

An immediate conclusion from the survey spectra shown in Figure 28 is that most of the emission in the top panel is due to reactions of plume species with air. Indeed, there is a known chemiluminescent reaction that probably generates much of the C_2 emission [Reference 32]. Hence, it is important to observe plume species and spectra in vacuum or in a neutral atmosphere such as He in order to measure plume properties that are directly connected with laser/materials interactions (rather than with secondary reaction processes).

3.3.3.1 CW Carbon Dioxide Laser/Materials Experiments (continued)

Reduction of spurious emissions is also desirable in order to obtain accurate target front surface temperature and spectral emittance measurements. Guided by similar plume emission spectra, HARC/Rice personnel selected six wavelengths for the multiwavelength optical pyrometer system (cf. Section 3.2.2) that correspond to relatively "dark" regions of the plume (so plume emission interference is minimized for the majority of target materials studied).

Many of the survey plume emission spectra obtained during STS-1/1A and STS-2 experiments [References 7-8] resemble that shown in the top panel of Figure 27. There are variations in the amount of "baseline" emission present in various structural composite spectra, but the prominent band features due to C_2 and CN electronic emissions are almost always observed. Since STS-2 spectra were obtained using N_2 (rather than air) as the purge gas, plume emissions are less intense and contain little CN emission near $\lambda = 390$ nm (cf. Figures 27 and 28). Evidently, oxygen (O_2) is needed in the purge gas to generate CN as a prominent plume reaction product.

Much more detailed cw plume emission spectra were obtained at HARC using a higher resolution OMA system (cf. Section 3.2.4); a sample experimental spectrum is shown in Figure 29. Each emission feature corresponds to a particular C_2 Swan system rovibronic transition, as shown by spectral simulation (cf. Section 3.3.3.4 below).
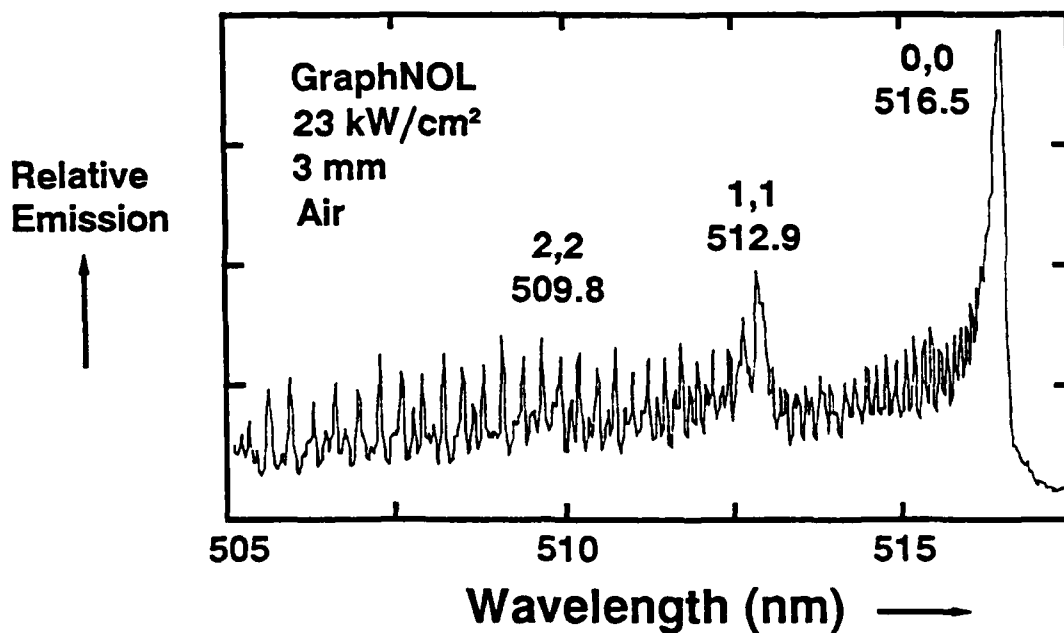
Figure 29. High Resolution Plume Emission Spectrum Produced by cw GraphNOL Ablation

Figure 30 (top panel) shows one of the typical OMA spectra obtained for material C101 at an irradiance of 100 kW/cm². The prominent emission features labelled C_2 (centered near $\lambda = 436$ nm, 468 nm, 513 nm, 556 nm, and 600 nm) are due to diatomic carbon (C_2) Swan system vibrational band sequences [References 33-35]. The bottom panel of Figure 30 shows a typical OMA spectrum for material C104 at an irradiance of 100 kW/cm². Note the additional prominent emission features labelled M (centered near $\lambda = 386$ nm, 412 nm, 438 nm, 457 nm, 468 nm, 486 nm, 570 nm, 609 nm, and 624 nm). We assign these features to metal atom transitions which must be due to vaporized metal atoms generated by C104 ablation. In the case of material C104, the vapor pressure of metal atom M_A is much higher than that of other metal atoms M_B and M_C that are loaded in materials C102 and C106 (as well as other CBMs).
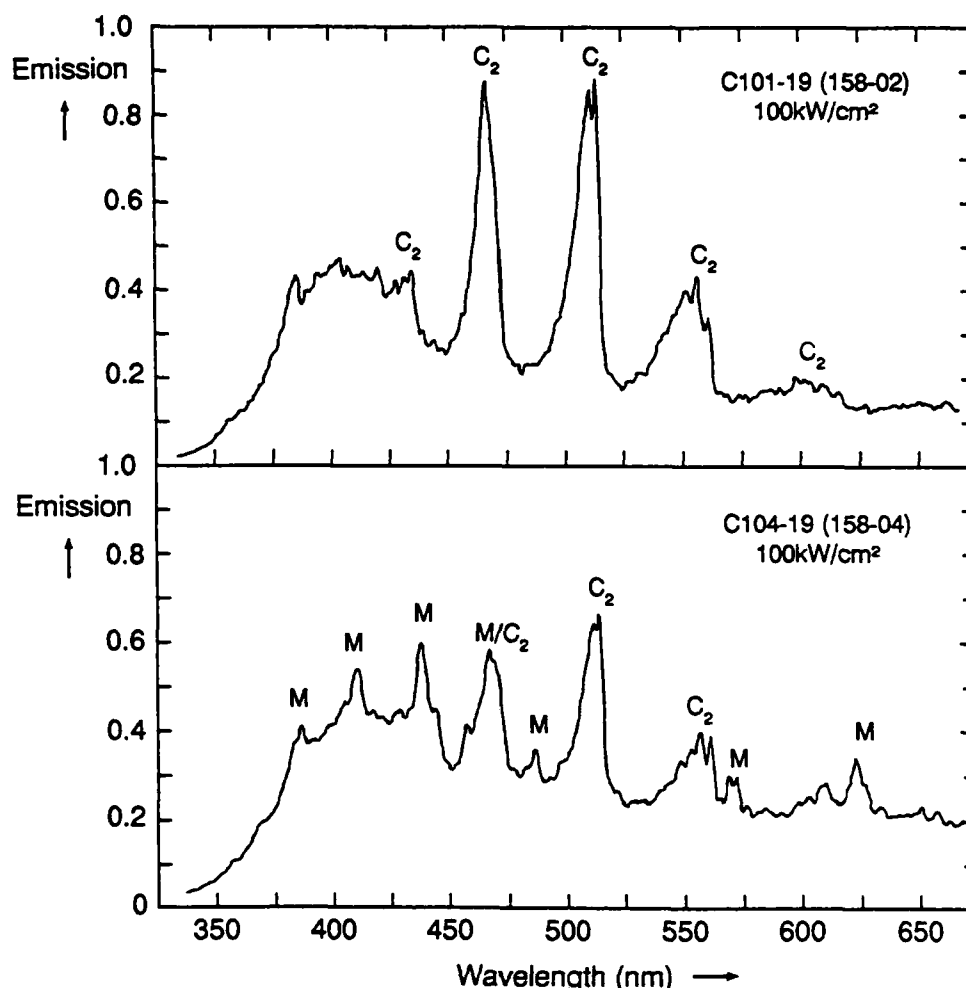
49

Figure 30. Plume Emission Spectra of Material C101 (top) and Material C104 (bottom)

Many other survey plume emission spectra are available from cw CO_2 laser ablation experiments [References 7, 8, and 30]. Spectra taken in air typically resemble Figure 27 and are not very sensitive to incident laser ablation conditions. Further high resolution experiments must be performed in vacuum to identify nascent vapor species and their states of excitation.

The small scale HARC cw CO_2 Laser Test Resource apparatus [Reference 4] and the CCLAS system shown in Figure 12 have been used to obtain high resolution absorption spectra of plume species [diatomic carbon (C_2) and atomic aluminum (Al)] generated by cw CO_2 laser ablation of graphNOL (G) and aluminum (Al). C_2 absorptions (as well as the emissions described above) are due to an intense electronic transition called the Swan system of C_2 [References 33 through 35] which produces blue-green absorption/emission features. Al absorptions are due to intense electronic transitions in the ultraviolet spectral region near $\lambda = 308$ nm. Spectroscopy of these systems is discussed in Section 3.3.3.4 below.

3.3.3.1 CW Carbon Dioxide Laser/Materials Experiments (continued)

GraphNOL (G) samples were irradiated by the HARC cw CO_2 laser at *ca.* 7, 10, 12, 17, 24, and 120 kW/cm^2 in a 760 torr air environment; plume absorption spectra were recorded with the dye laser probe beam positioned *ca.* 500 μm from the target front surface. Different G disc samples, measuring 3.0 mm diameter X 1.5 mm thickness, were used for experiments with CO_2 irradiances below 100 kW/cm^2 (all disc samples were of identical dimensions, $\pm$ 2% in diameter and $\pm$ 10% in thickness); the G disc samples were translated horizontally at a rate of *ca.* 0.25 mm/s. At laser irradiance levels above 100 kW/cm^2, G slabs measuring 20 mm X 3 mm X 2 mm (length X width X thickness) were used; the G slab samples were translated horizontally at a rate of *ca.* 0.5 mm/s. The probe laser beam transmitted signal was not ratioed to initial power due to a long time constant (1 second) in the ratiometer. The long time constant significantly skewed rotational lineshapes at scan rates greater than *ca.* 0.25 cm^{-1}/s. [A faster ratiometer was constructed for later experiments.] Therefore, on many CCLAS scans, small baseline drifts are present in the recorded experimental spectra. In all experiments, target front surface temperature was measured by a Thermogage silicon pyrometer viewing a central 500 μm diameter spot on each target; the corresponding CO_2 laser spot was larger at all irradiances (*ca.* 0.8-3.0 mm diameter), but due to radial conduction the average temperature determined by the silicon pyrometer is probably lower than the peak temperature at the target center.

Figure 31 shows a 3 cm^{-1} interval of the experimental plume absorption spectrum in the middle panel recorded during cw CO_2 laser irradiation of G in air at *ca.* 24 kW/cm^2 peak irradiance. The prominent absorptions are due to C_2 Swan system ($d^3\Pi_g \leftarrow a^3\Pi_u$) 0,0 band rovibronic transitions; these are assigned and labelled in the figure (*cf.* Section 3.3.3.4). The apparent front surface temperature was *ca.* 2925 K (2650 °C) – this is lower than expected. The top panel shows the iodine absorption spectrum used as a wavelength reference for the dye laser. The bottom panel of Figure 31 shows a computer simulation of the experimentally recorded spectrum (*cf.* Section 3.3.3.4); a 0.190 cm^{-1} FWHM Gaussian lineshape and 1000 °C rotational temperature were used as fitting parameters in the simulation. The 0.190 cm^{-1} FWHM Gaussian linewidth corresponds to a 4460 K (4190 °C) translational temperature; apparently the C_2 plume is rotationally cold and translationally hot compared to the sample front surface temperature.

The same 3 cm^{-1} interval of the C_2 absorption spectrum shown in Figure 31 was examined as a function of laser irradiance over the range 10-120 kW/cm^2. The relative intensities of rotational lines are all very similar to those shown in Figure 31, but the total absorption intensity increases as a function of irradiance due to higher ablation rates at higher irradiances. This behavior suggests that plume reactions in air [Reference 32] dominate the C_2 energy distribution and that little or no information on nascent ablated products is being obtained. Future experiments should be performed in a vacuum environment to observe nascent products directly.
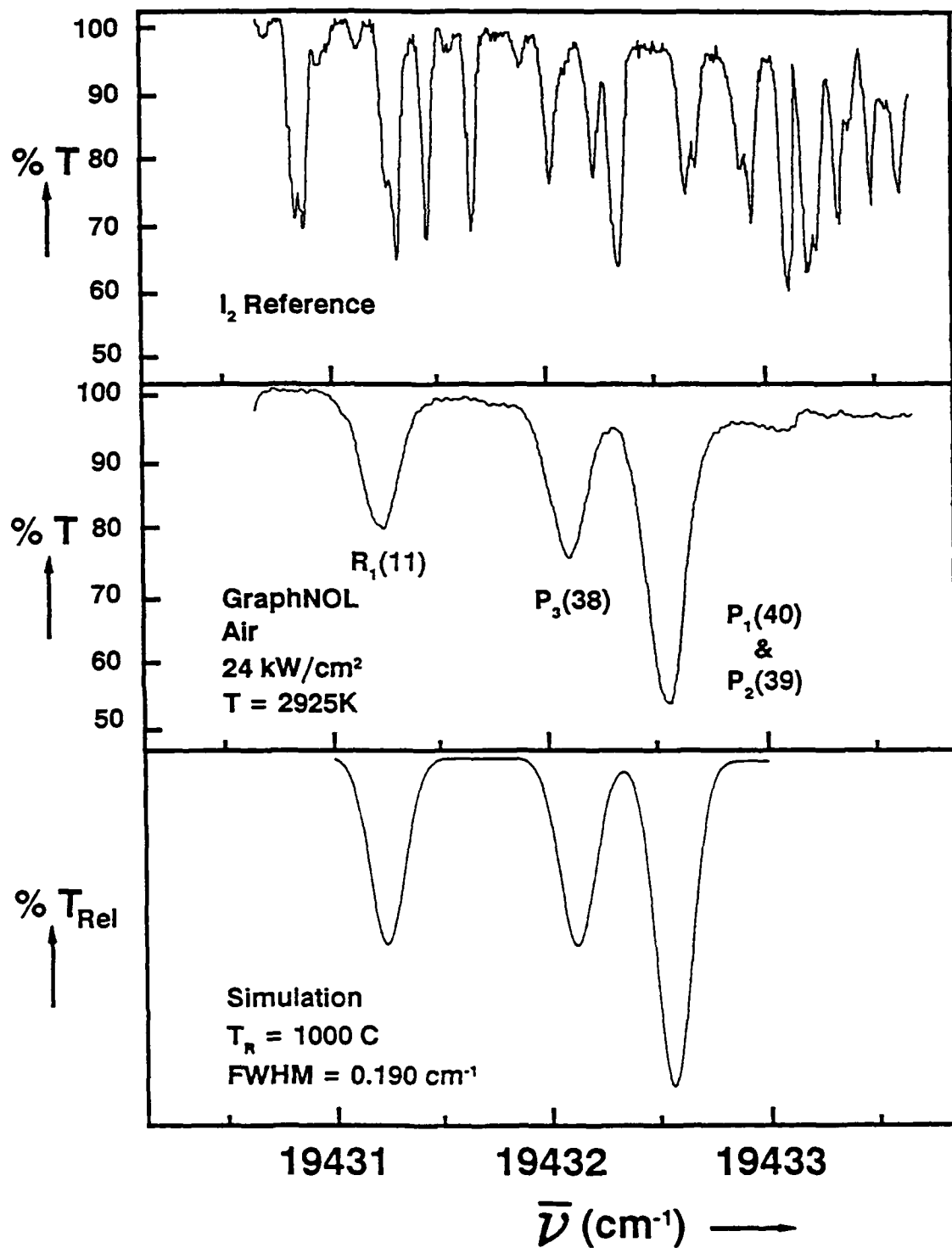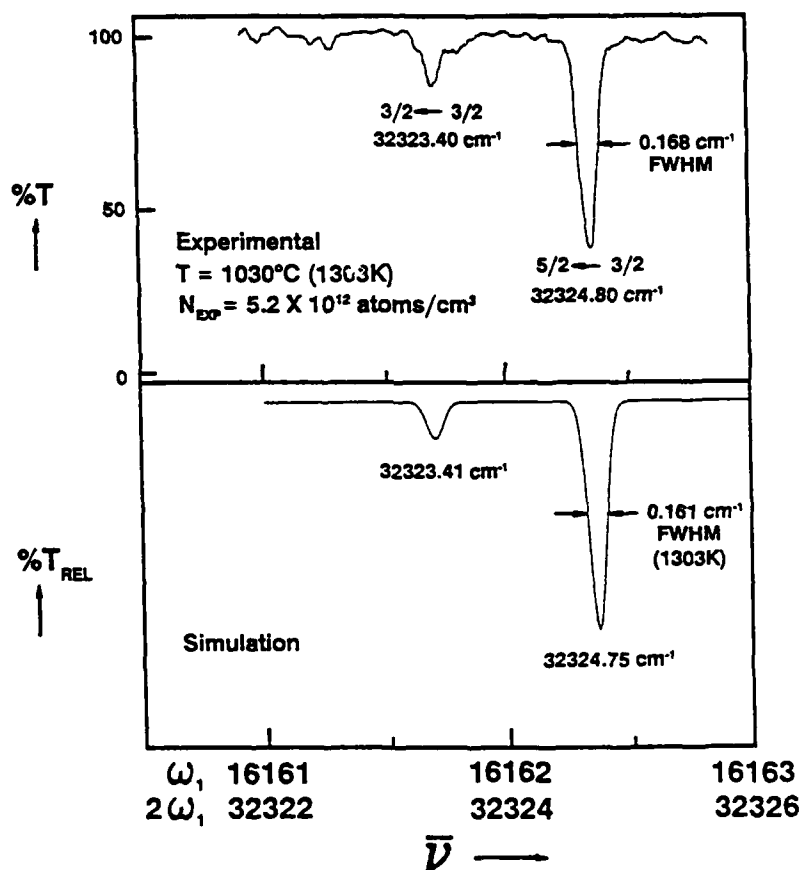
Figure 31. CCLAS Plume Absorption Spectrum Observed During CW GraphNOL Ablation

3.3.3.1 CW Carbon Dioxide Laser/Materials Experiments (continued)

Similar CCLAS plume absorption spectra (using tunable frequency-doubled cw dye laser probe radiation) were obtained for atomic aluminum (Al) generated by cw CO_2 laser ablation of pure aluminum. The top panel of Figure 32 shows the experimental plume absorption spectrum recorded during cw CO_2 laser irradiation of Al contained in a graphite crucible in a vacuum environment at *ca.* 2 kW/cm² peak irradiance. The two prominent absorptions shown are the $^2D_{3/2,5/2} \leftarrow {}^2P^{\circ}_{3/2}$ transitions near λ = 309 nm wavelength; these are assigned and labelled in the figure (*cf.* Section 3.3.3.4). The sample temperature was 1300 K, as measured by both a chromel-alumel thermocouple and an optical pyrometer. The number density of aluminum atoms calculated from the measured absorption and the known transition probability is 5.2×10^{12} atoms/cm³ (*cf.* Section 3.3.3.4); this very sensitive detection can be improved further by use of laser induced fluorescence techniques. The bottom panel of Figure 32 shows a computer simulation of the experimentally recorded spectrum (*cf.* Section 3.3.3.4) using a 0.161 cm⁻¹ FWHM Gaussian lineshape (corresponding to Doppler-broadening for the vapor temperature of 1300 K).

Figure 32. CCLAS Plume Absorption Spectrum Observed During CW Aluminum Ablation

3.3.3.1 CW Carbon Dioxide Laser/Materials Experiments (continued)

Earlier reports [References 18 and 36] described measurements on total plume extinction (*i.e.*, total attenuation by both absorption and scattering processes) of HeNe probe laser beams. Under single particle *counter* conditions [References 37-39], plume extinction measurements can be used to determine particle size and number density. AFOSR/HARC/Rice Program measurements have been extended to experiments at the EDCL 2 cw CO_2 Laser Test Facility at WL/TALE, Kirtland AFB, NM [Reference 7] to observe plume debris produced during cw laser ablation of structural composite materials.

Two probe lasers (HeNe at $\lambda = 0.6328$ μm and Nd:YAG at $\lambda = 1.06$ μm) were used to obtain plume extinction measurements in a similar manner as previous RACHL experiments [Reference 18]. The probe lasers were directed through ablation plumes at distances of 1 - 6 mm from the initial target surfaces and were directed onto fast silicon photodiodes for 1 MHz bandwidth recording by a transient digitizer. Spot sizes of less than 200 μm diameter were used, providing sensitive detection of particles with diameters ≥ 20 μm.

Figure 33 shows total HeNe laser probe beam attenuation measurements (A_T) recorded by passing the HeNe laser probe beam through an ablation plume at a distance of 5 mm from the initial target surface during Run #210-07 (irradiation of material A101 at 100 kW/cm^2). Three timebases [300 ms (top trace), 30 ms (middle trace), and 3 ms (bottom trace)] are used to show the detailed temporal structure of the particle attenuation signals. Analysis of these data using a geometric cross section model [References 18 and 37] indicates that plume particles have diameters ranging up to 150 μm, with a most probable diameter of *ca.* 40 μm. It is very likely that these debris particles account for significant mass removal in the case of many structural composite materials.

Plume extinction measurements have also been performed using the HARC cw CO_2 Laser Test Resource [Reference 4]. GraphNOL and other carbon barrier materials yielded almost no particles, while materials A101 and A105 (both structural composites) yielded copious amounts of particles. The enthalpy of mass removal H_{MR} is decreased from its equilibrium thermochemical ablation value if significant spallation occurs. Hence, it is recommended that total plume extinction measurements be calibrated and used routinely to determine the amount of discrete mass removal occuring in laser/materials interactions.
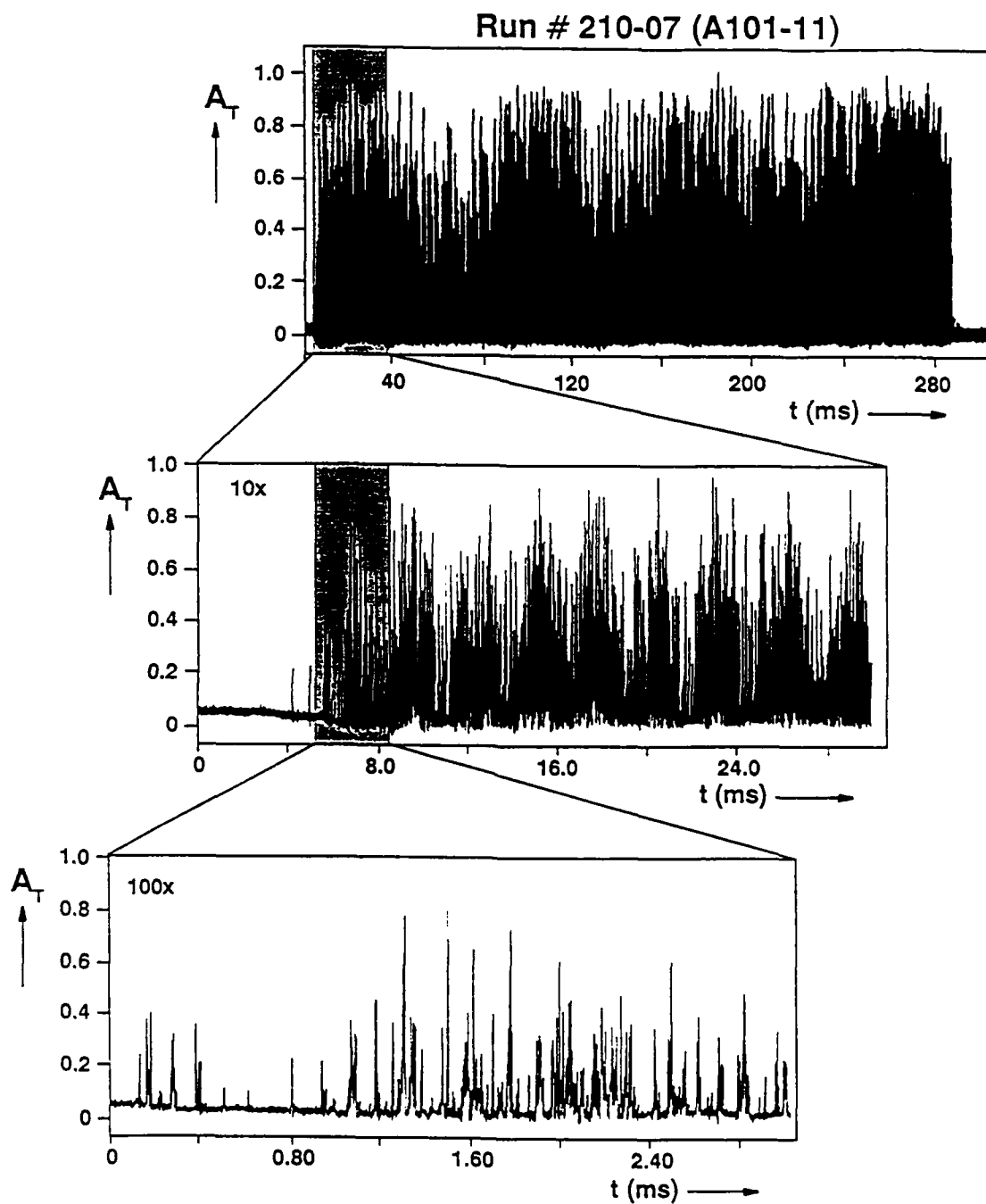
Figure 33. Plume Particle Total Attenuation Measurement A_T Data

3.3.3.2 RP Hydrogen Fluoride Chemical Laser/Materials Experiments

Extension of plume diagnostic instrumentation techniques to fast temporal measurements suitable for evaluating pulsed laser effects has been a major emphasis within the AFOSR/HARC/Rice Program. The following text describes initial fast time-resolved plume emission and absorption spectroscopy measurements completed during repetitively pulsed (rp) hydrogen fluoride (HF) chemical laser interactions with model and baseline materials.

The small scale HARC rp HF Chemical Laser Test Resource [Reference 5; *cf*. Appendix A] has been used to obtain survey plume emission spectra. Sample data are presented below, with special emphasis on carbon vapor plasma. Appendix D contains a series of survey plume emission spectra recorded during rp HF chemical laser irradiation of selected carbon barrier materials, structural composite materials, and metals.

Figure 34 shows plasma emissions generated by rp HF chemical laser irradiation of graphNOL (G) at a peak fluence of 50 J/cm^2 in vacuum as a function of delay time (0-200 ns) from the damage laser pulse peak (which occurs *ca*. 50 ns after pulse initiation). The optical multichannel analyzer (OMA) emission spectroscopy system (*cf*. Section 3.2.4) was used in low resolution mode to collect emission from a 1 mm diameter spot positioned *ca*. 2.5 mm in front of the target surface. The OMA gate width was 100 ns for each spectrum. Note the temporal evolution of prominent emission features at *ca*. λ = 427 nm and 465 nm wavelengths; the doublet components near 465 nm have different time dependences with respect to each other and to the apparent singlet near 427 nm. These features are due to ionic carbon transitions, as discussed in Section 3.3.3.4 below. Intense plasma emissions due to ionic carbon transitions are produced by irradiation of graphNOL at fluences above 25 J/cm^2; the relative abundances of different carbon ions are a strong function of pulse fluence.
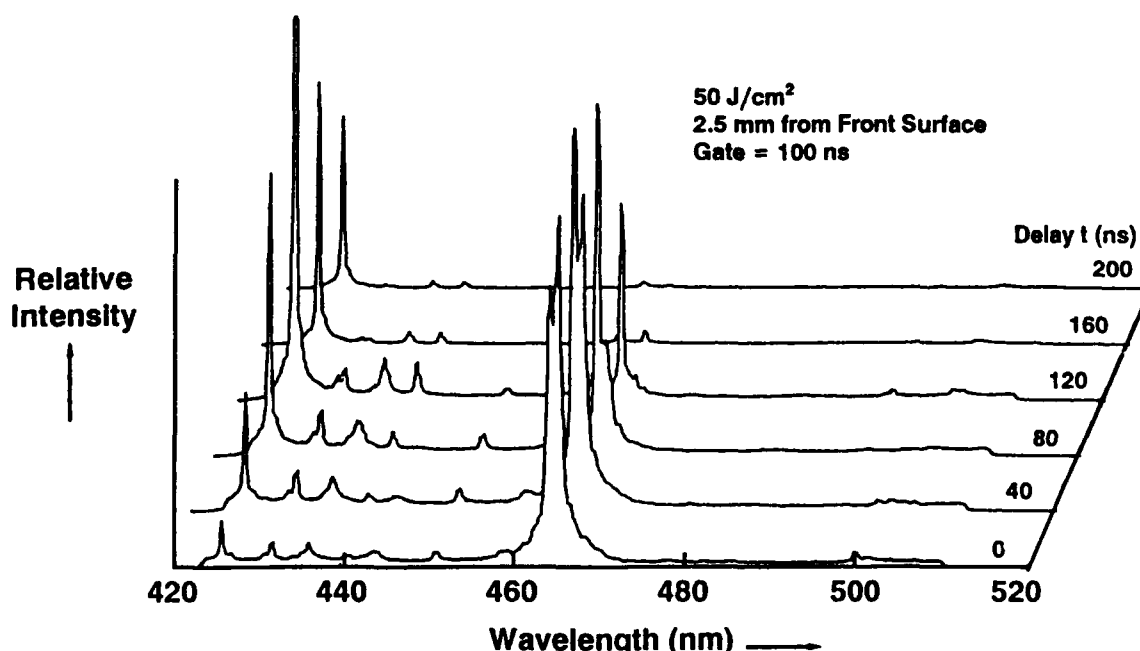
Figure 34. Plume Emission Spectra *vs*. Delay Time Observed During rp GraphNOL Ablation

3.3.3.2 RP Hydrogen Fluoride Chemical Laser/Materials Experiments (continued)

Figure 35 shows the spatial dependence of plasma emissions generated by rp HF chemical laser irradiation of G at a peak fluence of 75 J/cm² in vacuum. The CCD array detector of the OMA system was gated to record emission spectra at the peak of the incident HF laser pulse using a 100 ns gate width. Four different spectra at distances D_{surf} from the G surface of 300 μm, 800 μm, 1.4 mm, and 2.5 mm are shown. Note the decrease in Stark broadening (cf. Section 3.3.3.4) of the λ = 465 nm wavelength spectral features as a function of increasing D_{surf}. This decrease is caused by a large decrease of electron density as a function of distance from the target surface. Quantitative calculation of electron density from Stark broadening measurements is discussed in Section 3.3.3.4 below.
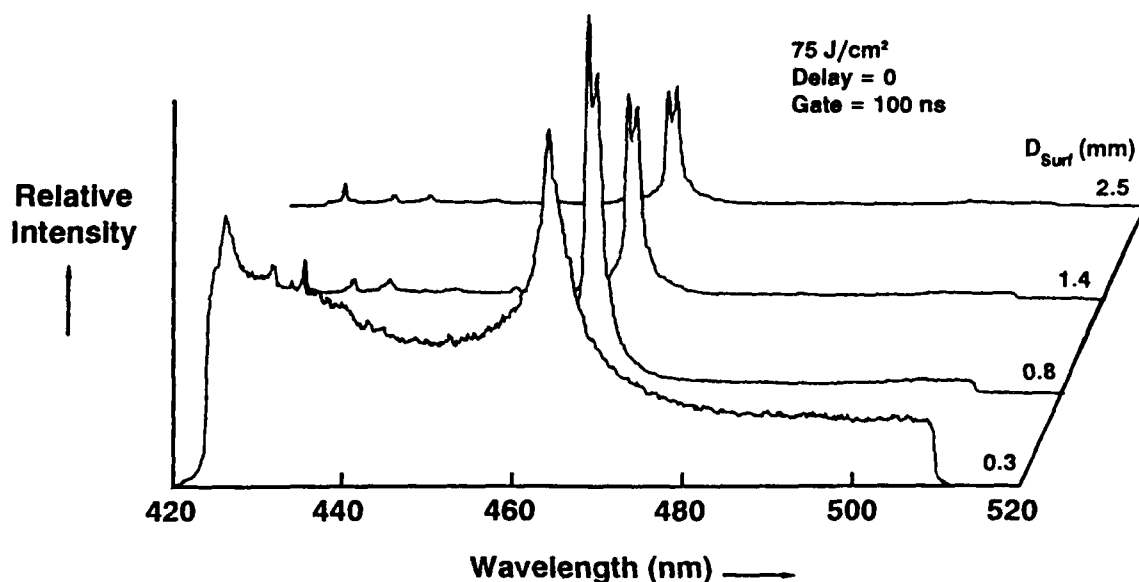
Figure 35. Plume Emission Spectra *vs.* Distance from the Target Surface Observed During rp GraphNOL Ablation

Plume emission spectra of numerous carbon-containing materials (G, C105, AF5, A101, A105, SR7, SR8, and A200) irradiated by the rp HF chemical laser have been obtained; sample spectra are contained in Appendix D. Except in the case of material A200, the most intense plume emission spectral features of all of the carbon barrier materials are produced by ionic carbon transitions. Although systematic experiments have not yet been completed, a preliminary conclusion derived from survey spectra in the λ = 350-650 nm wavelength region is that the presence of an epoxy resin matrix in a structural composite based on graphite fibers has two main effects on plume emission spectra: 1) the plasma formation "threshold" is raised to higher fluences compared to the "threshold" for pure carbon (possibly due to electron scavenging reactions by some plume species), and 2) the emission spectral features exhibit some differences from those of pure carbon at low fluences (e.g., at 30 J/cm²) near the plasma formation "threshold", but the differences become less evident as a function of increasing fluence. It is clear that further experiments and modelling projects on carbon vapor plasma should be completed.

3.3.3.2 RP Hydrogen Fluoride Chemical Laser/Materials Experiments (continued)

The same rp HF chemical laser apparatus [Reference 5] and the CCLAS system (cf. Section 3.2.4 above) have been used in the AFOSR/HARC/Rice Program to obtain high resolution absorption spectra of plume species [diatomic carbon (C_2), neutral atomic titanium (Ti I), and titanium ion (Ti⁺; also labelled Ti II)] generated by rp HF laser ablation of graphNOL (G) and titanium (Ti). C_2 absorptions are due to an intense electronic transition (the Swan system of C_2 [References 33-35]) which produces blue-green absorption features. Ti and Ti⁺ absorptions are due to intense electronic transitions in the visible and ultraviolet spectral regions. Spectroscopy of these systems is discussed in Section 3.3.3.4 below.

Figure 36 shows the same 3 cm⁻¹ interval CCLAS spectrum previously illustrated for cw graphNOL (G) ablation (cf. Figure 31). In the case of Figure 36, G samples were irradiated by a rp HF chemical using pulse energies of ca. 350 mJ/pulse in pulse widths of ca. 200 ns (FWHM) at 1 Hz repetition rate. The beam was focussed by a quartz lens to a spot size ca. 1.28 mm long X 0.55 mm wide (measured using an epoxy resin target) to produce a peak fluence of ca. 50 J/cm² on G slab samples. The CCLAS cw dye laser probe beam was positioned ca. 1 mm from the target front surface and was slowly scanned from 19430.5 to 19433.5 cm⁻¹. The probe dye laser beam transmitted through the plume was detected by a fast silicon detector (5 ns rise time) and averaged by a boxcar integrator (Stanford Research Systems Model SR250). The boxcar delay was set to 2 µs from the peak of the HF laser pulse (which was monitored by a fast InAs photodiode), and the boxcar gate width was set to 1 µs duration. Only a single scan was taken for this spectrum. In future experiments, better S/N absorption spectra will be obtained by signal averaging several sequential wavelength scans and/or by averaging several laser shots during a wavelength scan.
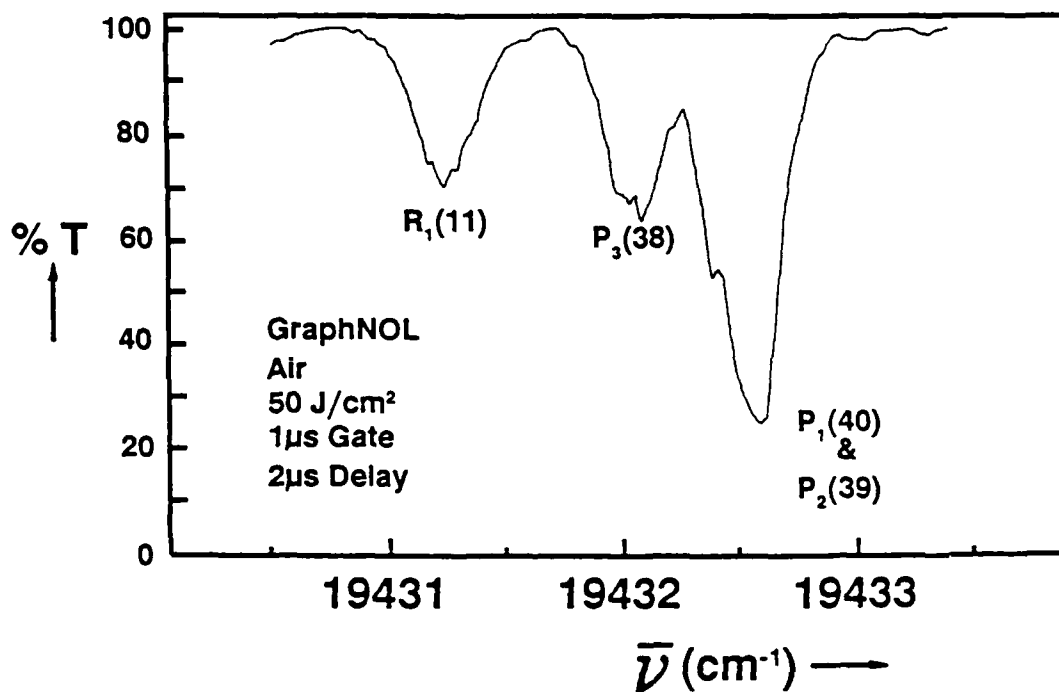
Figure 36. CCLAS Plume Absorption Spectrum Observed During rp GraphNOL Ablation

Simulation of the C_2 absorption spectrum shown in Figure 36 is discussed in Section 3.3.3.4 below. It is important to note that C_2 is only observed at moderately long delay times (2 µs or longer) after the rp HF laser pulse peak. It seems likely that the C_2 absorption is due, at least in part, to reaction processes such as recombination that generate species after the initial laser pulse.

58

3.3.3.2 RP Hydrogen Fluoride Chemical Laser/Materials Experiments (continued)

In future programs, CCLAS experiments will be extended to short wavelengths [e.g., the vacuum ultraviolet (VUV) spectral region] in order to monitor atomic and ionic carbon species (that are major prompt constituents of the laser generated plasma) in appropriate states using intense spectral transitions.

Since the CCLAS system was not configured for VUV experimentation in the AFOSR/HARC/Rice Program, visible and ultraviolet transitions of atomic and ionic titanium were used to demonstrate sensitive detection of plume species at early formation times. Figure 37 shows CCLAS spectra of atomic titanium (Ti I) recorded during rp HF chemical laser irradiation of pure titanium foil samples irradiated at peak fluences of 7 J/cm² (top panel) and 14 J/cm² (bottom panel) in a vacuum environment. The absorption monitored is the $w^5D^\circ_3 \leftarrow a^5P_2$ transition at a spectral peak frequency of 21624.48 cm⁻¹ (corresponding to $\lambda = 462.439$ nm vacuum wavelength) [Reference 40]. The boxcar integrator sampled a 230 ns duration gate at a delay time of 450 ns with respect to the rp HF laser pulse peak, thereby detecting prompt titanium species.
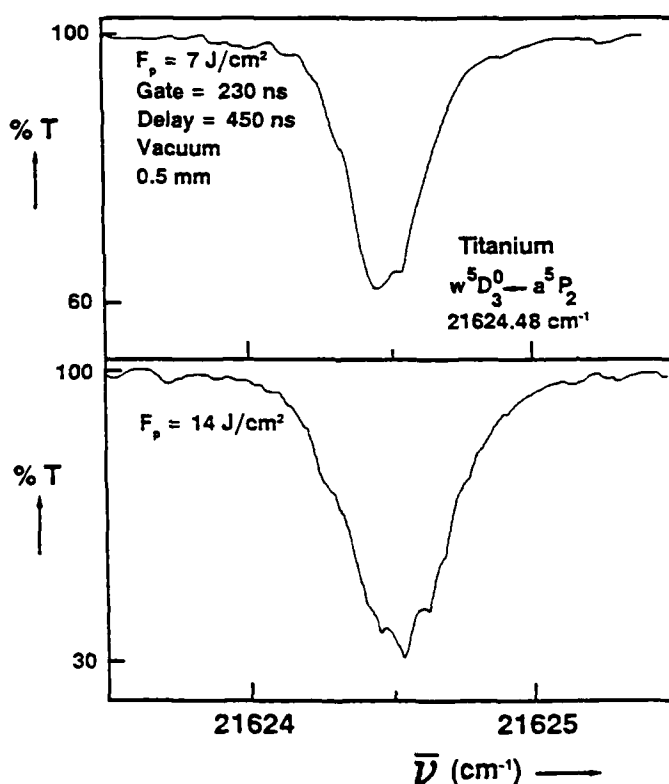
Figure 37. CCLAS Plume Absorption Spectrum Observed During rp Titanium Ablation

CCLAS plume absorption spectra of singly ionized titanium (Ti⁺; termed Ti II in spectroscopic notation) have been observed when titanium is irradiated at higher fluences (well above the plasma "threshold"). Figure 38 shows CCLAS spectra of ionic titanium (Ti II) recorded during rp HF chemical laser irradiation of pure titanium foil samples irradiated at a peak fluence of 66 J/cm² in a vacuum environment; the figure panels show spectra observed as a function of CCLAS probe beam distance (0.5-1.5 mm) from the target surface. The ultraviolet absorption monitored is the $z^2F^\circ_{7/2} \leftarrow a^4F_{9/2}$ transition at a spectral peak frequency of 31097.38 cm⁻¹ (corresponding to $\lambda = 321.571$ nm vacuum wavelength) [Reference 40].
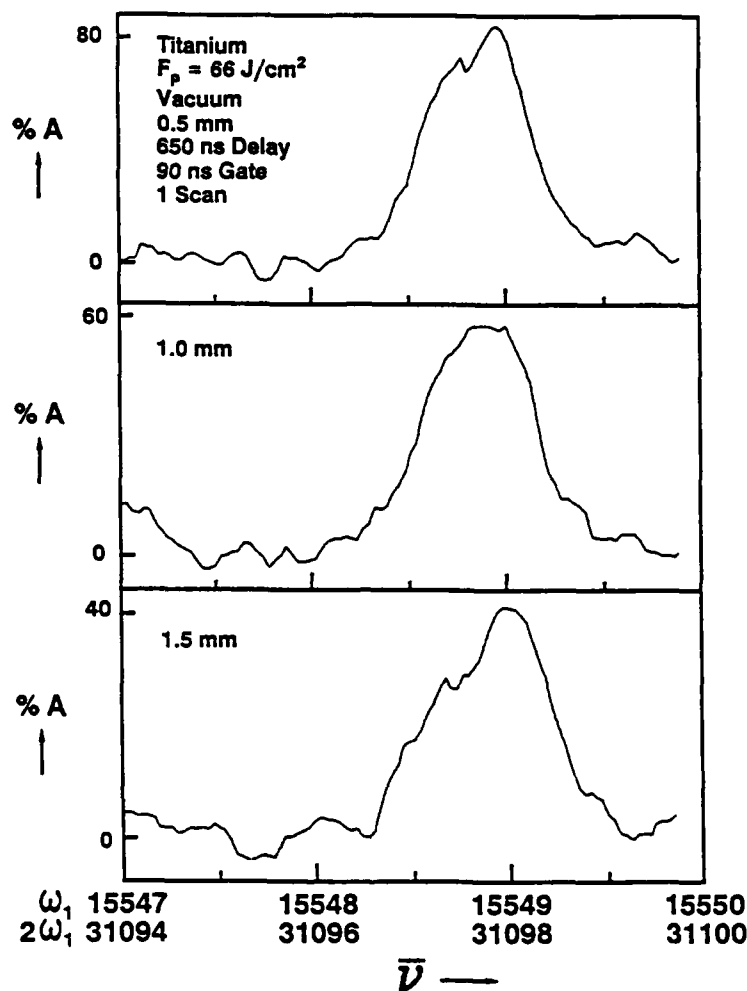
Figure 38. CCLAS Plume Absorption Spectra Observed During rp Titanium Ablation at High Fluence

All six of the $z^4G^\circ_{J'} \leftarrow a^4F_{J''}$ multiplet transitions of singly ionized titanium (Ti II) in the λ = 344-350 nm spectral region [References 40-41] have also been observed during rp HF chemical laser irradiation of pure titanium. However, these transitions absorbed 100% of the CCLAS probe beam even at the lowest HF peak fluence (8 J/cm^2) used. It is clear that significant titanium plasma formation occurs at even this relatively low fluence.

Time-resolved plume absorptions due to neutral and singly ionized titanium have been recorded. By measuring delay time vs. probe distance from the target surface, the peaks of the velocity distributions have been determined to be 1.1 X 10^5 cm/s and 5 X 10^4 cm/s, respectively, for neutral and singly ionized titanium ablation products. If these ablation products are generated with a Maxwell-Boltzmann (MB) distribution, the peaks in the velocity distributions correspond to translational temperatures of ca. 2800 K and 1900 K, respectively. Further experiments are, however, needed to determine the translational energy distributions of these ablated species; they are probably non-MB and they may change markedly as a function of vapor and plasma densities.

3.3.3.2 RP Hydrogen Fluoride Chemical Laser/Materials Experiments (continued)

Measurements on total plume extinction (*i.e.*, total attenuation by both absorption and scattering processes) of HeNe probe laser beams during rp HF chemical laser ablation of several materials have also been completed. The apparatus and methods were similar to those described for cw CO_2 laser ablation experiments (*cf.* Section 3.3.3.1 above).

Figure 39 shows representative time-resolved ablation plume measurements obtained using samples of materials SR7 (top panel), AF1 (second panel), AF4 (third panel), and AF5 (bottom panel) irradiated by the rp HF laser at an average fluence of 25 J/cm^2 and at 0.5 Hz PRF. All of the particle attenuations shown were measured during the first rp HF laser shot by a HeNe laser probe beam (with a 190 μm focussed spot diameter) positioned 1 mm from each initial target surface. Corresponding particle attenuation measurements were also taken at 5 mm distance and both sets of measurements were obtained for each rp HF laser shot. Additionally, similar particle attenuation measurements were obtained for many different rp HF laser average fluences (1, 5, 10, 15, 25, 40, and 80 J/cm^2; the highest average fluence measurement was made only on material AF5) and at other PRFs (10 Hz, *etc.*).

Some principal observations on these ablation plume particle measurements are:

1) material SR7 (a cured epoxy resin) generally yields the most particles at a given fluence, followed by materials AF5, AF4, and AF1; all of these materials produce many particles over the 5-40 J/cm^2 fluence range,

2) very few particles are evident at the lowest fluence studied (1 J/cm^2); the particle yield generally increases as a function of increasing fluence for all materials (corresponding to larger recession depths/pulse Δ_p and greater mass removal as a function of increasing fluence),

3) the first HF laser shot on each specimen generally produces the most particles and there is usually a decrease in the abundance of particles as a function of shot number,

4) the particle size distribution peaks at smaller particle diameters (*ca.* 20 μm or less; these particle diameters were determined by the same method described in Reference 18) than was found in the cw DF laser ablation case (*cf.* Reference 18), and

5) the arrival times of particles are long after the rp HF laser pulse is absorbed (*ca.* 1 μs); typical arrival times correspond to particle velocities of 5-100 m/s.

Additional experiments were completed to establish features of the axial and radial particle density distributions. Generally, it was found that the greatest particle density is along the incident rp HF laser beam and closest to each target surface. The angular distribution of particles was sampled; the ablation plume is contained within a cone with a half apex angle of 35-40 degrees.

Ablation plume products of material SR7 were collected on a salt window and an infrared absorption spectrum was obtained. The spectrum in the 2800-3600 cm^{-1} spectral region resemble pyrolyzed epoxy residues similar to those obtained in Reference 42. Therefore, it appears that the ablated particles of material SR7 include "fried" epoxy resin.
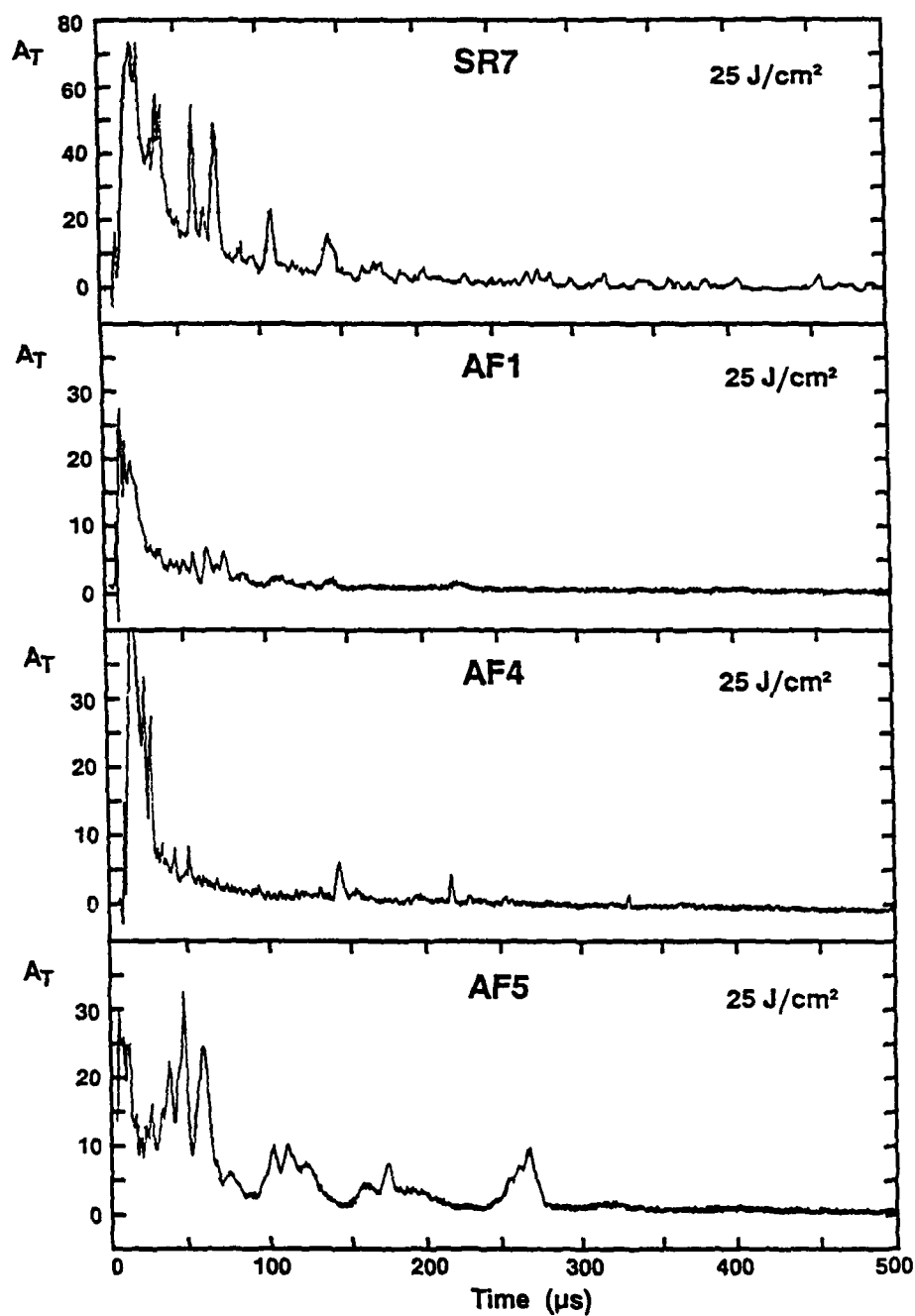
Figure 39. Time-Resolved Plume Particle Total Attenuation (A_T) Measurement Data Obtained During RP HF Laser Ablation

3.3.3.3 CW Hydrogen Fluoride Chemical Laser/Materials Experiments

As part of the transitioning of AFOSR/HARC/Rice Program emphasis from spacecraft survivability to other Air Force interests, the cw HF Chemical Laser Test Resource [Reference 3; cf. Appendix A] and the CCLAS system (cf. Section 3.2.4 above) have been applied to the detection of SiO in reaction plumes generated by oxidation of laser-heated ceramics (SiC and Si_3N_4). Both of these ceramic materials are candidates for oxidation-resistant coatings for carbon/carbon composites and other high and ultrahigh temperature composites. This work is important for the development of high and ultrahigh temperature materials for turbine engines, the National AeroSpace Plane (NASP), and other aircraft/spacecraft applications.

HARC/Rice personnel have obtained high resolution absorption spectra of SiO as a plume species generated by cw HF chemical laser heating of SiC in an O_2 atmosphere (5 torr pressure). The SiO absorptions are due to an intense electronic transition (the $A^1\Pi \leftarrow X^1\Sigma^+$ system [Reference 43]) in the ultraviolet spectral region near $\lambda = 235$ nm wavelength. SiO spectroscopy is discussed in Section 3.3.3.4 below. SiO concentration provides a measure of the oxidation rate of SiC; active oxidation generates much higher concentrations of SiO than passive oxidation (which occurs by diffusion through a SiO_2 coating).

Pure SiC samples were irradiated at a peak irradiance of 1.7 kW/cm² in an oxidizing atmosphere (5 torr O_2). The frequency-doubled CCLAS probe beam (produced by second harmonic generation of tunable cw dye laser radiation by a BBO doubling crystal; cf. Section 3.2.4) was positioned ca. 1 mm from the SiC surface. Front surface temperature was monitored using a two-color optical pyrometer.

The third panel of Figure 40 shows a 3 cm⁻¹ interval of the experimental SiO plume absorption spectrum. The prominent absorption features are rovibronic transitions of the A ← X 0,0 band of SiO. Other panels display the cw HF chemical laser power (top panel), the front surface temperature (second panel), and Te spectral calibration lines (bottom panel). Simulation and analysis of these SiO plume absorptions are discussed in Section 3.3.3.4 below.

Additional SiO plume absorptions were monitored at other O_2 pressures (to determine active/passive oxidation behavior) and in a time-resolved detection mode in which absorption at a particular spectral peak frequency was measured as a function of SiC front surface temperature during heating of the material by the cw HF chemical laser [Reference 31]. Similar measurements have also been performed on pure Si_3N_4 in the presence of an O_2 atmosphere [Reference 31]. Active/passive oxidation transition data are discussed in Section 3.3.5 below.

After the period of the AFOSR/HARC/Rice Program, improvements have been made to the apparatus to incorporate laser-induced fluorescence detection of the SiO product. Active/passive oxidation phenomena have now been measured with greatly increased sensitivity; initial results on SiC are in excellent agreement with other studies [Reference 44]. It is clear that plume diagnostic spectroscopic instrumentation provides a sensitive *in situ* method for mechanistic understanding, kinetic measurements, and performance assessment of candidate oxidation-resistant high and ultrahigh temperature materials.
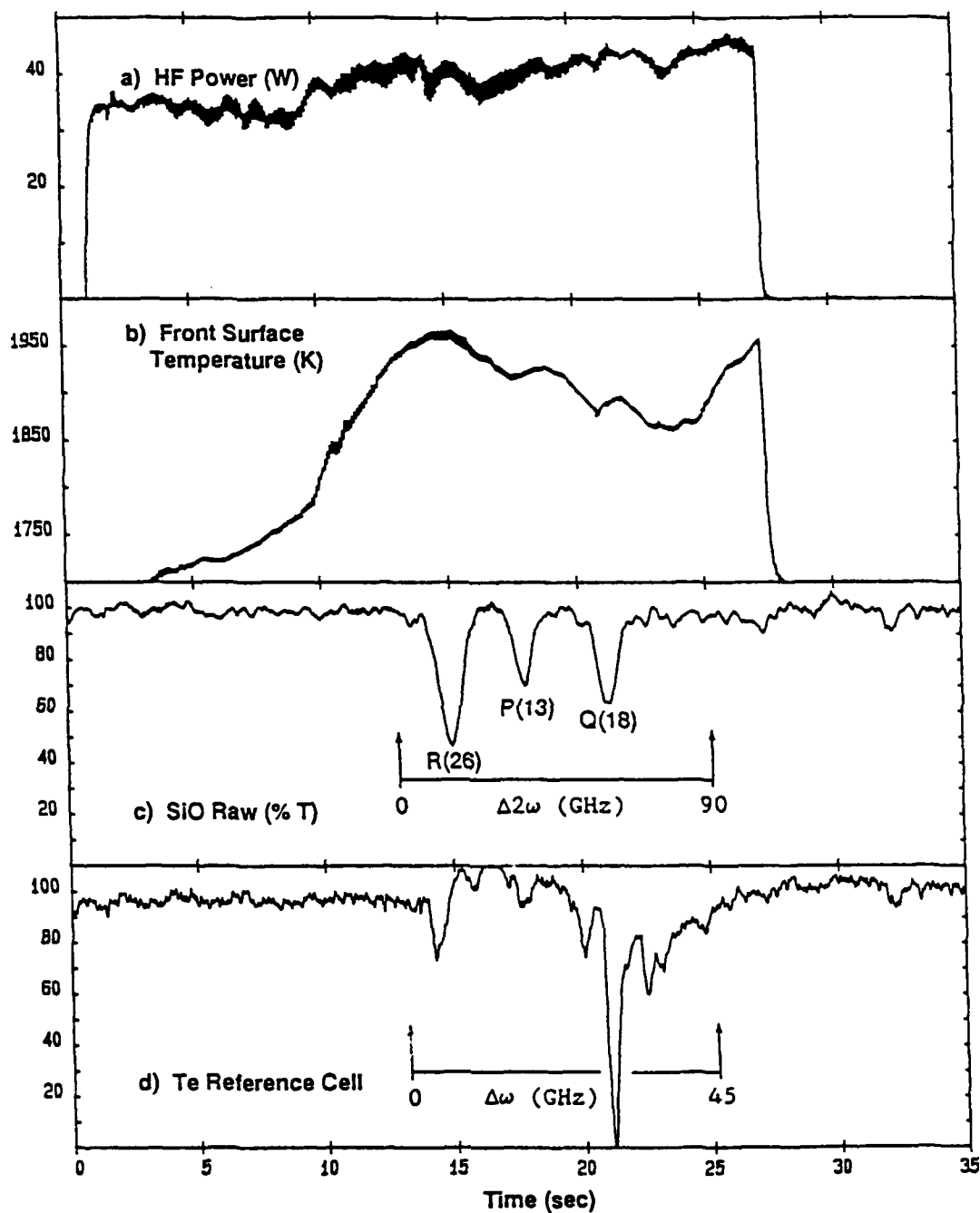
Figure 40. CCLAS Plume Absorption Spectrum and Other Measurements Obtained
During CW Laser Heating of SiC in O_2

3.3.3.4 Analysis of Spectroscopic Measurements

This section presents analyses and simulations of plume absorption/emission spectra obtained during the AFOSR/HARC/Rice Program. The ultimate aim of this work is to use plume spectroscopy measurements to determine plume species abundances, energy contents, and optical properties for complete understanding of mass and energy balances, including the efficiency of mass removal.

Atomic and Ionic Species

Three neutral and charged atomic species have been studied in the AFOSR/HARC/Rice Program: carbon (C), aluminum (Al), and titanium (Ti). This subsection presents some background information on their spectroscopy (transition assignments, energies, wavelengths, and transition probabilities) and the determination of pertinent physical properties (atomic/ionic number density, electron density, $etc.$) from spectroscopic measurements such as plume absorption intensities and transition linewidths. Under the cw laser irradiation conditions used in the studies reported, only neutral atomic species are generally important; ionic species can, however, be formed under very high irradiance ($I > 200$ kW/cm^2) conditions. Under the rp laser irradiation conditions (fluences up to 130 J/cm^2) used pulsed laser experiments, several ionization stages are observed in each atomic system.

Figure 41 shows a simplified energy level diagram for neutral carbon (C I), singly ionized carbon (C II), and doubly ionized carbon (C III) [Reference 45]. Ionization energies are indicated by IE$_i$ labels. The energy scale is in electron volt (eV; 1 eV = 8066 cm^{-1}) units. A few transitions observed in carbon plasma emission spectra are shown.
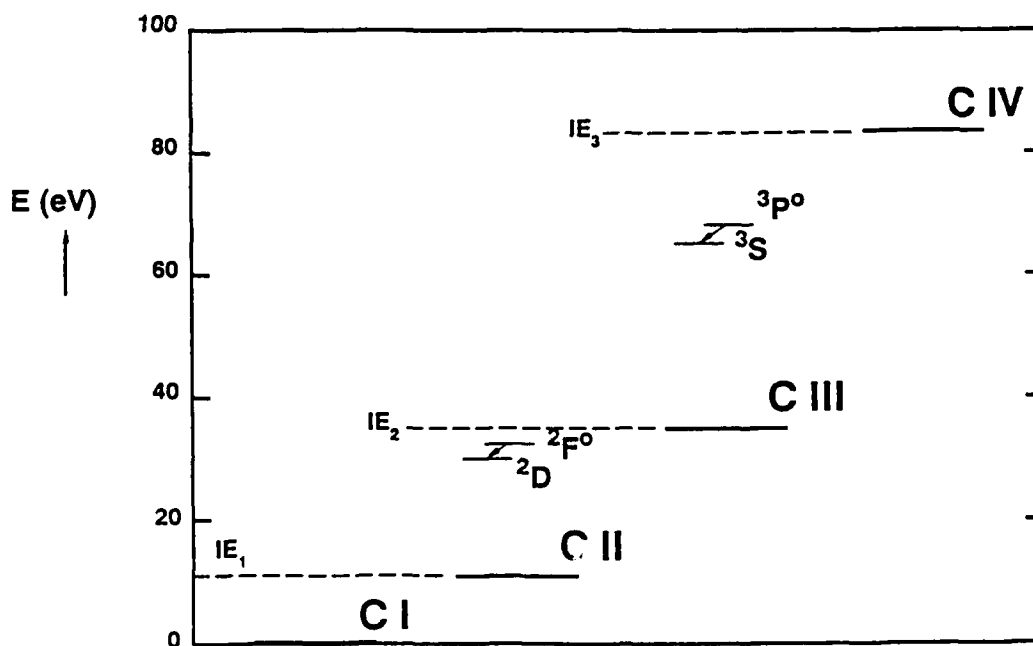
Figure 41. Energy Level Diagram for Atomic and Ionic Carbon Vapor Species

3.3.3.4 Analysis of Spectroscopic Measurements (continued)

Prominent features of plume emission spectra generated by rp HF chemical laser ablation of graphNOL and other carbon-containing materials (cf. Figure 34 and Appendix D) are readily assigned to ionic carbon transitions [References 45-46]: 1) $\lambda = 427$ nm: C^+ (C II) $^2F^\circ_{5/2,7/2} \rightarrow$ $^2D_{3/2,5/2}$, and 2) $\lambda = 465$ nm: C^{2+} (C III) $^3P^\circ_{0,1,2} \rightarrow {}^3S_1$. [Other transitions within the $\lambda = 350$-650 nm wavelength range are identified in the graphNOL plume emission spectra presented in Appendix D.] These particular transitions dominate the visible plume emission spectra of carbon-containing materials, but it is likely that many other transitions in the ultraviolet and vacuum ultraviolet spectral regions provide far more information on the nature of carbon vapor plasma species in our experiments. Hence, it is necessary to perform shorter wavelength plume emission (and absorption) spectroscopy measurements to identify and analyze a more significant set of transitions that monitor excited state populations that are generated in carbon vapor plasma.

The presence of intense multiply ionized carbon emission features indicates that the carbon vapor plasma generated at even modest fluences (ca. 30 J/cm^2) is highly ionized, in accord with Saha equation calculations [Reference 46]. The plasma "threshold" in pure carbon vapor probably occurs at fluences between 10-15 J/cm^2 under our rp HF chemical laser irradiation conditions. The degree of ionization rises strongly as a function of fluence above this "threshold" and the spatial/temporal populations of particular ionic excited states are highly dependent on plasma electron temperature, density, opacity, etc. (as well as on material, including important impurities that can either initiate or scavenge plasma species). A very extensive set of experiments with full spatial/temporal/spectral resolution is required to explore the complex plasma phenomenology that occurs during rp laser/materials interactions (and during very high irradiance cw laser/materials interactions). Only demonstration experiments have been performed in the present AFOSR/ HARC/Rice Program.

An example of the pertinent information that can be extracted from plasma emission spectra is provided by linewidth analysis of the prominent carbon plasma emission feature near $\lambda = 426.7$ nm assigned to the C^+ [singly ionized carbon, termed C II in spectroscopic notation] $^2F^\circ \rightarrow {}^2D$ transition multiplet. Although the emission appears to be a single broad feature, it includes three overlapping transitions. Transition assignments, energies, wavelengths, and Einstein A_{ki} values (spontaneous emission coefficients) [Reference 47] for the three transitions are:

C II Transition	Transition Energy (cm^{-1})	Wavelength (nm)	A_{ki} (s^{-1})
$^2F^\circ_{7/2} \rightarrow {}^2D_{5/2}$	23427.64	426.726	2.44 X 10^8
$^2F^\circ_{5/2} \rightarrow {}^2D_{3/2}$	23429.07	426.700	2.30 X 10^8
$^2F^\circ_{5/2} \rightarrow {}^2D_{5/2}$	23427.64	426.726	1.60 X 10^7

Using these transitions and Einstein A values, a simulation of the 426.7 nm emission was performed to determine the Stark broadened linewidth. Figure 42 shows the experimental and simulated spectra; a FWHM of 25 cm^{-1} (0.455 nm) was imposed on each transition in the simulation. [The wavelength of the experimental spectrum is slightly shifted in comparison with the simulated spectrum; this shift is due to a calibration error for the OMA monochromator used in a low resolution mode.]

The plasma electron density (N$_e$) can be calculated from [References 48-49]:

$$\text{FWHM} = 2WN_e/10^{16} \tag{7}$$

where FWHM is the full width at half maximum intensity of the line (nm),
W is the electron impact width parameter (nm), and
N$_e$ is the plasma electron density (cm^{-3}).

3.3.3.4 Analysis of Spectroscopic Measurements (continued)

The electron width parameter is reported as 0.11 nm at $N_e = 5.0 \times 10^{16}$ cm^{-3} and 0.87 nm at $N_e = 4.0 \times 10^{17}$ cm^{-3} [Reference 50]. Using the simulated FWHM value of 0.455 nm and rearranging Equation [7] leads to:

$$WN_e = 2.27 \times 10^{15} \qquad [8]$$

Since W is linearly dependent on N_e and only weakly dependent on the electron temperature, N_e and W are estimated to be 3.2×10^{16} cm^{-3} and 0.07 nm, respectively. These calculations can be refined by obtaining higher resolution emission (or absorption) spectra and by deconvoluting the instrumental profile (OMA monochromator) contribution to the linewidth.
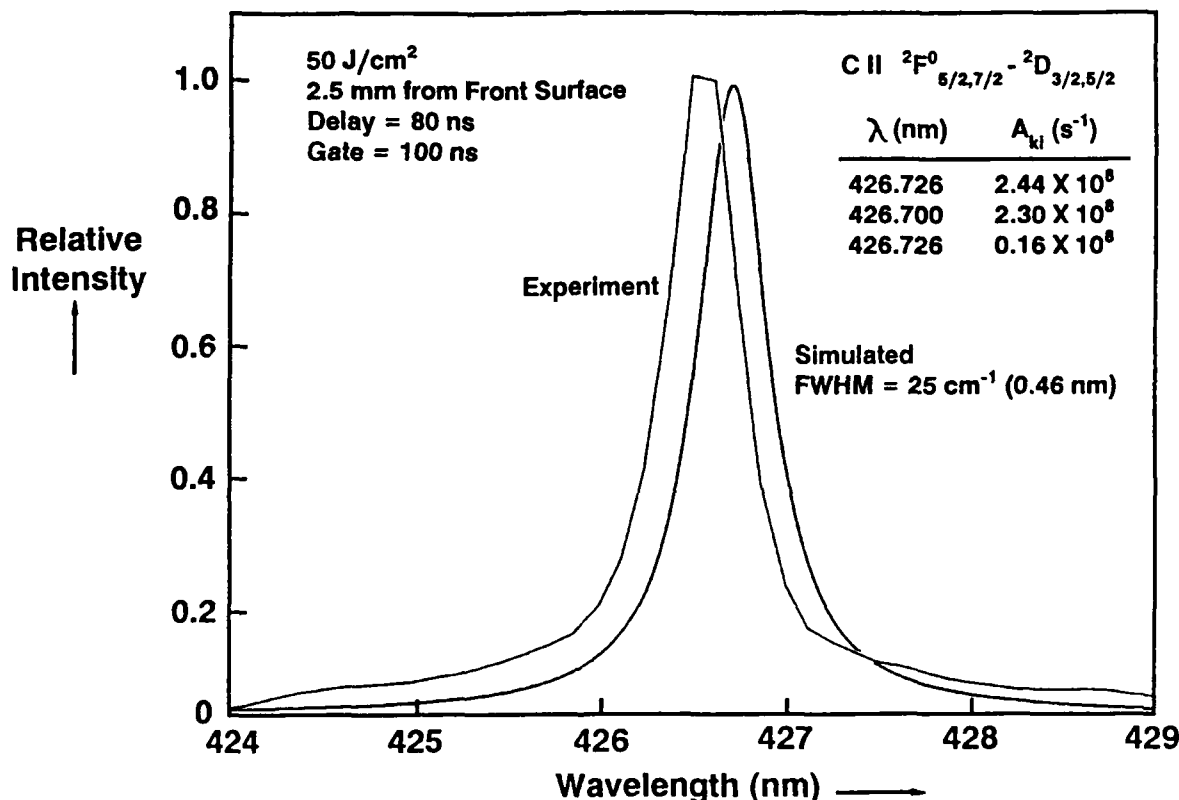
Figure 42. Experimental and Simulated C II Plasma Emission Spectra

In addition to providing improved Stark broadening measurements, future experiments will be directed toward determination of electron temperature by relative intensity measurements on transitions originating from different ionization state carbon atoms/ions [cf. References 48-49]. Electron density, temperature, and opacity will be determined with spatial and temporal resolution for comparison with modelling calculations.

3.3.3.4 Analysis of Spectroscopic Measurements (continued)

Aluminum plume absorption and emission spectroscopic measurements have also been analyzed. Figure 43 shows a simplified energy level diagram for neutral aluminum (Al I), singly ionized aluminum (Al II), and doubly ionized aluminum (Al III) states [References 45 and 51]. Ionization energies are indicated by IE_i labels. The energy scale is in electron volt (eV; 1 eV = 8066 cm^{-1}) units. A few transitions observed in absorption (cf. Figure 32) and emission (cf. Al and Al 6061-T6 spectra in Appendix D) are shown.
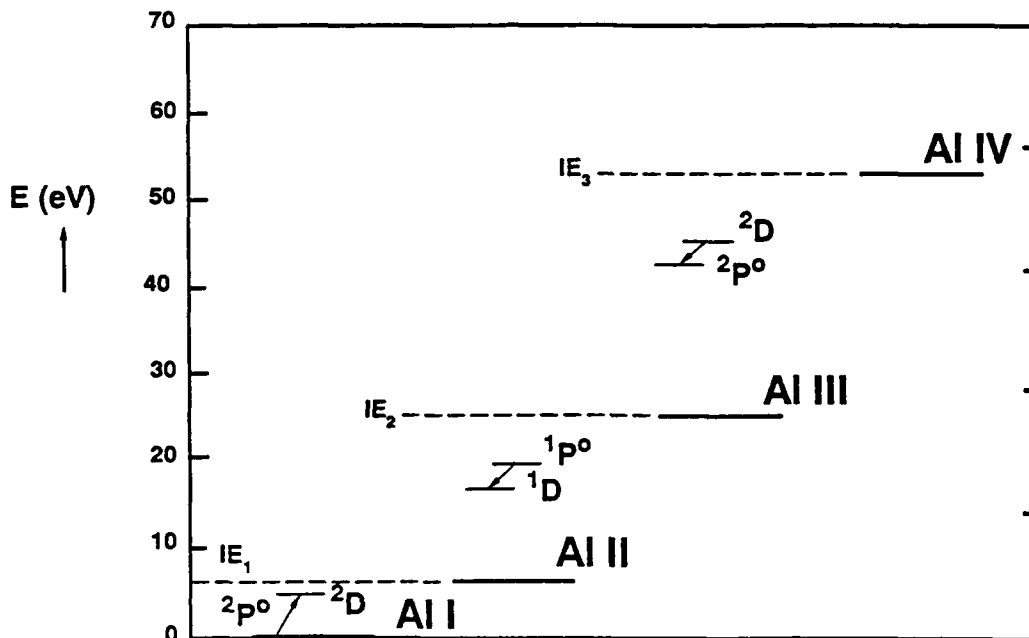
Figure 43. Energy Level Diagram for Atomic and Ionic Aluminum Vapor Species

Quantitative plume absorption spectroscopy measurements were completed for the aluminum transitions shown in Figure 32 (cf. Section 3.3.3.1 above). Using the known Einstein A-coefficient for the $^2D_{5/2} \leftarrow {}^2P^{\circ}_{3/2}$ transition (A_{ki} = 7.3 X 10^7 s^{-1} [Reference 52]), plume absorption pathlength (ℓ = 3.4 mm; assumed to be the same as the measured sample dimension), plume temperature (T = 1303 K; assumed to be the same as the measured surface temperature; cf. discussion below), and peak absorption (A = 0.64; measured), the atomic number density n is calculated to be 5.2 X 10^{12} cm^{-3} using the Beer-Lambert relation:

$$A = 1 - \exp(-\sigma n \ell), \qquad [9]$$

and the value of the Doppler-broadened peak absorption cross section σ :

$$\sigma = 1.85 \text{ X } 10^{-6} A_{ki} \nu^{-3} (M/T)^{1/2}, \qquad [10]$$

where ν is the transition energy (in cm^{-1} units) and M is the atomic mass (in amu units). [An implicit assumption in the above is that Q_e, the electronic partition function, is unity (i.e., the thermal populations of excited states are negligible)]. The actual value of the atomic number density n is 1.7 X 10^{12} cm^{-3} [Reference 53], ca. 1/3 the calculated value. Principal uncertainties in this quantitative comparison are the target front surface temperature and the plume pathlength; future experiments will measure these quantities accurately.

3.3.3.4 Analysis of Spectroscopic Measurements (continued)

Simulation of spectral lineshapes was also completed for aluminum plume absorption spectra. As shown in the bottom panel of Figure 32, a Doppler-broadened lineshape with a full width at half maximum intensity (FWHM) of 0.161 cm⁻¹ (corresponding to a translational temperature of 1300 K) matches the experimentally observed lineshape well. This plume translational temperature is the same as the measured target front surface temperature.

Figure 44 shows a simplified energy level diagram for neutral and ionic titanium states. The format is the same as for Figures 41 and 43. It was possible to perform plume measurements on titanium using transitions originating near the ground state for Ti I (the ^{5}F multiplet is *ca.* 0.8 eV above the ground state) and originating in the actual ground state for Ti II [assignments are from References 40 and 54]. Similar plume measurements should be performed on carbon, but the corresponding transitions occur in the vacuum ultraviolet (VUV) spectral region; hence, new laser sources and new experimental techniques are required to probe atomic and ionic carbon effectively.
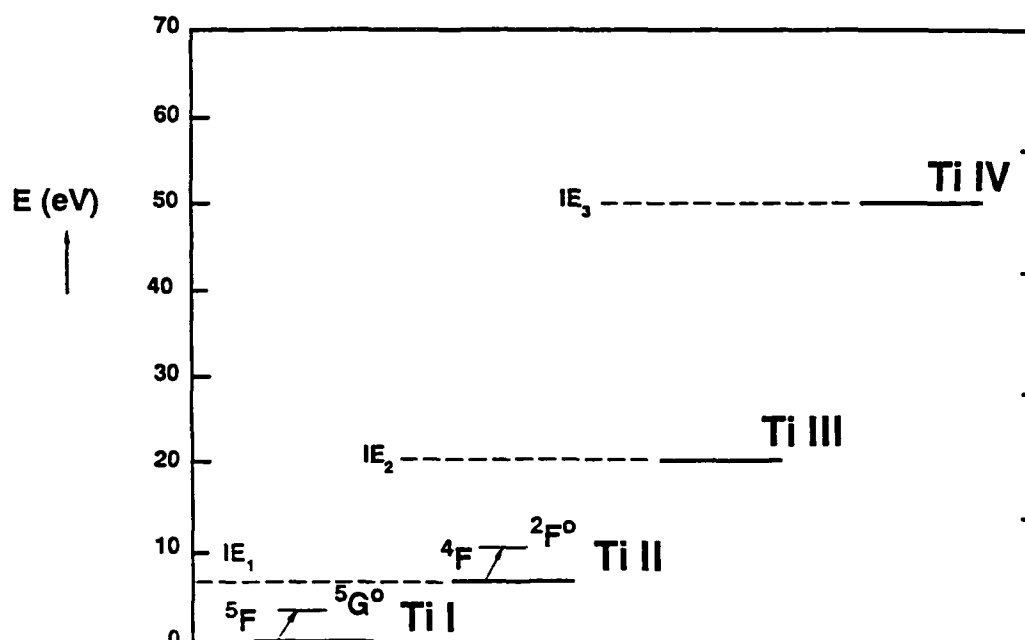
Figure 44. Energy Level Diagram for Atomic and Ionic Titanium Vapor Species

3.3.3.4 Analysis of Spectroscopic Measurements (continued)

Diatomic Carbon (C_2)

Diatomic carbon (C_2) is a principal constituent of ablated carbon plumes. This subsection presents background information on the spectroscopy (transition assignments, energies, wavelengths, and transition probabilities) of the electronic transition of C_2 (the Swan System [References 33-35]) which has been very useful in the AFOSR/HARC/Rice Program to perform plume measurements.

Figure 45 shows a simplified energy level diagram for excited ($d^3\Pi_g$) and ground ($a^3\Pi_u$) electronic/vibronic states of C_2 that are observed in HARC and EDCL 2 experiments [References 7-8]. The principal (0-0; notation: upper vibronic state - lower vibronic state) band used for both absorption and emission plume spectroscopy measurements is shown.
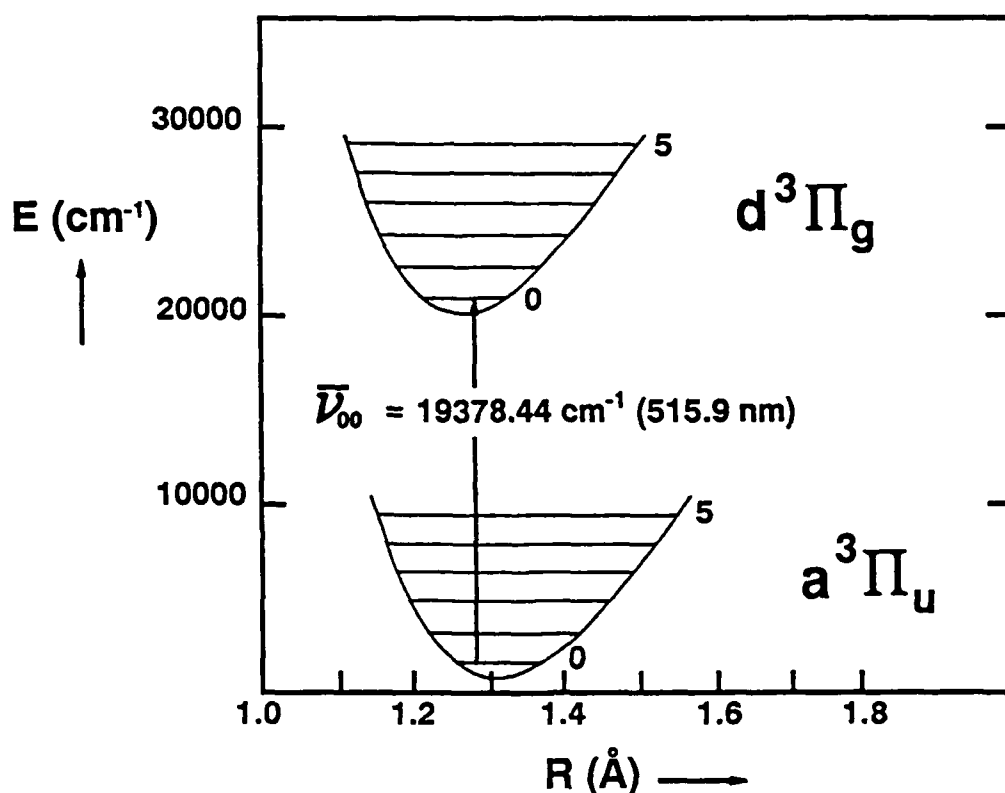
Figure 45. Energy Level Diagram for the Swan System of Diatomic Carbon

Referring back to the bottom panel of Figure 27 (cf. Section 3.3.3.1), the features observed in the emission spectra at λ = 435 nm (Δv = +2), 465 nm (Δv = +1), 510 nm (Δv = 0), 550 nm (Δv = -1), and 595 nm (Δv = -2) are all due to diatomic carbon (C_2) Swan system vibrational band sequences [cf. References 33-35]; Δv = +2, +1, 0, -1, and -2 band sequences are labelled in the figure. The broad short wavelength emission feature peaking at ca. λ = 400 nm is probably due to C_3 [Reference 55]. Prominent bands at λ = 355 nm, 385 nm, and 420 nm are due to the violet band ($B^2\Sigma^+$ - $X^2\Sigma^+$) system of CN [Reference 56]. Only the C_2 Swan bands are discussed and simulated in this AFOSR/HARC/Rice Program.

70

3.3.3.4 Analysis of Spectroscopic Measurements (continued)

Figure 46 (bottom panel) shows the experimental high resolution plume emission spectrum in the $\Delta v = 0$ band sequence of C_2 produced during cw laser ablation of graphNOL (*cf.* Section 3.3.3.1); the intense features at *ca.* 516.5 nm and 512.99 nm are the band heads of the 0,0 and 1,1 vibrational bands, respectively, of the C_2 Swan system. All the other features are individual rotational transitions or accidental pileups of two or more individual rotational transitions of these bands. The top panel of Figure 44 shows a computer simulation of the high resolution C_2 Swan 0,0 and 1,1 vibrational bands; spectroscopic constants for the simulation were taken from References 34 and 35. Intensities were calculated by accounting for the Boltzmann population distribution of rotational and vibrational levels in the upper state, individual rotational line strength factors (*i.e.*, the Hönl-London factors), and the Franck-Condon factors for the vibrational bands. The rotational and vibrational temperatures for the simulation were both fixed at 2000 °C, and the simulated spectrum was convoluted with a 3.0 cm^{-1} Lorentzian full-width at half-maximum (FWHM) linewidth on each individual rotational line. Only the 0,0 and 1,1 vibrational bands are included in the simulation. Discrepancies in the wavelengths of simulated and experimental spectral features are due to monochromator calibration errors, to inaccuracies in the upper and lower state rotational constants (the constants were derived from a least squares fitting to experimental data), and/or to perturbations in the energy levels. A better fit between the simulated and experimental spectrum may be possible by slight adjustment of the upper state rotational constants.
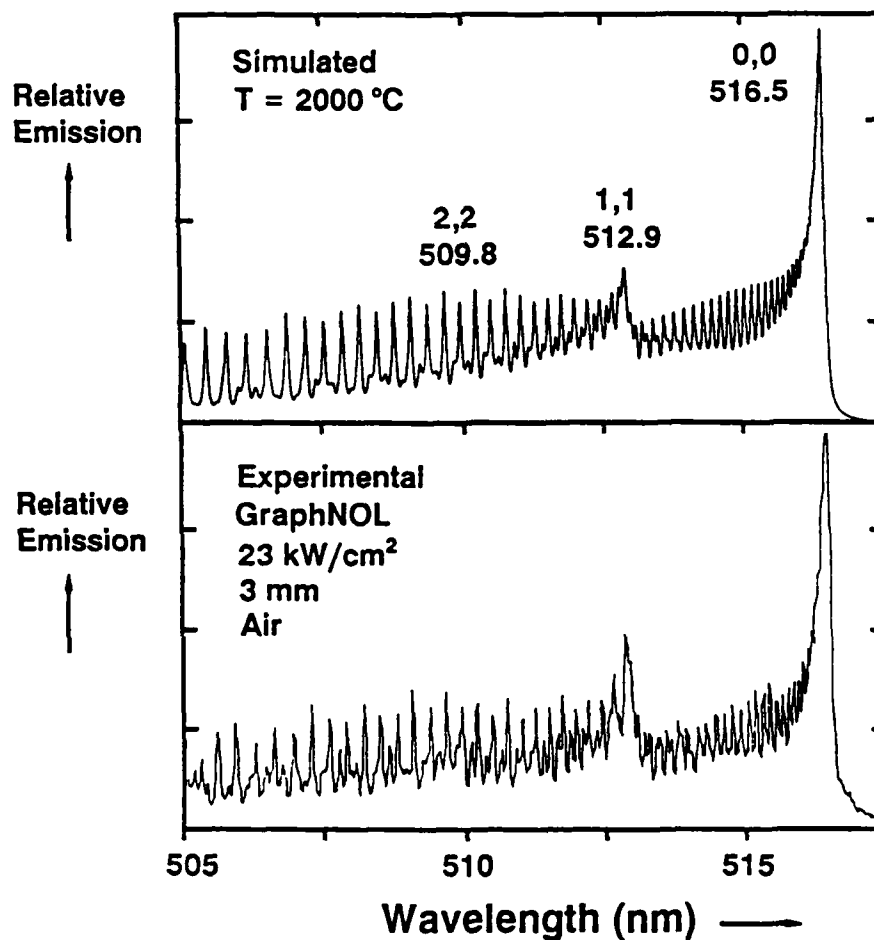
Figure 46. Experimental and Simulated Plume Emission Spectra for CW GraphNOL Ablation

3.3.3.4 Analysis of Spectroscopic Measurements (continued)

Figure 47 shows computer simulated C_2 Swan 0,0 and 1,1 vibrational bands as a function of vibrational/rotational temperature [1000 °C (top panel), 2500 °C (middle panel), and 4000 °C (bottom panel)]. Note that the change in appearance of the simulated spectrum as a function of temperature is detectable over this broad range. However, computer simulation of emission spectra is probably not a sensitive technique for accurate determination (within ± 200 °C) of the vibrational, rotational, and translational temperatures of plume species. Indeed, computer simulation of some emission spectra may be quite inaccurate due to underlying blackbody and other emission(s). High resolution absorption measurements are required to provide highly accurate determination of plume internal and translational energy distributions.
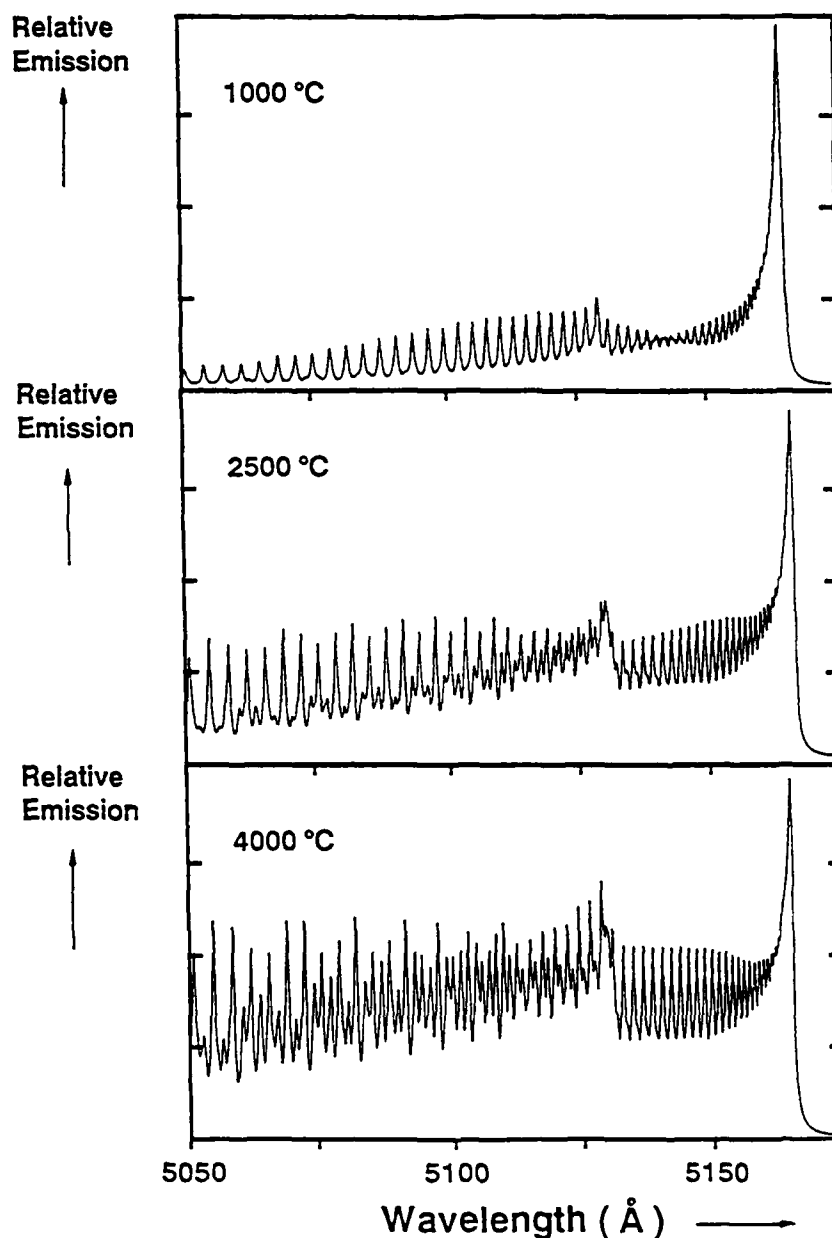
Figure 47. Computer Simulated C_2 Plume Emission Spectra as a Function of Temperature

3.3.3.4 Analysis of Spectroscopic Measurements (continued)

Analyses and simulations of C_2 plume absorption spectra were completed for a variety of experimental conditions: 1) cw CO_2 laser irradiation of graphNOL within the I = 7-400 kW/cm^2 peak irradiance range, and 2) rp HF chemical laser irradiation of graphNOL at ca. 50 J/cm^2 peak fluence. The plume absorption spectral simulation procedure is the same as that described for C_2 plume emission spectra (see above). Figure 31 (bottom vs. middle panels) shows the quality of simulation achieved for a cluster of rotational transitions. Figure 48 shows a comparison between experimental (top panel) and simulated (bottom panel) C_2 plume absorption spectra in the Swan system 0,0 band head region recorded during cw CO_2 laser irradiation of G in air. The experimental spectrum was constructed by splining together 3 separate wavelength scans recorded at 7 kW/cm^2 peak irradiance; the average G apparent front surface temperature was ca. 3300 K. The simulated C_2 spectrum was generated using a rotational temperature of 1000 °C and a 0.190 cm^{-1} FWHM Gaussian lineshape.
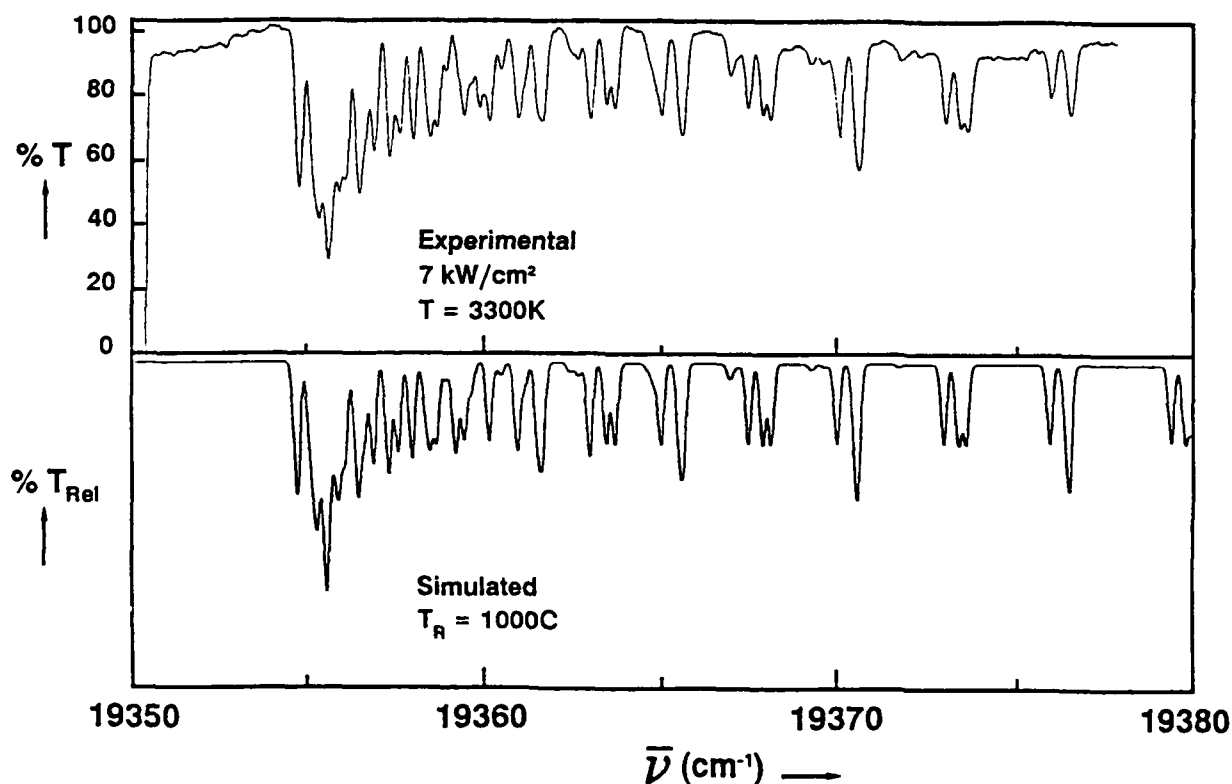
Figure 48. Experimental and Simulated C_2 Plume Absorption Spectra

In the case of rp laser experiments, the C_2 absorption spectrum recorded in Figure 36 is matched well by a set of rotational transitions with a FWHM Gaussian linewidth of 0.270 cm^{-1} (larger than the typical cw value of 0.190 cm^{-1}). This larger linewidth corresponds to a plume temperature of ca. 9000 K (compared to ca. 4460 K for the cw laser ablation case).

73

3.3.3.4 Analysis of Spectroscopic Measurements (continued)

Figure 49 shows a high resolution simulated spectrum of the particular rotational transitions observed during oxidation of SiC (cf. Figure 40). Spectroscopic constants for the simulation were obtained from Reference 43. A Lorentzian linewidth of 0.2 cm^{-1} and a rotational temperature of 1600 °C were also used in the overall simulation. Discrepancies between observed (cf. Figure 40, third panel) and calculated (cf. Figure 49) spectral features are due mainly to strong variations in sample temperature during cw laser heating of SiC (cf. Figure 40, second panel). In future experiments, a segmented mirror optical delivery system will be used to heat targets with nearly flood-loaded beams.
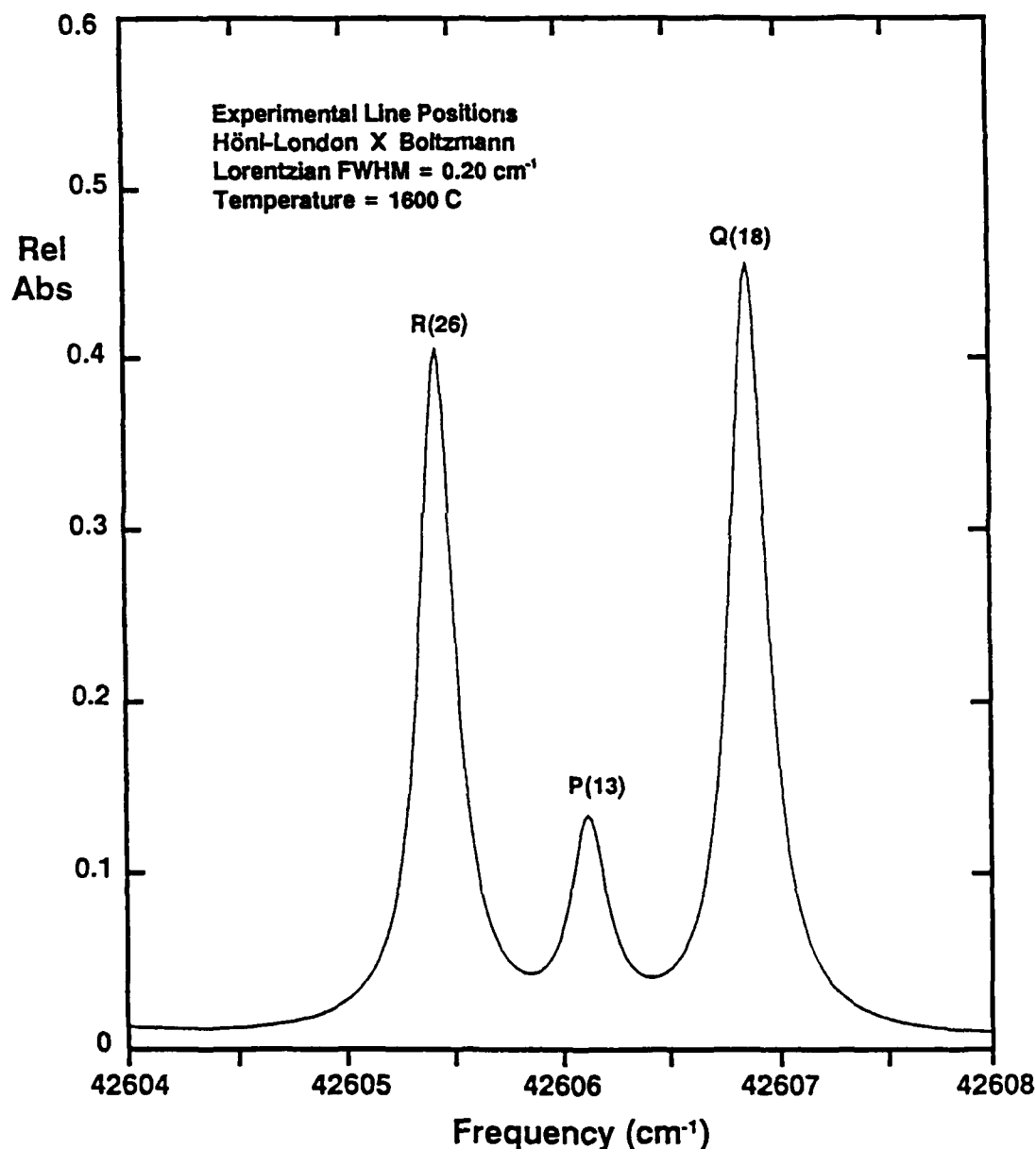
Figure 49. Simulated Expanded Section of the SiO A-X (0,0 Band) Electronic Spectrum

3.3.4 Ablation Experiments

Several types of ablation experiments have been performed on graphNOL and other materials as part of the AFOSR/HARC/Rice Program:

1) cw DF chemical laser ablation (using the HARC cw DF Chemical Laser Test Resource [Reference 3]) of graphNOL over an extended irradiance range [References 2 and 23] and of candidate carbon barrier materials [References 1, 36, and 57],

2) cw DF chemical laser ablation (using both the RACHL device at WL/TALE, Kirtland AFB, NM and the HARC cw DF Chemical Laser Test Resource [Reference 3]) of graphNOL, other carbon barrier materials (TBR and 101), and structural composite materials (AF1 through AF5) [Reference 18],

3) cw CO_2 laser ablation (using the EDCL 1 and EDCL 2 devices at WL/TALE, Kirtland AFB, NM) of graphNOL, other carbon barrier materials (C101 through C108, Ultramet materials, etc.), and structural composite materials (A101, A105, etc.) [References 1, 7, 8, and 57],

4) cw HF chemical laser ablation (using the HARC cw HF Chemical Laser Test Resource [Reference 3]) of graphNOL [References 14 and 15] and of cured epoxy resins (SR7 and SR8),

5) rp HF chemical laser ablation (using the HARC rp HF Chemical Laser Test Resource [Reference 5]) of graphNOL [Reference 29] and of cured epoxy resins and structural composite materials,

6) exploratory rp excimer laser ablation (using the HARC rp Excimer Laser Test Resource [Reference 6]) of graphNOL and structural composite materials [Reference 36], and

7) exploratory rp free electron laser (FEL) ablation (using the SCA and Mark III FEL devices at Stanford University, Stanford, CA) of graphNOL and structural composite materials.

GraphNOL ablation results are highlighted in this Final Technical Report. GraphNOL (G) is a fine-grained polycrystalline pure carbon with nearly isotropic and well-known thermal properties that has been used extensively as a baseline material in many laser effects programs [References 7, 8, and 17]. This carbon barrier material (CBM) is an excellent reference material for studies of laser/materials interactions with particular attention on the phenomenology, effects, and mechanisms of these interactions as a function of laser parameters (wavelength, irradiance, and waveform). Laser effects experiments on graphNOL are also unclassified, so the results can be discussed in detail in this unclassified document.

Sections 3.3.4.1 and 3.3.4.2 below summarize ablation experiments on graphNOL and other CBMs. Section 3.4.1 below treats the interaction physics and chemistry associated with thermal laser interactions with carbon barrier materials.

3.3.4.1 CW Laser Ablation

References 1 and 2 describe the basic experimental apparatus and methodology used to perform cw laser ablation experiments. Two primary measurements are important and are performed as a function of laser irradiance:

1) the measurement of the target front surface reflectance, leading to a determination of the wavelength-dependent thermal coupling coefficient α_λ, and

2) the measurement of the target burnthrough time, leading to a determination of the effective enthalpy of ablation Q^*.

For conductive materials studied with low power lasers and small engagement spots, the radial conduction loss I_{RT} (cf. Figure 1) is a very important contribution to the ablation rate; analysis of this two-dimensional (2D) loss [as well as analysis of one-dimensional (1D) radiative, convective, and conductive losses (cf. Figure 1)] is essential to obtain 1D values of Q^* that pertain to real engagement scenarios.

3.3.4.1 CW Laser Ablation (continued)

Figure 50 shows target front surface reflectance measurements on graphNOL (G) as a function of incident cw DF chemical laser irradiance on target [Reference 2]. Note that the reflectance at $\lambda = 3.8$ μm wavelength is low ($R_{3.8} = 0.14 \pm 0.01$) and is independent of irradiance level over the range I = 12 - 47 kW/cm^2. Since G has a transparent plume at all the wavelengths studied [Reference 9], equation [2] can be used to calculate the wavelength-dependent coupling coefficient α_λ from these data.
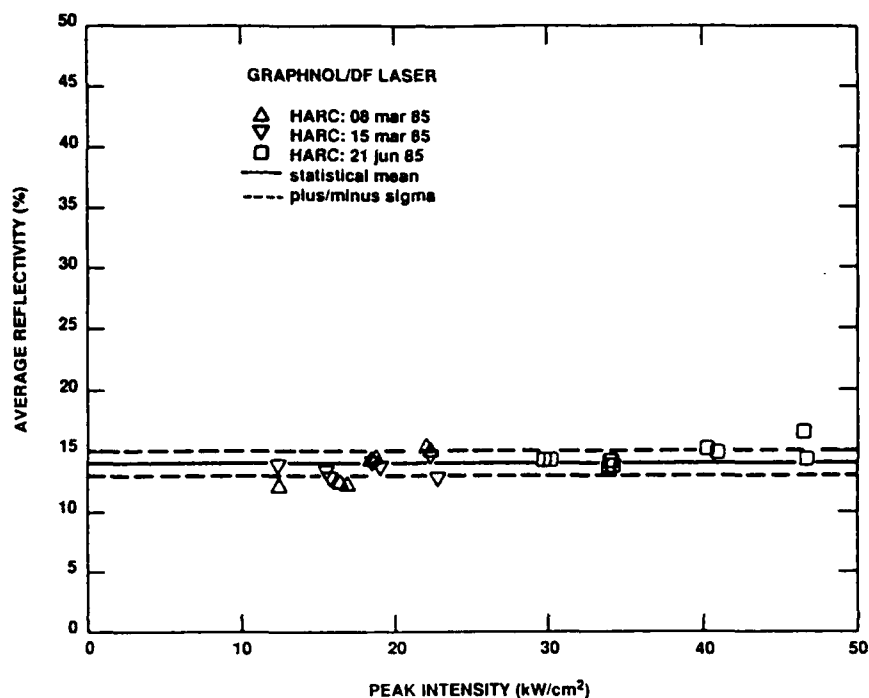
Figure 50. Average Reflectance of GraphNOL During CW DF Chemical Laser Ablation

Table 6 summarizes the values of α_λ determined from all R_λ and ϵ_λ measurements completed on G during cw laser ablation.

Table 6. Average GraphNOL Thermal Coupling Coefficients During CW Laser Ablation

λ (μm)	α_λ	Reference	Irradiance Range
0.515	0.96 ± 0.01	Table 4	9 and 100 kW/cm^2
0.53	0.94 ± 0.02	Table 5	25 - 150 kW/cm^2
0.99	0.93 ± 0.01	Table 5	25 - 150 kW/cm^2
1.06	0.94 ± 0.02	Table 4	9 and 100 kW/cm^2
2.7	0.85 ± 0.01	Refs. 14-15	11 - 18 kW/cm^2
2.9	0.86 ± 0.04	Table 4	9 and 100 kW/cm^2
3.8	0.86 ± 0.01	Ref. 2	12 - 47 kW/cm^2
10.6	0.83 ± 0.03	Table 3	9 and 100 kW/cm^2

76

3.3.4.1 CW Laser Ablation (continued)

GraphNOL reflectance/emittance data are highly consistent; data obtained in air are identical to those obtained in vacuum and all sets of data show a simple monotonic trend of increasing α_λ as a function of decreasing λ. This dark gray CBM should therefore be used as a reference material for future cw laser ablation experiments.

Figure 51 shows sample measured effective enthalpy of ablation Q^* data for graphNOL (G) ablation as a function of incident cw DF chemical laser irradiance on target [Reference 2]. Q^* values are obtained for each test on each material using measured values of the laser irradiance I, the burnthrough time t_{BT}, the material density ρ, and the sample thickness ℓ, together with the energy balance relation [Reference 2]:

$$Q^* = It_{BT}/(\rho\ell) \tag{11}$$
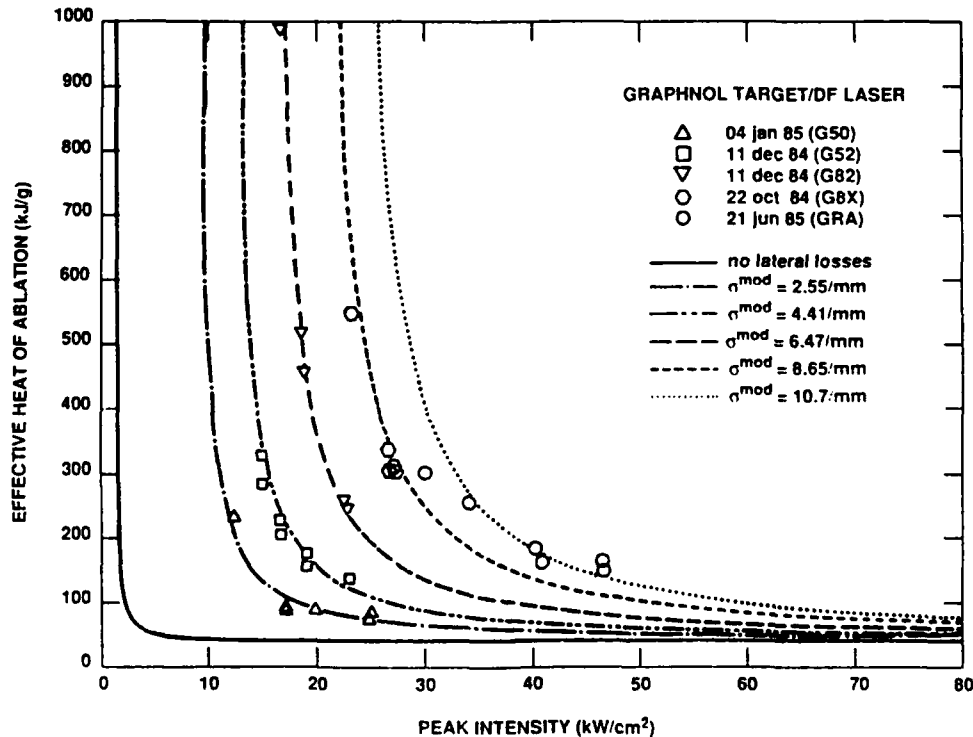
Figure 51. Measured and Calculated Q^*'s for CW DF Chemical Laser Ablation of G

The full theoretical form of Q^*, including 2D losses, is [Reference 15]:

$$Q^*_{2D} = H_A/\{(f_N/I)/(\exp[f_N/\alpha(I)I]-1) - I_{RAD}/I\}, \tag{12}$$

where H_A is the thermochemical enthalpy of ablation (set equal to 29.1 kJ/g for thermochemical ablation of carbon at 3600–3800 K [Reference 23]), f_N is the lateral loss factor (fit to burnthrough data using a nonlinear regression analysis procedure), I is the incident peak irradiance (measured from the incident power and the measured spot size on target), $\alpha(I)$ is the irradiance-dependent coupling coefficient (set equal to the measured value of $1-R_{average}$), and I_{RAD} is the 1D reradiation loss (set equal to 1.2 kW/cm^2 for graphNOL [Reference 2] and materials with similar emittances; set equal to smaller values for materials with lower emittances).

3.3.4.1 CW Laser Ablation (continued)

The parametric curves in Figure 51 shows the magnitude of the 2D effect for these experiments on graphNOL; the upper curves (labelled by their σ^{mod} values) are the 2D fits to the data using parametric values of f_N while the lower, solid, curve is calculated from the corresponding 1D expression (Reference 2, equation 37 in the limit that the absorbed irradiance is much larger than the lateral loss factor [$\alpha(I)I \gg f_N$]):

$$Q^*_{1D} = H_A/[\alpha(I) - I_{RAD}/I] \qquad [13]$$

GraphNOL has a coupling coefficient $\alpha(I)$ that is nearly independent of irradiance (cf. Figure 50 and Table 6). Other materials exhibit strong irradiance-dependent coupling coefficients.

Figure 51 indicates the pitfalls associated with determining the ablation performance of highly conductive materials (e.g., CBMs) using a microscale laser facility. However, the strong 2D effect associated with CBM ablation is still noticeable even on the scale of EDCL 2 experiments (using ca. 32 kW cw CO_2 laser power on target in a nearly flat-top beam with spot sizes of 0.6 - 1.2 cm [References 7-8]).

Figure 52 shows Q^* vs. irradiance I measurements for materials G and C105, together with two-dimensional (2D) ablation fits to the data derived from the model discussed in Reference 2. For material C105, means and standard deviations for multiple shots at several irradiance levels are plotted; the corresponding standard deviations for material G are within the plotted symbol size. Figure 53 shows the difference between one-dimensional (1D) and 2D behavior for each of these materials. It is clear that 2D effects are important for low coupling coefficient (α_λ) materials even using 32 kW delivered from the EDCL 2 laser device onto the target at high irradiances.
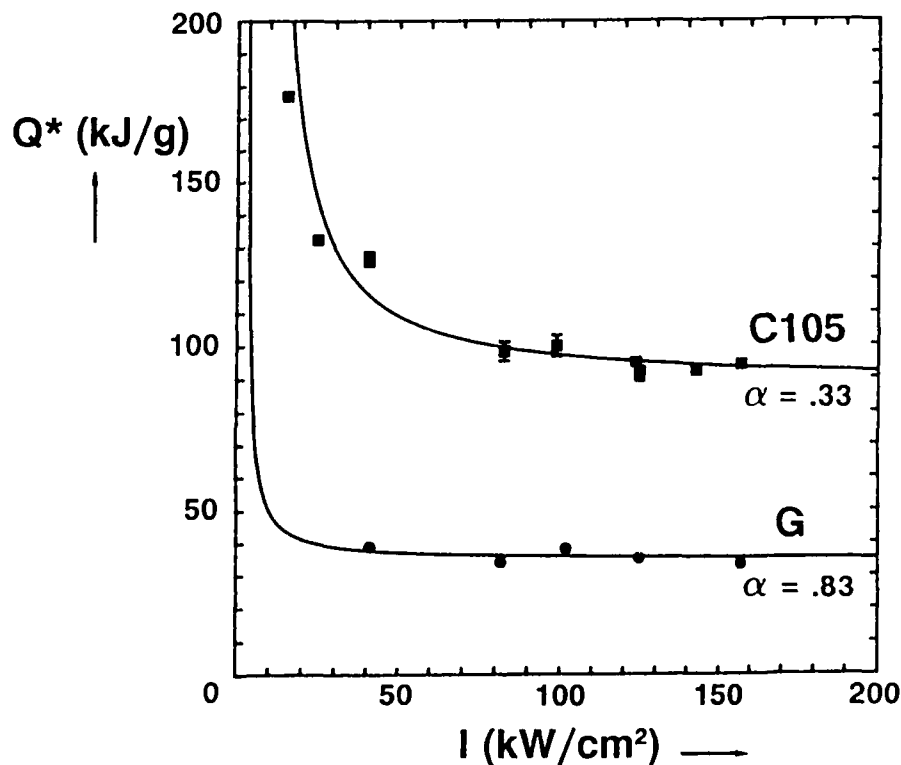
Figure 52. $Q^*(I)$ for Materials G and C105

3.3.4.1 CW Laser Ablation (continued)
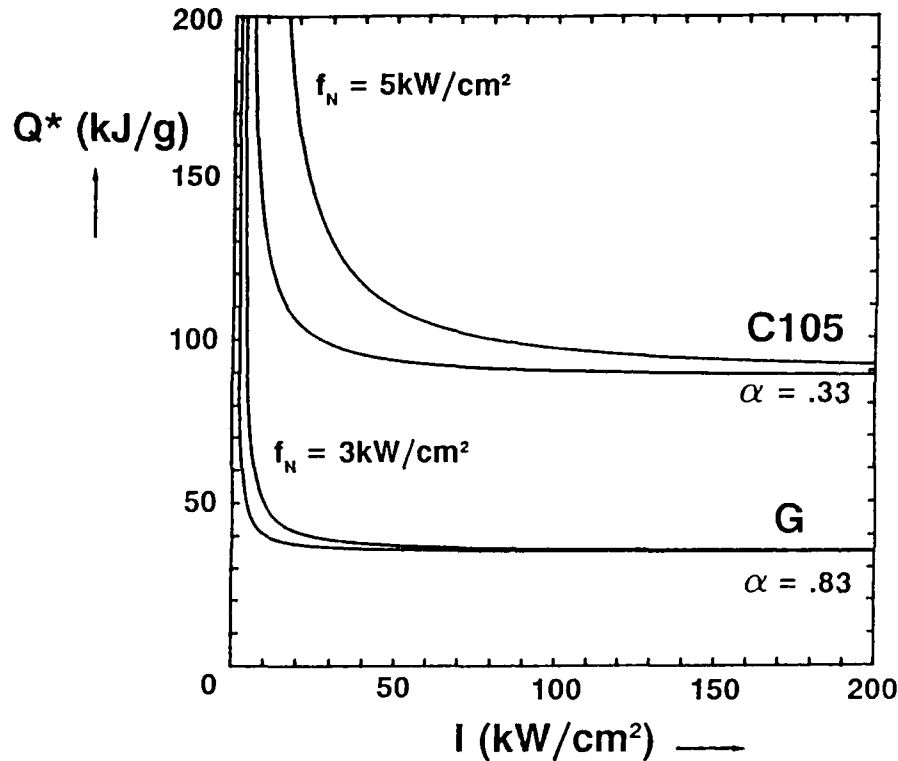
Figure 53. $Q^*(I)$ for Materials G and C105: 1D (Lower) vs. 2D (Upper, f_N = 3 and 5 kW/cm²) Curves

The data fits shown in Figures 52 and 53 are made using values of α_λ = 0.83 and 0.33 for materials G and C105, respectively, at λ = 10.6 μm wavelength. These values are in fairly good agreement with our independently determined coupling coefficients derived from reflectance measurements (cf. Table 4) at I = 100 kW/cm²: G has α_λ = 0.81 ± 0.01 and C105 has α_λ = 0.45 ± 0.03 at λ = 10.6 μm wavelength. Reflectance measurements on both these materials may be influenced by the "keyhole" effect (i.e., light trapping by multiple reflections inside an ablation crater with steep walls) in microscale experiments; hence, larger scale reflectance measurements should be completed to probe ablation craters with flat bottoms.

In view of the strong 2D effect on $Q^*(I)$ under cw irradiation conditions, we recommend the following procedure to calculate Q^*_∞, the high coupled irradiance limit ($\alpha_\lambda I >> I_{RAD}$) of Q^*_{1D} (cf. equation [13]):

$$Q^*_\infty = H_{MR}/\alpha_\lambda \tag{14}$$

1) assume that H_{MR} is equal to the thermochemical enthalpy of ablation H_A at the ablation temperature, and

2) measure the target front surface spectral reflectance (and/or spectral emittance) during ablation and use this measurement to calculate α_λ.

3.3.4.1 CW Laser Ablation (continued)

If there is discrete mass removal, H_A is an upper limit to the enthalpy of mass removal. If there is beam/plume interaction, α_λ (determined from reflectance measurements) is an upper limit to the effective coupling coefficient. However, in many practical cases of interest (*e.g.*, strong carbon barrier materials), equation [14] gives a very useful estimate of the true value of Q^*.

For convenience, Appendix E lists H_A for thermochemical ablation of carbon over the 3000 - 5000 K temperature range [References 23 and 58].

Mass spectrometry is potentially a very valuable technique for measuring the abundances of laser ablated products. These abundances, together with thermochemical data on enthalpies of formation, can be used to calculate H_{MR}. The AFOSR/HARC/Rice Program proposal originally requested funding for a laser photoionization time-of-flight (TOF) mass spectrometer (MS) system that would permit less ambiguous determination of the abundances of laser ablated products than conventional electron impact mass spectrometers. Capital equipment funds were not available for this proposed instrumentation, but exploratory experiments were performed with the quadrupole MS system described in Section 3.2.5.

Figure 54 shows sample laser pyrolysis mass spectra of material SR7 (a typical cured epoxy resin used in composite materials and furnished by Shell Development Company) irradiated by a cw CO_2 laser at *ca.* 2 kW/cm² peak irradiance in vacuum. The top panel of Figure 54 shows the total mass spectrum averaged over six scans (*ca.* 0.5 s for each scan) of the quadrupole mass spectrometer. The bottom panels show selected time-resolved individual mass peaks (masses 58 amu, 28 amu, 18 amu, and the total ion yield) *vs.* scan number. (Similar time-resolved data are available for all the other mass peaks shown in the top panel.) Identifications of prominent chemical species are shown in both sets of panels. The laser on and off times are indicated at the bottom of the figure. Note that the mass 18 amu peak (H_2O) is unique: it keeps growing in intensity long after the laser has been turned off; hence, significant water formation must be occurring at relatively low temperature as the pyrolyzed resin cools down.

Figure 55 shows comparison laser pyrolysis mass spectra of material AF4 (a composite material made with a reinforcement fiber embedded in SR7; this composite material has been used previously in laser effects programs [References 16 and 18]). Material AF4 was irradiated under the same conditions as material SR7 (*cf.* Figure 54). Again, water vaporization continues long after the laser irradiation stops.

As reviewed elsewhere [Reference 59], the tantalizing possibility that tantalum carbide [References 60-62], hafnium carbide [References 62 and 63], and other refractory carbides yield vapor enriched in atomic carbon can be determined by mass spectrometric (MS) analysis. Atomic carbon has a much larger enthalpy of ablation than other carbon species [Reference 59], so enrichment of its production is the basis of enhanced performance of laser armor.

Other interesting phenomena such as vaporization of refractory metal atoms can also be observed directly by MS techniques.

The laser pyrolysis quadrupole mass spectrometer system shown in Figure 13 (*cf.* Section 3.2.5) is versatile and useful for survey experiments at moderate heating rates. However, its time resolution is too slow to permit its use under high irradiance cw and/or rp laser irradiation conditions. Its ability to identify primary laser ablation products is also compromised because of the formation of secondary ionization products by electron impact ionization. It is therefore recommended that a laser photoionization TOF MS system be constructed for future MS experimentation; near-threshold photoionization is a "mild" ionizing technique that generates primarily parent ions whose abundances can be related directly to primary laser ablation products.
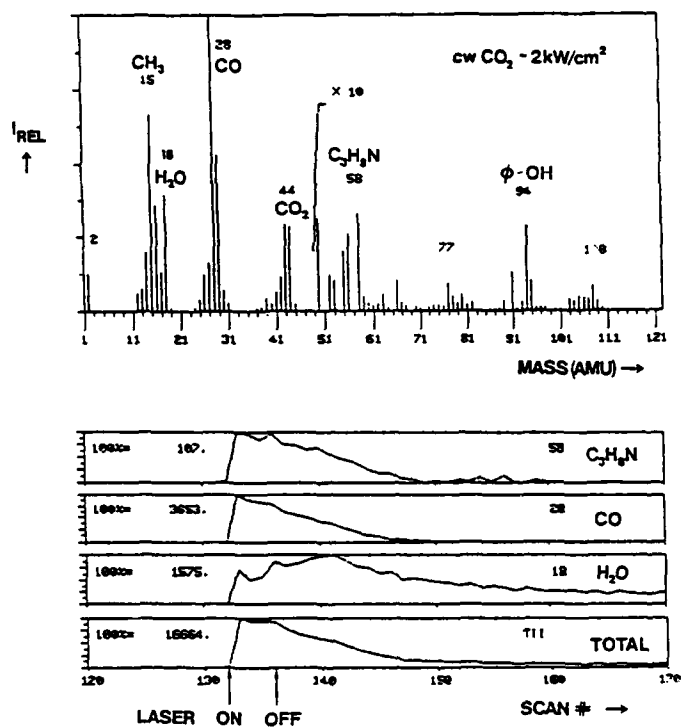
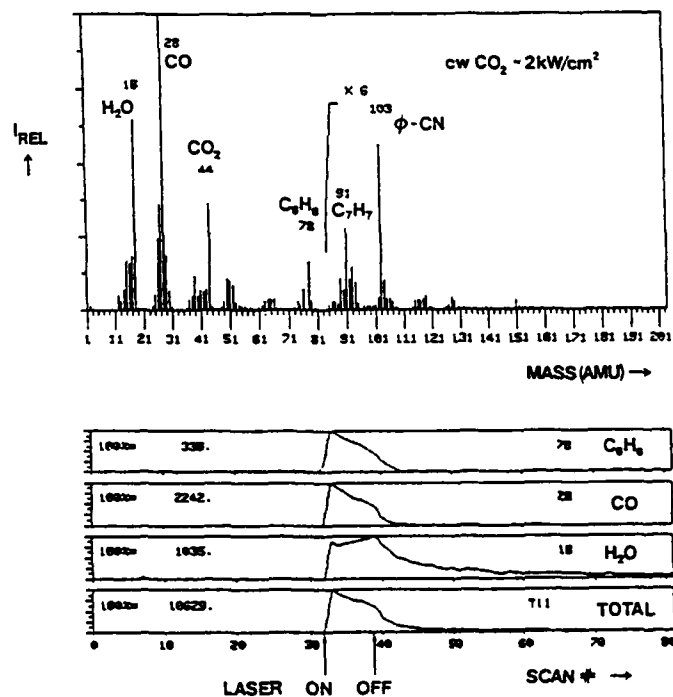Figure 54. CW CO_2 Laser Pyrolysis Mass Spectrum of Material SR7

Figure 55. CW CO_2 Laser Pyrolysis Mass Spectrum of Material AF4

81

3.3.4.2 RP Laser Ablation

The variation of phemonenology and effects of laser/materials interactions as a function of laser parameters is discussed briefly in Section 3.2.1 above. Important differences in laser ablation rates are observed when rp rather than cw lasers are used to damage targets. For CBMs evaluated at the same wavelength and total fluence (integrated over waveform), rp laser ablation is generally less efficient than cw laser ablation because of two loss phenomena:

1) the "residual energy" [Reference 64] remaining in the target after a laser pulse may be lost (*i.e.*, the target front surface may cool down), so the target has to be re-heated to the ablation temperature during each new pulse, and

2) the irradiance delivered by short pulse lasers may generate more excited ablation products, including absorptive plasmas that de-couple incident radiation from the target front surface.

Both losses increase the effective enthalpy of ablation Q^* for pulsed laser ablation compared to cw laser ablation. For pulsed laser/material interactions, Q^* can be determined experimentally by measuring the pulse fluence F_p (pulse areal energy density - also termed the radiant exposure [Reference 65]; units: J/cm² per pulse) and the areal mass loss per pulse $\mathcal{M}_p$ (units: g/cm² per pulse):

$$Q^* = F_p/\mathcal{M}_p \qquad [15]$$

Q^* can also be determined by measuring the pulse fluence F_p, the material density ρ (units: g/cm³), and the recession depth (also termed the etch depth or the ablation rate) per pulse Δ_p (units: cm per pulse):

$$Q^* = F_p/(\rho\Delta_p) \qquad [16]$$

In the present experiments, a rp (1.3 Hz PRF) hydrogen fluoride (HF) multiline 200mJ/pulse chemical laser system [Reference 5] irradiated small disc specimens (2.0 mm diameter X 0.5 mm thickness) in a vacuum environment. Two different laser spot sizes (*ca.* 1.55 mm X 0.68 mm and 1.12 mm X 0.50 mm) were used in lower and higher fluence regions, respectively. Attenuators were used to change the fluence distributions on target.

Figure 56 shows the output wavelengths and relative pulse energies at each wavelength, together with typical time-resolved pulses for two wavelengths. The power-weighted average of the HF laser output is at *ca.* λ = 2.9 μm and the FWHM pulse duration is *ca.* 200 ns. Fluence distributions were characterized by burn patterns obtained in graphNOL and other materials. The beam profile is quite irregular, with two prominent "hot" spots on the ends of the approximately rectangular spot. The peak to average fluence ratio is *ca.* 3 to 1. Average fluences of *ca.* 2.5, 5, 15, 20, and 40 J/cm² were used in most experiments.

Figure 57 shows experimental measurements on Q^* (determined using equation [16]) for graphNOL as a function of peak pulse fluence F_p. The sharp increase in the slope of the plot occurs near the plasma "threshold". The existence of carbon vapor plasma (*i.e.*, ionized vapor with high electron and ion densities) at peak fluences above *ca.* 50 J/cm² was confirmed by OMA emission spectroscopic observation of characteristic carbon vapor plasma emissions (*cf.* Section 3.3.3.2 and Appendix D). The plasma "threshold" also coincides with strong reductions of the measured reflectance as carbon vapor plasma absorbs the incident rp HF chemical laser radiation (*cf.* Section 3.3.2.2 above).

Q^* values for graphNOL ablation at high peak fluences are much larger than corresponding cw laser ablation values (*cf.* Section 3.3.4.1). For example, graphNOL cw HF chemical laser ablation Q^* data range between *ca.* 57 - 130 kJ/g at irradiances between 11 - 18 kW/cm² [Reference 15]; rp Q^* values are similar (ca. 77 - 128 kJ/g; *cf.* Figure 57) below the plasma threshold, but grow markedly (up to 820 kJ/g) as a function of peak rp laser fluence above the plasma threshold. These very large values of Q^* are caused by strong plasma absorption.
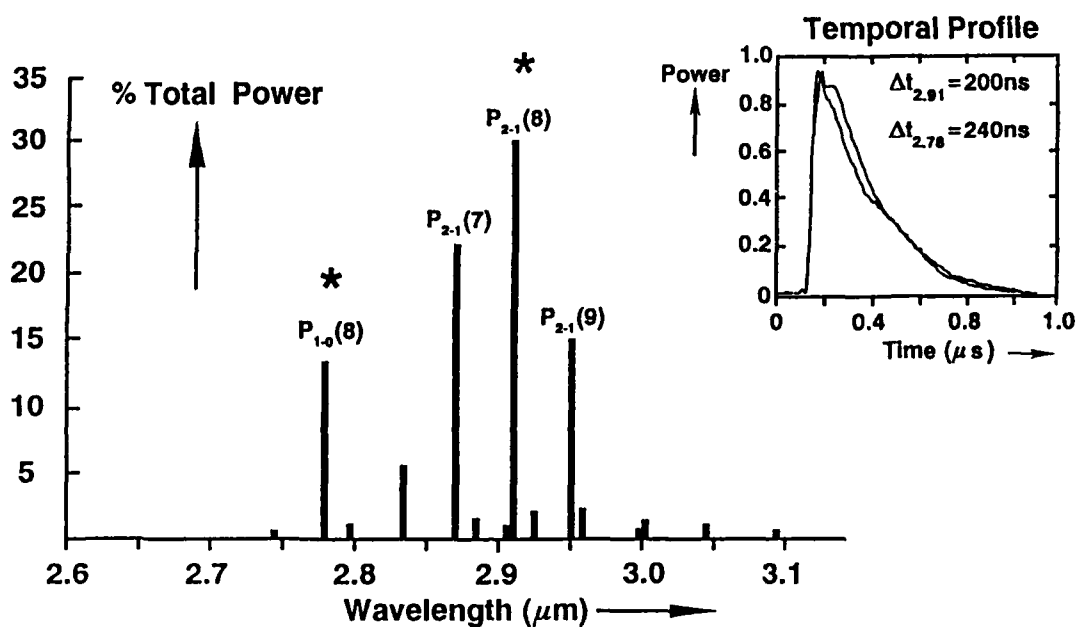
Figure 56. RP HF Chemical Laser Output Spectral Power Distribution and Pulse Temporal Profiles (for two transitions marked by an asterisk *)
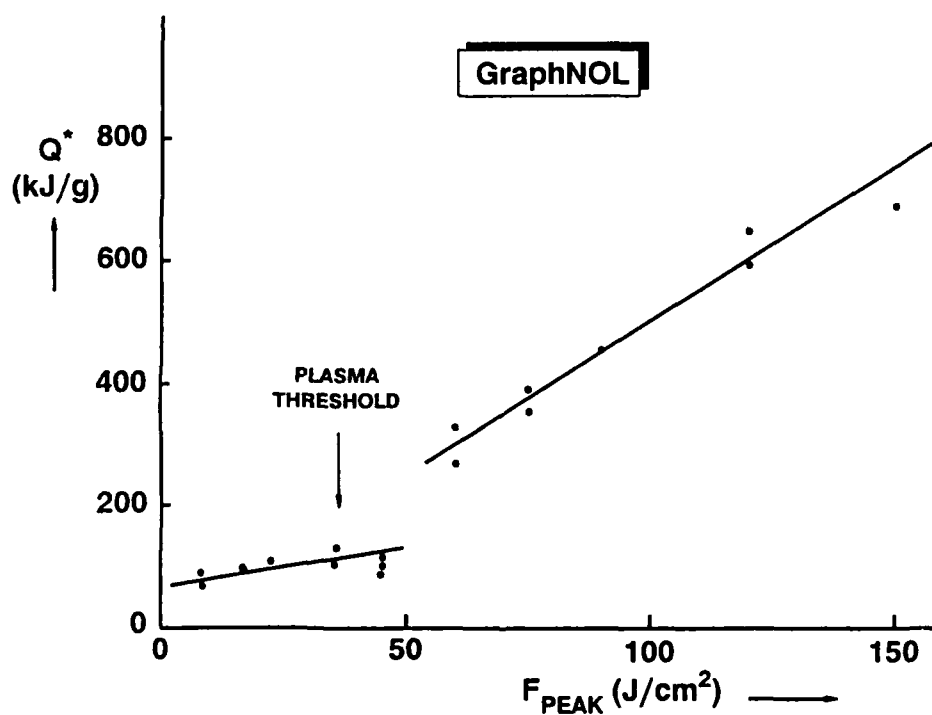

Figure 57. GraphNOL: Q^* as a Function of Peak Laser Fluence

83

3.3.4.2 RP Laser Ablation (continued)

There may be a delicate balance of effects in the plasma regime - significant ablation is required to achieve high vapor densities that can, in turn, generate high plasma densities. Q^* is then a combined property that depends on the joint probability that material is ablated and that the ablated material ionizes to form a given plasma density. [Note that there may also be several plasma absorption mechanisms involving inverse bremsstrahlung (free-free) transitions, as well as bound-bound and other transitions - the mix of these may be different for different vapor species generated by ablation of graphNOL *vs.* other CBMs.]

Plasma absorption scales with wavelength in a complex manner. In general, for a given plasma density, long wavelength laser radiation is much more efficiently absorbed than short wavelength laser radiation; for example, inverse bremsstrahlung absorption cross sections scale roughly as λ^2. Plasma thresholds also depend sensitively on laser irradiation parameters. The rationale design of a laser hardened substrate must therefore address several key laser parameters: wavelength, pulse fluence/irradiance, and pulse waveform. It is likely that particular coated substrates with high front surface reflectance are preferable for short wavelength, low fluence, high PRF irradiation conditions. Conversely, low threshold plasma formers are preferable for long wavelength, high fluence, low PRF irradiation conditions. Hardening "trades" must be considered explicitly in order to address broadband (*e.g.*, wavelength agile), variable fluence, and variable PRF laser threats.

Another phenomenon/mechanism that contributes to larger Q^* values under rp compared to cw HF chemical laser irradiation conditions is the loss of retained energy between pulses. A certain amount of each incident laser pulse is required to heat the target front surface to the ablation temperature; once the laser pulse is completed, any retained energy present in the target dissipates to the bulk material during the cooldown prior to irradiation by the next pulse. Thus, even under one-dimensional (1D) irradiation conditions [which the present experiments approximate closely since thermal diffusion out of the "hot spot" cannot occur during the short (submicrosecond) laser pulse], there is a new type of heat loss that is important for pulsed laser interactions. It is expected that rp laser ablation approaches the cw limit as the pulse repetition frequency (PRF) increases.

Cursory rp laser ablation experiments were completed with other rp laser sources (*e.g.*, excimer and free electron lasers) [Reference 36]. Excimer lasers should be somewhat more efficient than rp HF chemical lasers (or planned infrared and near infared free electron lasers) in ablating CBMs such as graphite since plasma absorption is less important for short wavelength (λ = 193 - 351 nm) excimer laser radiation. In addition, reflectances of all CBMs (even those coated with metals and/or metal carbides) should be much lower at ultraviolet wavelengths compared to infrared wavelengths. Direct experiments under controlled conditions must, however, be performed to confirm these expectations.

3.3.5 High Temperature Oxidation Resistance Measurements

The experimental apparatus and general procedure used to test the high temperature oxidation resistance of ceramic materials is described in Section 3.3.3.3 above and in Reference 31. This section presents sample data obtained during laser heating of pure SiC and Si_3N_4 samples in an oxygen atmosphere at various pressures. An improved apparatus incorporating laser induced fluorescence (LIF) detection of the SiO vapor phase product was employed to extend studies to lower temperatures than previously reported [Reference 31]. Samples were laser heated in low pressure (*ca.* 0.25 - 10 torr) O_2 at a fixed temperature while SiO LIF signal levels at line center of the Q(18) transition of the 0,0 band of the A-X system were monitored. Sample front surface temperatures were measured by both single color and two-color optical pyrometers.

Figure 58 shows the SiO LIF signal detected during laser heating of SiC in oxygen pressures of 0.3 - 9.5 torr at an average temperature of *ca.* 1470 °C (1740 K). The sharp drop in the SiO LIF signal at *ca.* 2 torr O_2 pressure corresponds to the active/passive transition for SiC at 1740 K.

Figure 59 shows a corresponding SiO LIF signal detected during laser heating of Si_3N_4 over the same oxygen pressure range but at a much higher average temperature of *ca.* 1910 °C (2180 K). The sharp drop in the SiO LIF signal below *ca.* 1 torr O_2 pressure corresponds to the active/passive transition for Si_3N_4 at 2180 K.

Both uncoated and coated composite materials are being tested in a similar manner. In contrast to standard weight loss measurements [*e.g.*, Reference 44], the present LIF detection technique permits real-time evaluation of candidate materials' performance. It is planned to combine other diagnostic techniques with the existing apparatus to obtain microstructural/microchemical information on test specimens during high temperature experimentation.
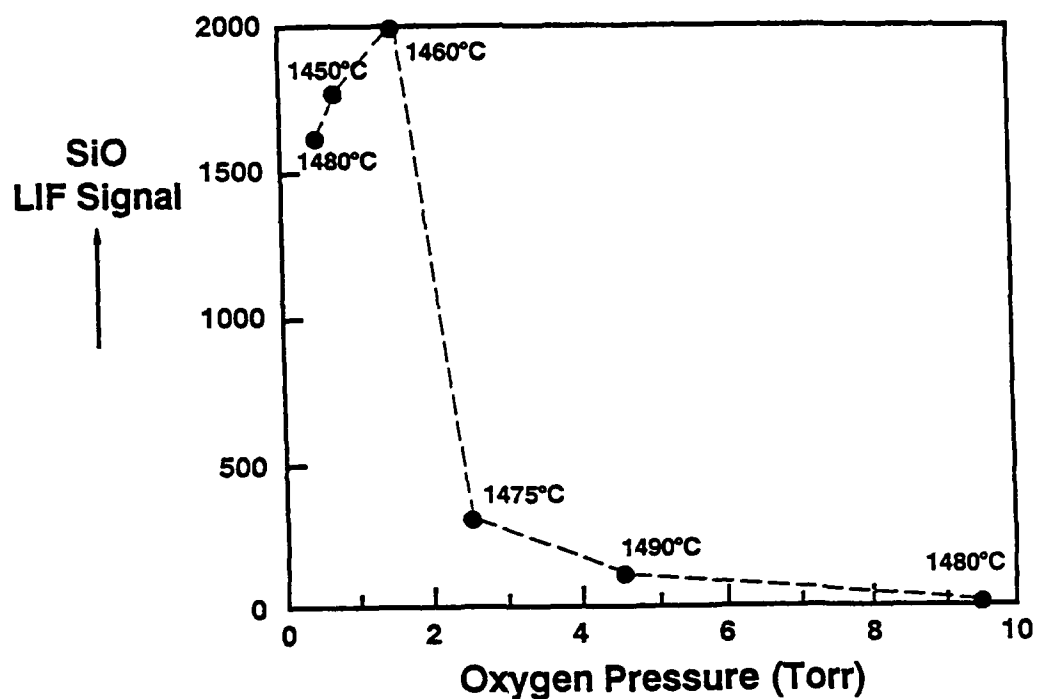
Figure 58. SiC Oxidation *vs.* Oxygen Pressure at T ≈ 1470 °C
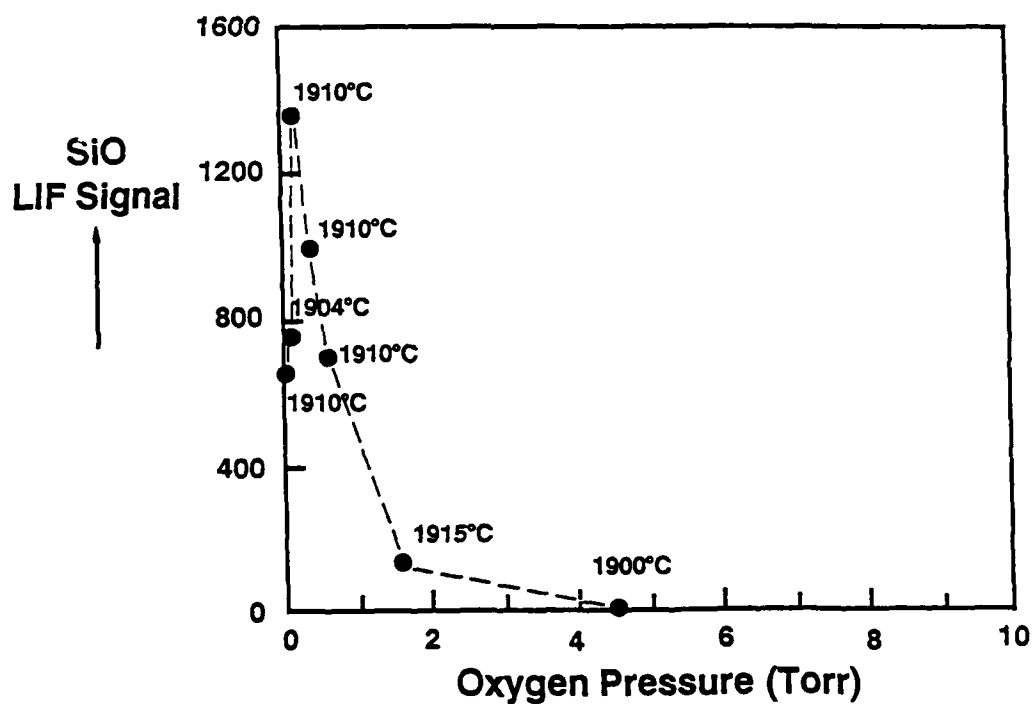
Figure 59. Si₃N₄ Oxidation *vs.* Oxygen Pressure at T ≈ 1910 °C

3.4 SHORT WAVELENGTH INTERACTION PHENOMENA and EFFECTS

HARC/Rice personnel completed several fundamental studies on the short wavelength performance of candidate Spacecraft Survivability materials as part of the AFOSR/HARC/Rice Program:

1) the basic phenomenology of interaction physics and chemistry pertinent to short wavelength laser irradiations of candidate materials has been determined,

2) optical properties of metals (and other conductive materials) have been summarized for use in predicting laser effects at low irradiances,

3) apparatus and methodology suitable for predicting the wavelength scaling of coupling coefficients have been developed, and

4) mechanistic analyses on ablation of graphNOL and other carbon barrier materials have been performed.

The following Sections 3.4.1 through 3.4.4 present summary results for these AFOSR/HARC/Rice Program studies. More complete discussion is contained in several publications [References 1-2, 23-24, 59, and 66].

3.4.1 Interaction Physics and Chemistry

Sections 2.0 and 3.3.4 above summarize aspects of the important physics and chemistry associated with laser/materials interactions. Two principal physical properties of materials (the enthalpy of mass removal H_{MR} and the thermal coupling coefficient α_λ) determine their ablation performance under high coupled irradiance conditions ($\alpha_\lambda I \gg$ all 1D and 2D losses).

The enthalpy of mass removal H_{MR} can be determined for the equilibrium thermochemical ablation limit, leading to calculated values of the enthalpy of ablation H_A such as those we have presented for carbon [References 23 and 58; Appendix E]. This performance must, however, be tested for model and candidate materials by direct measurements on ablated species.

In laser/materials interactions, a variety of physical and chemical phenomena are responsible for the overall process of "thermal coupling" between the incident laser radiation and the irradiated target. As shown schematically in Figure 60, the thermal coupling coefficient α is the fraction of the incident laser energy that is converted into thermal effects in the material. A thermal coupling coefficient of unity implies complete absorption of laser energy by the target and complete conversion of this absorbed energy into thermal effects such as pyrolysis and ablation. Enhanced lethality can be achieved by finding appropriate conditions to obtain $\alpha = 1$. Enhanced survivability can be achieved by finding the conditions required to obtain $\alpha = 0$.

Figure 60 also portrays the "flow" of energy from laser photon energy through (typically) electronic excitation and into vibrational excitation that causes thermal effects. In the AFOSR/HARC/Rice Program, we have been concerned with the first step in the overall flow, which is controlled primarily by the material reflectance and by vapor/plasma effects that may cause plume blockage.

The thermal coupling coefficient α is a function of wavelength λ, temperature T, angle of incidence θ, polarization $\mathcal{P}$, and irradiance I of the incident radiation [Reference 66]. The dependence of α on angle of incidence and polarization have been treated elsewhere [Reference 66; cf. Appendix F] and ca⁀ be determined readily for a particular material using its optical constants (e.g., n and k, the real and imaginary parts of the complex index of refraction, respectively). The dependence of α on irradiance must be determined by experiment since it is caused by changes in physical structure, chemical composition, etc. that are not possible to model. The dependence of α on temperature can be modelled for long wavelength laser interactions with materials, as discussed in Appendix F of this report. However, there are in general no theoretical and/or modelling approaches that are suitable for treating the wavelength and temperature dependence of α at short wavelengths pertinent to laser DEWs.

87

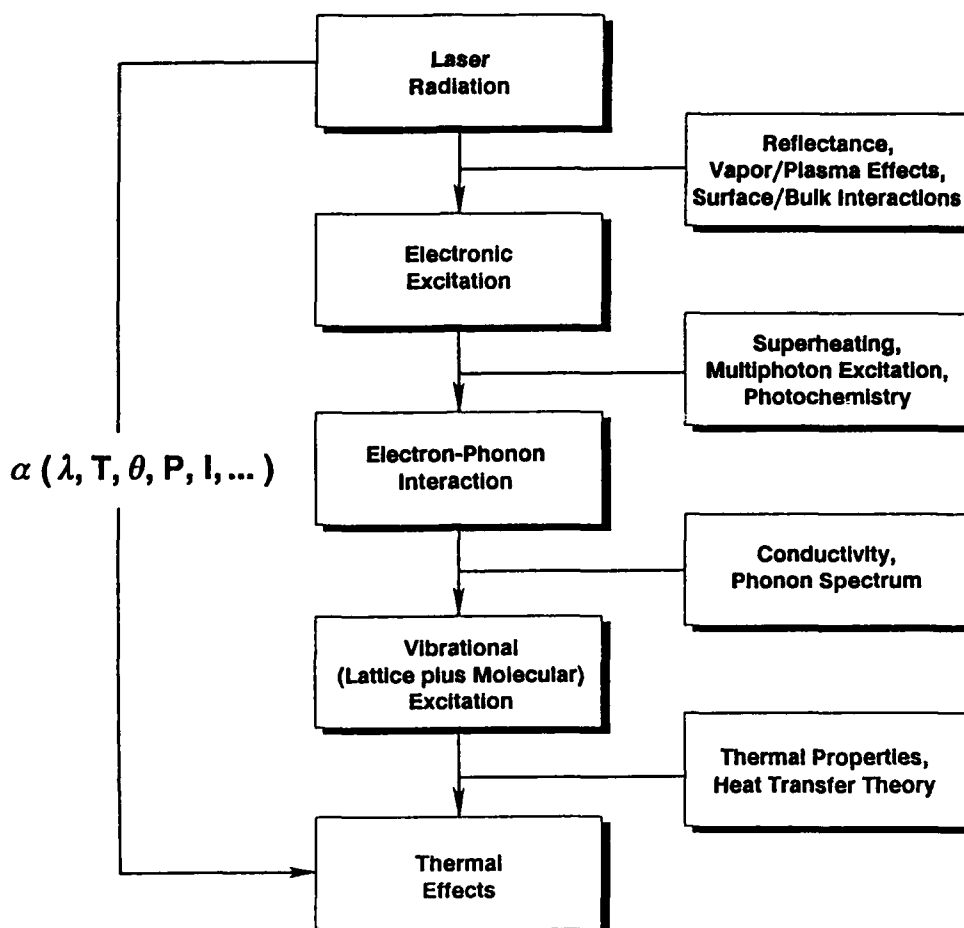## 3.4.1 Interaction Physics and Chemistry (continued)

```
                          ┌──────────────┐
                     ┌────│     Laser    │
                     │    │   Radiation  │
                     │    └──────┬───────┘
                     │           │              ┌────────────────────────┐
                     │           │              │      Reflectance,      │
                     │           ◄──────────────│  Vapor/Plasma Effects, │
                     │           │              │ Surface/Bulk Interactions│
                     │           ▼              └────────────────────────┘
                     │    ┌──────────────┐
                     │    │   Electronic │
                     │    │   Excitation │
                     │    └──────┬───────┘
                     │           │              ┌────────────────────────┐
                     │           │              │      Superheating,      │
                     │           ◄──────────────│  Multiphoton Excitation,│
                     │           │              │      Photochemistry     │
        α (λ,T,θ,P,I,...)  ▼              └────────────────────────┘
                     │    ┌──────────────┐
                     │    │ Electron-Phonon│
                     │    │  Interaction │
                     │    └──────┬───────┘
                     │           │              ┌────────────────────────┐
                     │           ◄──────────────│      Conductivity,      │
                     │           │              │     Phonon Spectrum     │
                     │           ▼              └────────────────────────┘
                     │    ┌──────────────┐
                     │    │  Vibrational │
                     │    │(Lattice plus Molecular)│
                     │    │   Excitation │
                     │    └──────┬───────┘
                     │           │              ┌────────────────────────┐
                     │           ◄──────────────│   Thermal Properties,   │
                     │           │              │  Heat Transfer Theory   │
                     │           ▼              └────────────────────────┘
                     │    ┌──────────────┐
                     └───►│    Thermal   │
                          │    Effects   │
                          └──────────────┘
```

Figure 60. Schematic Flow Diagram for Conversion of Laser Energy Into Thermal Effects

Time-resolved and average reflectance measurements obtained during cw CO_2 laser ablation (cf. Section 3.3.2 above) are consistent with expected trends in wavelength and temperature dependence:

1) reflectances are highest at long wavelength ($\lambda = 10.6$ μm) and decrease as a function of decreasing wavelength, and

2) reflectances drop as a function of increasing temperature, except when a shiny coating builds on the target front surface (as is the case for materials such as C102, C104, and C106).

Discussion of individual materials is presented in Section 3.5 below. A principal conclusion of the AFOSR/HARC/Rice Program is that although several materials have excellent ablation performance when irradiated by cw CO_2 lasers due to their high reflectances at $\lambda = 10.6$ μm wavelength, their performance will be degraded considerably at shorter wavelengths [even at the $\lambda = 2.9$ μm wavelength of operation of a candidate space based laser (the hydrogen fluoride chemical laser)]. The degradation is particularly large for all materials at visible to near infrared wavelengths where reflectances during ablation are much lower than at $\lambda = 10.6$ μm.

3.4.1 Interaction Physics and Chemistry (continued)

One other aspect of interaction physics and chemistry must be treated: the behavior of spacecraft materials at sub-ablation laser irradiances. In this low irradiance limit, the crucial figure-of-merit (FOM) of a candidate laser armor material is the ratio of the coupling coefficient α to the total emittance ϵ at the temperature of the material.

Figure 61 shows the energy balance associated with use of radiator materials (assuming that the rear surface is insulated). When steady state conditions are achieved, the laser energy coupled into the target front surface must equal the energy reradiated by the front surface (assuming that there are negligible losses due to conduction and other mechanisms apart from reradiation):

$$\alpha I = \epsilon \sigma_{SB} T_{ss}^4 \tag{17}$$

where α is the thermal coupling coefficient at wavelength λ and temperature T, ϵ is the emittance at temperature T integrated over all wavelengths λ, σ_{SB} is the Stefan-Boltzmann constant (5.67×10^{-8} W m^{-2} K^{-4}), and T_{ss} is the steady-state temperature.
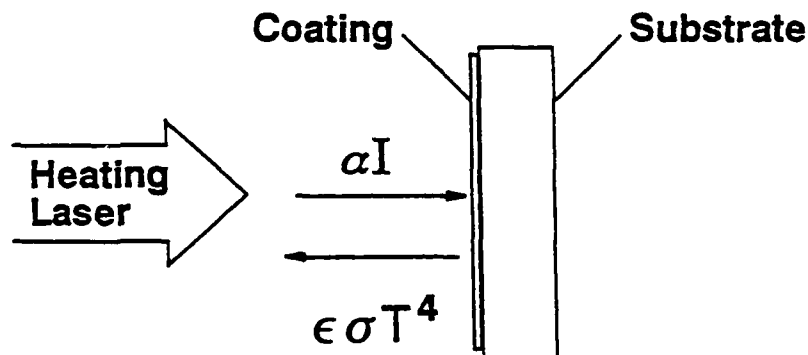
Figure 61. Energy Balance for Absorbed Laser Irradiance and Reradiated Emission

Figure 62 shows families of curves for the steady-state temperature T_{ss} as a function of incident laser irradiance for several values of the FOM α/ϵ. In the form of a coating, a given radiator material will survive up to its melting point T_m ; above (or even somewhat below) this temperature, the material will fail by beading or by pulling away from its substrate. The best radiator materials to defeat long wavelength (i.e., infrared) laser threats are typically the most refractory metals. Section 3.4.2 and Appendix F discuss the optical properties of metals and other conductive materials.

The present AFOSR/HARC/Rice Program has addressed the basic science of laser interactions with materials. It is also necessary to address several engineering issues in connection with the application of radiator and/or ablator materials on real spacecraft. In addition, other threats such as nuclear blast and atomic oxygen must be considered in order to develop truly practical materials for enhancing spacecraft survivability.

3.4.1 Interaction Physics and Chemistry (continued)
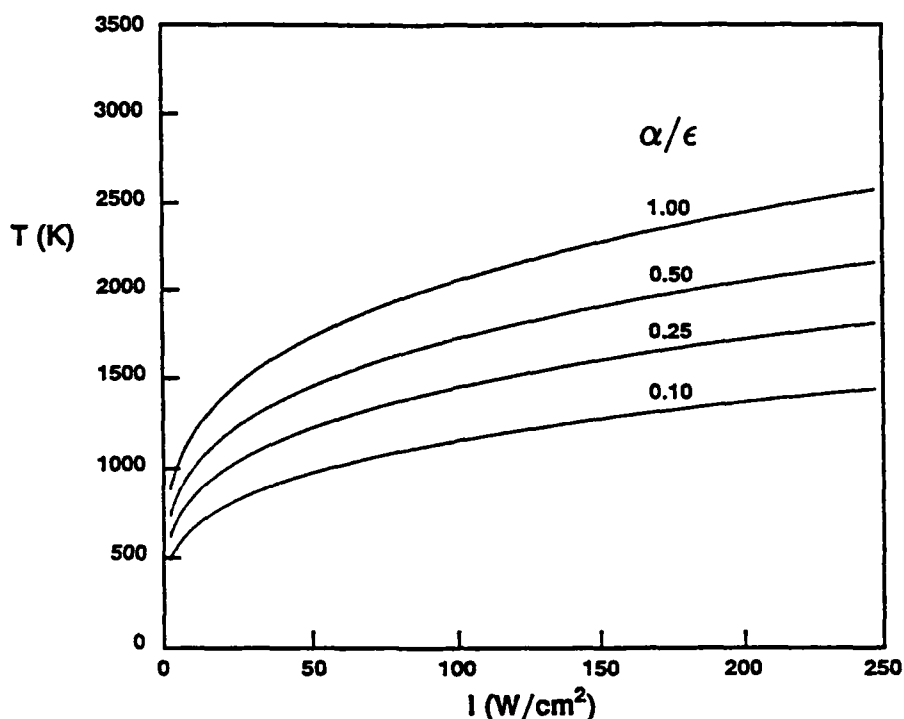
Figure 62. Steady-State Temperature *vs.* Laser Irradiance for Several Values of α/ϵ

3.4.2 Optical Properties of Metals

A particularly important case of laser/materials interactions involves the irradiation of highly conductive materials (such as metals and metal carbides) by long wavelength threat lasers. This case has been considered extensively in the AFOSR/HARC/Rice Program; an updated version of our earlier report [Reference 66] is appended to this Final Technical Report (*cf.* Appendix F). The discussion of optical properties in Appendix F is very general and applies, with minor modifications, to the treatment of optical properties of carbon barrier materials.

3.4.3 Wavelength Scaling of Coupling Coefficients

The only "workhorse" laser test facilities with sufficient power to irradiate full spacecraft structures currently in operation in the United States are cw CO_2 laser test facilities such as LHMEL 2 at Wright Research and Development Center (WRDC) at Wright-Patterson AFB, OH. These cw CO_2 lasers can irradiate large spacecraft structures uniformly in order to simulate laser threat effects. However, more realistic laser threats involve shorter wavelength lasers that: 1) propagate efficiently through the earth's atmosphere, 2) require smaller optics to produce a given irradiance on target at range, and 3) have enhanced lethality (*i.e.*, larger thermal coupling coefficients) for anti-satellite (ASAT) applications. Therefore, it is essential to scale expected laser effects from the typical laser test facility results obtained at $\lambda = 10.6$ μm wavelength to those which may be obtained at shorter wavelengths.

3.4.3 Wavelength Scaling of Coupling Coefficients (continued)

In many practical cases (*e.g.*, for relatively low irradiance laser threats which do not produce ablated material), the diagnostic instrumentation described in Sections 3.2.2 and 3.2.3 above will be exceptionally useful for extrapolating laser effects data to the short wavelengths of interest. If "workhorse" laser test facilities such as LHMEL 2 are equipped with multiwavelength optical pyrometers and spectral emittance measurement systems, it will be possible to determine the optical properties of materials in sufficient detail to assess their utility as laser armor for enhancement of spacecraft survivability.

Deductions about wavelength scaling of coupling coefficients and the resultant implications for laser hardness of materials that have been examined in the AFOSR/HARC/Rice Program are presented in Section 3.5 (Materials Evaluation) below.

3.4.4 Mechanistic Analyses

For graphNOL and other carbon barrier materials (CBMs) irradiated by cw lasers in the high coupled irradiance ablation regime (*e.g.*, $\alpha_\lambda I \gg I_{loss}$ where the loss is due to all 1D and 2D contibutions) for periods of time long enough to eliminate transient effects, the mechanism of mass removal is dominated by simple thermochemical ablation at all wavelengths of interest (infrared through near ultraviolet spectral regions). Equation [14] (*cf.* Section 3.3.4.1) can then be used to calculate Q^* from the thermochemical enthalpy of ablation H_A and the wavelength-dependent coupling coefficient α_λ. If the ablation plume is transparent, α_λ is simply the material front surface absorptance A_λ. The material front surface absorptance cannot be measured easily by direct techniques, but can be determined readily by spectral emittance and/or spectral reflectance measurements (cf. Sections 3.3.1 and 3.3.2 above).

Departures from this "baseline" thermochemical ablation mechanism occur when:

1) the coupled irradiance $\alpha_\lambda I$ is sufficiently low (or is applied for sufficiently short periods of time) that transient effects and losses (reradiation, conduction, *etc.*) are important – then, detailed thermal analyses are required to determine Q^*,

2) the ablation plume is not transparent (*e.g.*, in the case of dense plasma formation) – then, detailed beam/plume interactions experiments and analyses are required to determine the effective coupling coefficient, and

3) new types of mass removal (*e.g.*, spallation, melting with subsequent removal of liquid droplets, *etc.*) are important – then, detailed mass balance measurements and analyses are required to determine the true enthalpy of mass removal.

3.5 MATERIALS EVALUATION

HARC/Rice personnel completed evaluation of one reference material (graphNOL - G) and several candidate Spacecraft Survivability materials (metals and carbon barrier materials - CBMs) as part of the AFOSR/HARC/Rice Program. In the non-ablation regime (*i.e.*, for low irradiance laser threat conditions), the highest melting point material with the lowest value of α_λ/ϵ (*cf.* Section 3.4.1) is generally preferred (assuming that this material is also compatible with non-laser threats). In the ablation regime, the material with the highest value of Q^* is generally preferred.

Combining information discussed in Section 3.3.2.1 and Appendix E (taking $H_A = 29.0$ kJ/g), we determine the following high coupled irradiance limit values of Q^* (*cf.* equation [14]) for G and other CBMs subjected to cw laser ablation:

Table 6. Average Effective Enthalpies of Ablation $\overline{Q^*}_\lambda$ During Laser Ablation.

$$\boxed{I_{peak} = 100 \text{ kW/cm}^2}$$

Material	$\overline{Q^*}_{0.515}$	$\overline{Q^*}_{1.06}$	$\overline{Q^*}_{2.9}$	$\overline{Q^*}_{10.6}$
G	30.2 ± 0.3	30.5 ± 0.3	34.9 ± 0.8	35.8 ± 0.4
C101	33.0 ± 0.4	34.1 ± 0.8	(112 ± 17)**	49 ± 3
C102	33.0 ± 0.8	34.1 ± 0.8	73 ± 18	71 ± 9
C104	32.2 ± 0.4	32.6 ± 1.1	(81 ± 22)**	55 ± 6
C105	32.6 ± 0.4	35.4 ± 0.4	44.6 ± 1.4	64 ± 4
C106	38.2 ± 0.5	40.3 ± 0.6	(138 ± 33)**	63.0 ± 1.4
C107	40.8 ± 0.6	47.5 ± 0.8	54 ± 14	78 ± 21
C108	38.7 ± 0.5	42.6 ± 0.6	55 ± 3	161 ± 27

**Contaminated by specular reflections

Q^* values listed for materials C102, C104, and C106 are probably lower limits since full reflective coatings may not have formed during HARC microscale experiments. In addition, reflectance measurement on material C105 may have been influenced by "keyhole" effects. Nevertheless, the potential superior performance of material C108 at long wavelength is evident. The coating on this material should be applied to better substrates (perhaps material C106) to achieve a truly "hard" ablator.

An important conclusion derived from Table 6 is that short wavelength ($\lambda = 0.5$ - 1.0 μm) lasers are much more difficult to defeat - although some short wavelength Q^* values are respectable, there are no outstanding laser armor candidate materials among the CBMs studied.

Detailed discussion about hardening concepts and specific materials that should be developed further for spacecraft survivability applications can only be presented in a classified format. The principal investigator will present this discussion to AFOSR personnel in classified meetings, *etc.*

3.6 PUBLICATIONS

Five papers have been published under AFOSR/HARC/Rice Program sponsorship:

1. M. J. Berry, "Laser/Materials Interactions: CW Laser Interactions with Carbon-Based Materials", in Proceedings of the Sixth DoD Conference on DEW Vulnerability, Survivability and Effects, Volume 1 (Office of the Chief of Naval Research, Arlington, VA, 1987), pp. 333-342. CONFIDENTIAL.

2. C. A. Klein, R. F. Menefee, B. D. Krenek, and M. J. Berry, "Small Scale Laser Effects Experiments on Graphite: Coupling Coefficient, Lateral Loss, and Effective Heat of Ablation", J. Appl. Phys., 61, 1701-1712 (1987).

3. C. A. Klein, M. J. Berry, and P. A. Miles, "Thermochemical Heat of Ablation of Solid Carbon", J. Appl. Phys., 65, 3425-3429 (1989).

4. L. M. A. Levine, L. G. Fredin, and M. J. Berry, "Infrared Absorption Spectra of Cured Epoxy Resin and Human Corneal Tissue at Temperatures Up To 450 °C", SPIE Proceedings, Vol. 1064 - Thermal and Optical Interactions with Biological and Related Composite Materials, 131-134 (1989).

5. T. D. Kunz, R. F. Menefee, B. D. Krenek, L. G. Fredin, and M. J. Berry, "Laser Probe Absorption Spectroscopy Measurements on Laser Induced Plumes", High Temp. Sci., 27, xxx (1989).

Abstracts of these publications are contained in Appendix F. In addition, several other papers based on AFOSR/HARC/Rice Program work will be prepared. Copies of the above and future publications have been or will be forwarded to the Air Force Office of Scientific Research.

4.0 RECOMMENDATIONS FOR FUTURE STUDIES

For Spacecraft Survivability considerations, our principal recommendations are to:

1) develop diagnostic instrumentation systems of the type described in Section 3.2 further - properly instrumented experiments that can determine the enthalpy of mass removal H_{MR} and the wavelength-dependent coupling coefficient α_λ are essential to providing materials screening and performance assessment capabilities,

2) conduct experiments on pure constituent materials as well as on candidate state-of-the-art or developmental materials - many high temperature properties and materials performance parameters are unknown under realistic laser heating rate conditions,

3) consider plasma barrier formation as an important potential hardening concept, and

4) organize highly effective teams of materials scientists, laser testers, modellers, and other critical personnel required to refine hardening concepts, produce test specimens and other materials, and evaluate materials performance in a "feedback loop" that leads to the identification and validation of outstanding laser armor materials.

For general materials research and development considerations (*e.g.*, identification of oxidation-resistance high temperature composite materials), our principal recommendations are to:

5) develop dedicated versions of key diagnostic instrumentation systems (*e.g.*, multiwavelength optical pyrometer, plume probing spectrometer, *etc.*) that are well-suited to the temperature ranges, vapor phase species, and surface characteristics that are specific to a particular program's applications,

6) test and evaluate pure constituent materials to determine fundamental properties using inexpensive microscale facilities of the type used in the AFOSR/HARC/Rice Program (*cf.* Appendix A), and

7) organize similar highly effective teams as in recommendation #4 above to generate outstanding oxidation-resistant and other high temperature materials.

5.0 REFERENCES

1. M. J. Berry, "Laser/Materials Interactions: CW Laser Interactions with Carbon-Based Materials", in Proceedings of the Sixth DoD Conference on DEW Vulnerability, Survivability and Effects, Volume 1 (Office of the Chief of Naval Research, Arlington, VA, 1987), pp. 333-342. CONFIDENTIAL.

2. C. A. Klein, R. F. Menefee, B. D. Krenek, and M. J. Berry, "Small Scale Laser Effects Experiments on Graphite: Coupling Coefficient, Lateral Loss, and Effective Heat of Ablation", J. Appl. Phys., 61, 1701-1712 (1987).

3. M. J. Berry, "The HARC cw HF/DF Chemical Laser Test Resource", Houston Area Research Center, The Woodlands, TX, September, 1988; copy appended (cf. Appendix A).

4. M. J. Berry, "The HARC cw Carbon Dioxide Laser Test Resource", Houston Area Research Center, The Woodlands, TX, June, 1988; copy appended (cf. Appendix A).

5. M. J. Berry, "The HARC rp HF/DF Chemical Laser Test Resource", Houston Area Research Center, The Woodlands, TX, September, 1988; copy appended (cf. Appendix A).

6. M. J. Berry, "The HARC rp Excimer Laser Test Resource", Houston Area Research Center, The Woodlands, TX, September, 1988; copy appended (cf. Appendix A).

7. R. F. Menefee, L. G. Fredin, T. D. Kunz, B. D. Krenek, S. J. Ulvick, and M. J. Berry, "High Irradiance 2 Program Screening Test Series-1/1A", Final Technical Report, Contract F29650-88-WU160, Air Force Weapons Laboratory, Kirtland AFB, NM, September 29, 1988.

8. R. F. Menefee, L. G. Fredin, T. D. Kunz, D. T. Halligan, B. D. Krenek, and M. J. Berry, "High Irradiance 2 Program Screening Test Series-2", Final Technical Report, Contract F29601-87-C-0005, Subtask 01-19, Subcontract RDA-89-0005-0031, Weapons Laboratory, Kirtland AFB, NM, October 30, 1989.

9. T. D. Kunz, R. F. Menefee, B. D. Krenek, L. G. Fredin, and M. J. Berry, "Diagnostic Instrumentation for Wavelength Scaling of Coupling Coefficients", Final Technical Report, Contract DNA001-88-C-0163, Defense Nuclear Agency, Washington, DC, June 21, 1989.

10. G. B. Hunter, C. D. Allemand, and T. W. Eagar, "Multiwavelength Pyrometry: An Improved Method", Opt. Eng., 24, 1081-1085 (1985).

11. D. Wonica, "Optical Pyrometry Measurement Methods and Error Considerations", Report No. 88-SED-LTH-41-060 (R&D Associates, Marina del Rey, CA, 11 January 1988).

12. D. W. Marquardt, "An Algorithm for Least Squares Estimation of Nonlinear Parameters", J. Soc. Ind. Appl. Math., 11, 431 (1963).

13. J. C. De Vos, Physica, 20, 690 (1954).

14. M. J. Berry, "Reflectance and Ablation Measurements on General Atomics DSD Samples, Part 7", Report dated August 30, 1988 (Antropix Corporation, Woodlands, TX).

15. S. J. Ulvick, B. D. Krenek, and M. J. Berry, "Reflectance and Ablation Measurements on General Atomics DSD Samples, Part 8", Report dated November 23, 1988 (Antropix Corporation, Woodlands, TX).

16. R. F. Menefee, B. D. Krenek, and M. J. Berry, "CW Deuterium Fluoride Chemical Laser Interactions with Composite Materials", Final Technical Report, Contract F29650-85-W0782, Air Force Weapons Laboratory, Kirtland AFB, NM, August 12, 1985.

17. C. M. Stickley, R. Raphael, M. Olson, J. Lowder, P. Miles, R. Gentilman, R. Taylor, M. Berry, and A. Bailey, "Laser Countermeasure Materials Development Program: Final Technical Report", Report BDM/MCL-86-0759-TR (The BDM Corporation, McLean, VA, September, 1986). SECRET.

5.0 REFERENCES (continued)

18. R. F. Menefee, B. D. Krenek, and M. J. Berry, "Ablation Plume Measurements", Final Technical Report, Contract F29650-86-W0638, Air Force Weapons Laboratory, Kirtland AFB, NM, September 20, 1986.

19. L. F. Costa, K. D. Mielenz, and F. Grum, "Correction of Emission Spectra", Chapter 4 of K. D. Mielenz (editor), Optical Radiation Measurements, Volume 3, Measurement of Photoluminescence (Academic Press, New York, 1982), pp. 139-174.

20. R. R. Hall, "Laser Photoacoustic Spectroscopy of Forbidden Transitions: Acetylene and Alkyne High Energy Vibrational States and Their Interactions", Ph. D. Dissertation, Rice University, Houston, TX, 1984.

21. T. D. Kunz, "Vibrational Spectroscopy and Photochemistry of Formyl Fluoride", Ph. D. Dissertation, Rice University, Houston, TX, 1986.

22. L. Fredin, G. P. Hansen, M. P. Sampson, J. L. Margrave, and R. G. Behrens, "A High Temperature Quadrupole Mass Spectrometer for Studying Vaporization of Materials Heated by a CO_2 Laser", Report LA-10744, Los Alamos National Laboratory, Los Alamos, NM, September, 1986.

23. C. A. Klein, M. J. Berry, and P. A. Miles, "Thermochemical Heat of Ablation of Solid Carbon", J. Appl. Phys., 65, 3425-3429 (1989).

24. T. D. Kunz, R. F. Menefee, B. D. Krenek, L. G. Fredin, and M. J. Berry, "Laser Probe Absorption Spectroscopy Measurements on Laser Induced Plumes", High Temp. Sci., 27, xxx (1989).

25. R. B. Blackman and J. W. Tukey, The Measurement of Power Spectra (Dover, New York, 1958). See also Asyst 2.0, Vol. 2 - Analysis (Macmillan, New York, 1987), Chapter 5.

26. T. Risch and J. T. Kelly, "A Model for Radiation Driven Ablation of Carbon Under Low Pressures", Fifteenth Intersociety Conference on Environmental Systems, SAE Paper 851396, July, 1985.

27. T. Risch, personal communication.

28. R. L. Baker and M. A. Covington, "The High Temperature Thermochemical Properties of Carbon", Report SD-TR-82-19 (Aerospace Corporation, El Segundo, CA, 1982).

29. L. G. Fredin, R. F. Menefee, B. D. Krenek, and M. J. Berry, "Reflectance and Ablation Measurements on General Atomics DSD Samples, Part 9", Report dated May 14, 1989 (Antropix Corporation, Woodlands, TX).

30. T. D. Kunz, L. G. Fredin, R. F. Menefee, and M. J. Berry, "Plume Diagnostic Instrumentation: Laser Probe Absorption Spectroscopy System for Vapor and Plasma Measurements", Final Technical Report, Contract DNA001-87-C-0271, Defense Nuclear Agency, Washington, DC, October 21, 1988.

31. J. T. Porter, G. H. Reynolds, T. D. Kunz, and M. J. Berry, "Laser Probe Vaporization/Oxidation Testing of High Temperature Composites", Report WRDC-TR-89-4081, Materials Laboratory, Wright Research and Development Center, Air Force Systems Commano, Wright-Patterson AFB, OH, 45433-6533, July, 1989.

32. B. G. Wicke, "Chemiluminescent Oxidation of Gas Phase Carbon Species by Molecular Oxygen", Carbon, 23, 131 (1985).

33. D. C. Tyte, S. H. Innanen, and R. W. Nichols, Identification Atlas of Molecular Spectra, #5, The C_2 Swan System (York University, Toronto, Canada, 1967).

5.0 REFERENCES (continued)

34. J. G. Phillips and S. P. Davis, The Swan System of the C_2 Molecule: Berkeley Analyses of Molecular Spectra, Vol. 2 (University of California, Berkeley, 1968).

35. C. Amiot, "Fourier Spectroscopy of the $^{12}C_2$, $^{13}C_2$, and $^{12}C^{13}C$ (0-0) Swan Bands", Astrophys. J. Suppl., 52, 329-340 (1983).

36. M. J. Berry, "Short Wavelength Laser/Materials Interactions - Annual Technical Report", Report Number TR-86-001, Grant AFOSR-85-0365 (Houston Area Research Center, Woodlands, TX, November, 1986).

37. C. F. Bohren and D. R. Huffman, Absorption and Scattering of Light by Small Particles (Wiley, New York, 1983).

38. K. T. Whitby and K. Willeke, "Single Particle Optical Counters: Principles and Field Use", in D. A. Lundgren, et al. (editors), Aerosol Measurement (University of Florida Press, Gainesville, FL, 1979), pp. 145-182.

39. A. B. Pluchino, S. S. Goldberg, J. M. Dowling, and C. M. Randall, "Refractive Index Measurements of Single Micron-Sized Carbon Particles", Appl. Opt., 19, 3370-3372 (1980).

40. J. Sugar and C. Corliss, Atomic Energy Levels of the Iron-Period Elements: Potassium through Nickel, J. Phys. Chem. Ref. Data, 14, Suppl. 2 (1985).

41. W. L. Wiese and J. R. Fuhr, "Atomic Transition Probabilities for Scandium and Titanium (A Critical Data Compilation of Allowed Lines)", J. Phys. Chem. Ref. Data, 4, 263-352 (1975).

42. L. M. A. Levine, L. G. Fredin, and M. J. Berry, "Infrared Absorption Spectra of Cured Epoxy Resin and Human Corneal Tissue at Temperatures Up To 450 °C", SPIE Proceedings, Vol. 1064 - Thermal and Optical Interactions with Biological and Related Composite Materials, 131-134 (1989).

43. R. W. Field, A. Lagerqvist, and I. Renhorn, "The Low Lying Electronic States of SiO", Physica Scripta, 14, 298-319 (1976).

44. W. L. Vaughn and H. G. Maahs, "Active-to-Passive Oxidation Transition and Other Limitations on the Use of Silicon-Based Coatings for Carbon-Carbon Composites", Paper Number 41 presented at the Seventh National AeroSpace Plane Technology Symposium, 23-27 October, 1989.

45. S. Bashkin and J. O. Stoner, Jr., Atomic Energy Levels and Grotrian Diagrams, Vol. 1 (North-Holland Publishing Co., Amsterdam, 1975), pp. 55-98.

46. R. J. Glumb, R. C. Hilyard, R. B. Perry, M. B. Petach, I. Rubin, and W. L. Shackleford, "Spectroscopic Studies and High-Speed Imaging of Plasma and Plume Formation Above Laser-Irradiated Composite Materials", AIAA Paper No. 88-1078 (American Institute of Aeronautics and Astronautics, New York, 1988).

47. W. L. Wiese, M. W. Smith, and B. M. Glennon, Atomic Transition Probabilities, Vol. 1, NSRDS-NBS 4 (U. S. Government Printing Office, Washington, DC, 1966).

48. G. Bekefi (editor), Principles of Laser Plasmas (Wiley, New York, 1976).

49. J. T. Knudtson, W. B. Green, and D. G. Sutton, "The UV-Visible Spectroscopy of Laser-Produced Aluminum Plasmas", J. Appl. Phys., 61, 4771-4780 (1987).

50. N. Konjevic and W. L. Wiese, "Experimental Stark Widths and Shifts for Non-Hydrogenic Spectral Lines of Ionized Atoms", J. Phys. Chem. Ref. Data, 5, 259-308 (1976).

51. W. C. Martin and R. Zalubas, "Energy Levels of Aluminum, Al I Through Al XIII", J. Phys. Chem. Ref. Data, 3, 817-864 (1979).

5.0 REFERENCES (continued)

52. W. L. Wiese, M. W. Smith, and B. M. Miles, Atomic Transition Probabilities, Vol. 2, NSRDS-NBS 22 (U. S. Government Printing Office, Washington, DC, 1969).

53. M. W. Chase, Jr., C. A. Davies, J. R. Downey, Jr., D. J. Frurip, R. A. McDonald, and A. N. Syverud, JANAF Thermochemical Tables, Third Edition, J. Phys. Chem. Ref. Data, *14*, Supplement No. 1 (1985), p. 65.

54. S. Bashkin and J. O. Stoner, Jr., Atomic Energy-Level and Grotrian Diagrams, Vol. 2 (North-Holland Publishing Co., Amsterdam, 1978), pp. 513-598.

55. D. M. Cooper and J. J. Jones, "An Experimental Determination of the Cross Section of the Swings Band System of C_3", J. Quant. Spectrosc., Radiat. Transfer, *22*, 201-208 (1979).

56. B. Brocklehurst, G. R. Hébert, S. H. Innanen, R. M. Seel, and R. W. Nicholls, Identification Atlas of Molecular Spectra, #9, The CN B - X Violet System (York University, Toronto, Canada, 1972).

57. M. J. Berry, "Short Wavelength Laser/Materials Interactions - Annual Technical Report", Report dated 30 June 1988, Grant AFOSR-85-0365 (Houston Area Research Center, Woodlands, TX).

58. The calculations described in Reference 23 are corrected, updated, and extended as follows:

    A - H_A is calculated using mass fractions, rather than mole fractions [Reference 6 in Appendix E] and

    B - carbon vapor species up to C_7 are included, with improved JANAF thermochemical data and vapor pressures for monatomic (C_1) and diatomic (C_2) carbon vapor species [Reference 4 in Appendix E] and previous LLNL thermochemical data and vapor pressures for othee (n>3) carbon vapor species C_n [References 3 and 5 in Appendix E].

59. M. J. Berry, "Carbon Vapor Species", Report dated 1 August 1983 (Rice University, Houston, TX).

60. W. Weltner and D. McLeod, Jr., "Spectroscopy of Carbon Vapor Condensed in Rare Gas Matrices at 4 K. III", J. Chem. Phys., *45*, 3096 (1966).

61. R. T. Meyer, A. W. Lynch, and J. M. Freese, "Chemical Reactions of Carbon Atoms and Molecules from Laser-Induced Vaporization of Graphite and Tantalum Carbide", J. Phys. Chem., *77*, 1083-1092 (1973).

62. R. T. Meyer, "Pulsed Laser Induced Vaporization of Graphite and Carbides", 11th Biennial Conference on Carbon, Extended Abstracts Program, 1973.

63. F. M. Wachi and D. E. Gilmartin, High Temp. Sci., *4*, 423 (1972).

64. A. Bailey, J. Baker, C. Rollins, E. Pugh, L. Popper, and P. Nebolsine, "Simple Models for Laser-Material Interaction", Report PSI-9445/SR-420, to be published in Proceedings of the Seventh DoD Conference on DEW Vulnerability, Survivability, and Effects (Office of the Chief of Naval Research, Arlington, VA, 1989).

65. D. Sliney and M. Wolbarsht, Safety with Lasers and Other Optical Sources (Plenum, New York, 1980), Section 2.16.

66. M. J. Berry, "Optical Properties of Metals", Report dated 31 August 1987 (Antropix Corporation, Woodlands, TX); updated copy appended (*cf*. Appendix F).

6.0 PERSONNEL

The principal investigator (Michael Berry), a senior research associate (Leif Fredin), four research associates (David Halligan, Terry Kunz, Leanna Levine, and Sydney Ulvick), a laser scientist (Richard Menefee), and a laser technician (Brendan Krenek) have all been supported on the AFOSR/HARC/Rice Program.

7.0 INTERACTIONS with OTHER GROUPS

Extensive interactions with personnel at the Air Force Wright Research and Development Center Materials Laboratory (Laser Hardened Materials Branch: WRDC/MLPJ), at the Air Force Weapons Laboratory (Technology Assessment/Laser Effects Branch: WL/TALE), at the Defense Nuclear Agency (Shock Physics Special Projects Branch: DNA/SPSP), and at the Strategic Defense Initiative Organization (SDIO) have been developed over the life of the AFOSR/HARC/Rice Program. The principal investigator and several HARC staff members have been active as part of the Textron team on the Defensive Shields Demonstration Program, which is a high priority spacecraft survivability effort supported through WRDC/MLPJ. The same personnel have also been active on laser experimentation projects at WL as part of the High Irradiance 2 Program.

Other interactions include extensive collaborations with several materials manufacturers (Textron Specialty Materials, General Atomics, Ultramet, MSNW, and Hitco) which have led to the development of new laser hardened materials for spacecraft survivability and related applications.

APPENDICES

The following appendices are attached:

A - Descriptions of HARC Laser Test Resources (4 sets of descriptions; 14 pages total)

* HARC cw Carbon Dioxide Laser Test Resource
* HARC cw HF/DF Chemical Laser Test Resource
* HARC rp HF/DF Chemical Laser Test Resource
* HARC rp Excimer Laser Test Resource

B - Target Front Surface Temperature/Spectral Emittance Data (28 pages total)

C - Target Spectral Reflectance Measurements (16 pages total)

D - Survey Plume Emission Spectra (11 pages total)

E - Carbon Vapor Species (1 page)

F - Optical Properties of Metals (20 page report)

G - Publication Abstracts (5 pages total)

APPENDIX A: Descriptions of HARC Laser Test Resources

Four sets of descriptions are attached:

* HARC cw Carbon Dioxide Laser Test Resource
* HARC cw HF/DF Chemical Laser Test Resource
* HARC rp HF/DF Chemical Laser Test Resource
* HARC rp Excimer Laser Test Resource

HARC

LASER APPLICATIONS RESEARCH CENTER

4802 Research Forest Drive
The Woodlands. Texas 77381
713/363-7920

HARC cw Carbon Dioxide Laser Test Resource: Statement of Capabilities

The Houston Area Research Center (HARC) continuous wave (cw) carbon dioxide (CO_2) laser test resource can be used to:

1) irradiate samples with a well-characterized cw CO_2 laser beam (using either a flat-top or a near-Gaussian beam profile), peak irradiances up to 1 MW/cm², and peak powers up to 1 kW;

2) irradiate samples for fixed and well-measured periods of time (10 ms up to minutes) in vacuum (as low as 10^{-8} torr) or under controlled atmospheres (air, inert gas, *etc.*) at pressures up to 1 atmosphere;

3) carry out time-resolved measurements of target responses and laser/materials interaction phenomena as functions of laser parameters (irradiance, spot size, angle of incidence, *etc.*), sample geometry, and atmosphere; these time-resolved measurements include:

   A) burnthrough time (and times for partial burnthroughs),

   B) front and back surface temperatures,

   C) front surface reflectance at CO_2 laser wavelengths and (optionally) at other infrared, near infrared, visible, and ultraviolet wavelengths, and

   D) plume absorptions and/or emissions due to atomic, molecular, particulate, and plasma species;

4) record these time-resolved data with transient digitizers, a digital oscilloscope, and a fast minicomputer system for rapid analysis and processing;

5) obtain videotape and fast framing camera movies of target responses during laser irradiation;

6) measure mass losses, morphological changes, and other post-irradiation properties of samples; and

7) obtain photomicrographic records of pre- and post-irradiated materials.

Other optional experiments that can be performed include irradiation at HF/DF, excimer, and other wavelengths, irradiation by lasers with pulsed waveforms, measurements of other target optical properties (*e.g.*, transmittance), and analyses of post-irradiated solids and ablated species by mass spectrometry, infrared spectroscopy, and fluorescence microscopy.

Certain experimental capabilities are mobile for use at other laser test facilities.

The attached description on "The Houston Area Research Center (HARC) cw Carbon Dioxide Laser Test Resource" provides details on the experimental apparatus.

For further information, contact Dr. Michael Berry at (713) 363-7970.

HARC

The Houston Area Research Center (HARC) cw Carbon Dioxide Laser Test Resource

The HARC cw carbon dioxide (CO_2) laser test resource includes a cw CO_2 laser system, a test chamber, and beam, target, and plume diagnostic instrumentation equipped with a realtime computer data acquisition and processing system. The facility has been used to study cw CO_2 laser interactions with materials in order to analyze their intrinsic ablation (and/or oxidation) performance and to measure their time-resolved responses, properties, and ablation (and/or oxidation) products under well-characterized laser irradiation conditions. Fundamental studies of laser/materials interactions are performed in order to obtain mechanistic understanding of the physical and chemical processes that produce the phenomenology and effects associated with thermal coupling and thermochemical ablation of carbon-based and other materials irradiated by cw infrared lasers at irradiances up to 1 MW/cm^2. In addition, the facility is being used for screening measurements on candidate laser hardened (and/or oxidation resistant) materials in preparation for larger scale laser effects testing.

Figure 1 shows a typical experimental configuration. The basic apparatus components are:

1) a cw CO_2 laser system (Laser Corporation of America Model Falcon/800™) that produces up to 1 kW output power at 10.6 μm wavelength with low beam divergence (1.5 mrad),

2) an optical delivery system that is suitable for irradiating samples with excellent control of beam position, irradiance, and time on target,

3) laser beam diagnostics that characterize wavelengths, short term and long term power levels, beam profiles, and irradiance distributions on target,

4) a high vacuum (10^{-8} torr) sample chamber that incorporates a carousel with several samples and accurate positioning controls; the chamber permits experiments in vacuum and in controlled atmospheres and has several viewing ports together with an internally mounted integrating sphere reflectance measurement system,

5) a computer controlled laser probe absorption spectrometer system that provides quantitative time-resolved measurements on plume vapor and plasma species,

6) additional target and plume diagnostics instrumentation (an optical multichannel analyzer for plume emission spectroscopy, fixed frequency lasers for debris measurements, optical pyrometers for front and back surface temperature measurements, a burnthrough detector, a microbalance for determination of mass losses, videotape and fast framing cameras and recorders, a photomicrography system, and a quadrupole mass spectrometer for analysis of ablated species), and

7) fast (up to 125 MHz bandwidth) transient digitizers and digital oscilloscopes plus a minicomputer system for experimental control and data acquisition and processing (for sixteen channels of information with a 40 kHz/channel acquisition rate).

The laser test resource is being used to identify new high performance materials, to measure their important properties, to test and refine mechanistic models that facilitate the development of advanced laser resistant materials with exceptional hardness against thermochemical laser ablation, to screen candidate laser hardened materials, and to evaluate high temperature composite materials for applications in oxidizing and/or reducing atmospheres.

For further information, contact Dr. Michael Berry at (713) 363-7970.

Figure (attached)

CO_2 laser/materials interaction apparatus. A cw CO_2 laser irradiates samples contained within the vacuum chamber at the far right of the figure. Portions of the laser beam are directed by a beamsplitter BS1 and a wedged chamber window onto beam diagnostics equipment (a power meter, a fast response power monitor, and a fast response beam profile monitor). A fast acting shutter S controls irradiation times on target. An optical delivery system (comprising attenuators, beam steering mirrors M1 and M2, and a focussing lens) provides accurately positioned beams on target with controlled and measured irradiance distributions. An alignment scope facilitates accurate positioning of the focussed laser beam onto the target surface. Realtime target responses are monitored with time-resolved target diagnostics instrumentation [optical pyrometers for front and back surface temperature measurements, a burnthrough detector, an integrating sphere IS with a filter plus fast response detector for reflectance measurements, camera systems (both videotape and fast framing cameras, not shown), and an optical multichannel analyzer (OMA) system for plume emission measurements]. Signals from the beam, target, and plume diagnostics are digitized, recorded, and processed using transient digitizers, digital oscilloscopes, and a minicomputer system.

A laser probe absorption spectrometer is also combined with the laser/materials interaction apparatus to provide spectroscopic measurements on plume vapor and plasma species. In the bottom part of the figure, a cw ion laser pumps a single frequency tunable cw ring dye laser system (Coherent, Inc. Model 699-21) which produces spectral outputs over the visible/near infrared (λ = 400-900 nm wavelength) spectral regions. The dye laser system can also be combined with intracavity (not shown) and external second harmonic (2ω) generation crystals to produce tunable ultraviolet (λ = 200-400 nm wavelength) spectral outputs. The visible spectral region of the cw dye laser systems is scanned electronically over a 30 GHz bandwidth and is passed through an electro-optical modulator (a "noise eater"; not shown) to obtain stable low noise probe signals. A reference cavity within the dye laser system is used to verify single frequency operation during scans. The low noise scanned (or fixed frequency) dye laser probe beam is directed toward the vacuum chamber by the beam discriminator (used to isolate the frequency doubled beam from the fundamental dye laser beam), focussed to a narrow beam waist in front of the target surface and within the ablation plume by lens L, and detected by a filter and/or small monochromator plus fast photodiode PD1 combination. Beamsplitter BS2 directs a portion of the probe beam to photodiode PD2 for power and ratioed absorption measurements. The dye laser output wavelength is calibrated by monitoring tellurium (Te) or iodine (I_2; not shown) cell absorption signals detected by photodiode PD3 and by using an interferometric measurement system (wavemeter). The probe beam can be positioned accurately within the ablation plume for spatial resolution of plume absorptions as functions of distance from the sample surface and of distance from the plume centerline (*i.e.*, the axis of cylindrical symmetry). The laser probe absorption spectrometer and all the detection electronics are computer controlled by a LSI-11/Camac-based system.

Various fixed frequency probe lasers are also used to obtain quantitative measurements on atomic, molecular, particulate, and plasma species contained in the laser induced ablation plumes.

cw CO₂ LASER TEST RESOURCE
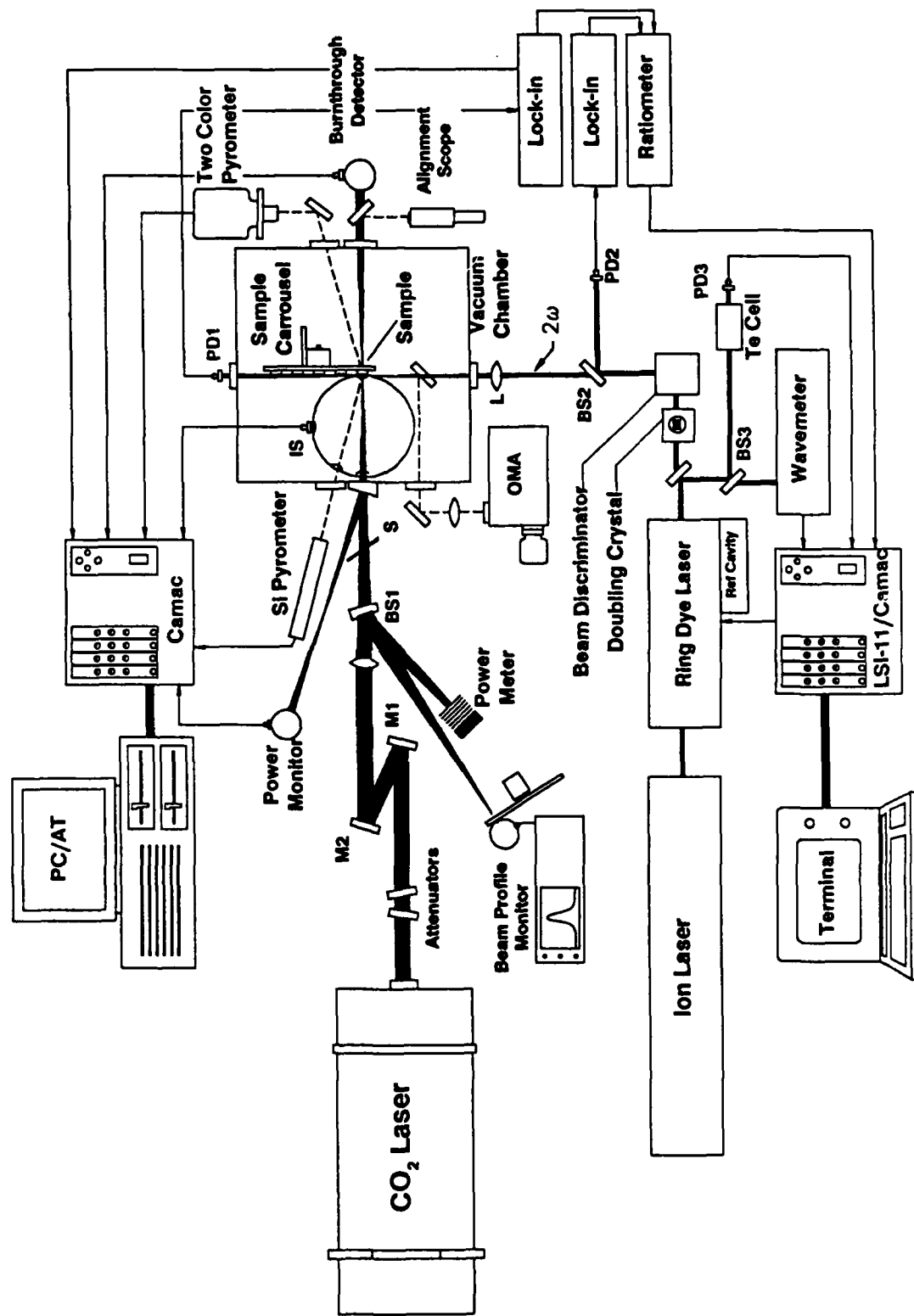
HARC

LASER APPLICATIONS RESEARCH CENTER

4802 Research Forest Drive
The Woodlands. Texas 77381
713/363-7920

HARC cw HF/DF Chemical Laser Test Resource: Statement of Capabilities

The HARC continuous wave (cw) hydrogen fluoride (HF) and deuterium fluoride (DF) chemical laser test resource can be used to:

1) irradiate samples with very well-characterized cw HF/DF chemical laser beams with a near-Gaussian beam profile, peak irradiances up to 200 kW/cm^2, and peak powers up to 150 W;

2) irradiate samples for fixed and well-measured periods of time (10 ms up to minutes) in vacuum or under controlled atmospheres (air, inert gas, *etc.*) at pressures up to 1 atmosphere;

3) carry out time-resolved measurements of target responses and laser/materials interaction phenomena as functions of laser parameters (irradiance, spot size, angle of incidence, *etc.*), sample geometry, and atmosphere; these time-resolved measurements include:

   A) burnthrough time (and times for partial burnthroughs),

   B) front and back surface temperatures,

   C) front surface reflectance at HF/DF laser wavelengths and (optionally) at other infrared, near infrared, visible, and ultraviolet wavelengths, and

   D) plume absorptions and/or emissions due to atomic, molecular, particulate, and plasma species;

4) record these time-resolved data with transient digitizers and a fast minicomputer system for rapid analysis and processing;

5) obtain videotape and fast framing camera movies of target responses during laser irradiation;

6) measure mass losses, morphological changes, and other post-irradiation properties of samples; and

7) obtain photomicrographic records of pre- and post-irradiated materials.

Other optional experiments that can be performed include irradiation at CO_2, excimer, and other wavelengths (including the overtone HF chemical laser near $\lambda = 1.3$ μm), irradiation by lasers with pulsed waveforms, and analyses of ablated species by mass spectrometry and by matrix isolation infrared spectroscopy.

Many experimental capabilities are mobile for use at other laser test facilities.

The attached description on "The Houston Area Research Center (HARC) cw HF/DF Chemical Laser Test Resource" provides details on the experimental apparatus.

For further information, contact Dr. Michael Berry at (713) 363-7970.

HARC

LASER APPLICATIONS RESEARCH CENTER

4802 Research Forest Drive
The Woodlands. Texas 77381
713/363-7920

The Houston Area Research Center (HARC) cw HF/DF Chemical Laser Test Resource

The HARC cw hydrogen fluoride (HF)/deuterium fluoride (DF) chemical laser test resource includes a cw HF/DF chemical laser system, a test chamber, and beam, target, and plume diagnostic instrumentation equipped with a realtime computer data acquisition and processing system. The facility has been used to study cw HF/DF chemical laser interactions with more than 120 different materials in order to analyze their intrinsic ablation performance and to measure their time-resolved responses and properties under well-characterized laser irradiation conditions. Fundamental studies of laser/materials interactions have been performed in order to obtain mechanistic understanding of the physical and chemical processes that produce the phenomenology and effects associated with thermal coupling and thermochemical ablation of carbon-based and other materials irradiated by cw infrared lasers at irradiances up to 200 kW/cm². In addition, the facility has been used to complete screening measurements on candidate laser hardened materials in preparation for larger scale laser effects testing.

Figure 1 shows a typical experimental configuration. The basic apparatus components are:
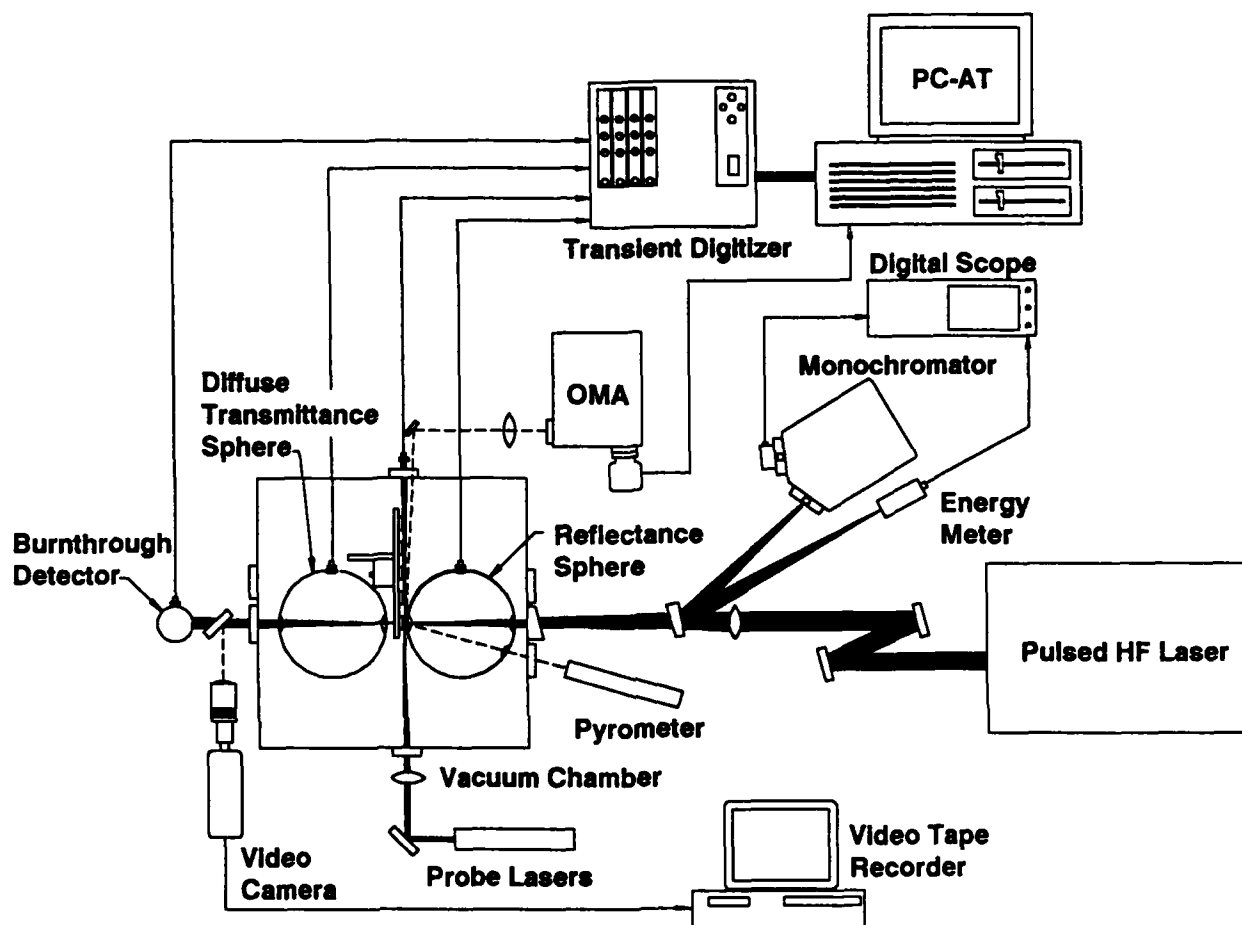
1) a cw HF/DF chemical laser system (Helios Model CLIV) that produces up to 150 W multiline output in the 2.6-3.1 μm (HF) and 3.7-4.1 μm (DF) spectral regions [the system also produces up to 40 W single line output in grating-tuned operation],

2) an optical delivery system that is suitable for irradiating samples with excellent control of beam position, irradiance, and time on target,

3) laser beam diagnostics that characterize wavelengths, short term and long term power levels, beam profiles, and irradiance distributions on target,

4) an evacuable sample chamber that incorporates a carousel with sixteen samples and accurate positioning controls; the chamber permits experiments in vacuum and in controlled atmospheres and has several viewing ports together with an internally mounted integrating sphere reflectance measurement system,

5) a computer controlled laser probe absorption spectrometer system that provides quantitative time-resolved measurements on plume species,

6) additio:.al target and plume diagnostics instrumentation (an optical multichannel analyzer for plume emission spectroscopy, optical pyrometers for front and back surface temperature measurements, a burnthrough detector, a microbalance for determination of mass losses, videotape and fast framing cameras and recorders, a quadrupole mass spectrometer for analysis of ablated species, and a photomicrography system), and

7) fast (up to 100 MHz bandwidth) transient digitizers and digital oscilloscopes plus a minicomputer system for experimental control and data acquisition and processing (for sixteen channels of information with a 40 kHz/channel acquisition rate).

The experimental program has led to the identification of new high performance materials and their important properties and to the development of mechanistic models that guide the design of superior laser hardened and/or oxidation resistant materials.

For further information, contact Dr. Michael Berry at (713) 363-7970.

Figure (attached)

Continuous wave (cw) hydrogen fluoride (HF)/deuterium fluoride (DF) laser/materials interaction apparatus. A cw HF/DF chemical laser irradiates samples contained within a vacuum chamber. Portions of the laser beam are directed by a beamsplitter BS1 and a wedged chamber window onto beam diagnostics equipment (a power meter, a fast response power monitor, and a fast response beam profile monitor). A fast acting shutter S controls irradiation times on target. An optical delivery system (comprising attenuators, beam steering mirrors M1 and M2, and a focussing lens) provides accurately positioned beams on target with controlled and measured irradiance distributions. An alignment scope facilitates accurate positioning of the focussed laser beam onto the target surface. Realtime target responses are monitored with time-resolved target diagnostics instrumentation [optical pyrometers for front and back surface temperature measurements, a burnthrough detector, an integrating sphere with a filter plus fast response detector for reflectance measurements, camera systems (both videotape and fast framing cameras, not shown), and an optical multichannel analyzer for target and plume emission measurements]. Signals from the beam, target, and plume diagnostics are digitized, recorded, and processed using transient digitizers, digital oscilloscopes, and a minicomputer system.

A laser probe absorption spectrometer is also combined with the laser/materials interaction apparatus to provide spectroscopic measurements on plume vapor and plasma species. In the bottom part of the figure, a cw ion laser pumps a single frequency tunable cw ring dye laser system (Coherent, Inc. Model 699-21) which produces spectral outputs over the visible/near infrared (λ = 400-900 nm wavelength) spectral regions. The dye laser system can also be combined with intracavity (not shown) and external second harmonic (2ω) generation crystals to produce tunable ultraviolet (λ = 200-400 nm wavelength) spectral outputs. The visible spectral region of the cw dye laser systems is scanned electronically over a 30 GHz bandwidth and is passed through an electro-optical modulator (a "noise eater"; not shown) to obtain stable low noise probe signals. A reference cavity within the dye laser system is used to verify single frequency operation during scans. The low noise scanned (or fixed frequency) dye laser probe beam is directed toward the vacuum chamber by the beam discriminator (used to isolate the frequency doubled beam from the fundamental dye laser beam), focussed to a narrow beam waist in front of the target surface and within the ablation plume by lens L, and detected by a filter and/or small monochromator plus fast photodiode PD1 combination. Beamsplitter BS2 directs a portion of the probe beam to photodiode PD2 for power and ratioed absorption measurements. The dye laser output wavelength is calibrated by monitoring tellurium (Te) or iodine (I_2; not shown) cell absorption signals detected by photodiode PD3 and by using an interferometric measurement system (wavemeter). The probe beam can be positioned accurately within the ablation plume for spatial resolution of plume absorptions as functions of distance from the sample surface and of distance from the plume centerline (*i.e.*, the axis of cylindrical symmetry). The laser probe absorption spectrometer and all the detection electronics are computer controlled by a LSI-11/Camac-based system.

Various fixed frequency probe lasers are also used to obtain quantitative measurements on atomic, molecular, particulate, and plasma species contained in the laser induced ablation plumes.

cw HF/DF LASER TEST RESOURCE
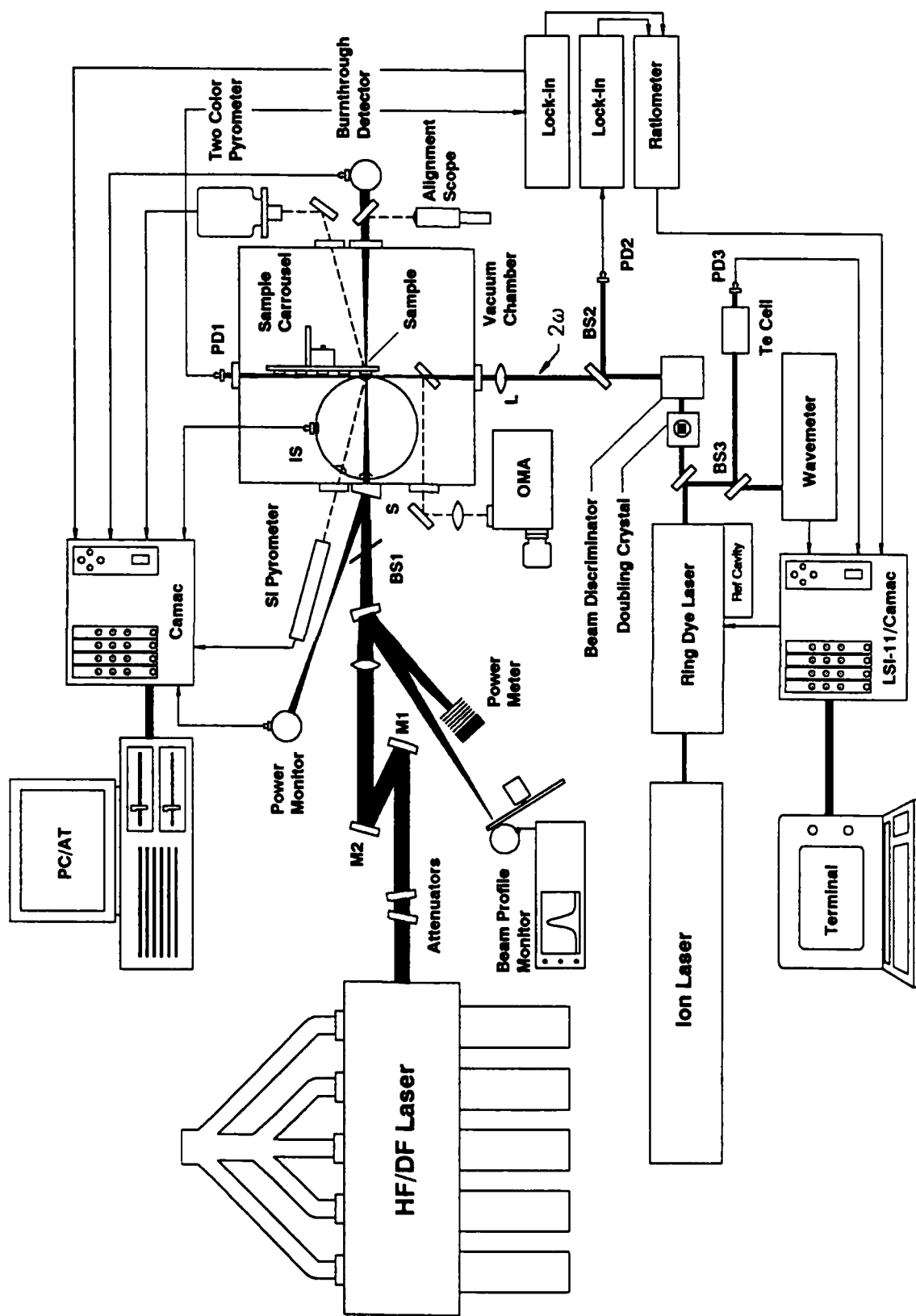
HARC

LASER APPLICATIONS RESEARCH CENTER

4802 Research Forest Drive
The Woodlands. Texas 77381
713/363-7920

HARC rp HF/DF Chemical Laser Test Resource: Statement of Capabilities

The HARC repetitively pulsed (rp) hydrogen fluoride (HF) and deuterium fluoride (DF) chemical laser test resource can be used to:

1) irradiate samples with well-characterized rp HF/DF chemical laser beams with a near-uniform beam profile, pulse energies (E_p) up to 1 J/pulse, peak irradiances up to 10 MW/cm², pulse fluences (F_p) up to 200 J/cm², pulse durations (τ_p) of 100-500 ns with variable pulse repetition frequencies up to 500 Hz, and average powers up to 100 W;

2) irradiate samples for fixed and well-measured periods of time (100 ns up to minutes) with a selected number of pulses (single pulse up to 500 Hz pulse trains) in vacuum or under controlled atmospheres (air, inert gas, *etc.*) at pressures up to 1 atmosphere;

3) carry out time-resolved measurements of target responses and laser/materials interaction phenomena as functions of laser parameters (irradiance, pulse waveform, spot size, angle of incidence, *etc.*), sample geometry, and atmosphere; these time-resolved measurements include:

   A) burnthrough time (and times for partial burnthroughs),

   B) front and back surface temperatures,

   C) front surface reflectance at HF/DF laser wavelengths and (optionally) at other infrared, near infrared, visible, and ultraviolet wavelengths, and

   D) plume absorptions and/or emissions due to atomic, molecular, particulate, and plasma species;

4) record these time-resolved data with transient digitizers and a fast minicomputer system for rapid analysis and processing;

5) obtain videotape and fast framing camera movies of target responses during laser irradiation;

6) measure mass losses, morphological changes, and other post-irradiation properties of samples; and

7) obtain photomicrographic records of pre- and post-irradiated materials.

Other optional experiments that can be performed include pulsed irradiations using excimer, tunable dye and frequency-doubled dye, Nd:YAG, CO, and CO_2 lasers, measurements of other target optical properties (*e.g.*, transmittance), and analyses of post-irradiated solids and ablated species by mass spectrometry, infrared spectroscopy, fluorescence and scanning electron microscopy, and other characterization techniques.

Many experimental capabilities are mobile for use at other laser test facilities.

The attached description on "The Houston Area Research Center (HARC) rp HF/DF Chemical Laser Test Resource" provides details on the experimental apparatus.

For further information, contact Dr. Michael Berry at (713) 363-7970.

LASER APPLICATIONS RESEARCH CENTER

4802 Research Forest Drive
The Woodlands, Texas 77381
713/363-7920

The Houston Area Research Center (HARC) rp HF/DF Chemical Laser Test Resource

The HARC rp hydrogen fluoride (HF)/deuterium fluoride (DF) chemical laser test resource includes a rp HF/DF chemical laser system, a test chamber, and beam, target, and plume diagnostic instrumentation equipped with a realtime computer data acquisition and processing system. The facility has been used to study rp HF/DF chemical laser interactions with materials in order to analyze their intrinsic ablation performance and to measure their time-resolved responses and properties under well-characterized laser irradiation conditions. Fundamental studies of laser/materials interactions have been performed in order to obtain mechanistic understanding of the physical and chemical processes that produce the phenomenology and effects associated with thermal coupling and thermochemical ablation of carbon-based and other materials irradiated by rp infrared lasers at fluences up to 200 J/cm^2. In addition, the facility has been used to complete screening measurements on candidate laser hardened materials in preparation for larger scale laser effects testing.

Figure 1 shows a typical experimental configuration. The basic apparatus components are:

1) a rp (500 Hz maximum PRF) HF/DF chemical laser system (Lambda Physik Model EMG-204 MSC, converted from excimer to chemical laser operation) that produces up to 1 J/pulse multiline output in the 2.6-3.1 μm (HF) and 3.7-4.1 μm (DF) spectral regions,

2) an optical delivery system that is suitable for irradiating samples with excellent control of beam position, irradiance, and time on target,

3) laser beam diagnostics that characterize wavelengths, short term and long term power levels, beam profiles, and irradiance distributions on target,

4) an evacuable sample chamber that incorporates a carousel with sixteen samples and accurate positioning controls; the chamber permits experiments in vacuum and in controlled atmospheres and has several viewing ports,

5) a laser probe attenuation measurement system and a computer controlled laser probe absorption spectrometer system that provide quantitative time-resolved measurements on plume species (atoms, molecules, particles, and/or plasmas),

6) integrating spheres plus detector/filter combinations for time-resolved measurements on target reflectances and transmittances,

7) additional target and plume diagnostics instrumentation (an optical multichannel analyzer for plume emission spectroscopy, optical pyrometers for target front and back surface temperature measurements, a burnthrough detector, a microbalance for determination of mass losses, videotape and fast framing cameras and recorders, and a photomicrography system), and

8) fast (up to 100 MHz bandwidth) transient digitizers and digital oscilloscopes plus a minicomputer system for experimental control and data acquisition and processing (for sixteen channels of information with a 40 kHz/channel acquisition rate).

The experimental program has led to the identification of new high performance materials and their important properties and to the development of mechanistic models that guide the design of superior laser hardened materials.

For further information, contact Dr. Michael Berry at (713) 363-7970.

LASER APPLICATIONS RESEARCH CENTER

4802 Research Forest Drive
The Woodlands, Texas 77381
713/363-7920

Figure 1. Laser/materials interaction apparatus. A rp HF chemical laser irradiates samples contained within the vacuum chamber at the far left of the figure. Portions of the laser beam are beamsplit by a CaF_2 wedge and are characterized by beam diagnostic instrumentation [an ARC 0.3 m monochromator plus fast InAs detector, a Gentec ED200 pyroelectric pulse energy meter, an InAs detector/amplifier pulse temporal monitor (not shown), and a translating aperture beam profile measurement system (not shown)]. An optical delivery system [Mo beam steering mirrors and/or variable reflectance optical flats (ZnSe, CaF_2, or NaCl) plus a CaF_2 focussing lens] provide accurately positioned beams on target with controlled and measured fluence distributions. Realtime target and plume properties and responses are monitored with time-resolved target and plume diagnostics instrumentation [an optical pyrometer for front surface temperature measurements, a burnthrough detector, integrating spheres with filters and fast response InAs detectors for reflectance and transmittance measurements, a CKC 200 CCD video camera system, a HeNe probe laser for plume particle measurements, and an optical multichannel analyzer (OMA) system (Instruments SA Model HR-320 monochromator plus Princeton Instruments Model P/IRY-700 OMA) for target and plume emission measurements]. Signals from both the laser beam and the target and plume diagnostics are digitized, recorded, and processed using transient digitizers, a digital oscilloscope, and a minicomputer system.

HARC

HARC rp Excimer Laser Test Resource: Statement of Capabilities

The HARC repetitively pulsed (rp) excimer laser test resource can be used to:

1) irradiate samples with well-characterized rp excimer laser beams with a combined flat-top/Gaussian beam profile, pulse energies (E_p) up to 400 mJ/pulse, peak irradiances up to 10 GW/cm², peak pulse fluences (F_p) up to 200 J/cm², pulse durations (τ_p) of 10-20 ns with variable pulse repetition frequencies up to 500 Hz, and average powers up to 100 W at several excimer wavelengths: 193 nm (ArF), 248 nm (KrF), 308 nm (XeCl), and 351 nm (XeF);

2) irradiate samples for fixed and well-measured periods of time (10 ns up to minutes) with a selected number of pulses (single pulse up to 500 Hz pulse trains) in vacuum or under controlled atmospheres (air, inert gas, *etc.*) at pressures up to 1 atmosphere;

3) carry out time-resolved measurements of target responses and laser/materials interaction phenomena as functions of laser parameters (irradiance, pulse waveform, spot size, angle of incidence, *etc.*), sample geometry, and atmosphere; these time-resolved measurements include:

   A) burnthrough time (and times for partial burnthroughs),

   B) front and back surface temperatures,

   C) front surface reflectance at excimer laser wavelengths and (optionally) at infrared, near infrared, visible, and other ultraviolet wavelengths, and

   D) plume absorptions and/or emissions due to atomic, molecular, particulate, and plasma species;

4) record these time-resolved data with transient digitizers and a fast minicomputer system for rapid analysis and processing;

5) obtain videotape and fast framing camera movies of target responses during laser irradiation;

6) measure mass losses, morphological changes, and other post-irradiation properties of samples; and

7) obtain photomicrographic records of pre- and post-irradiated materials.

Other optional experiments that can be performed include pulsed irradiations using tunable dye and frequency-doubled dye, Nd:YAG, HF, DF, CO, and CO_2 lasers, measurements of other target optical properties (*e.g.*, transmittance), and analyses of post-irradiated solids and ablated species by mass spectrometry, infrared spectroscopy, fluorescence and scanning electron microscopy, and other characterization techniques.

Many experimental capabilities are mobile for use at other laser test facilities.

The attached description on "The Houston Area Research Center (HARC) rp Excimer Laser Test Resource" provides details on the experimental apparatus.

For further information, contact Dr. Michael Berry at (713) 363-7970.

LASER APPLICATIONS RESEARCH CENTER

4802 Research Forest Drive
The Woodlands, Texas 77381
713 363-7920

The Houston Area Research Center (HARC) rp Excimer Laser Test Resource

The HARC repetitively pulsed (rp) excimer laser test resource includes a rp excimer laser system, a test chamber, and beam, target, and plume diagnostic instrumentation equipped with a realtime computer data acquisition and processing system. The facility has been used to study rp excimer laser interactions with materials in order to analyze their intrinsic ablation performance and to measure their time-resolved responses and properties under well-characterized laser irradiation conditions. Fundamental studies of laser/materials interactions have been performed in order to obtain mechanistic understanding of the physical and chemical processes that produce the phenomenology and effects associated with rp excimer laser ablation of carbon-based and other materials. In addition, the facility has been used to complete screening measurements on candidate laser hardened materials in preparation for larger scale laser effects testing.

Figure 1 shows a typical experimental configuration. The basic apparatus components are:

1) a rp (500 Hz maximum PRF) excimer laser system (Lambda Physik Model EMG-204 MSC) that produces up to 400 mJ/pulse, short duration (10-20 ns) pulses with 100 W average power at KrF (248 nm) and XeCl (308 nm) wavelengths as well as 60 W average power at ArF (193 nm) and XeF (351 nm) wavelengths,

2) an optical delivery system that is suitable for irradiating samples with excellent control of beam position, irradiance, pulse fluence, and total fluence on target,

3) laser beam diagnostics that characterize wavelengths, short term and long term power levels, beam profiles, and irradiance/fluence distributions on target,

4) an evacuable sample chamber that incorporates a carousel with sixteen samples and accurate positioning controls; the chamber permits experiments in vacuum and in controlled atmospheres and has several viewing ports,

5) a laser probe attenuation measurement system and a computer controlled laser probe absorption spectrometer system that provide quantitative time-resolved measurements on plume species (atoms, molecules, particles, and/or plasmas),

6) integrating spheres plus detector/filter combinations for time-resolved measurements on target reflectances and transmittances,

7) additional target and plume diagnostics instrumentation (an optical multichannel analyzer for plume emission spectroscopy, optical pyrometers for target front and back surface temperature measurements, a burnthrough detector, a microbalance for determination of mass losses, videotape and fast framing cameras and recorders, and a photomicrography system), and

8) fast (up to 100 MHz bandwidth) transient digitizers and digital oscilloscopes plus a minicomputer system for experimental control and data acquisition and processing (for sixteen channels of information with a 40 kHz/channel acquisition rate).

This excimer laser test resource is being used to observe laser effects and target responses, including plume and plasma blockage, for rp excimer laser irradiations of baseline and hardened materials over a range of incident wavelengths, pulse waveforms, and irradiance levels.

For further information, contact Dr. Michael Berry at (713) 363-7970.

LASER APPLICATIONS RESEARCH CENTER

4802 Research Forest Drive
The Woodlands. Texas 77381
713/363-7920
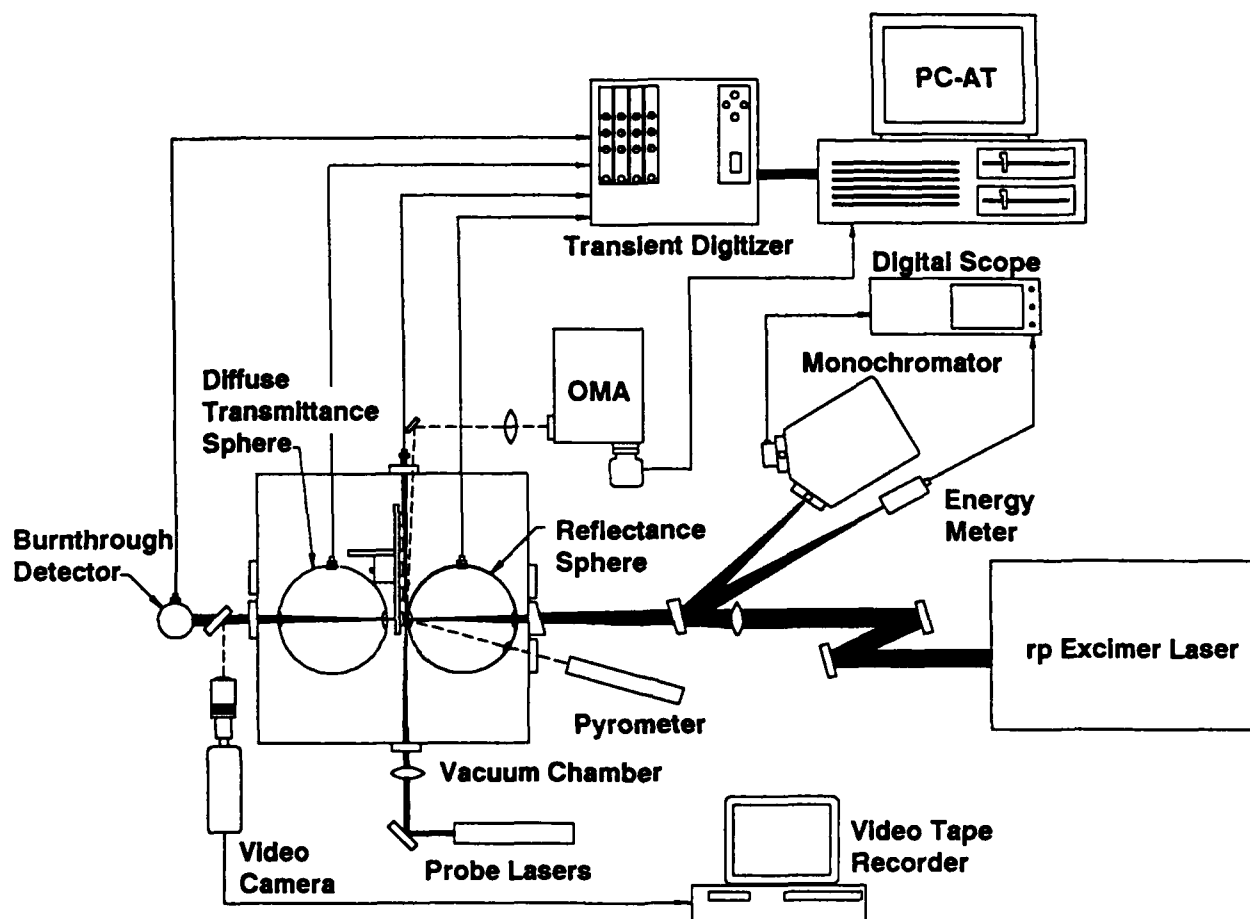
Figure 1.   Laser/materials interaction apparatus.   A rp excimer laser irradiates samples contained within the vacuum chamber at the far left of the figure. Portions of the laser beam are beamsplit by a quartz wedge and are characterized by beam diagnostic instrumentation [an ARC 0.3 m monochromator plus fast Si detector, a Gentec ED200 pyroelectric pulse energy meter, a Si detector/amplifier pulse temporal monitor (not shown), and a translating aperture beam profile measurement system (not shown)].   An optical delivery system [beam steering mirrors and/or variable reflectance optical flats plus a quartz focussing lens] provide accurately positioned beams on target with controlled and measured fluence distributions. Realtime target and plume properties and responses are monitored with time-resolved target and plume diagnostics instrumentation [an optical pyrometer for front surface temperature measurements, a burnthrough detector, integrating spheres with filters and fast response Si detectors for reflectance and transmittance measurements, a CKC 200 CCD video camera system, a HeNe probe laser for plume particle measurements, and an optical multichannel analyzer (OMA) system (Instruments SA Model HR-320 monochromator plus Princeton Instruments Model P/IRY-700 OMA) for target and plume emission measurements].   Signals from both the laser beam and the target and plume diagnostics are digitized, recorded, and processed using transient digitizers, a digital oscilloscope, and a minicomputer system.

APPENDIX B

Appended are target front surface temperature/spectral emittance data in the format of Figure 14 for the following materials, irradiances, and run #s:

Material	25 kW/cm²	60 kW/cm²	100 kW/cm²	150 kW/cm²
G	153-11	153-2	156-22	153-18, 156-2
C101		157-21	156-15	157-10
C102		157-4	156-16	156-12, 157-11
C104		157-5	156-17	157-13
C105		143-9	156-24	157-14
C106		157-6	145-7	157-15
C107	144-16	143-14	156-20	142-15
C108		143-15	156-19	142-14

GraphNOL (153-11) 25kW/cm²
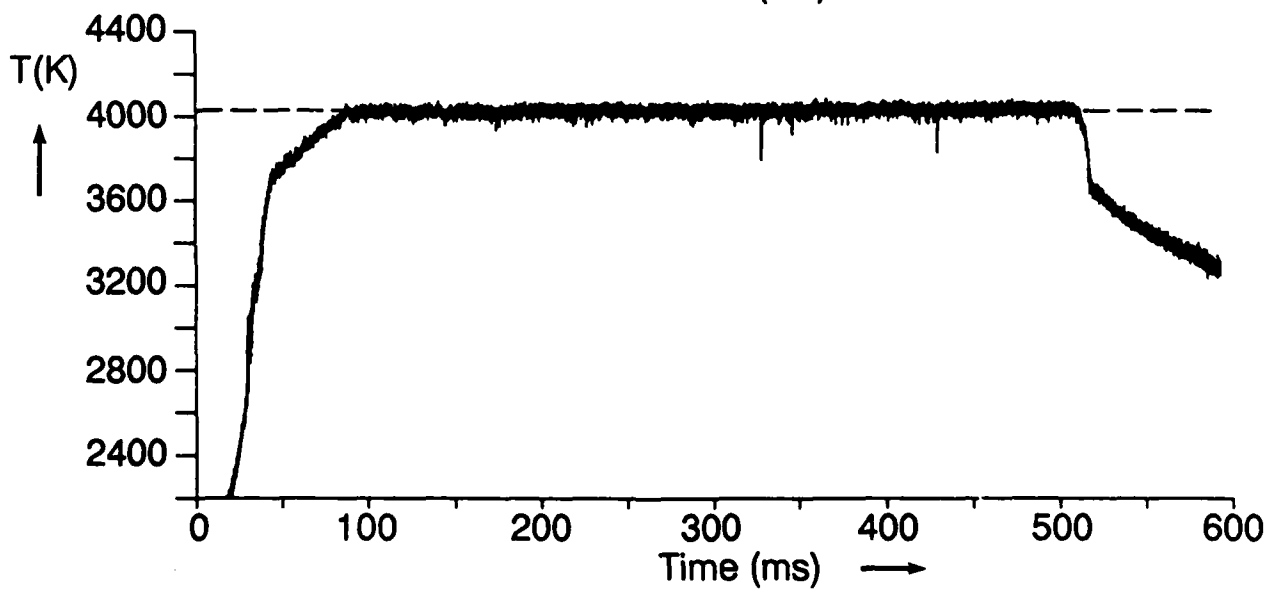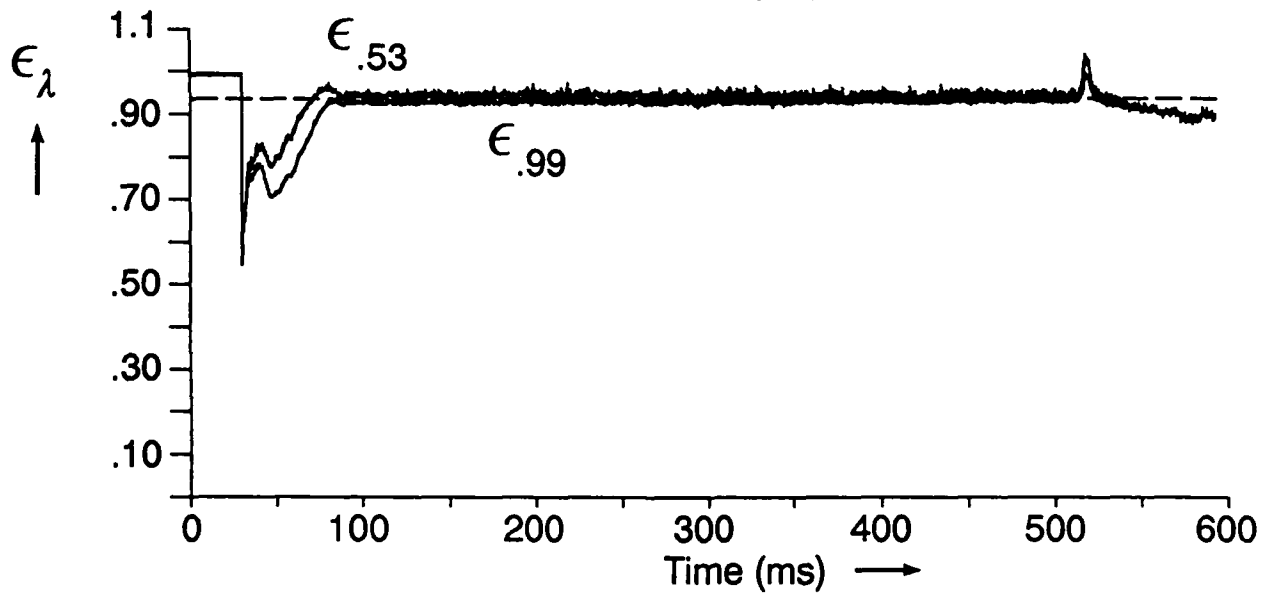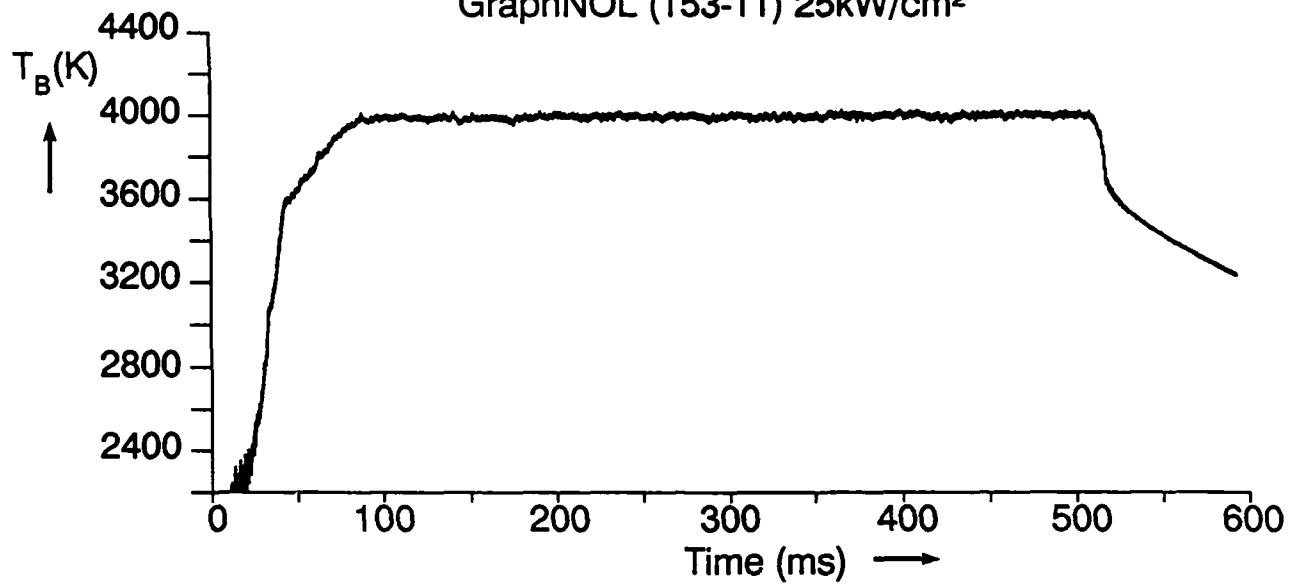
GraphNOL (153-02) 60kW/cm²
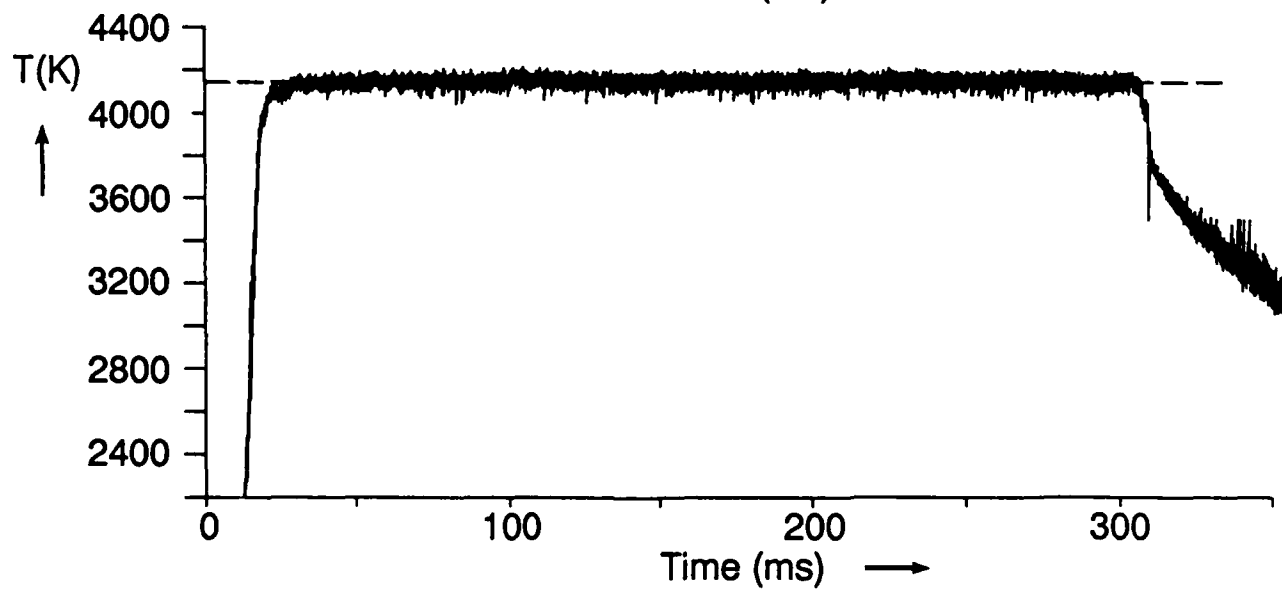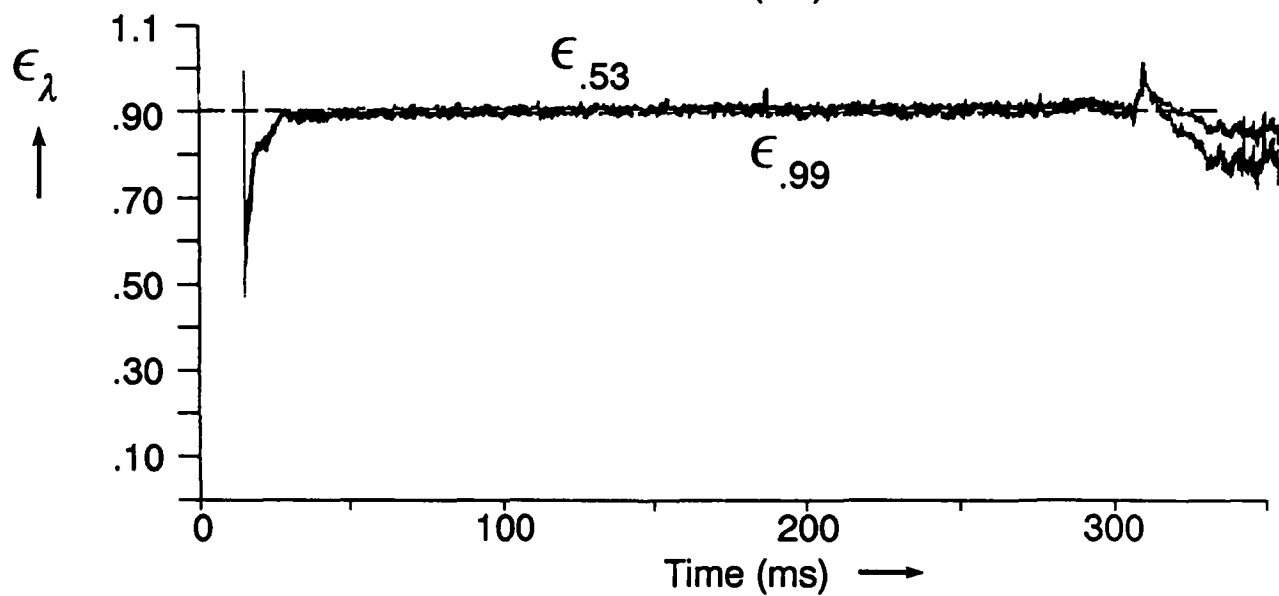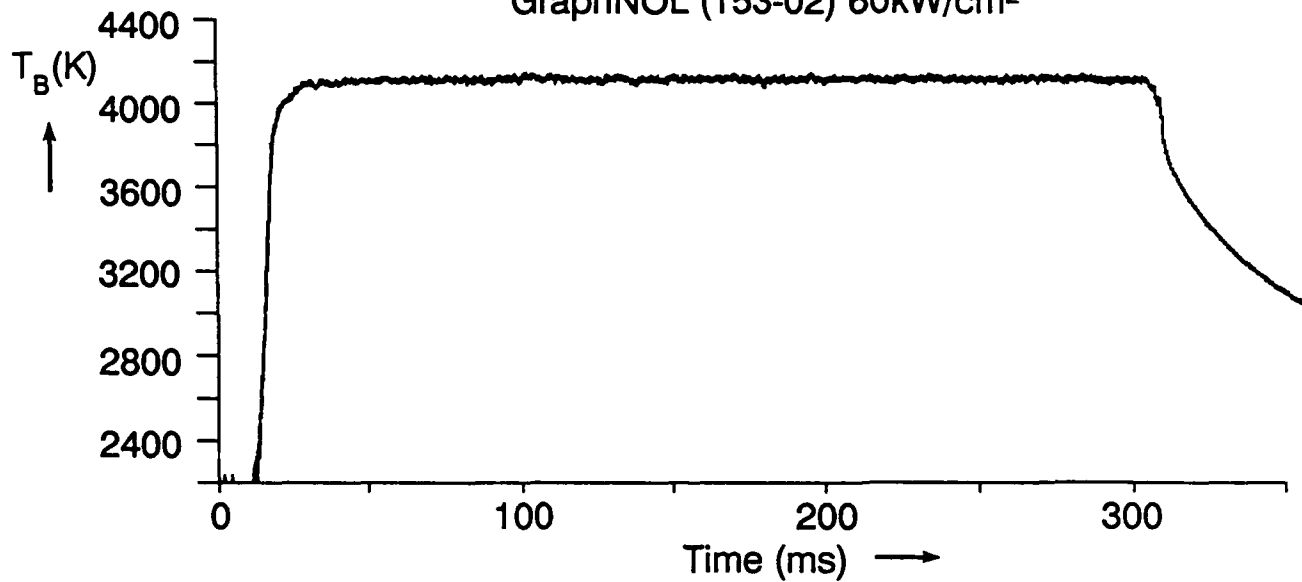
GraphNOL (156-22) 100kW/cm²
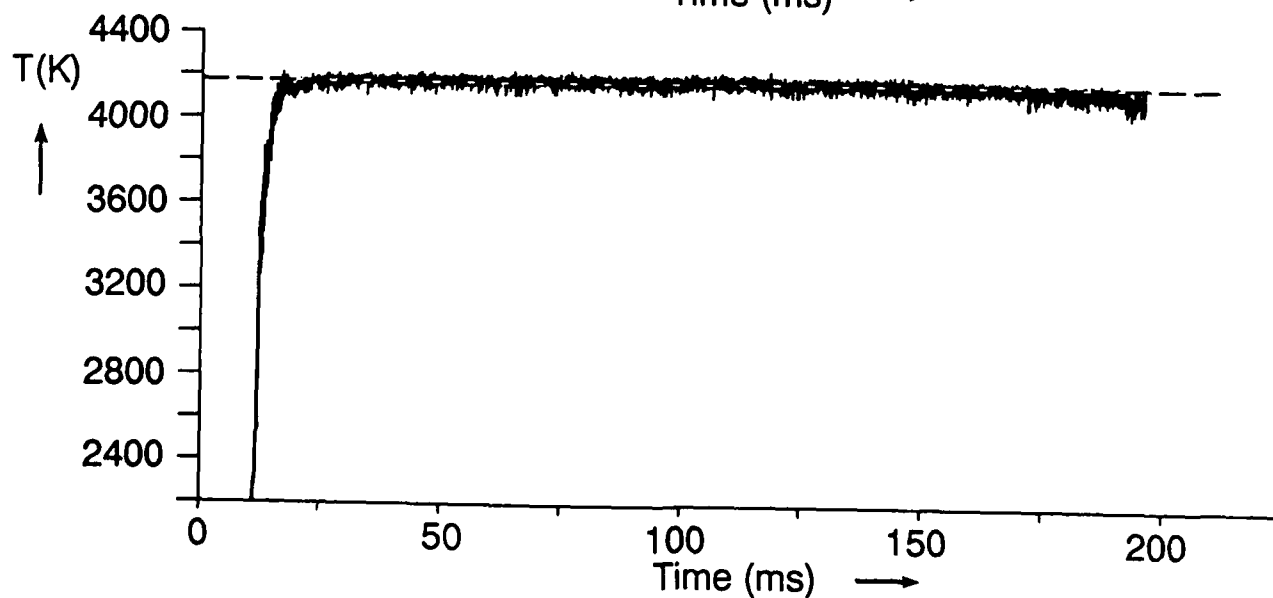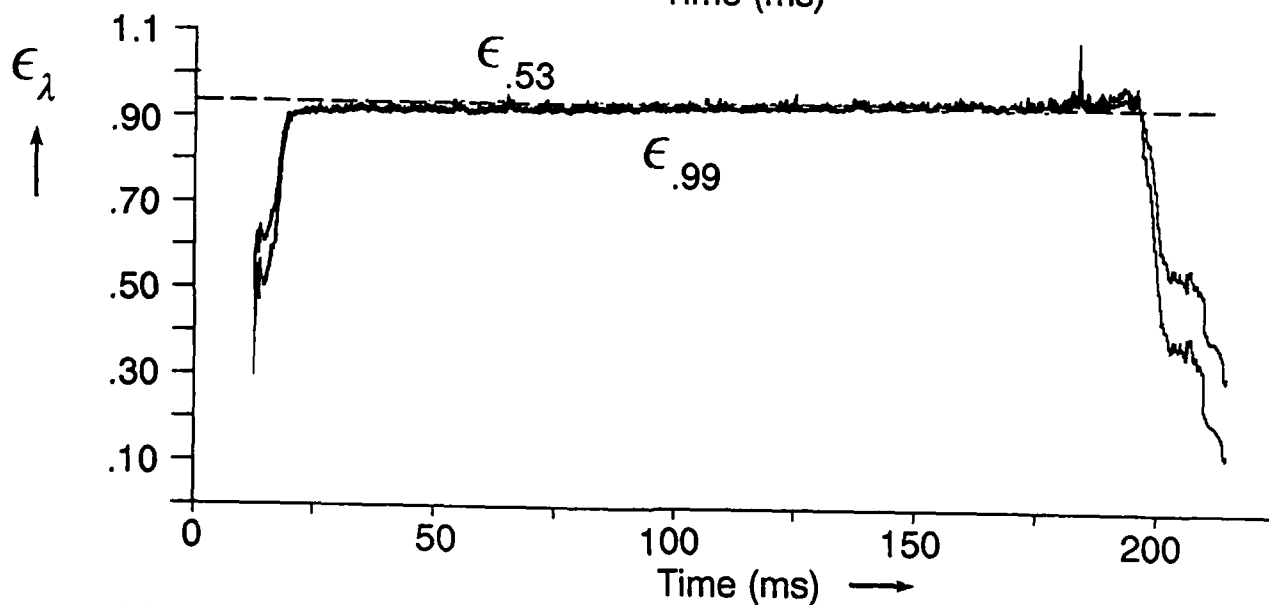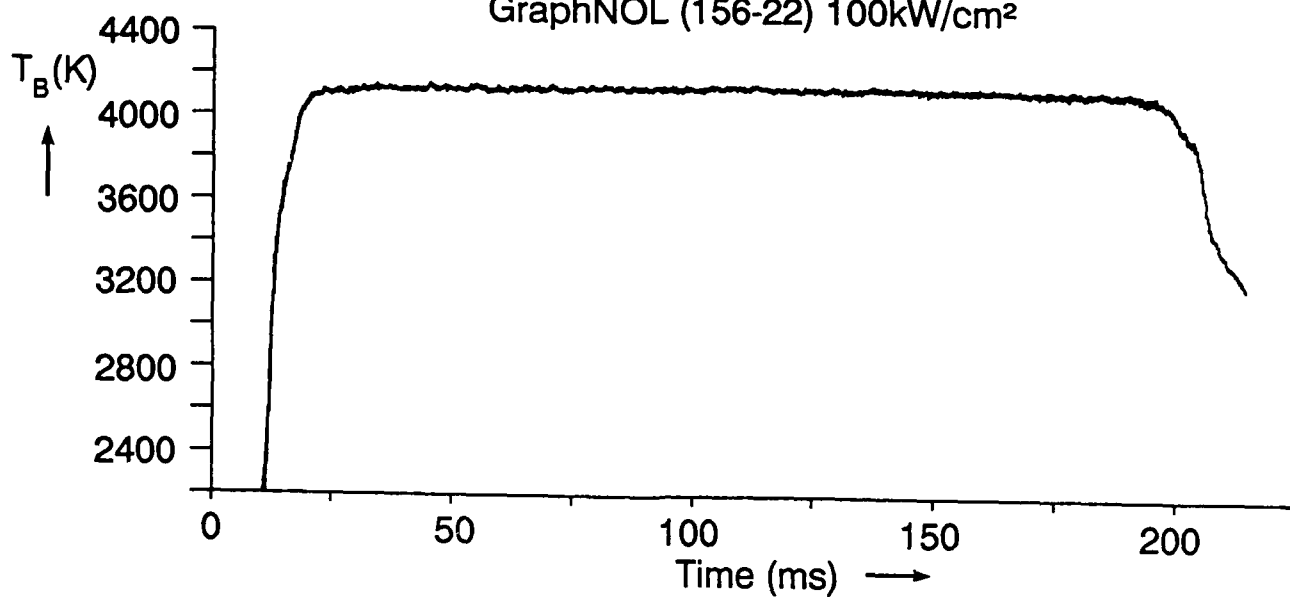
GraphNOL (153-18) 150kW/cm²
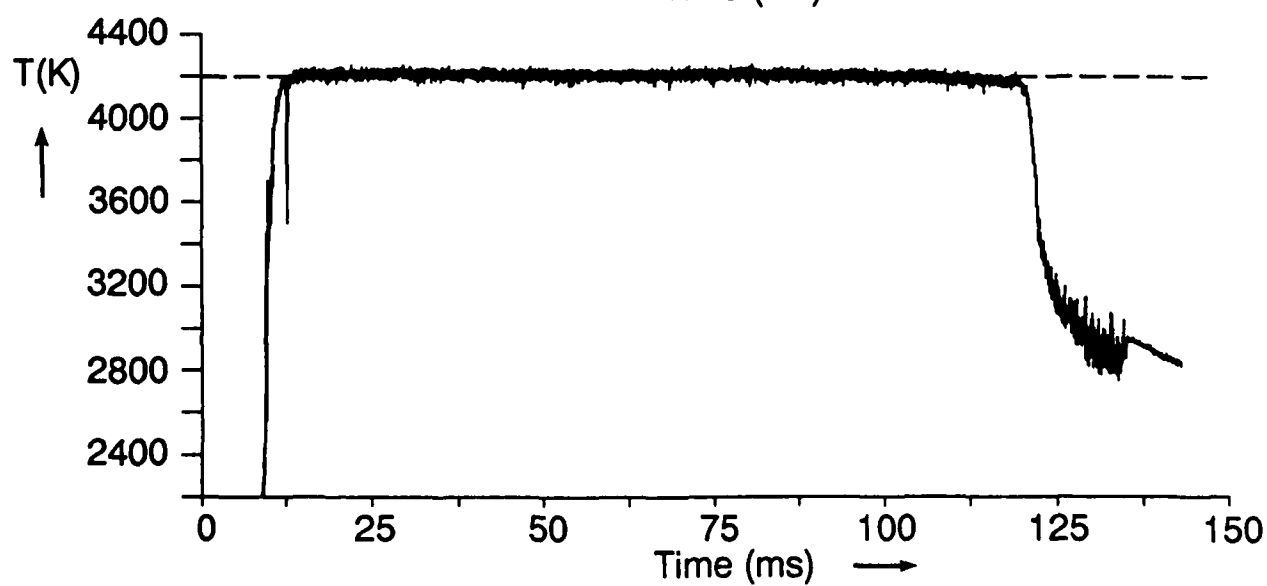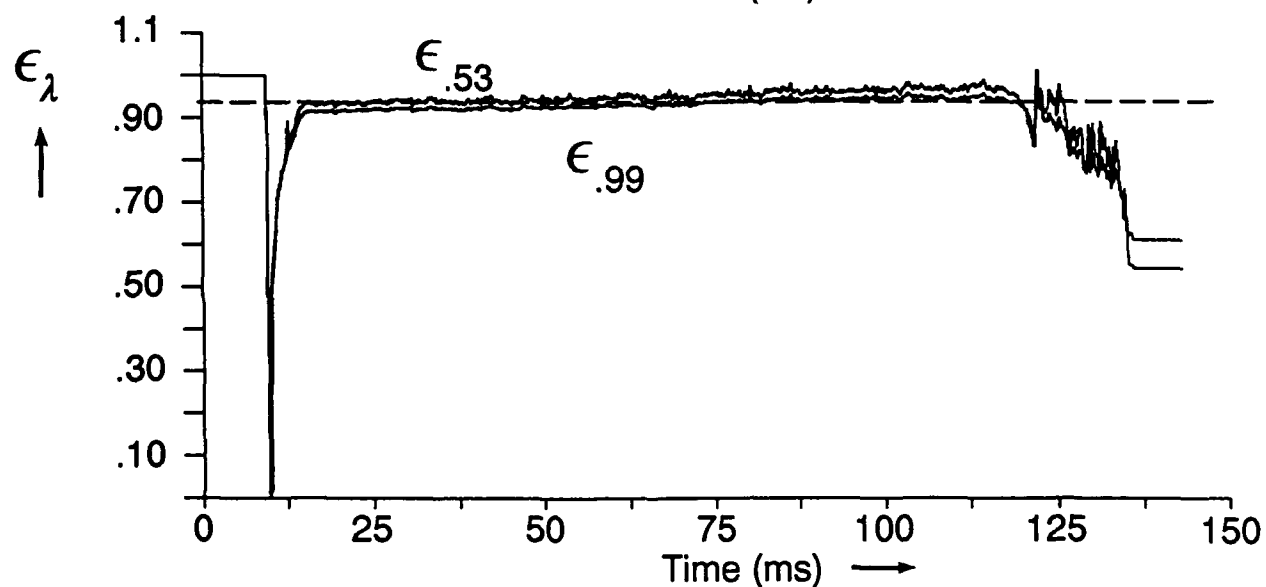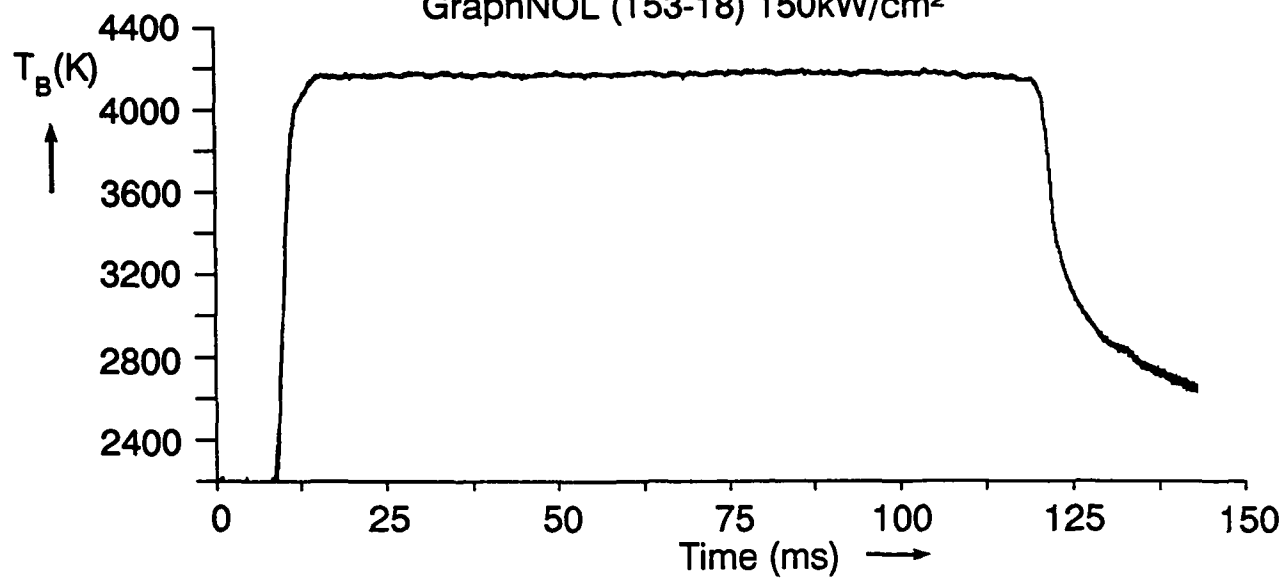
GraphNOL (156-02) 150kW/cm²
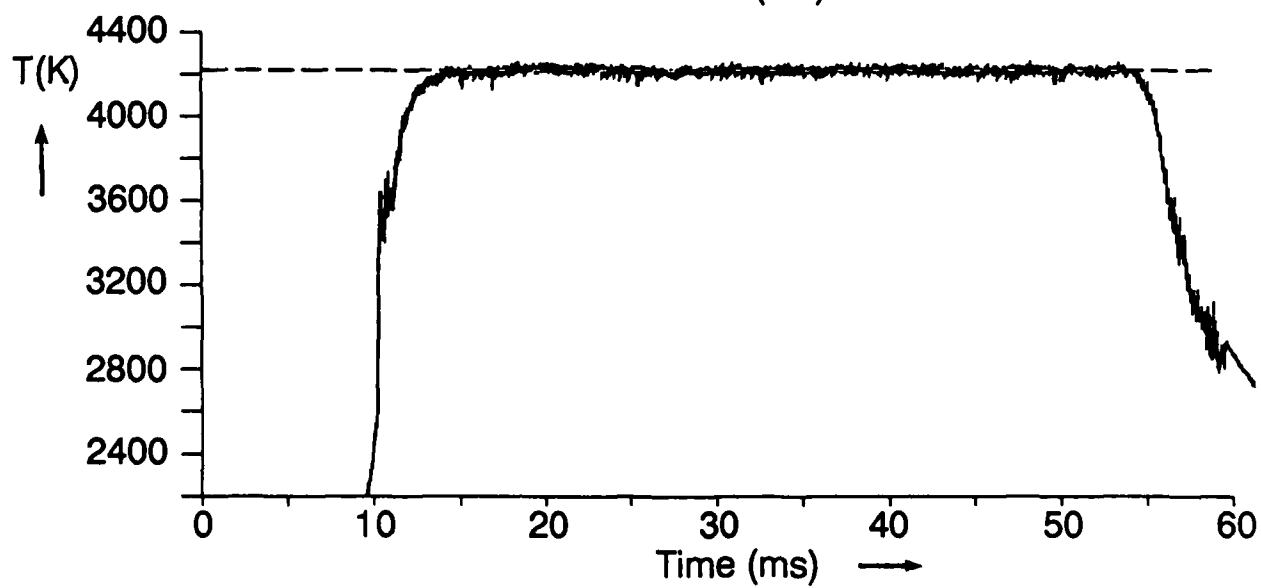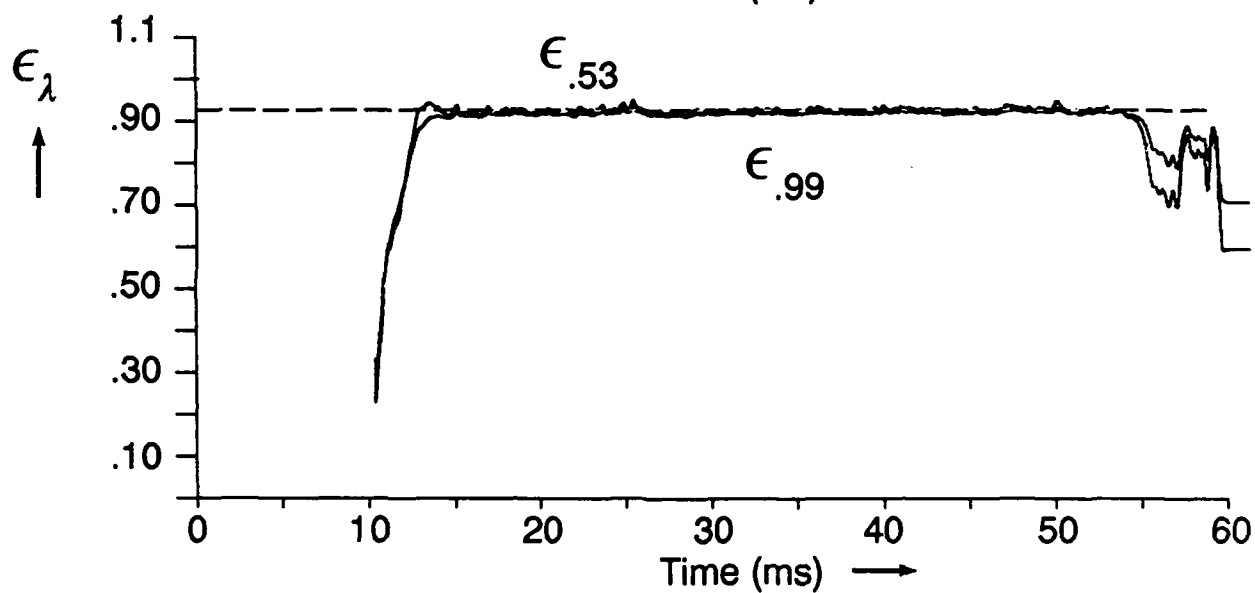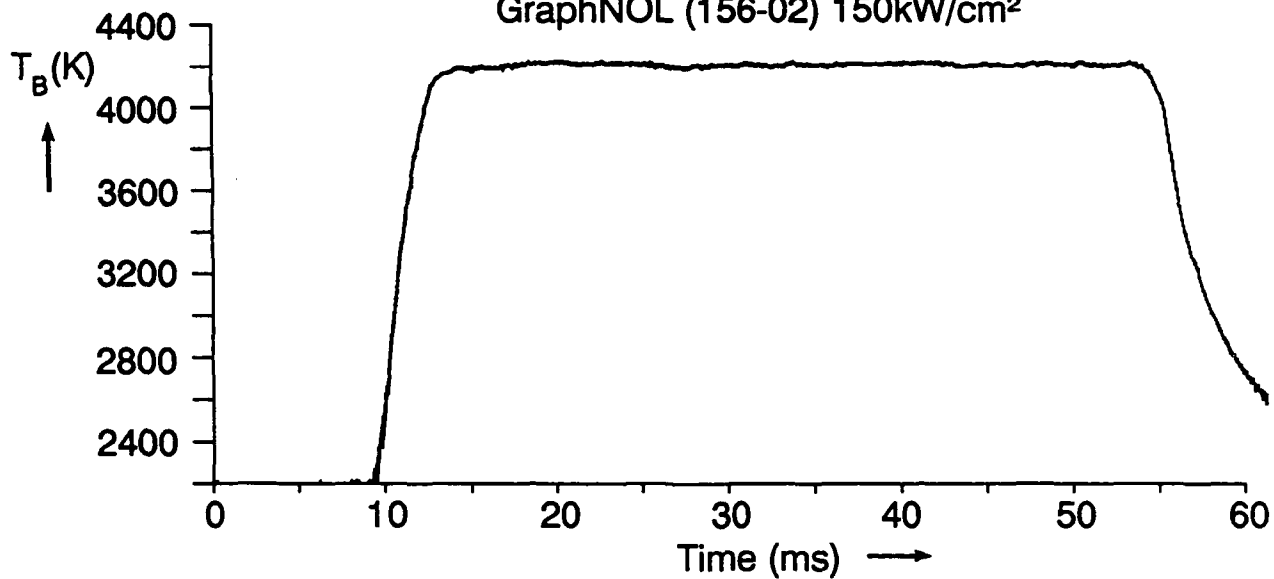
C101-10 (157-21) 60kW/cm²
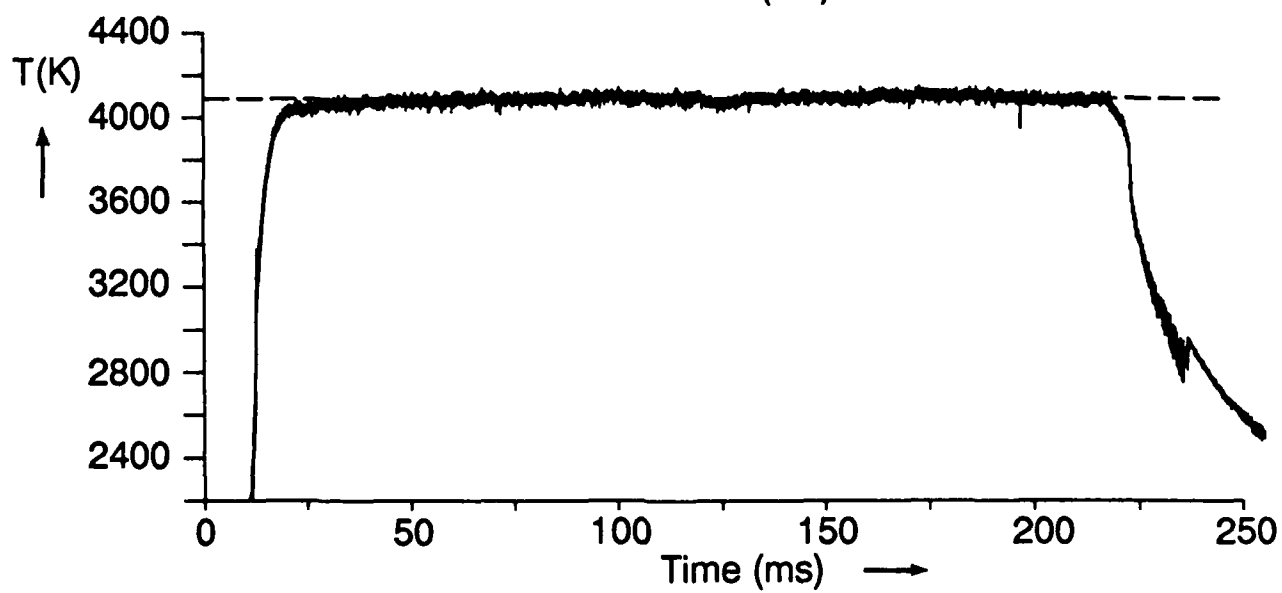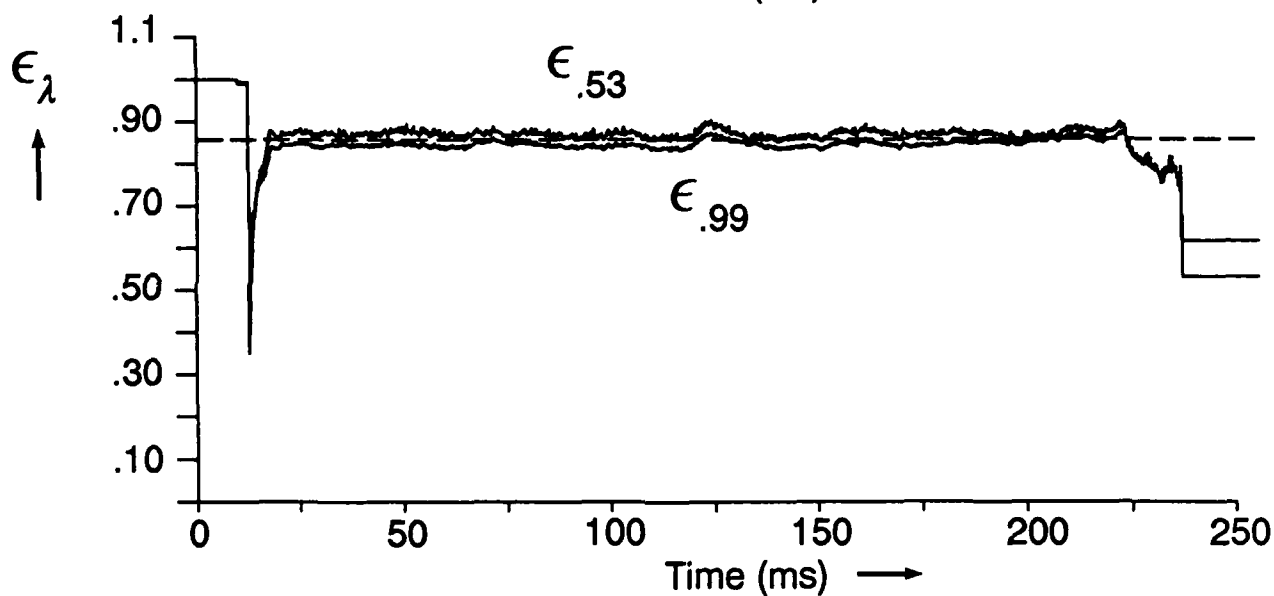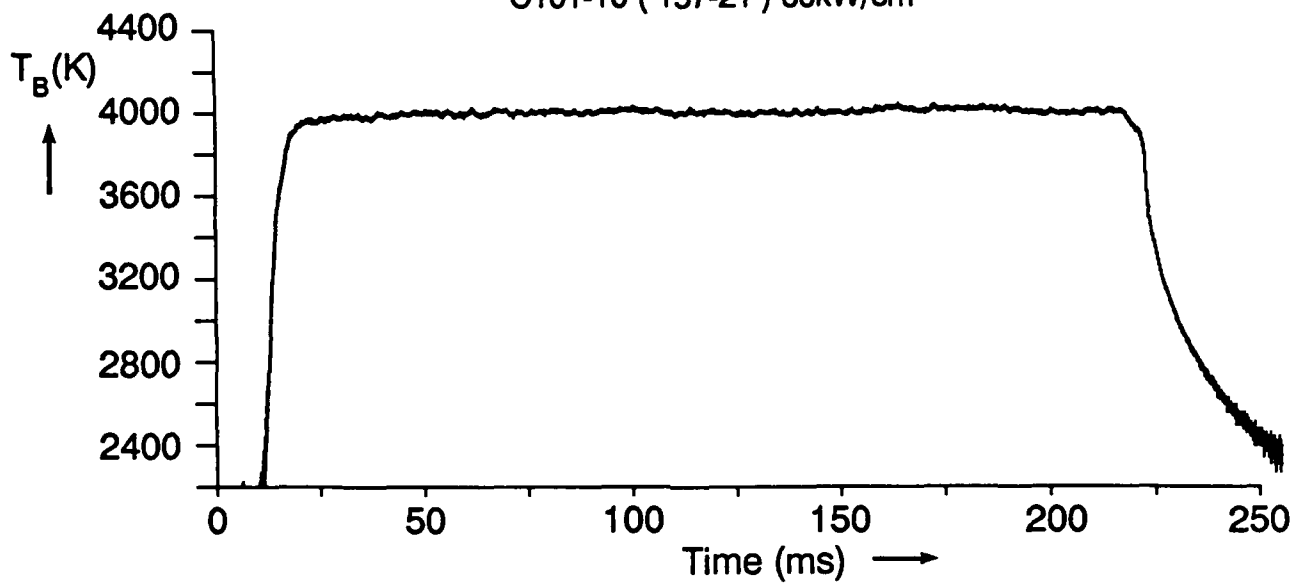
C101-18 (156-15) 100kW/cm²
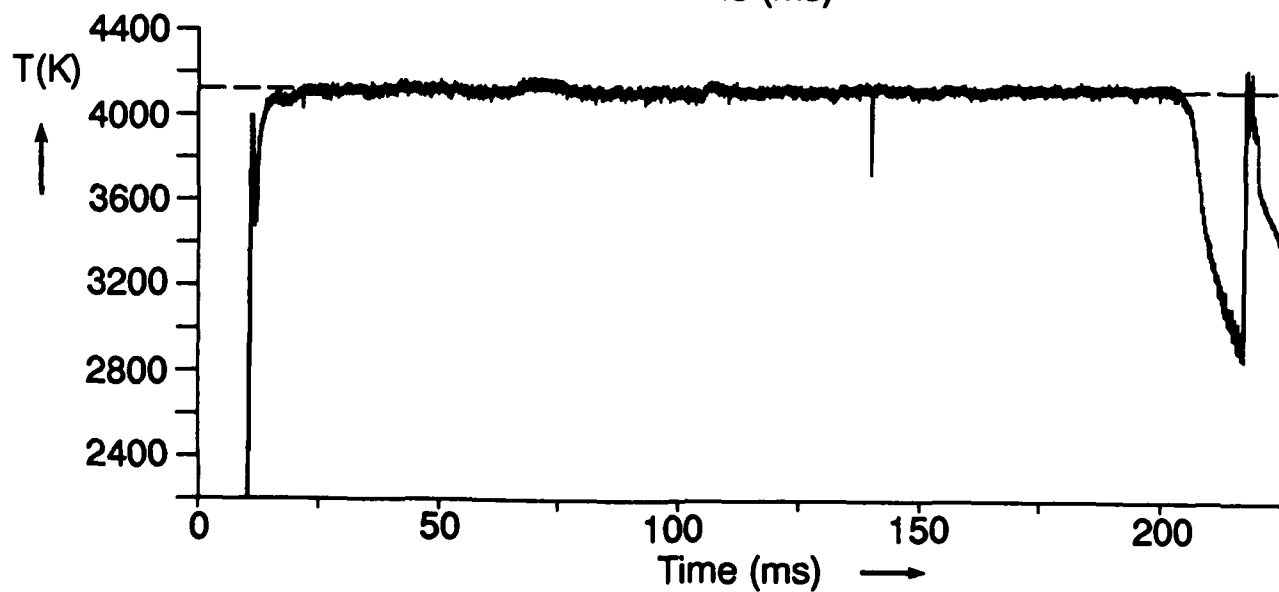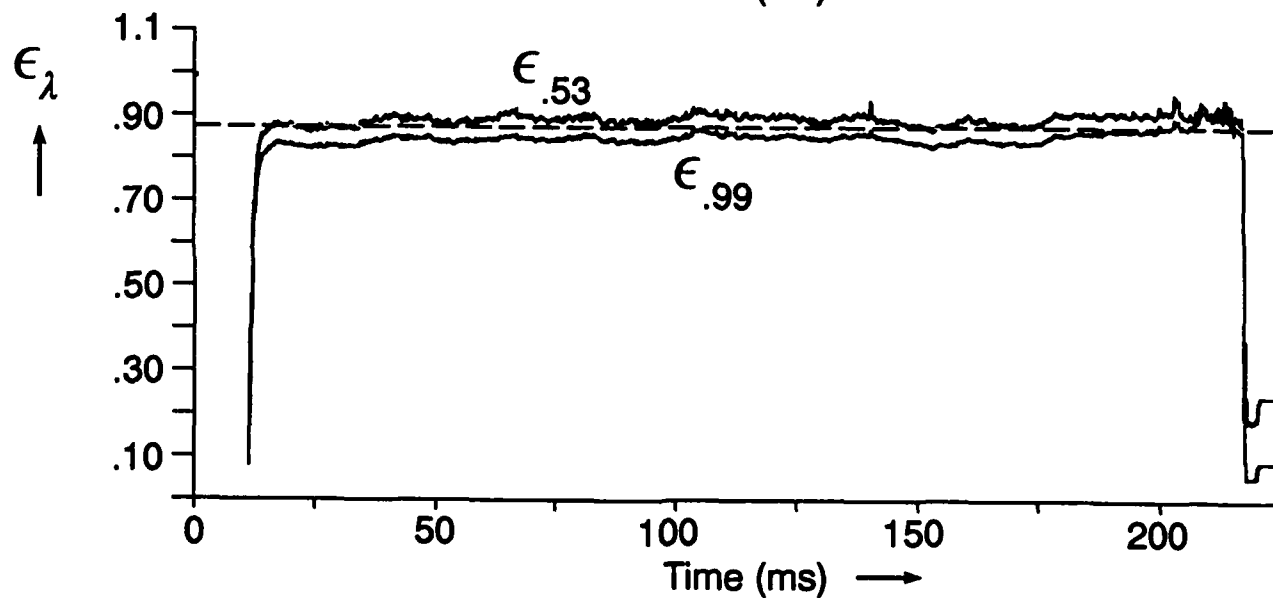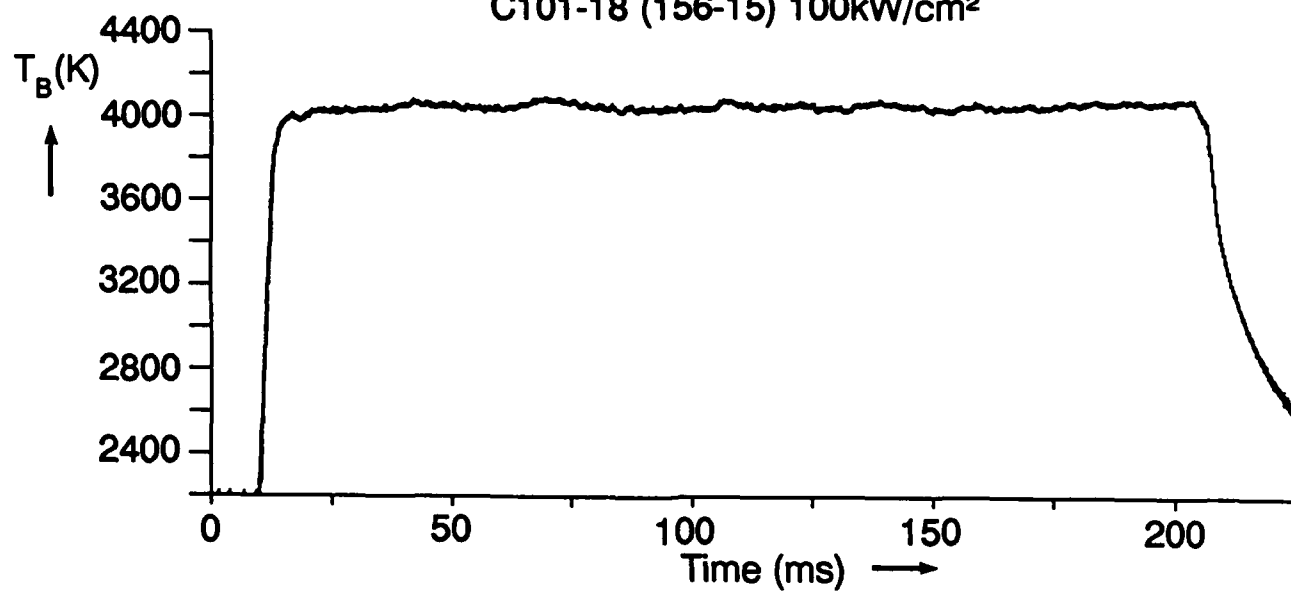
C101-22 (157-10) 150kW/cm²
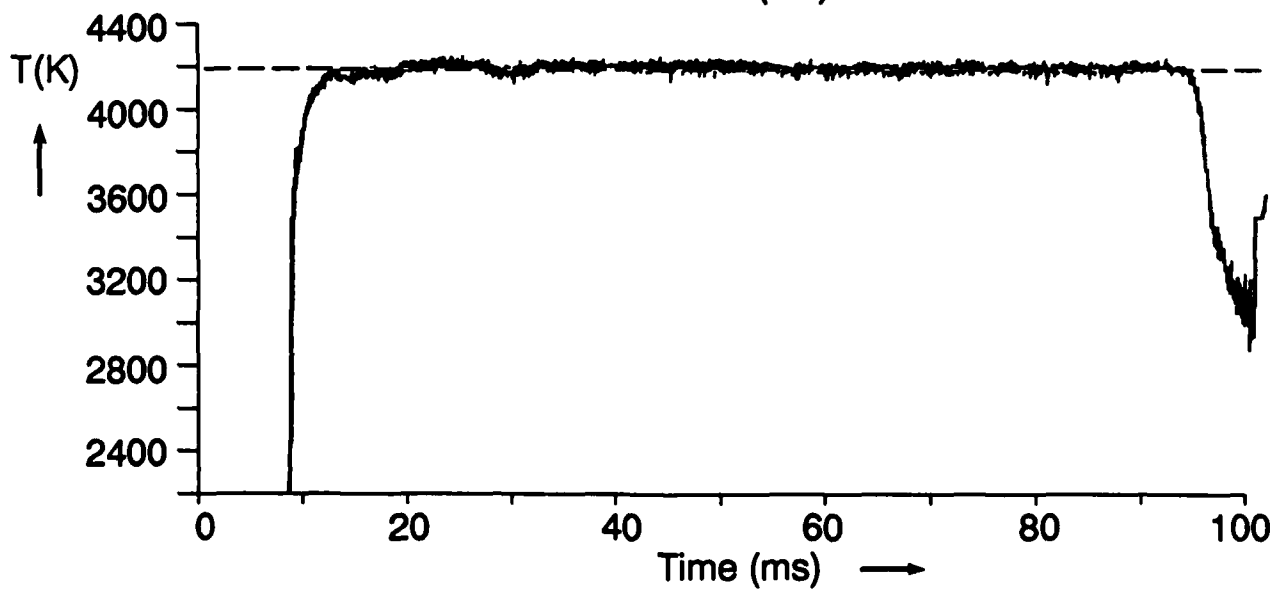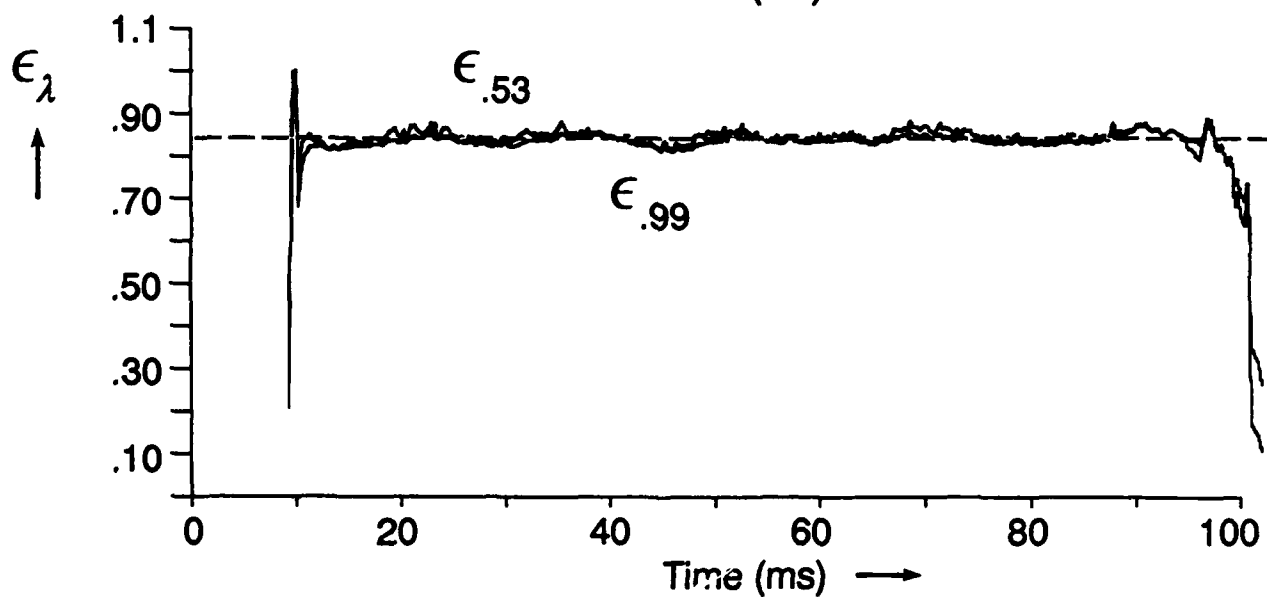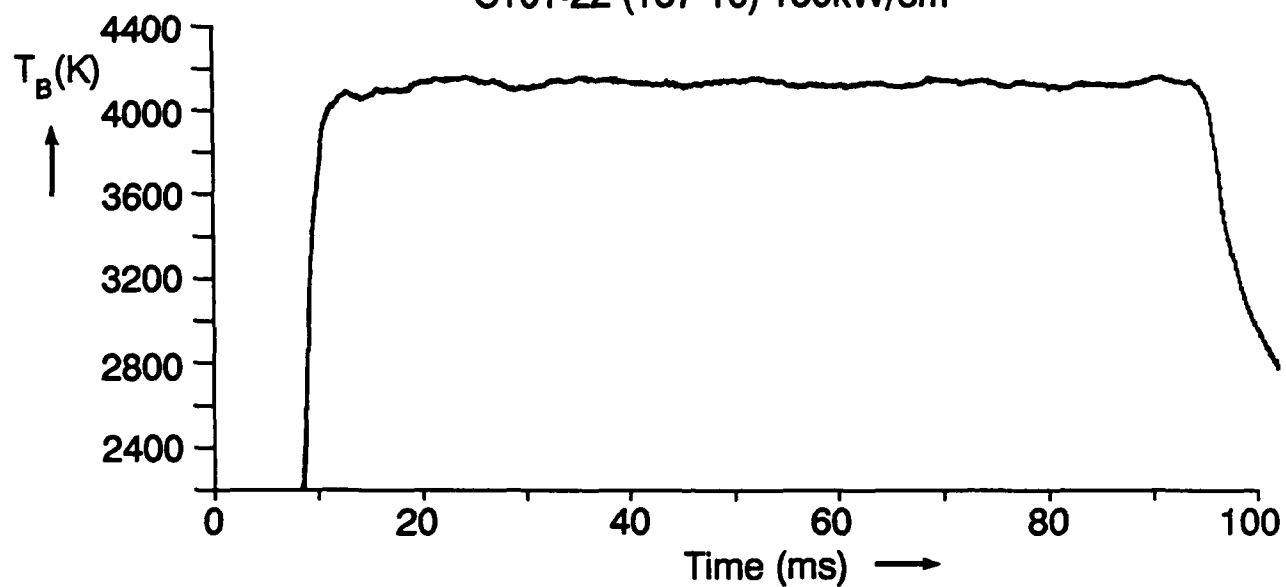
C102-10 (157-04) 60kW/cm²
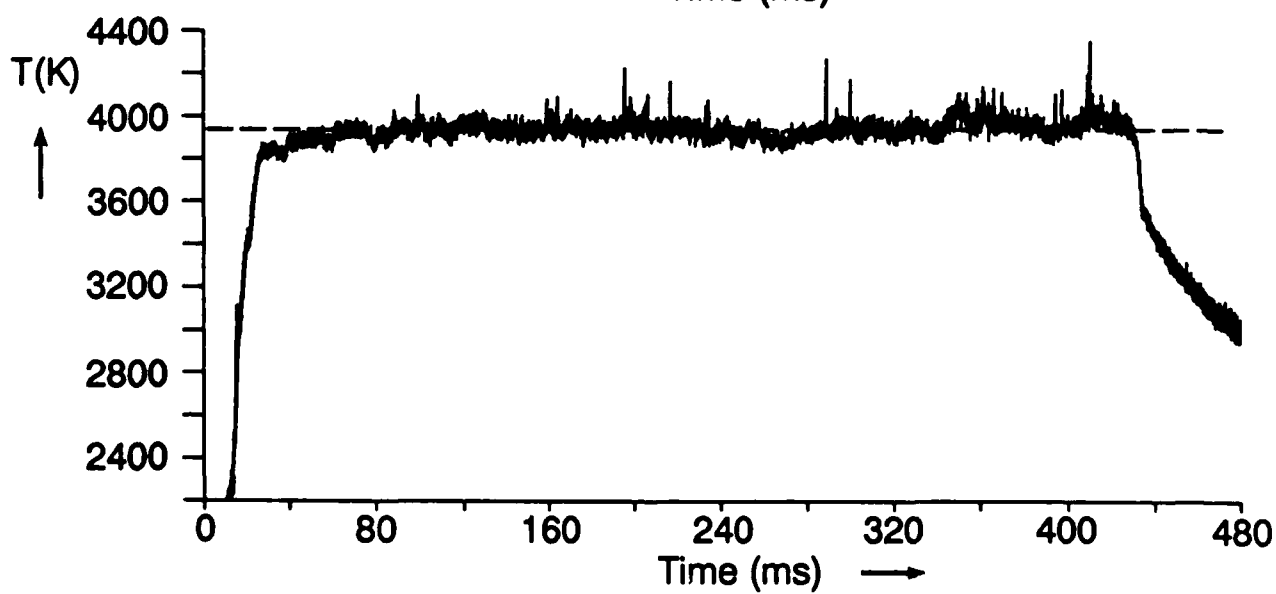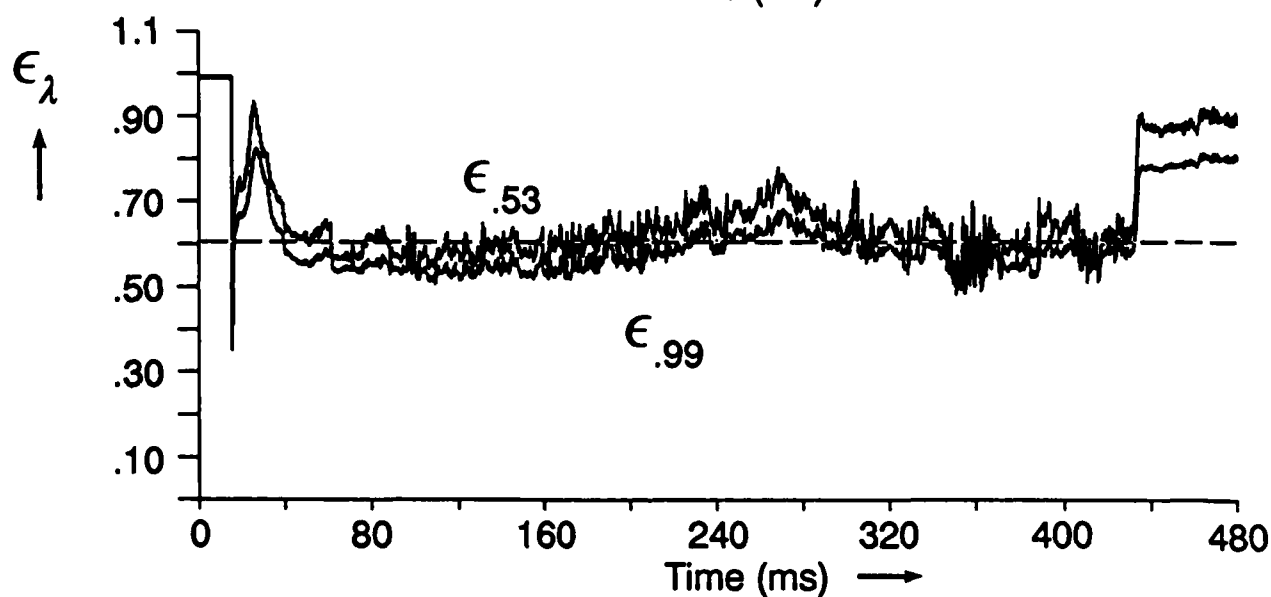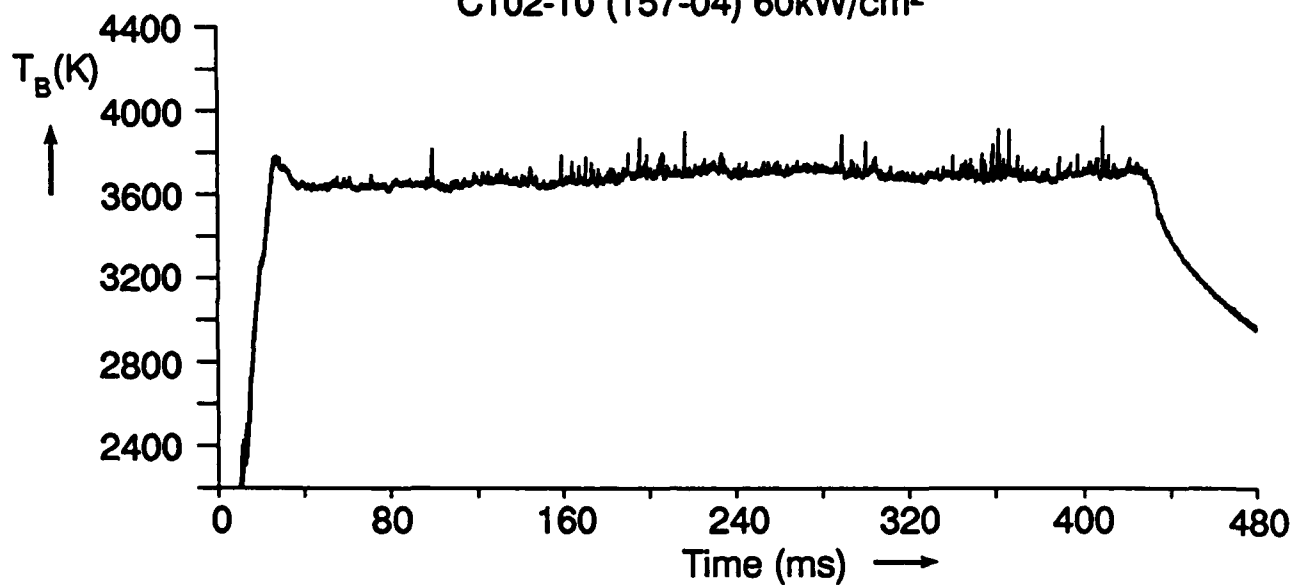
C102-17(156-16) 100kW/cm²
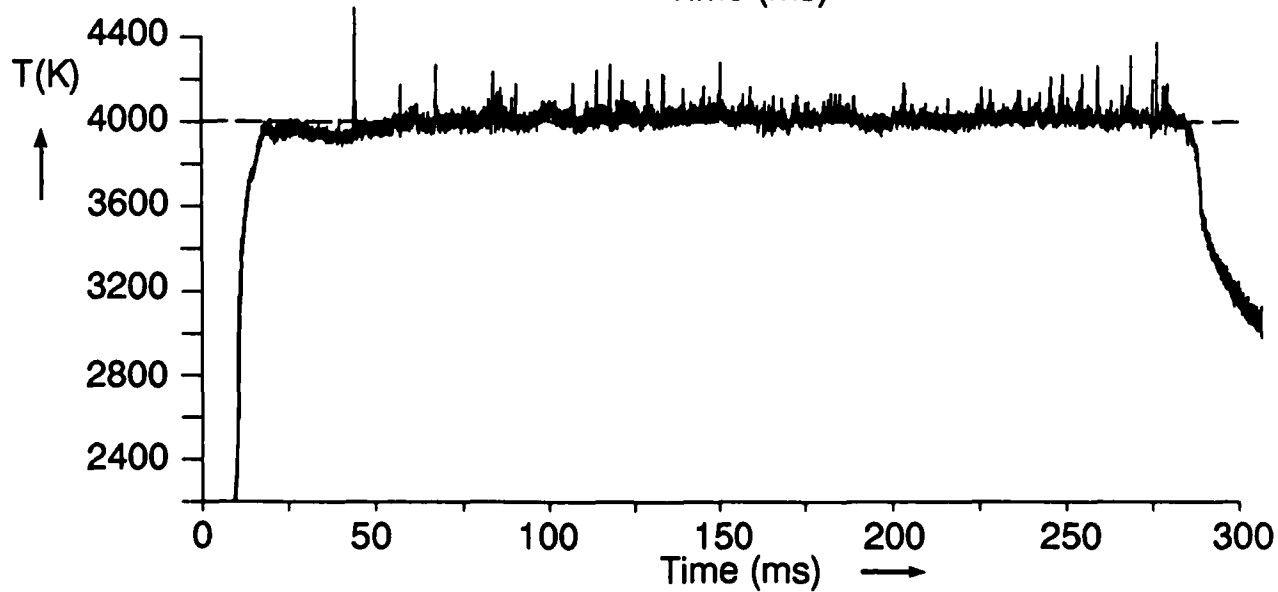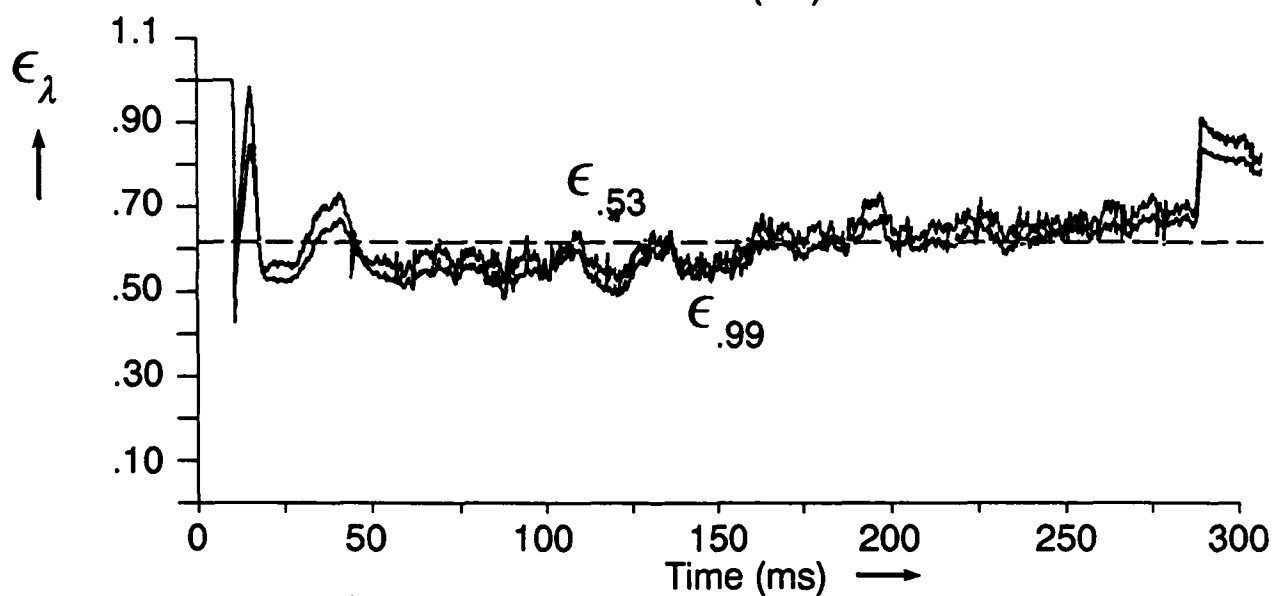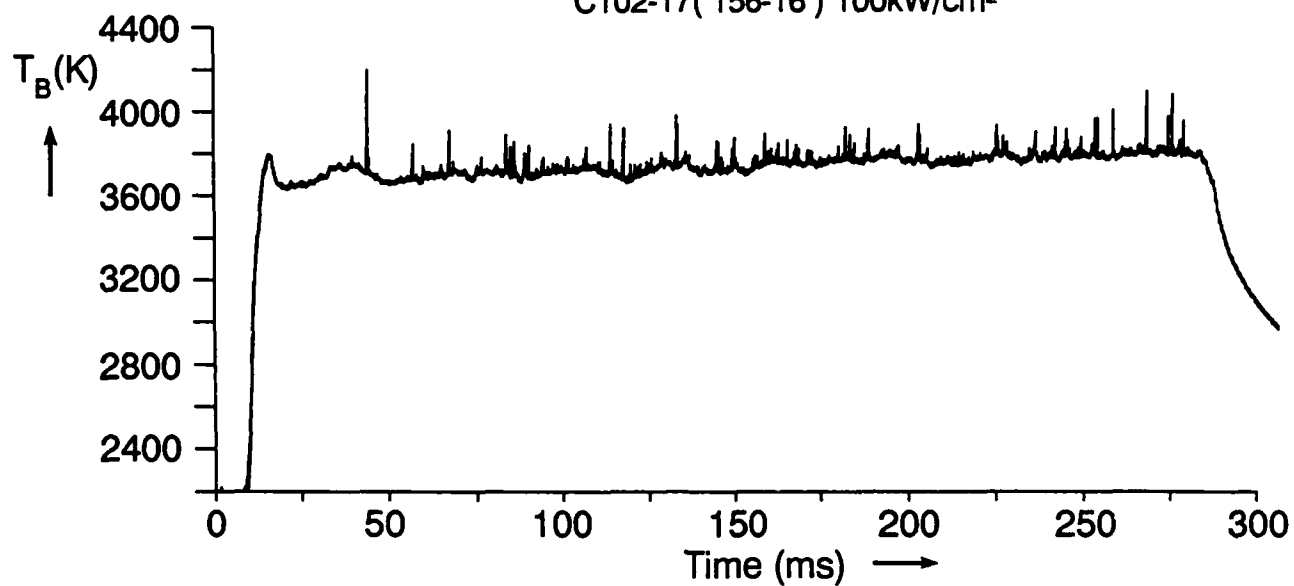
C102-22 (156-12) 150kW/cm²
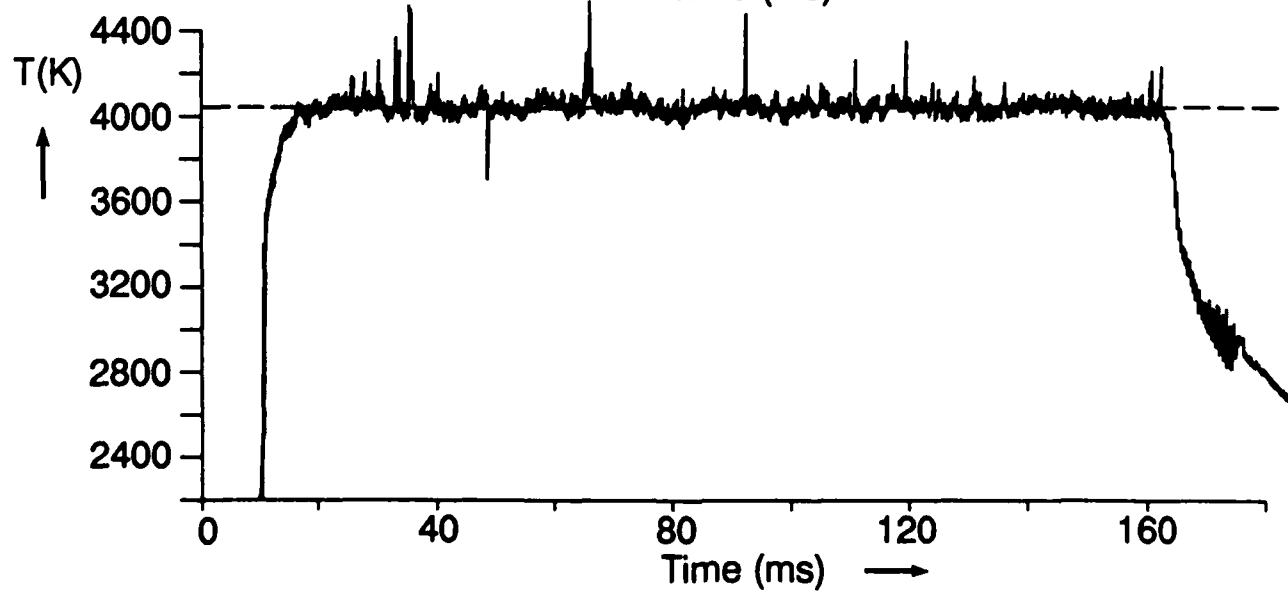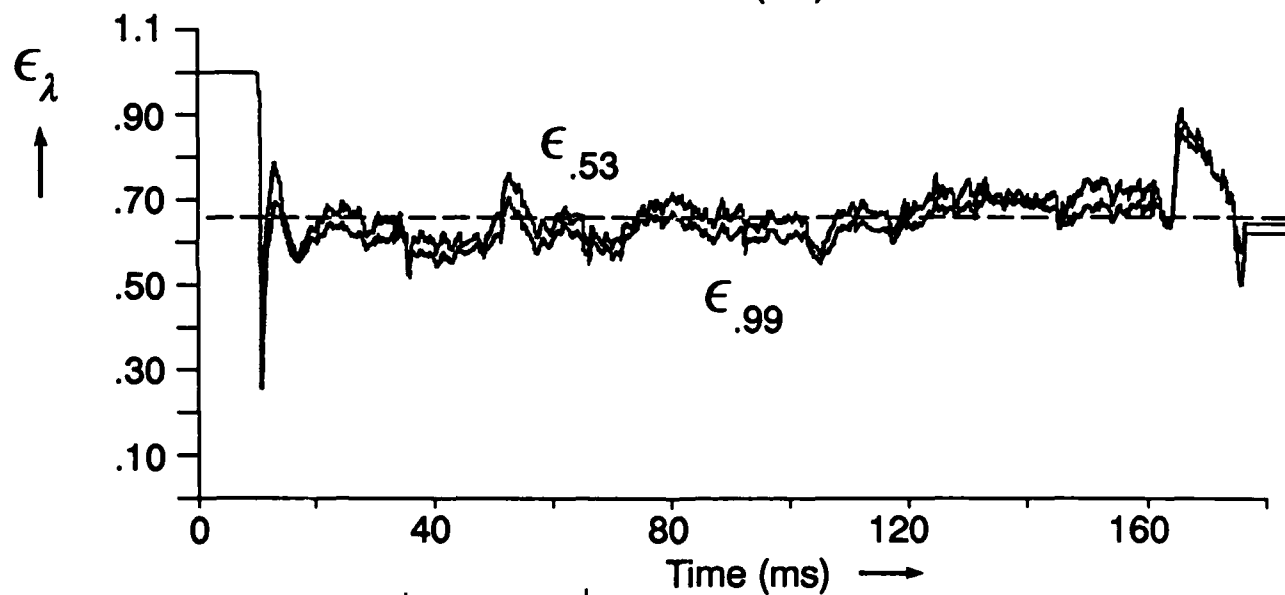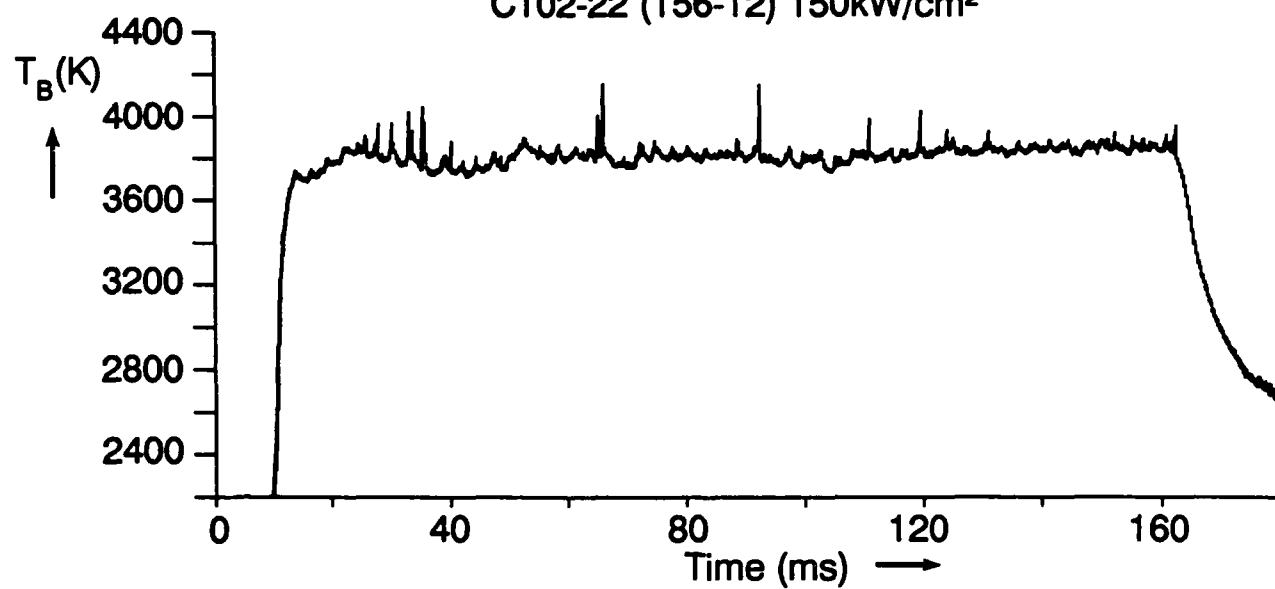
C102-23 (157-11) 150kW/cm²
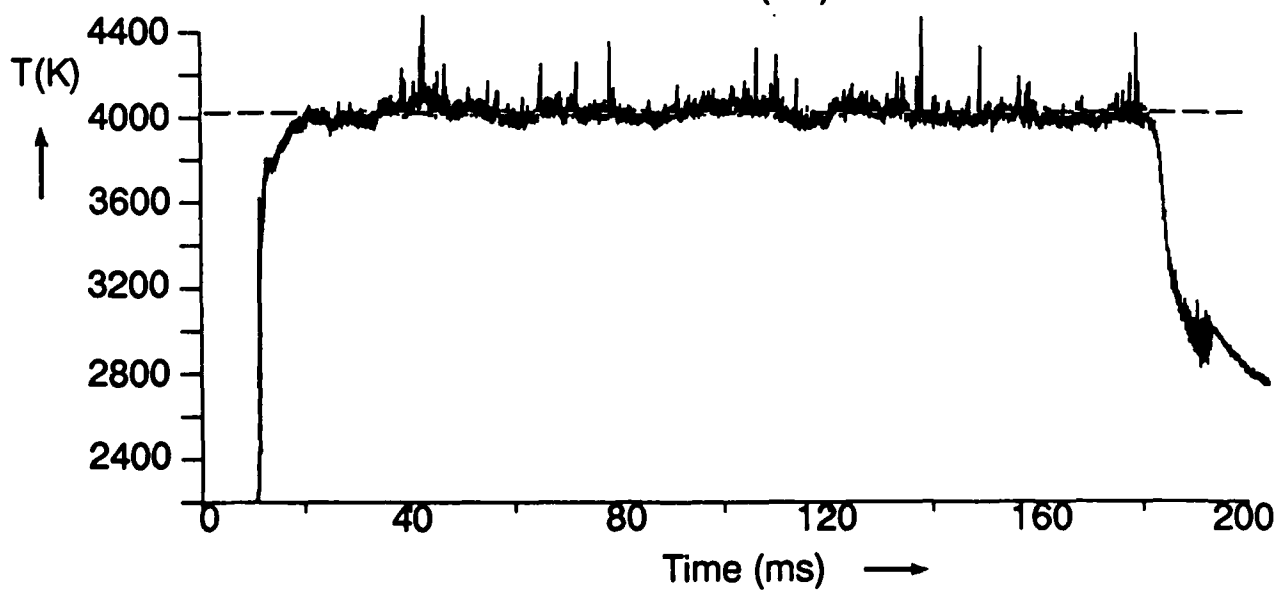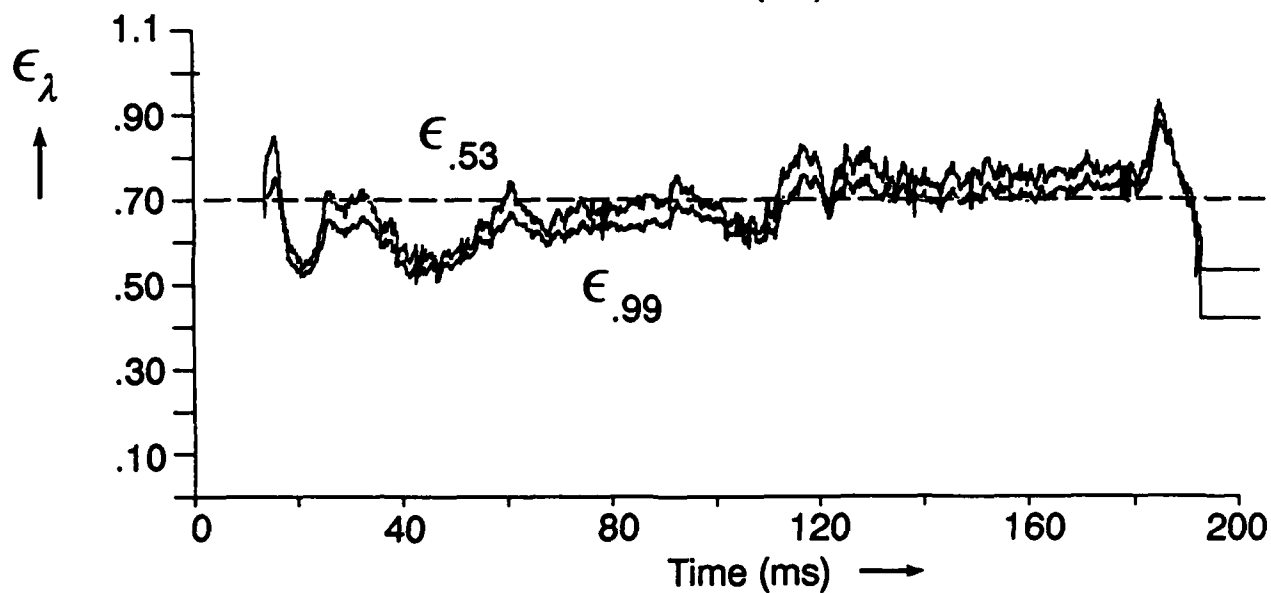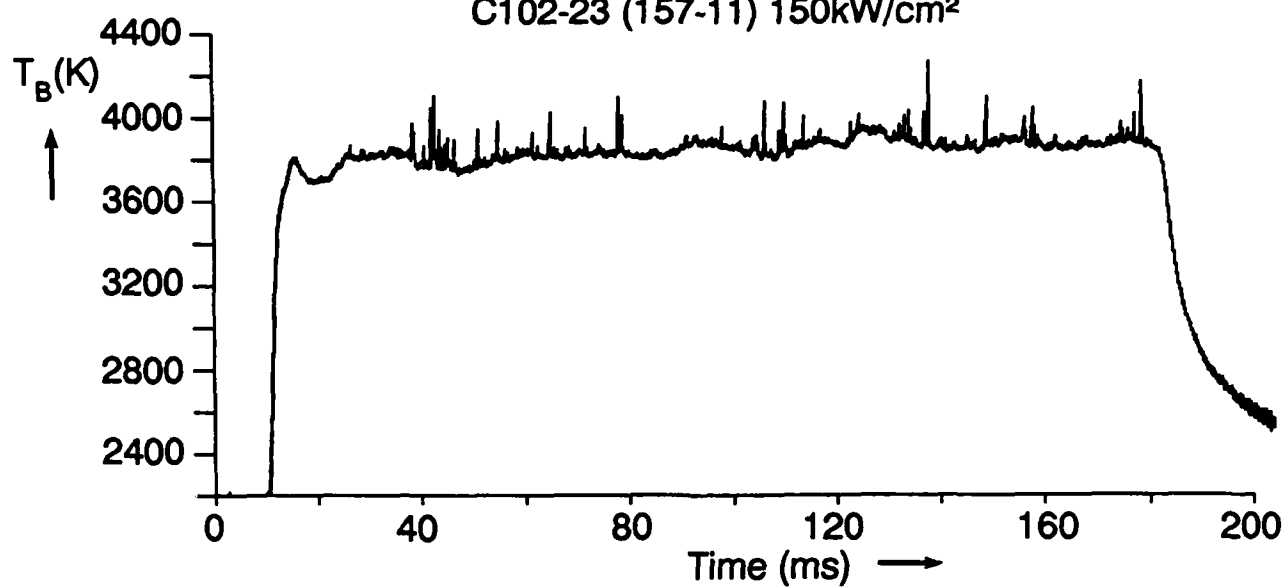
C104-10 (157-05) 60kW/cm²
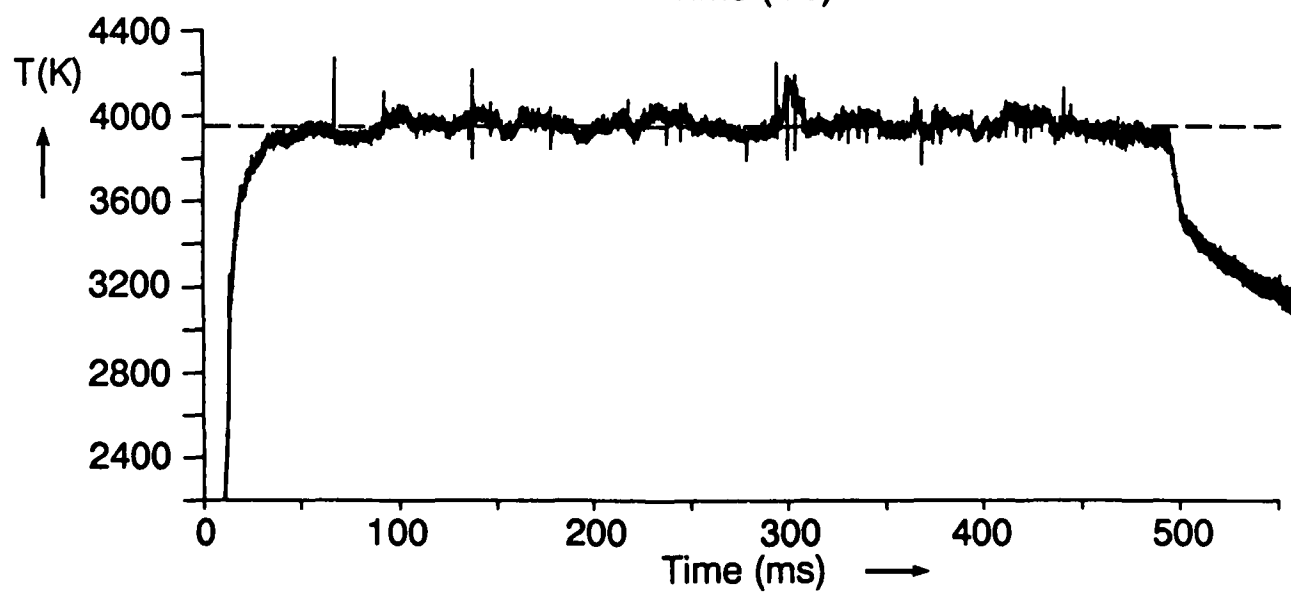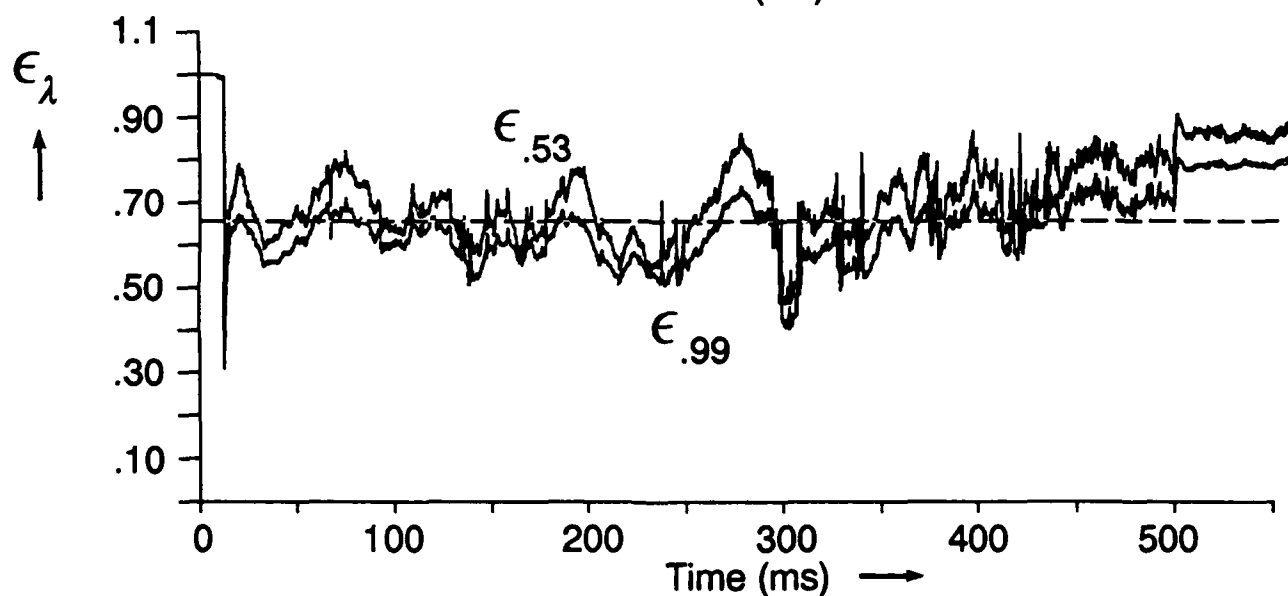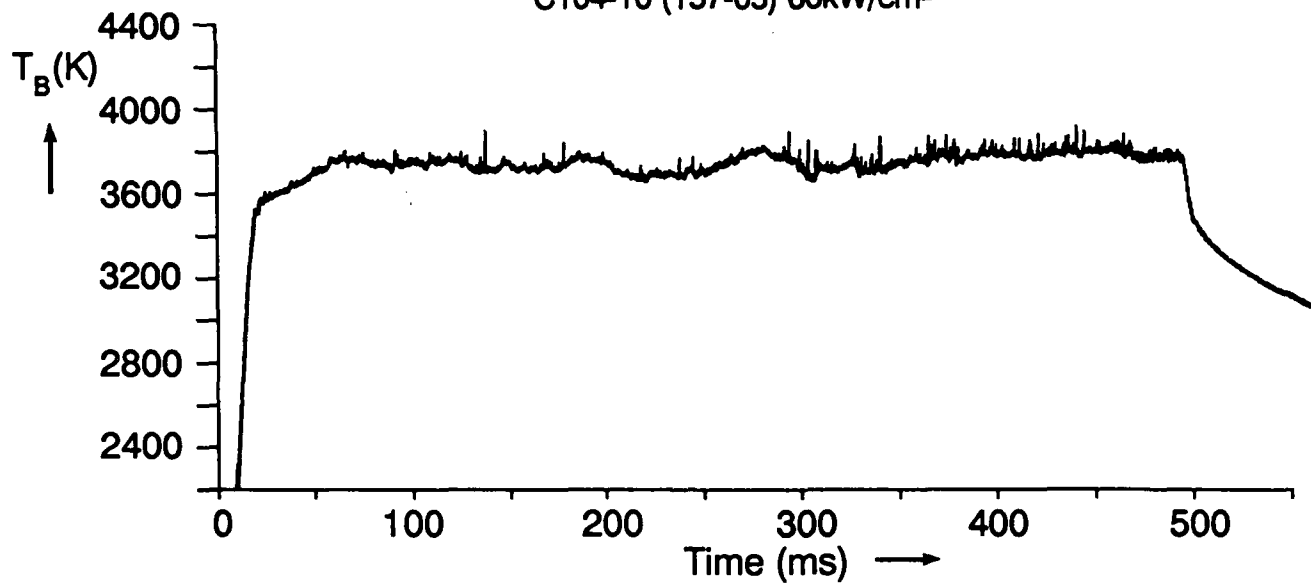
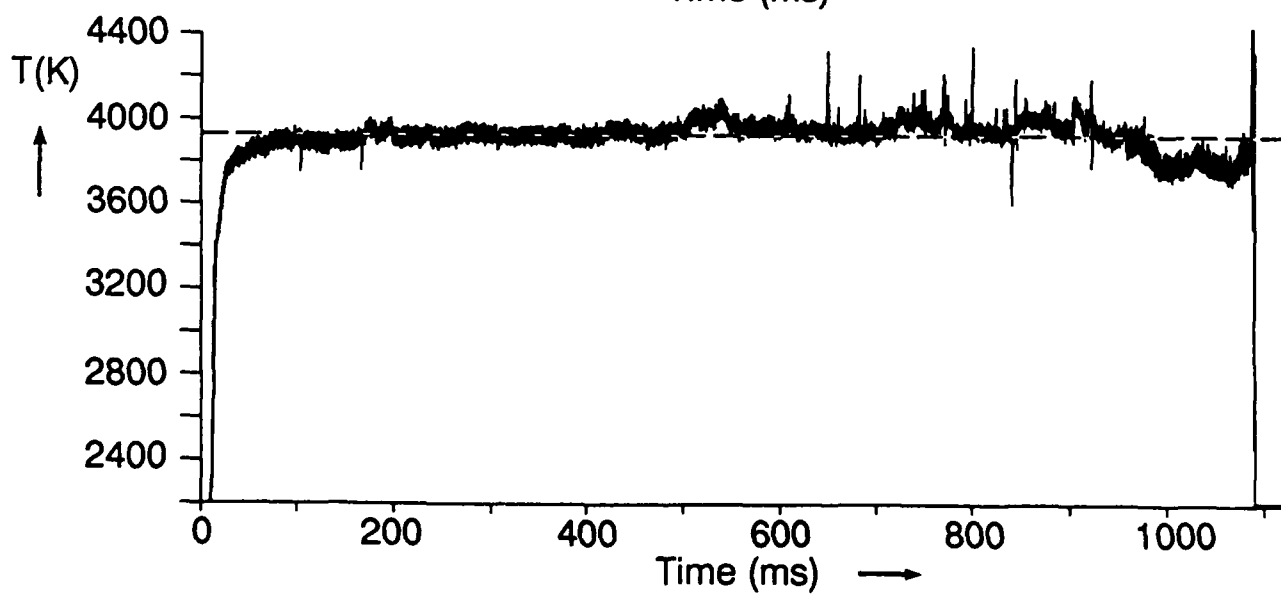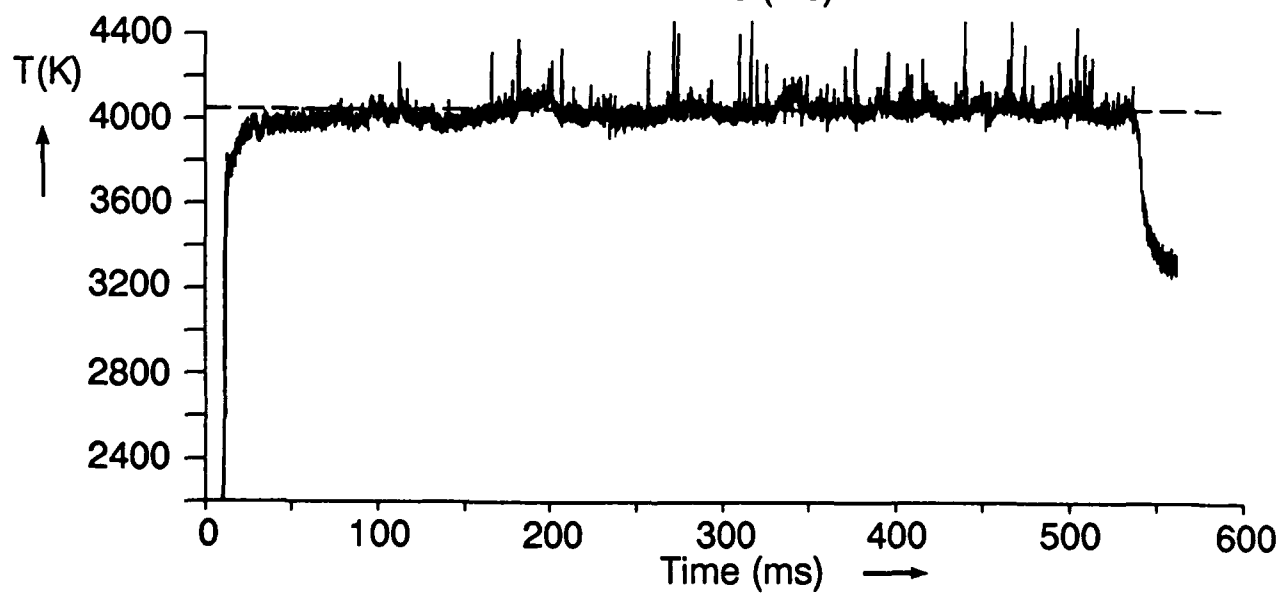C104-18 (156-17) 100kW/cm²
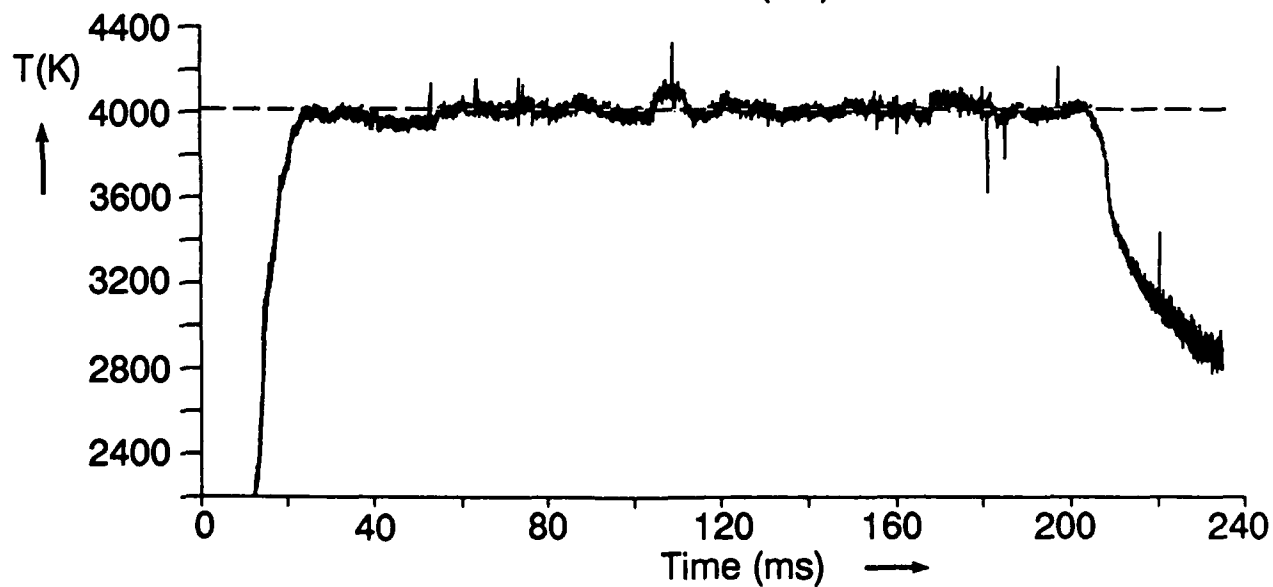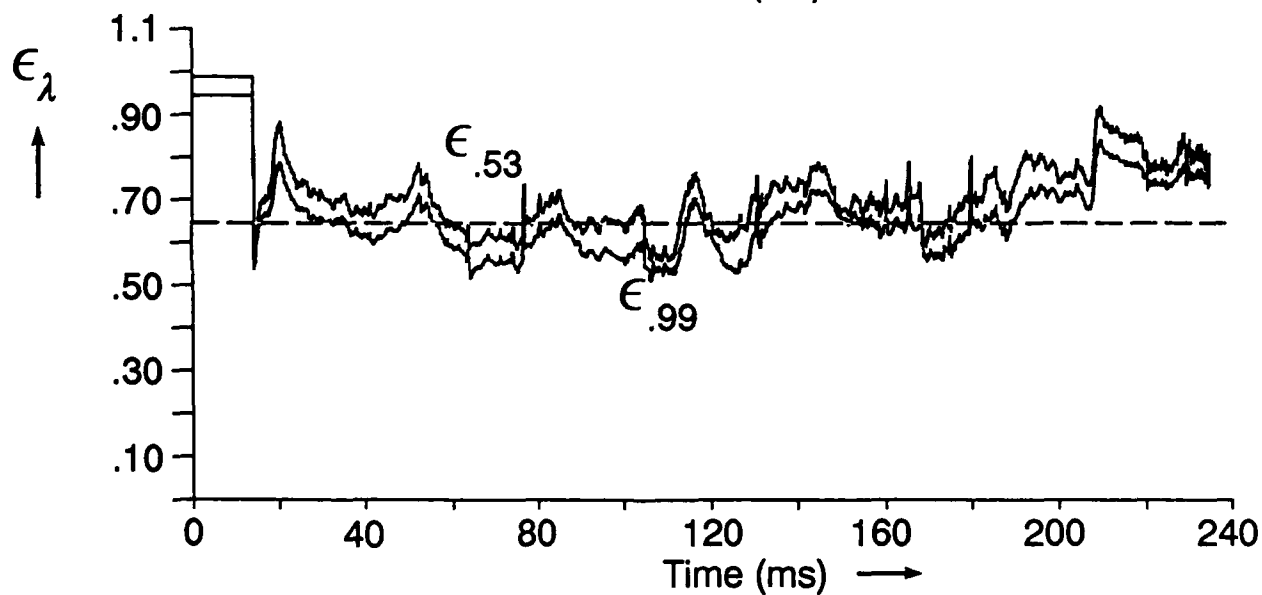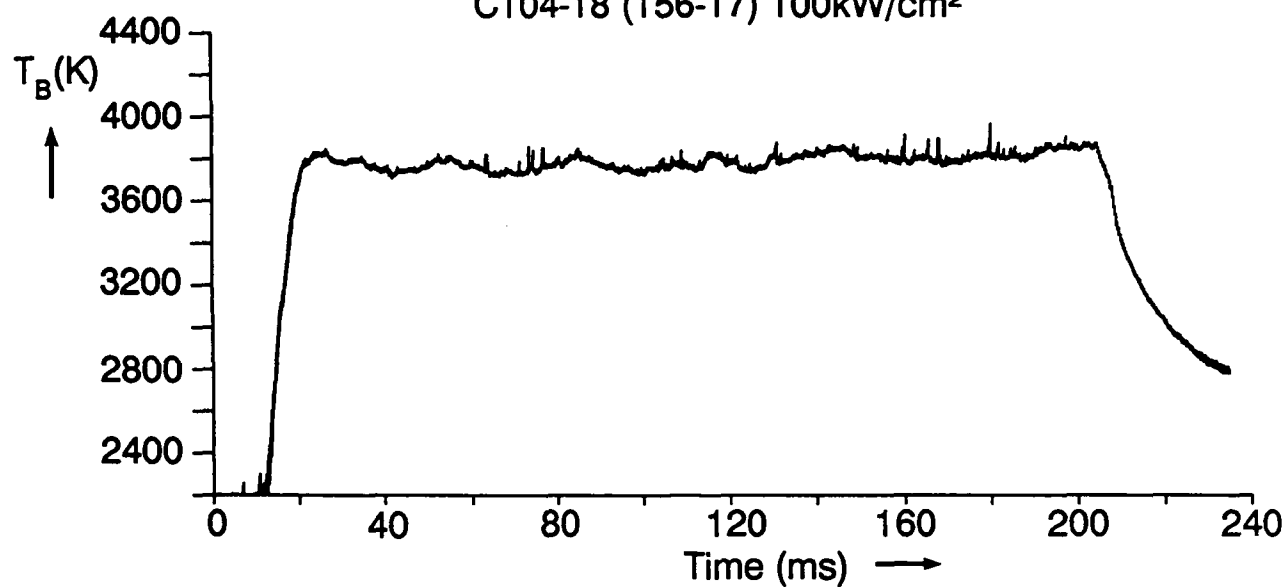
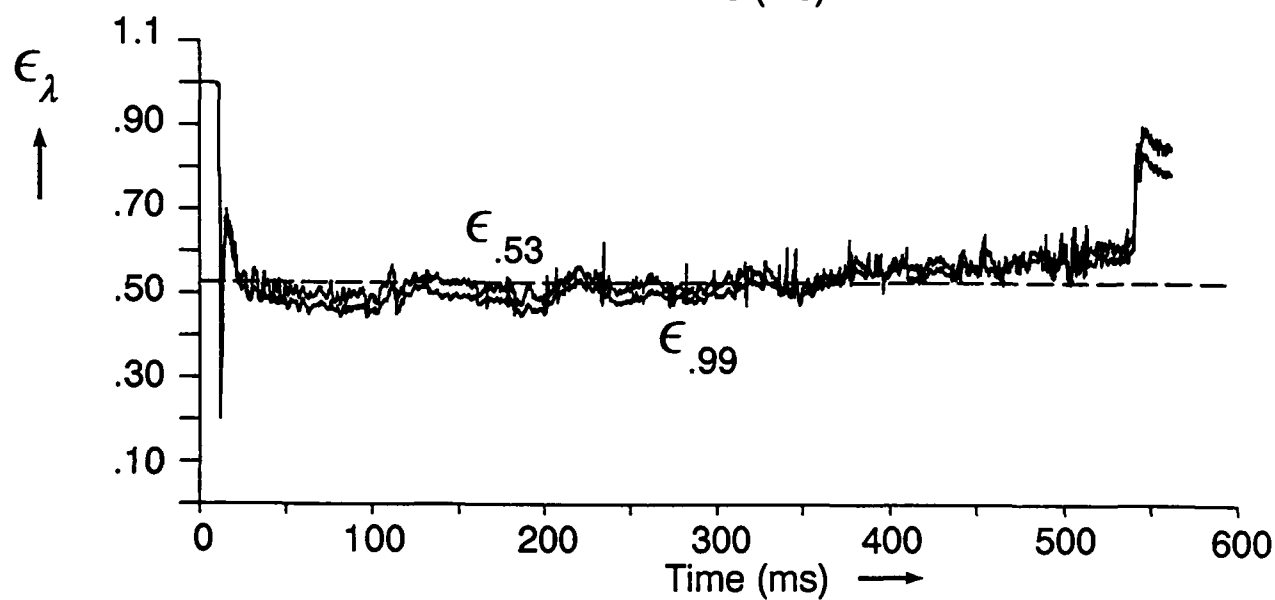C104-22 (157-13) 150kW/cm²
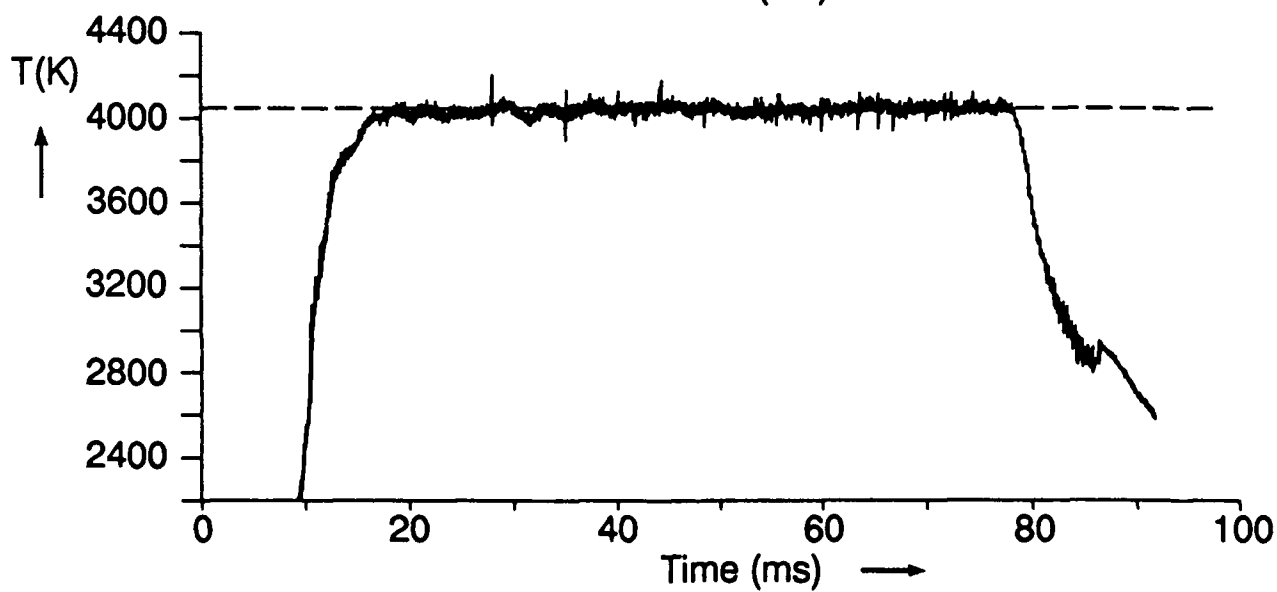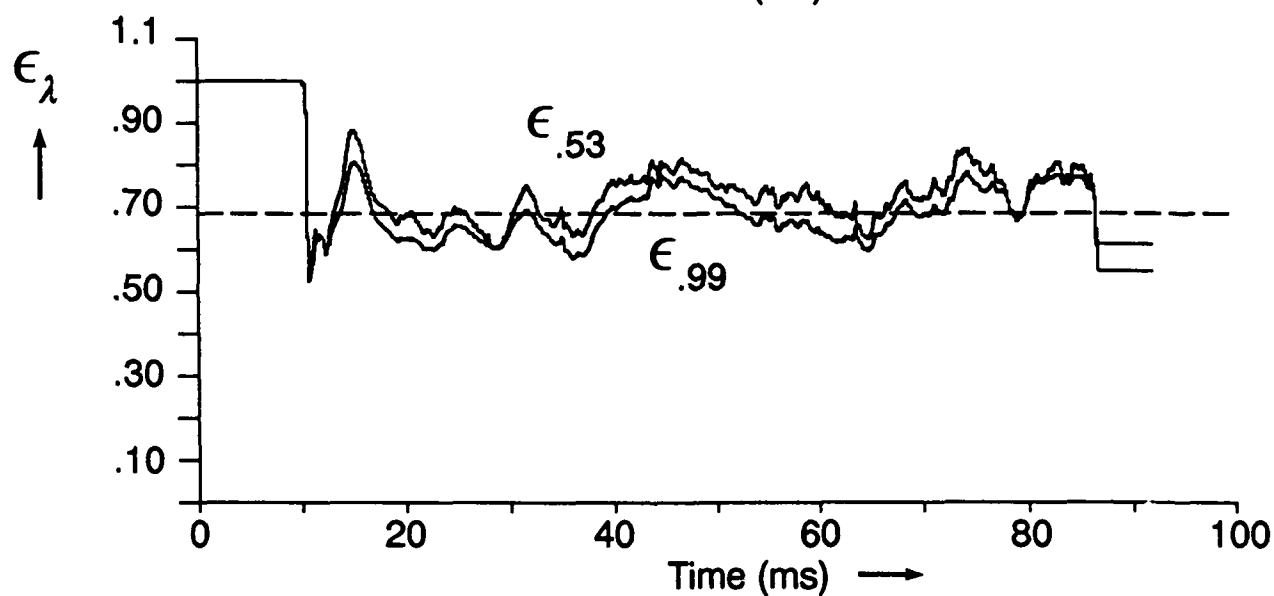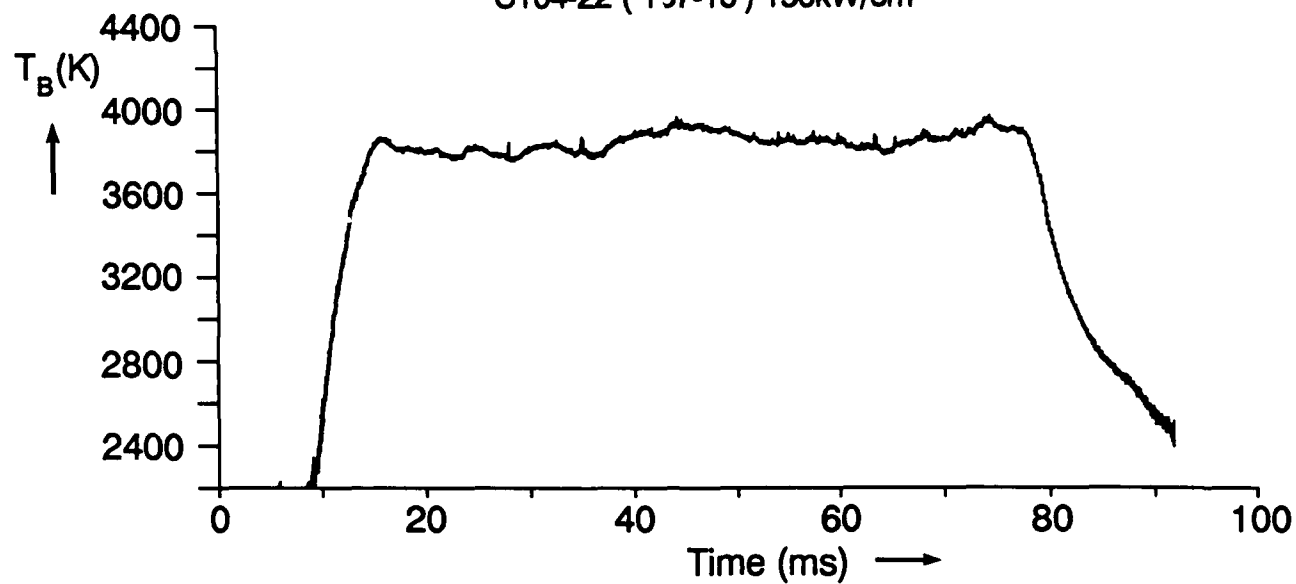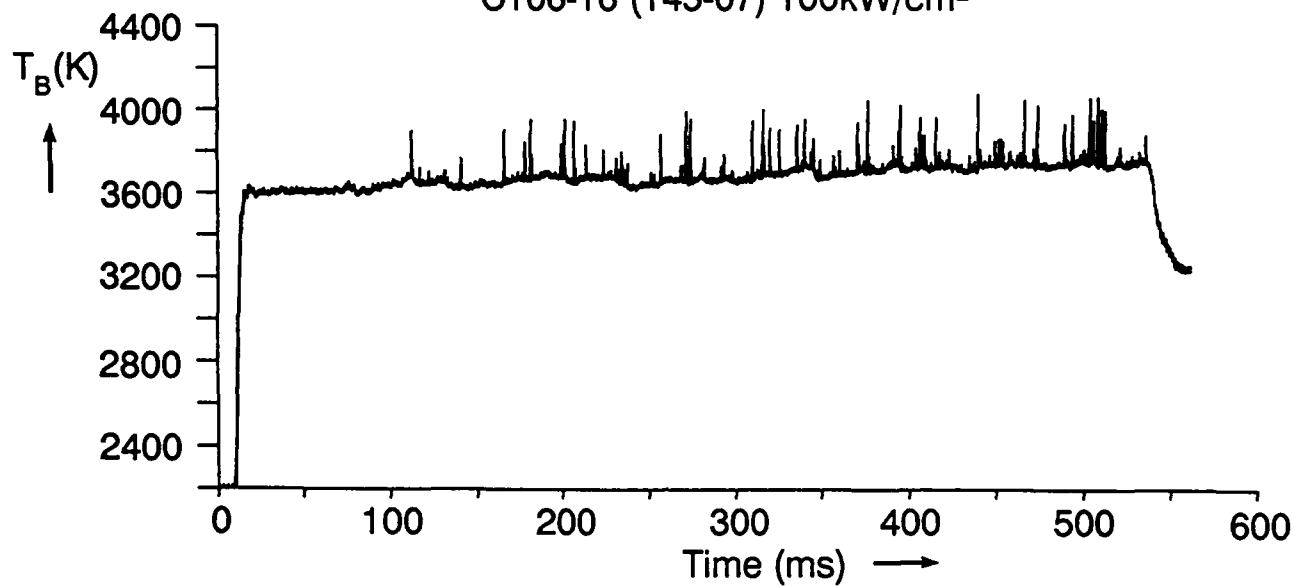
C105-08 (143-09) 60kW/cm²
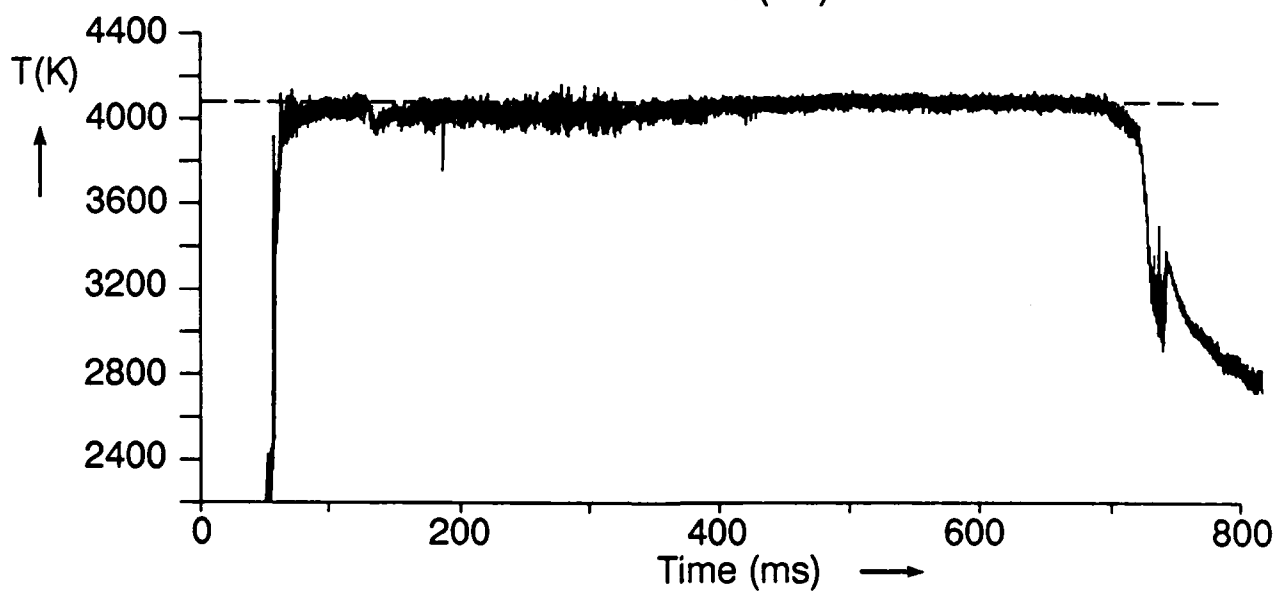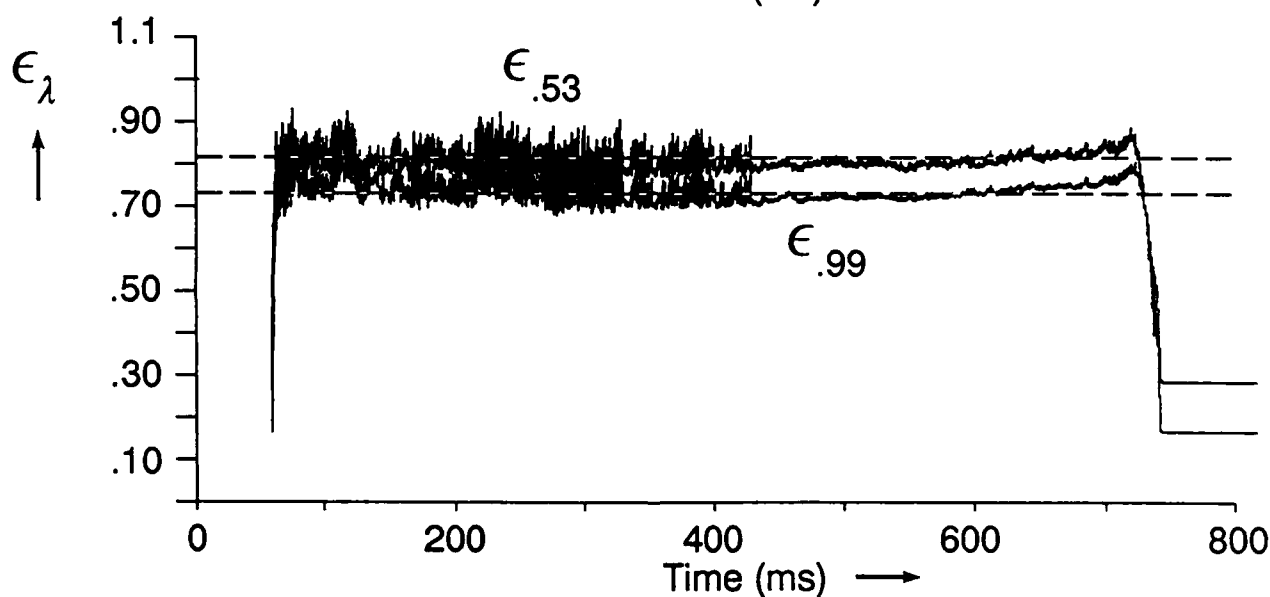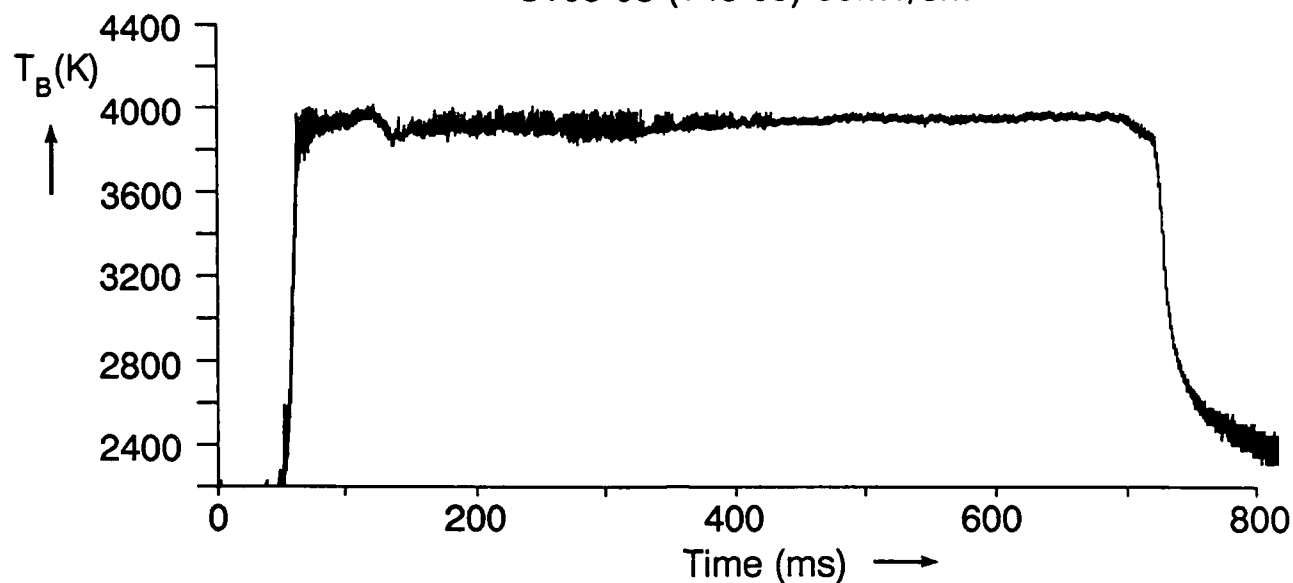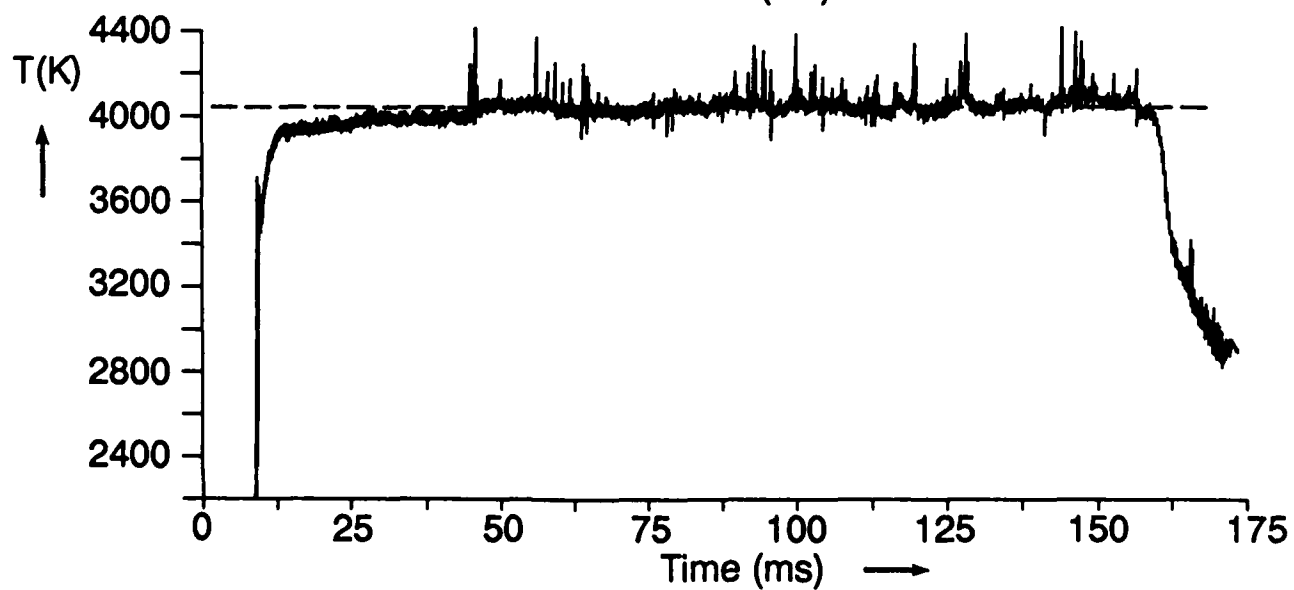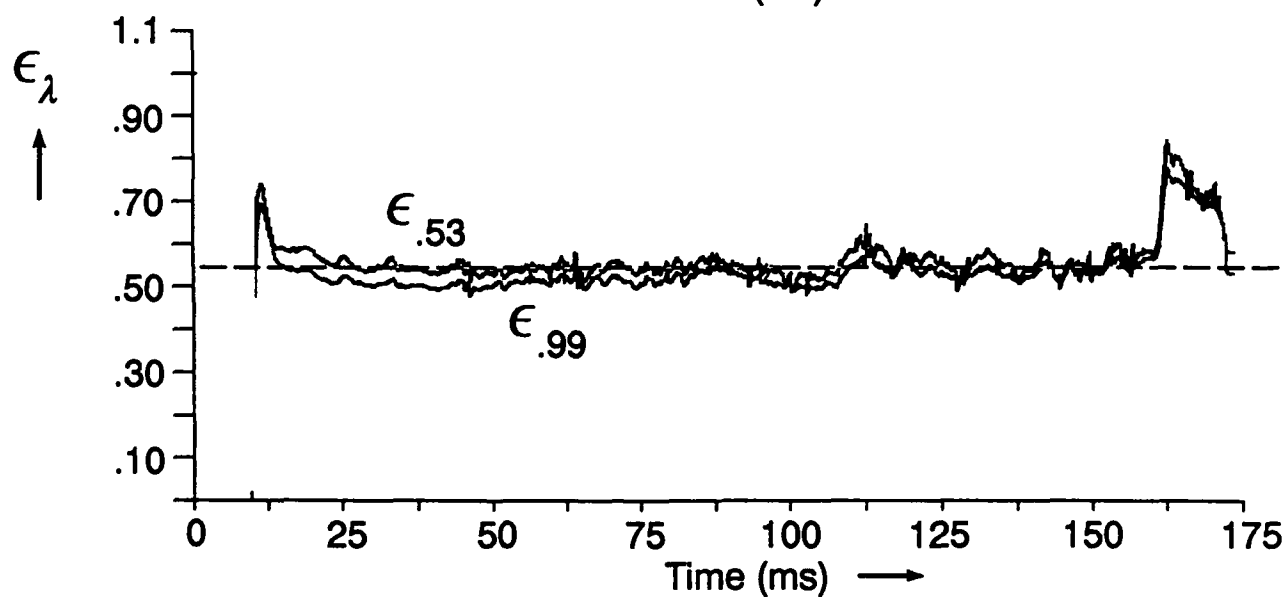
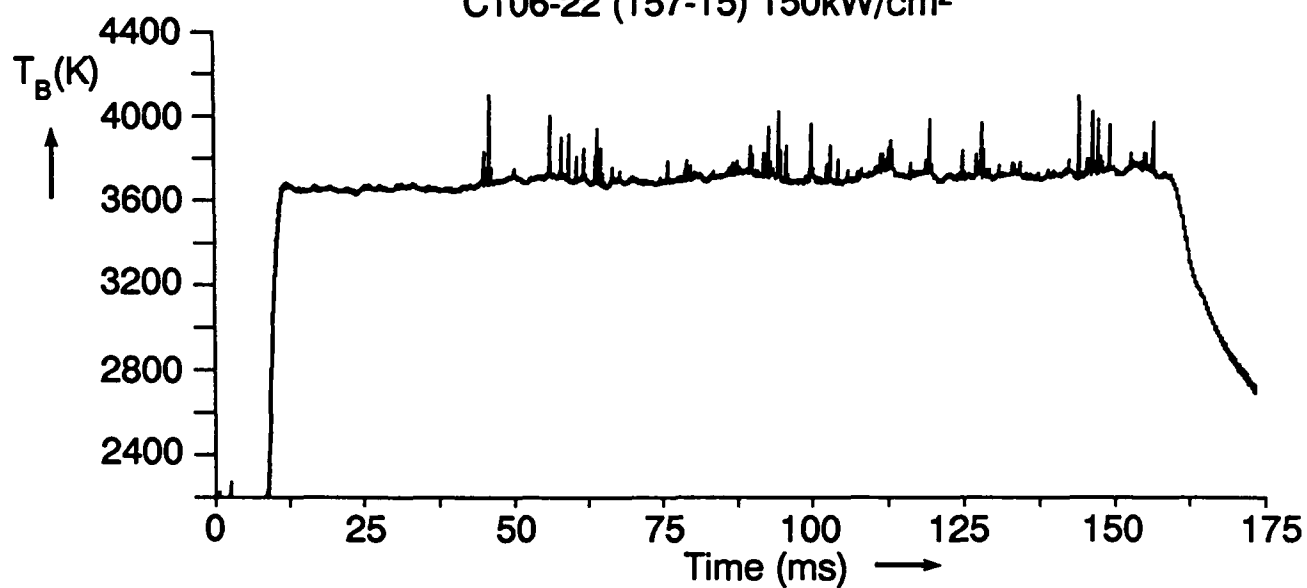C105-19(156-24) 100kW/cm²
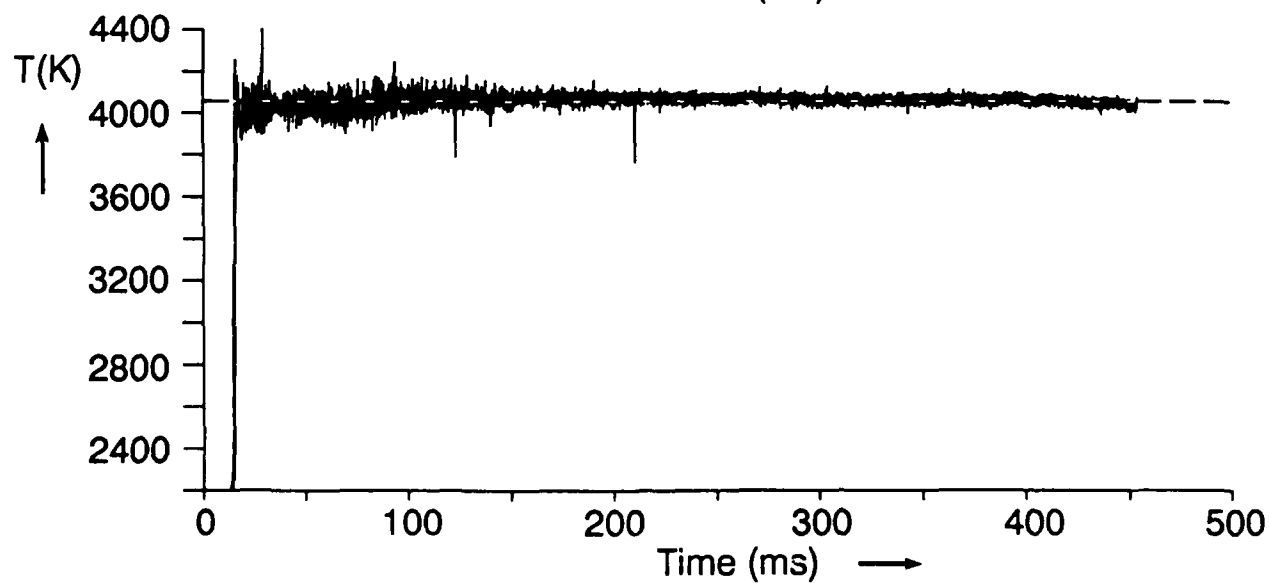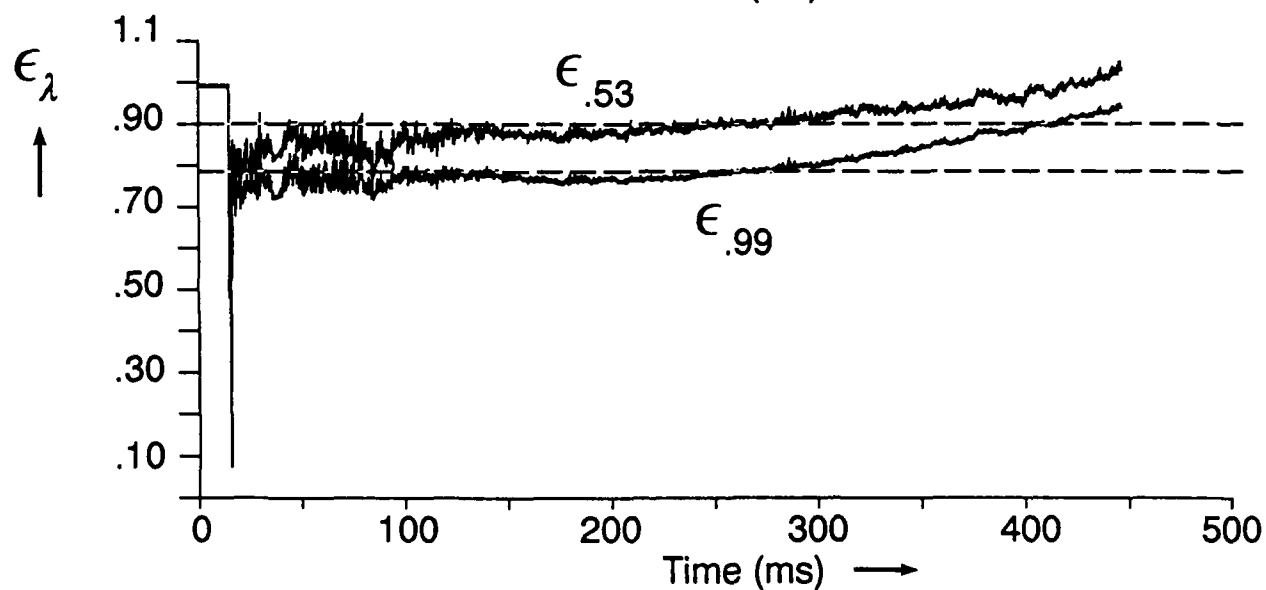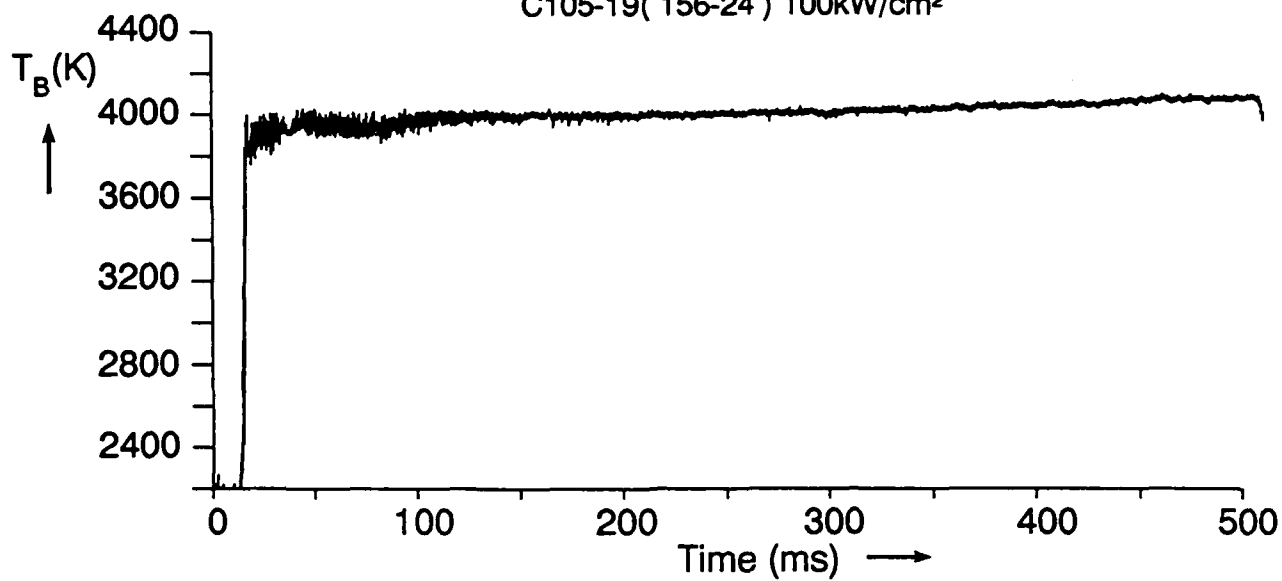
C105-22 (157-14) 150kW/cm²
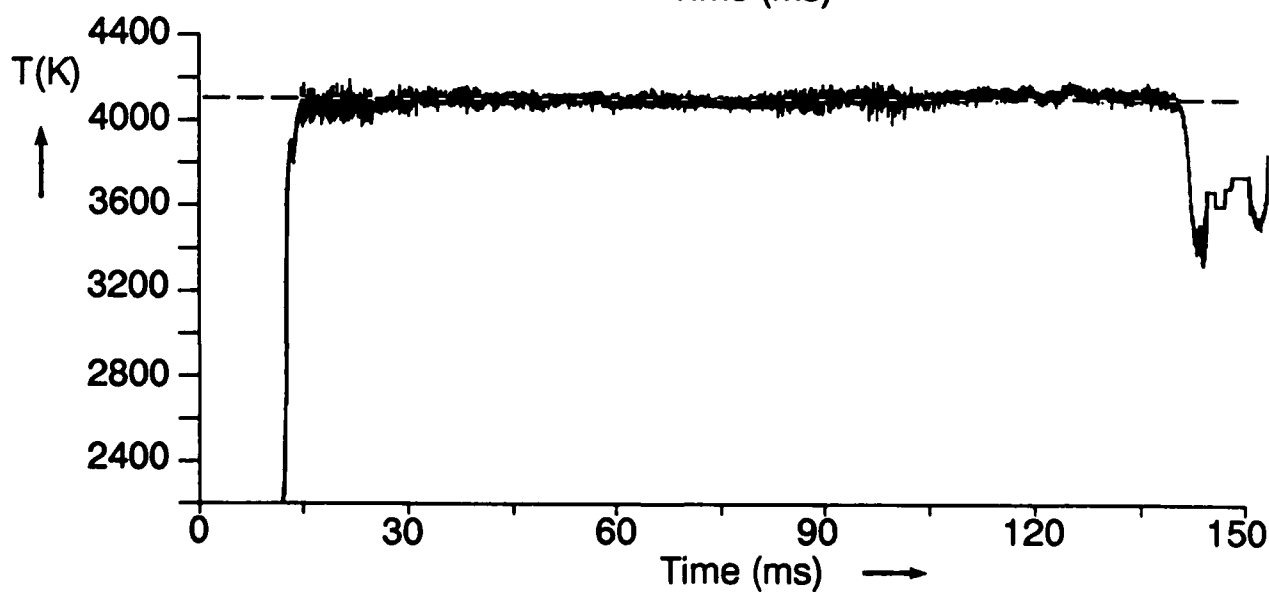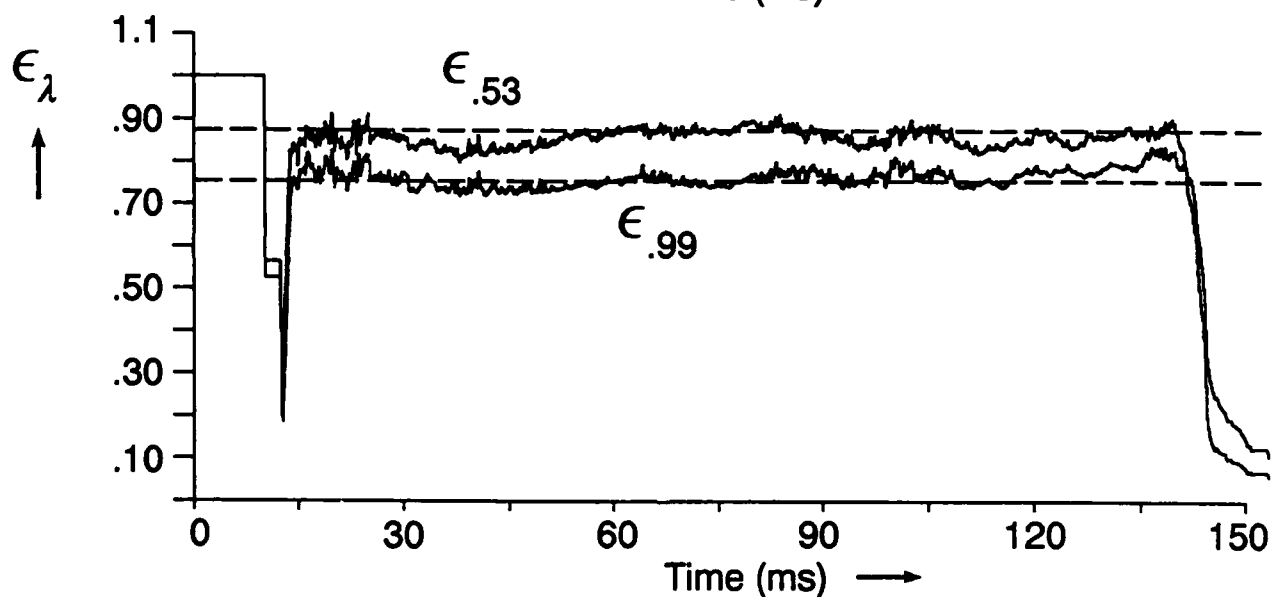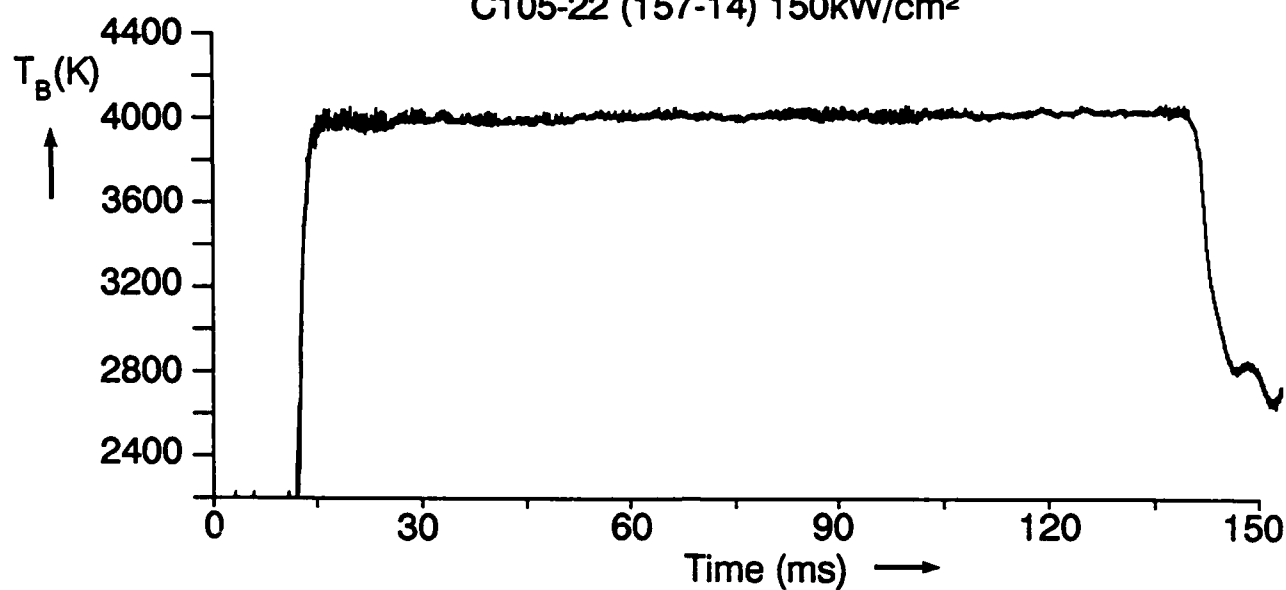
C106-10(157-06) 60kW/cm²
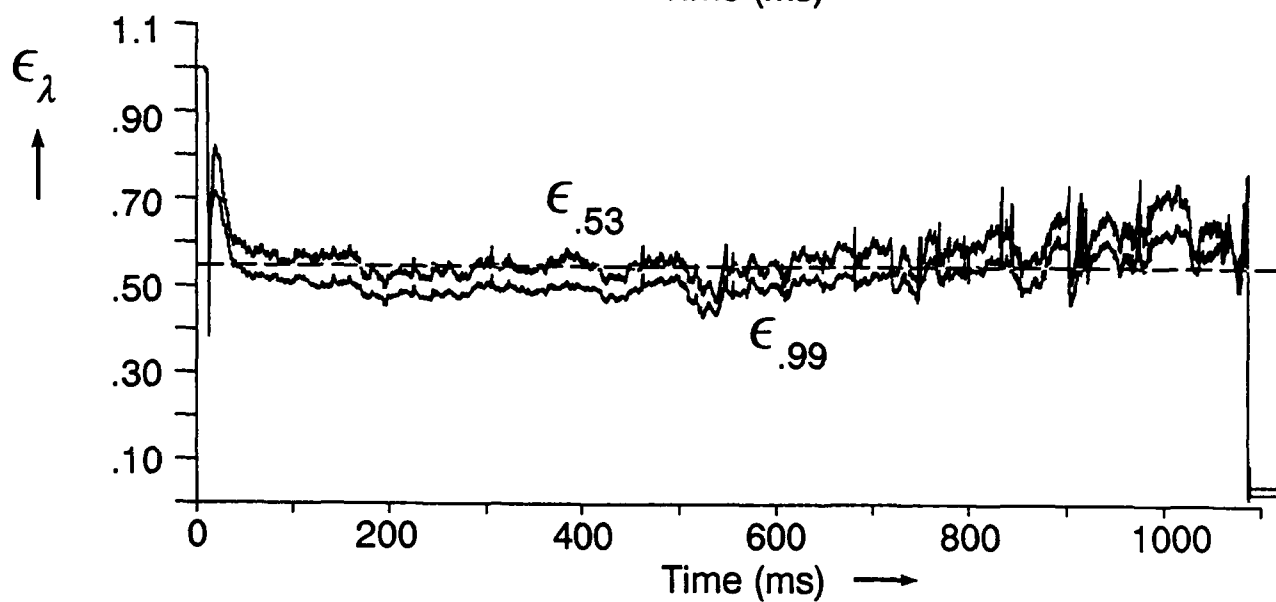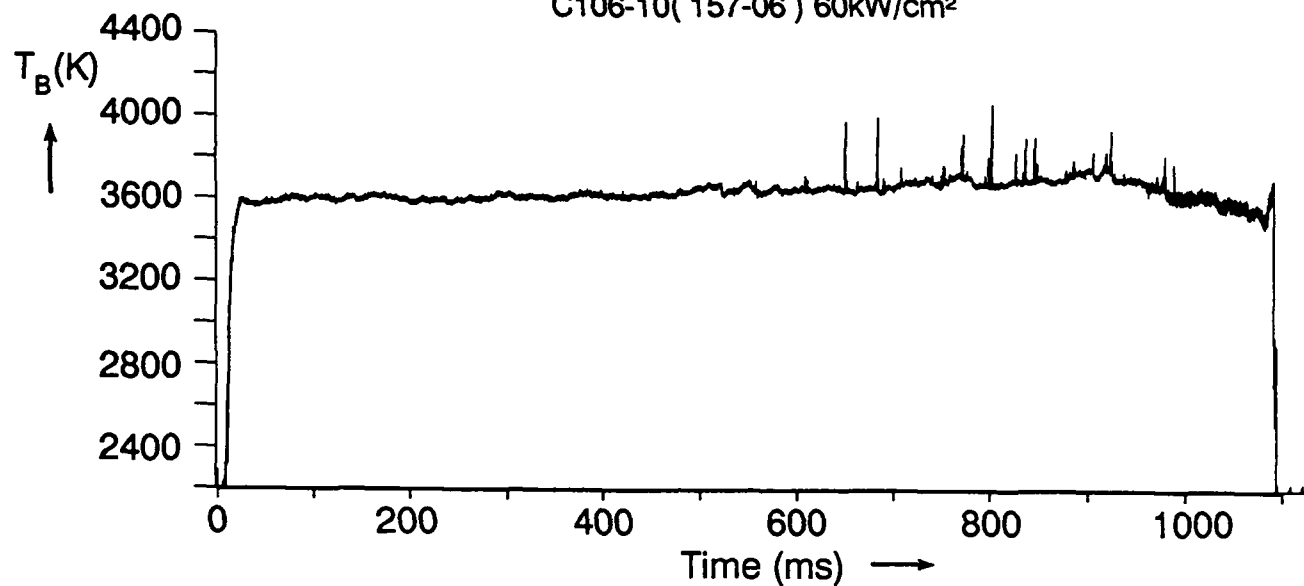
C106-16 (145-07) 100kW/cm²

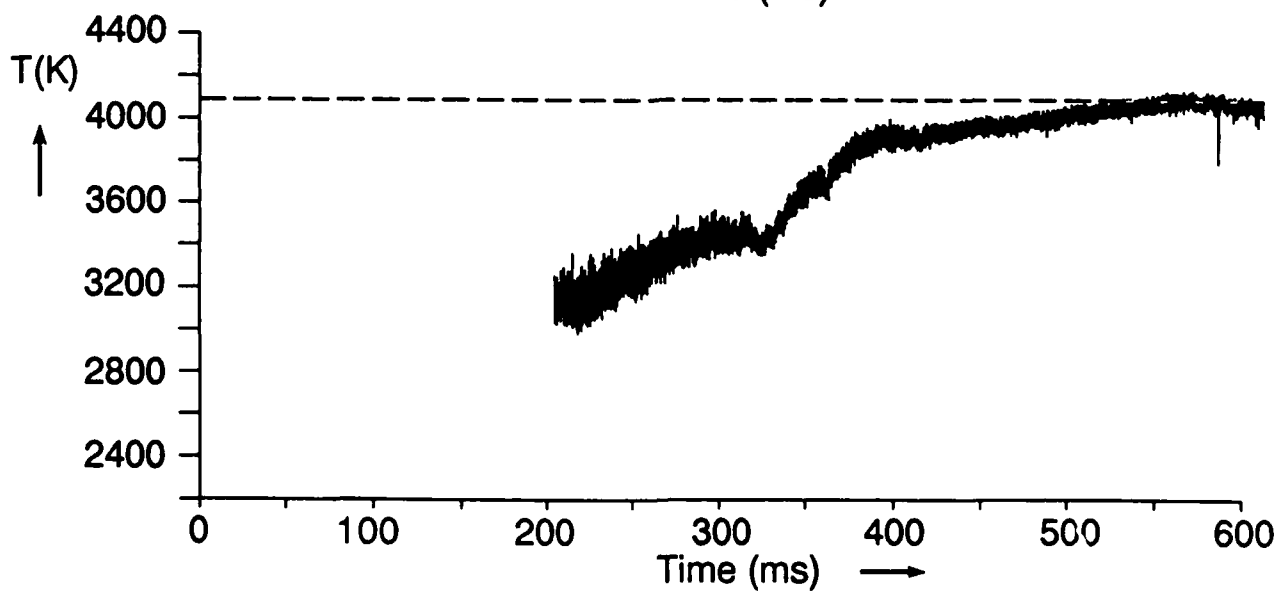C106-22 (157-15) 150kW/cm²

C107-02(144-16) 25kW/cm²
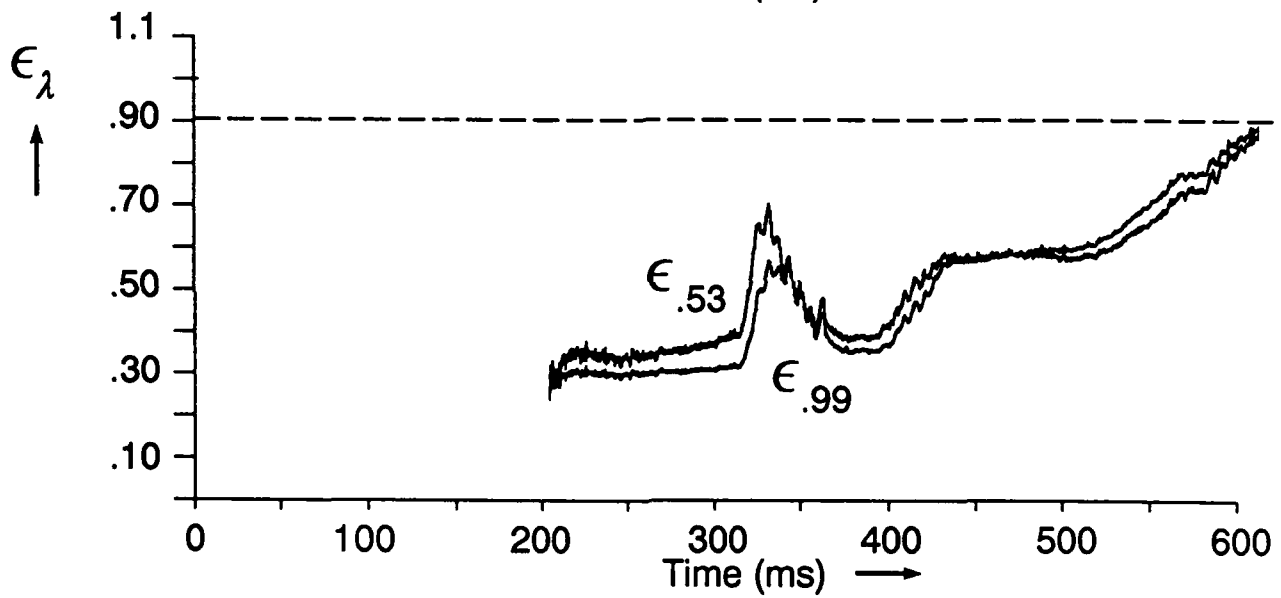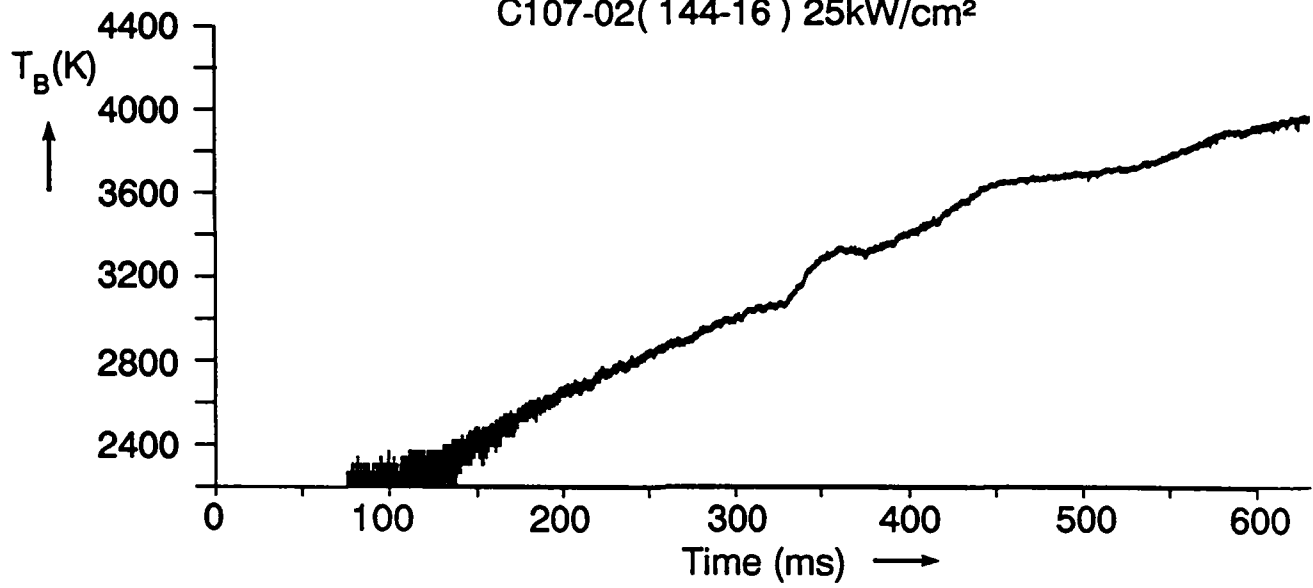
C107-09 (143-14) 60kW/cm²
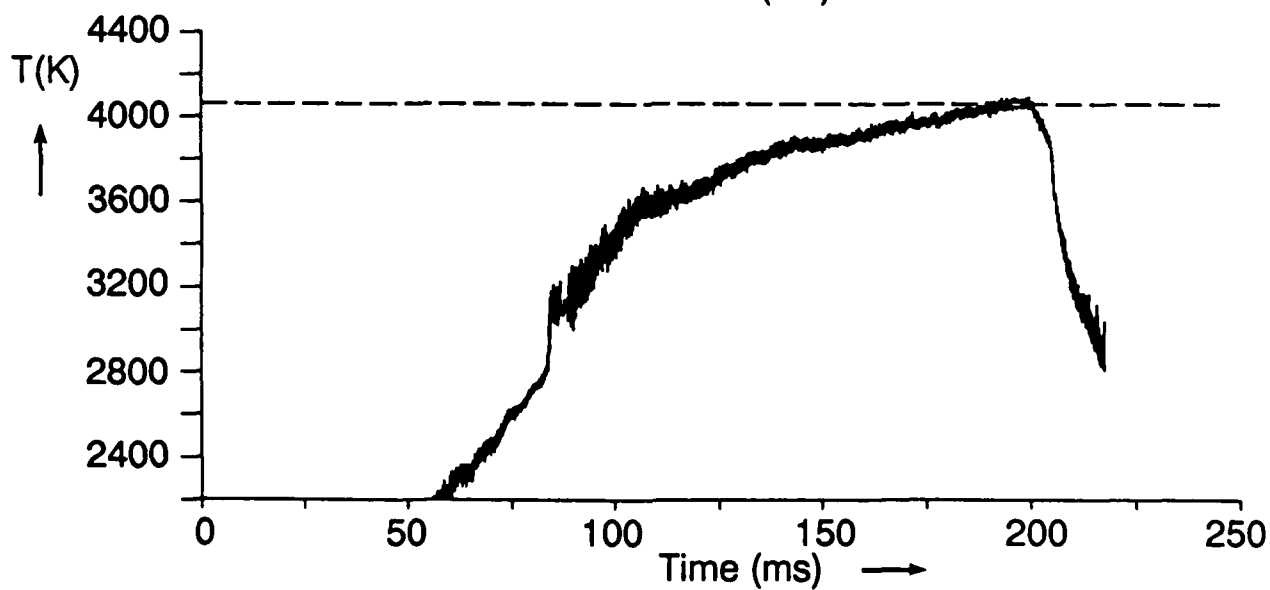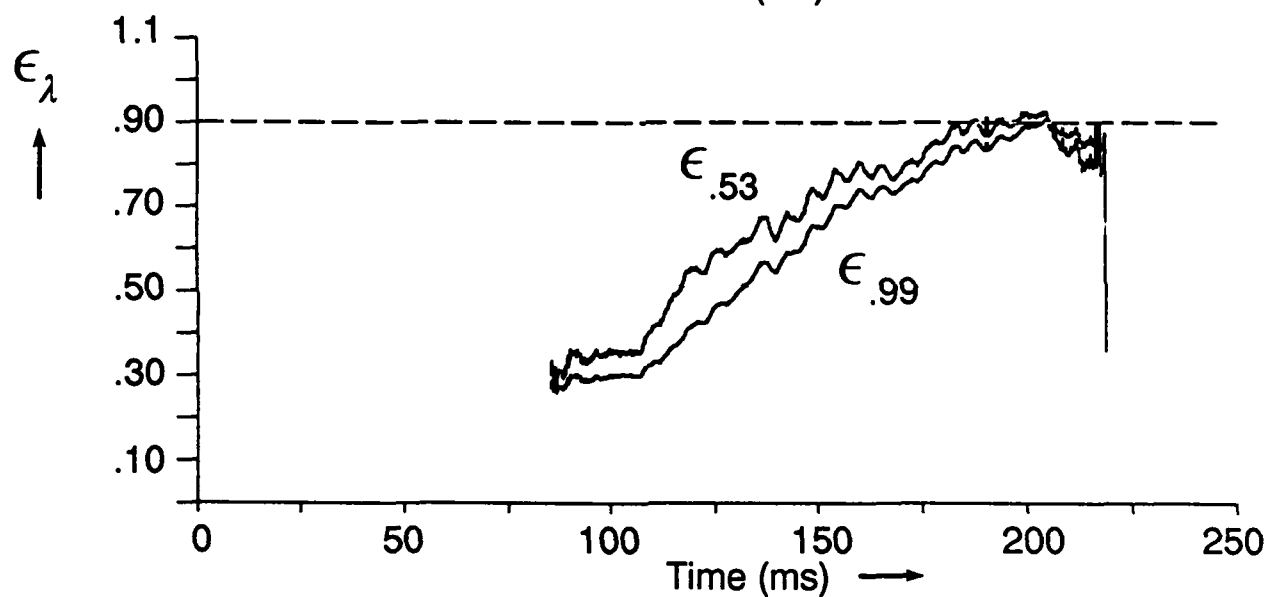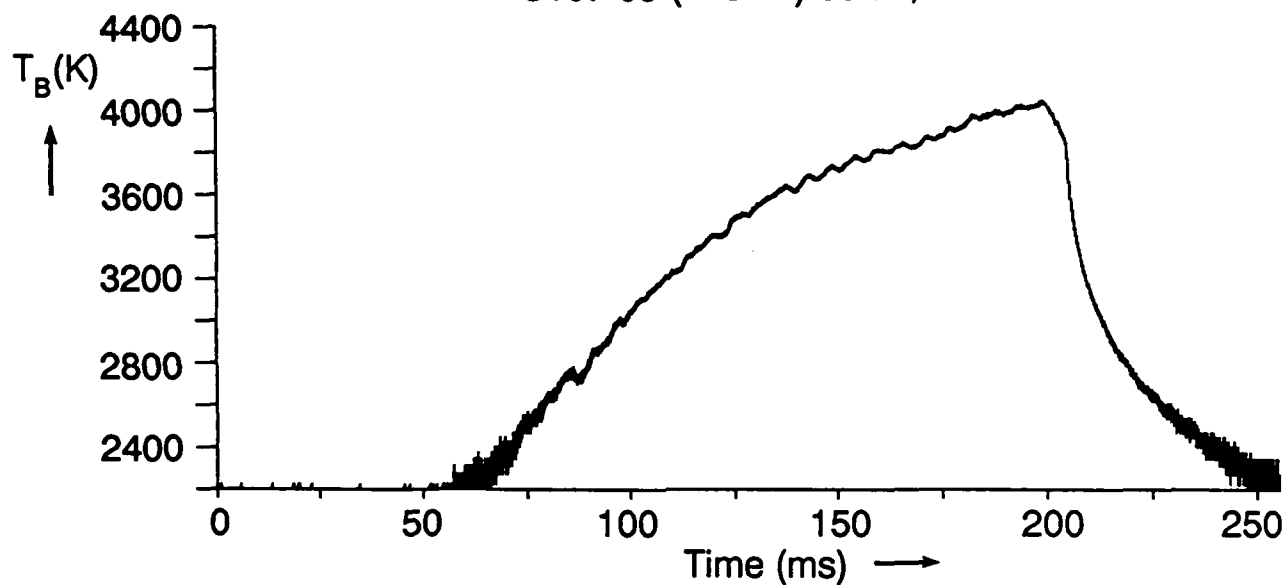
C107-17 (156-20) 100kW/cm²
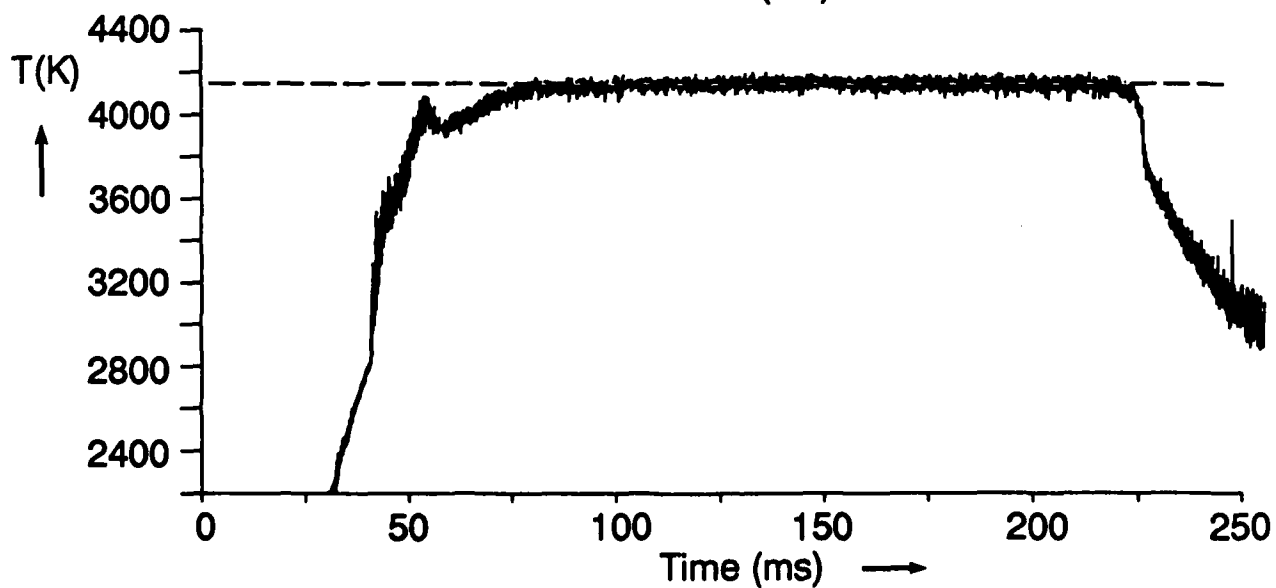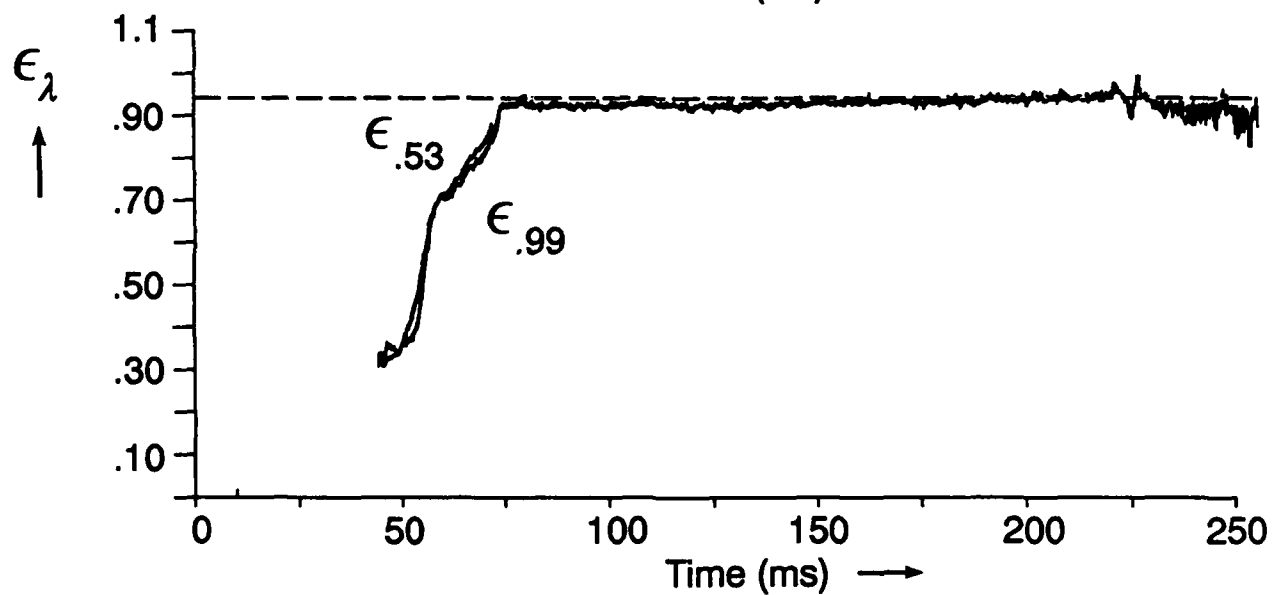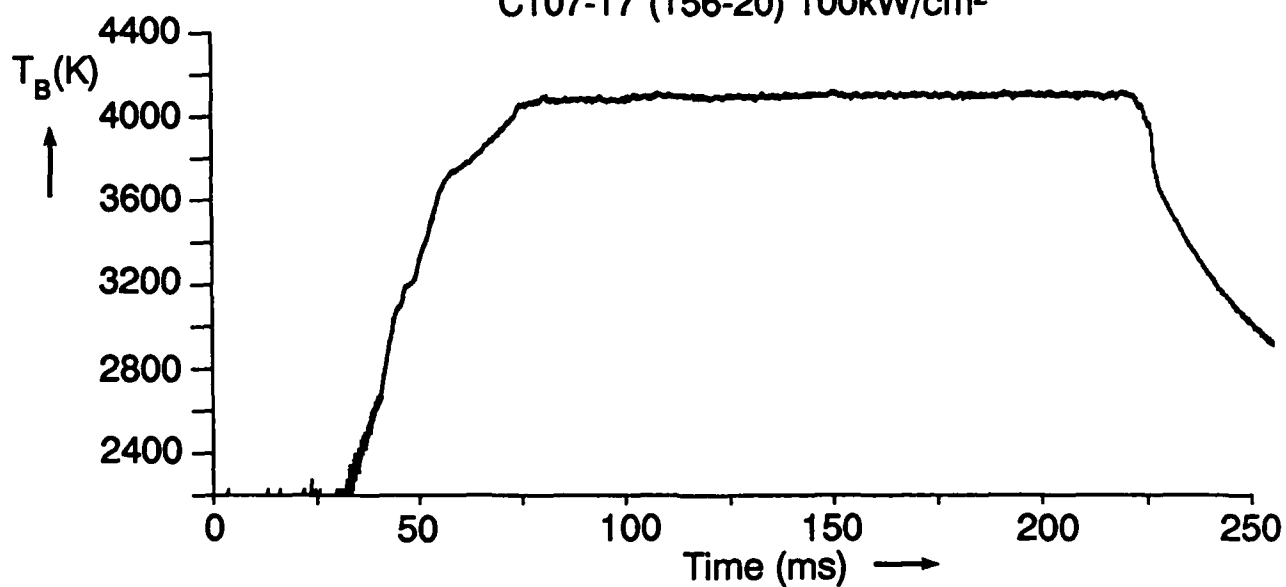
C107-22 (142-15) 150kW/cm²
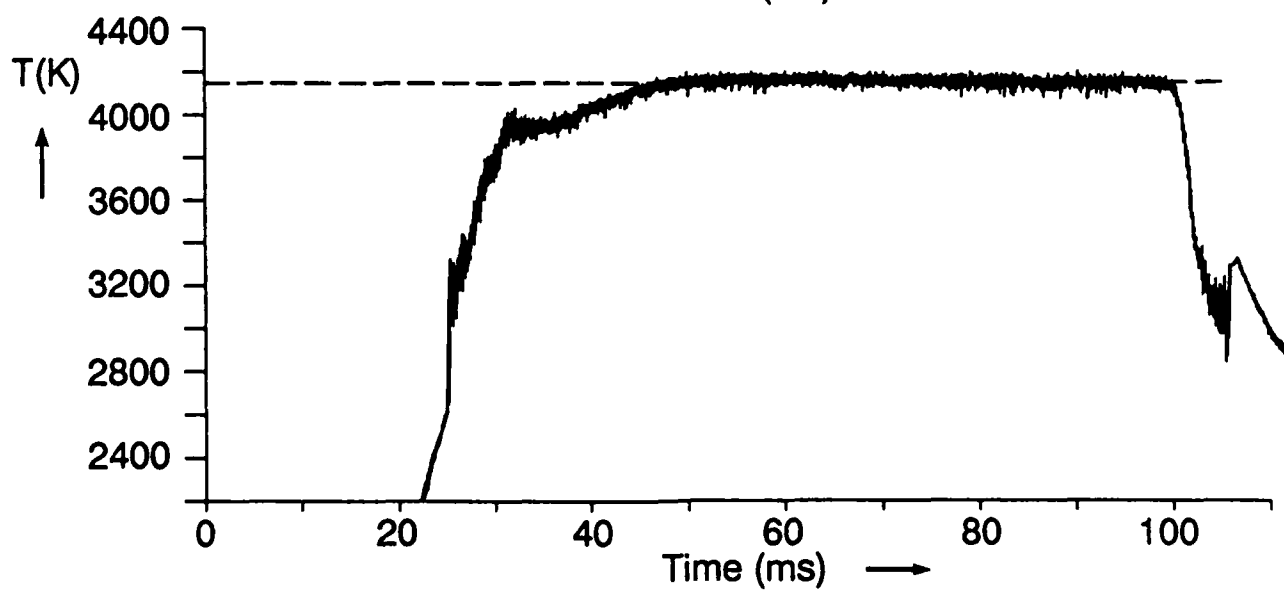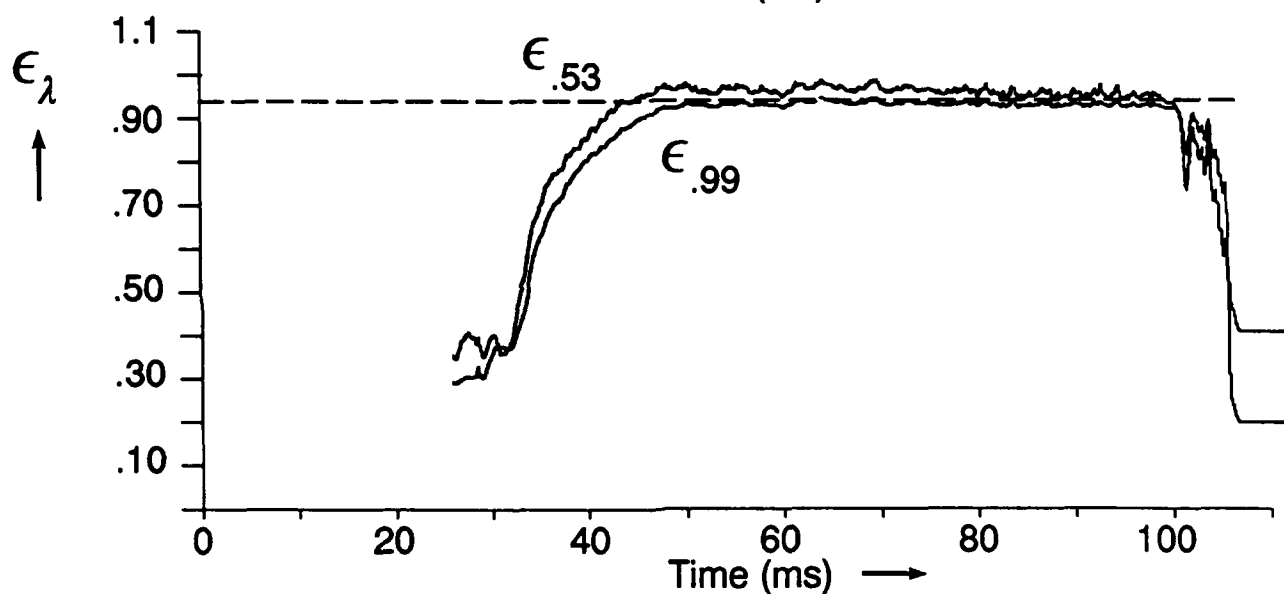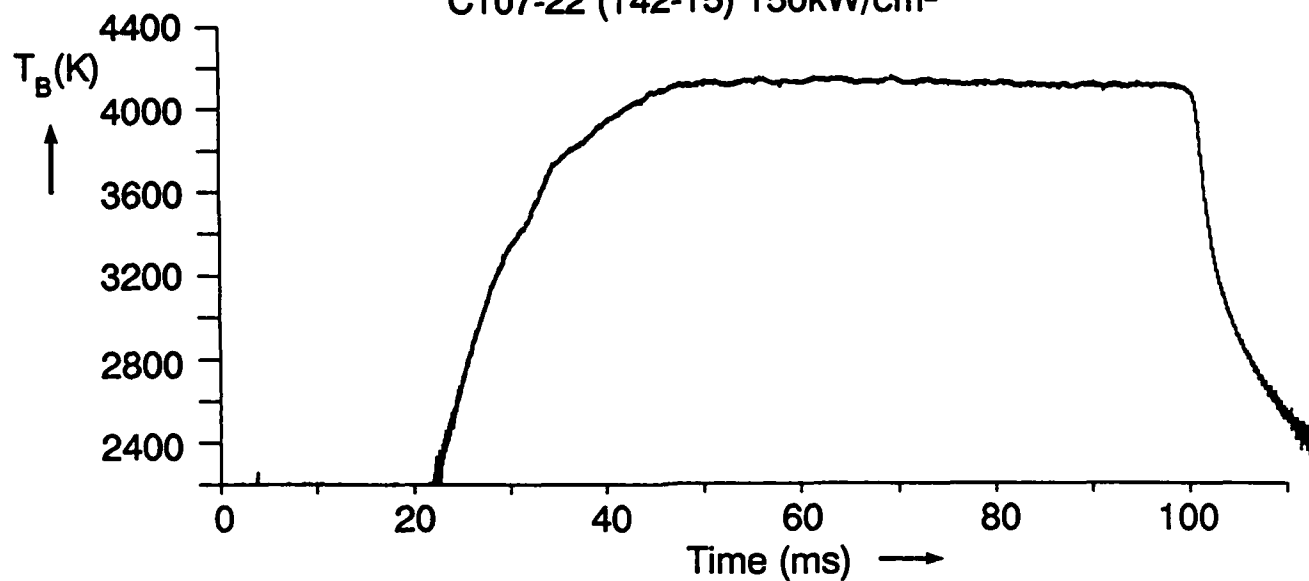
C108-08 (143-15) 60kW/cm²

C108-16 (156-19) 100kW/cm²

$T_B(K)$ vs Time (ms)

ϵ_λ vs Time (ms)

$\epsilon_{.53}$

$\epsilon_{.99}$

$T(K)$ vs Time (ms)
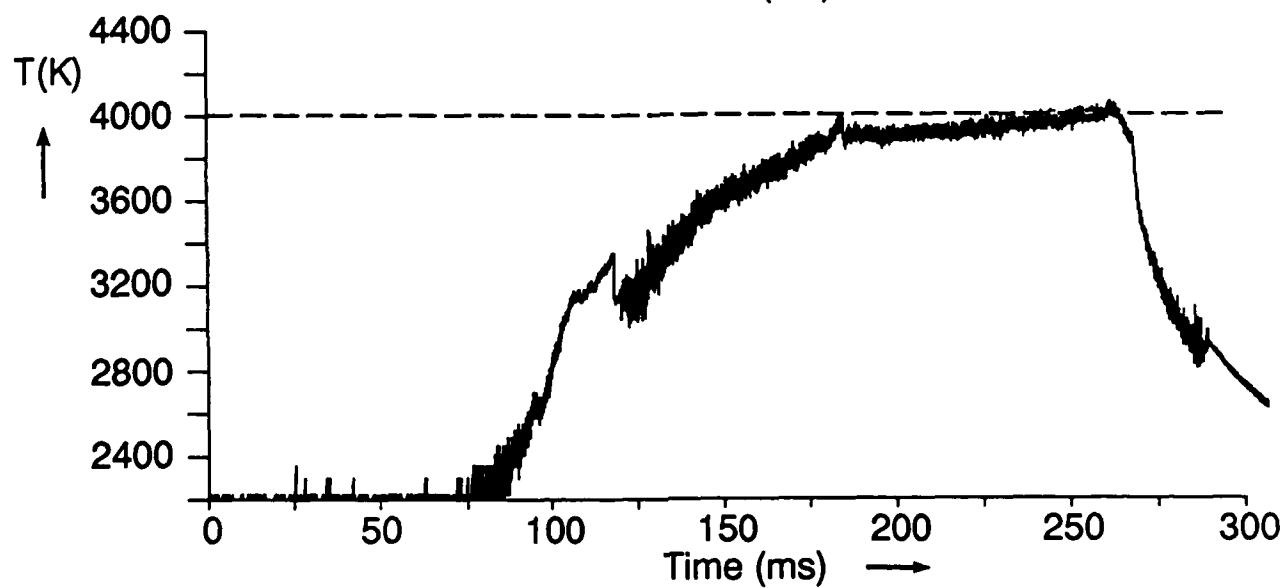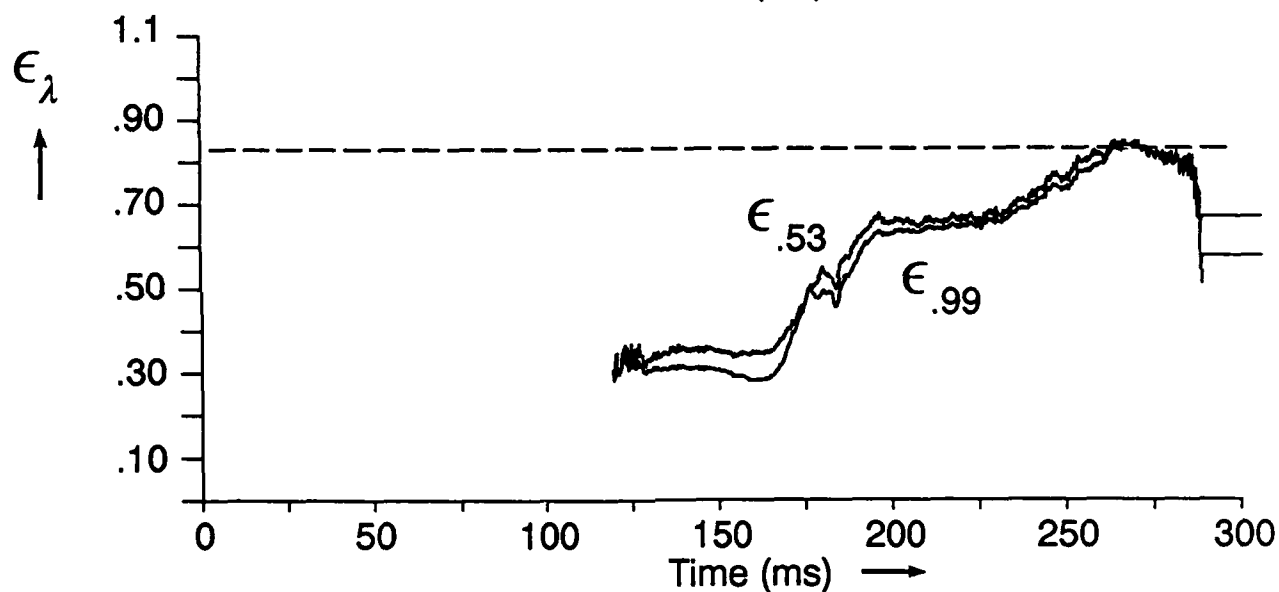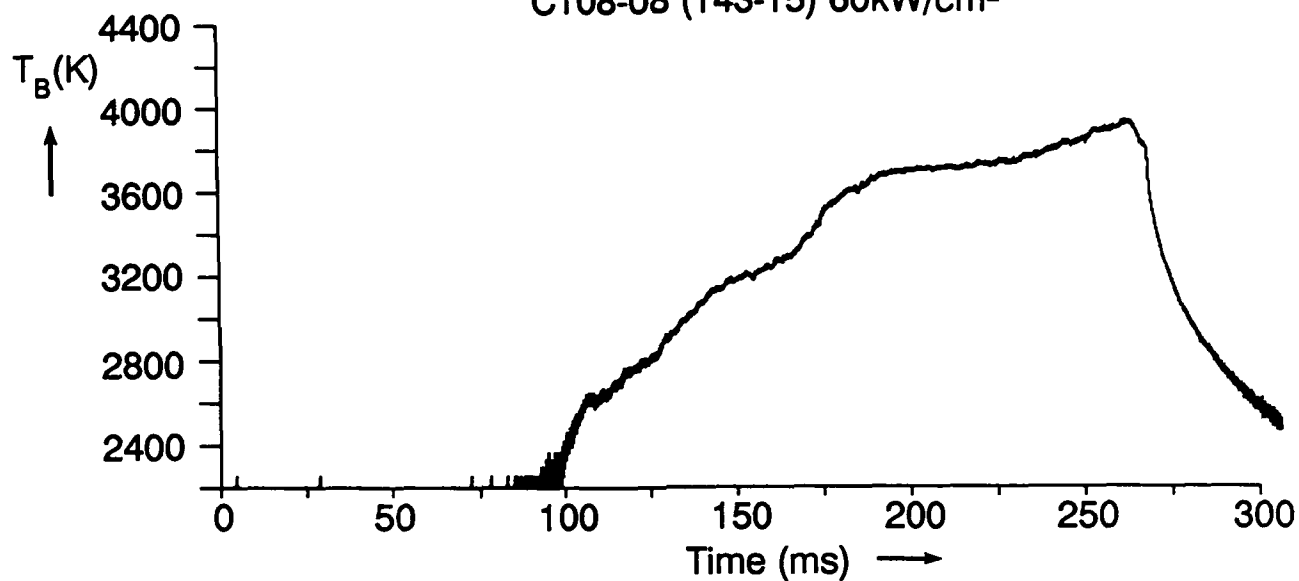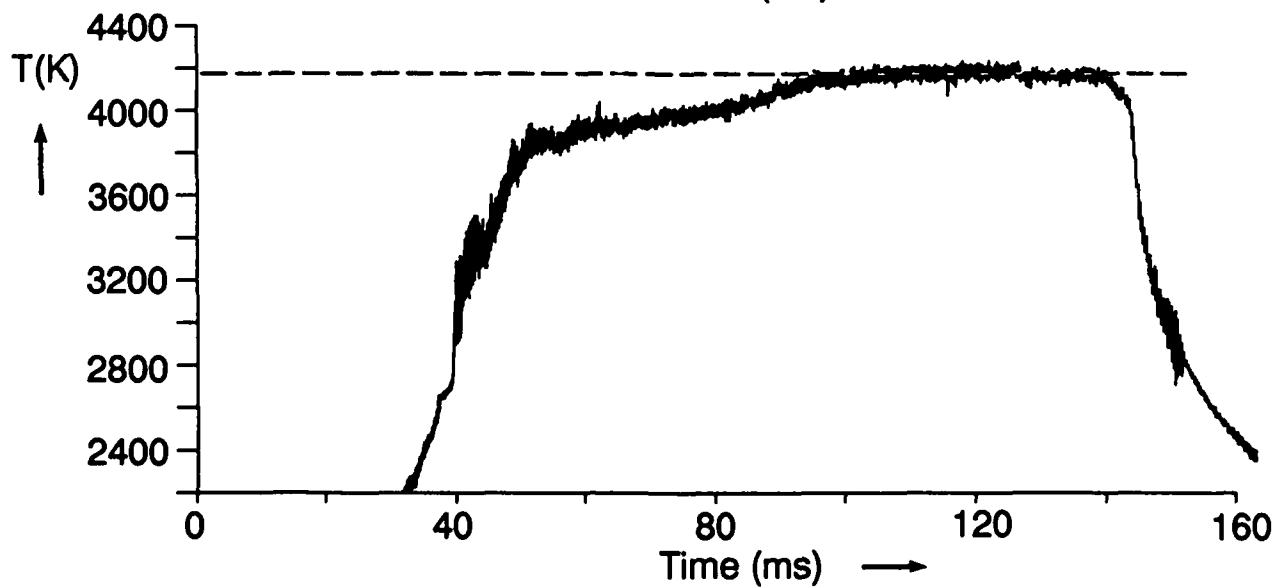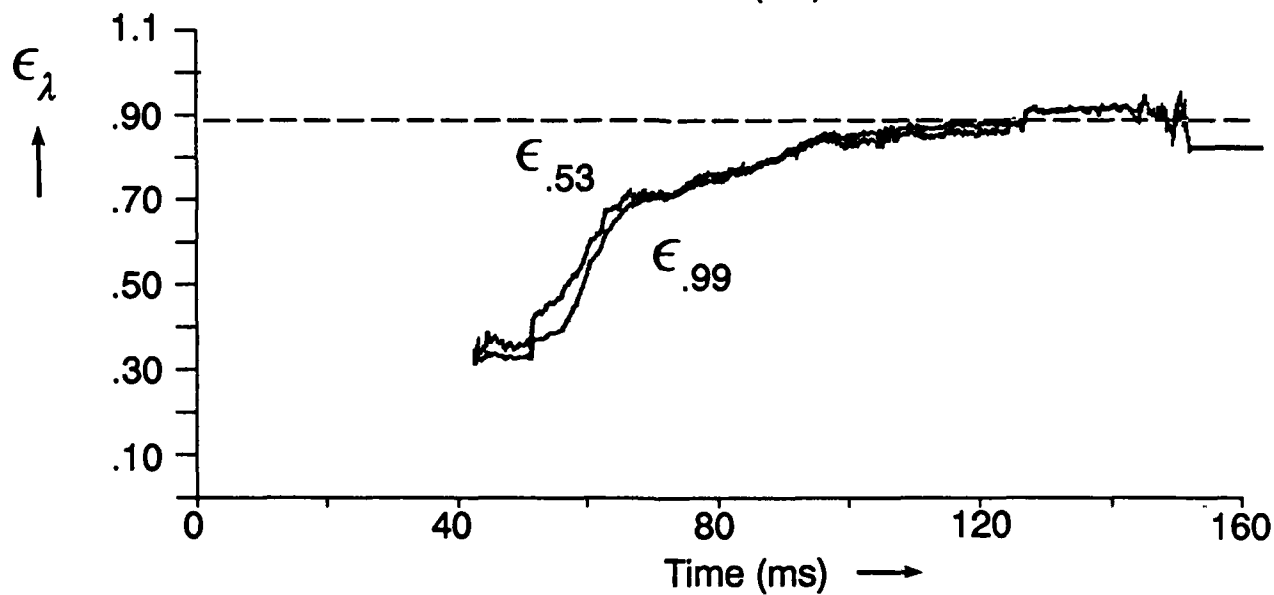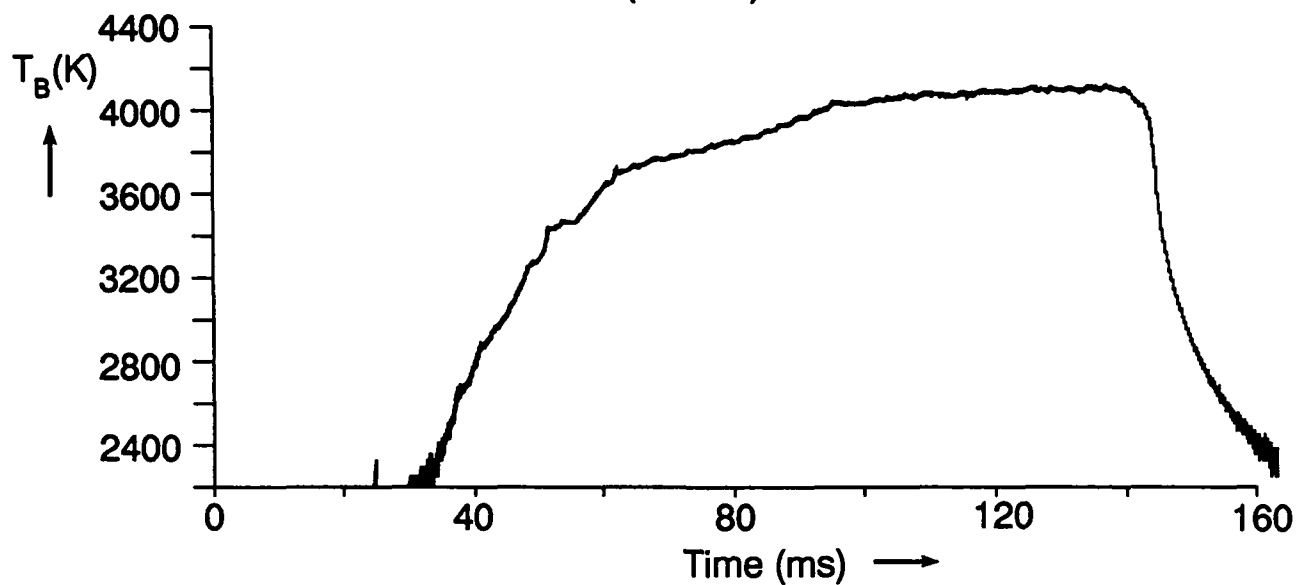
C108-23 (142-14) 150kW/cm²
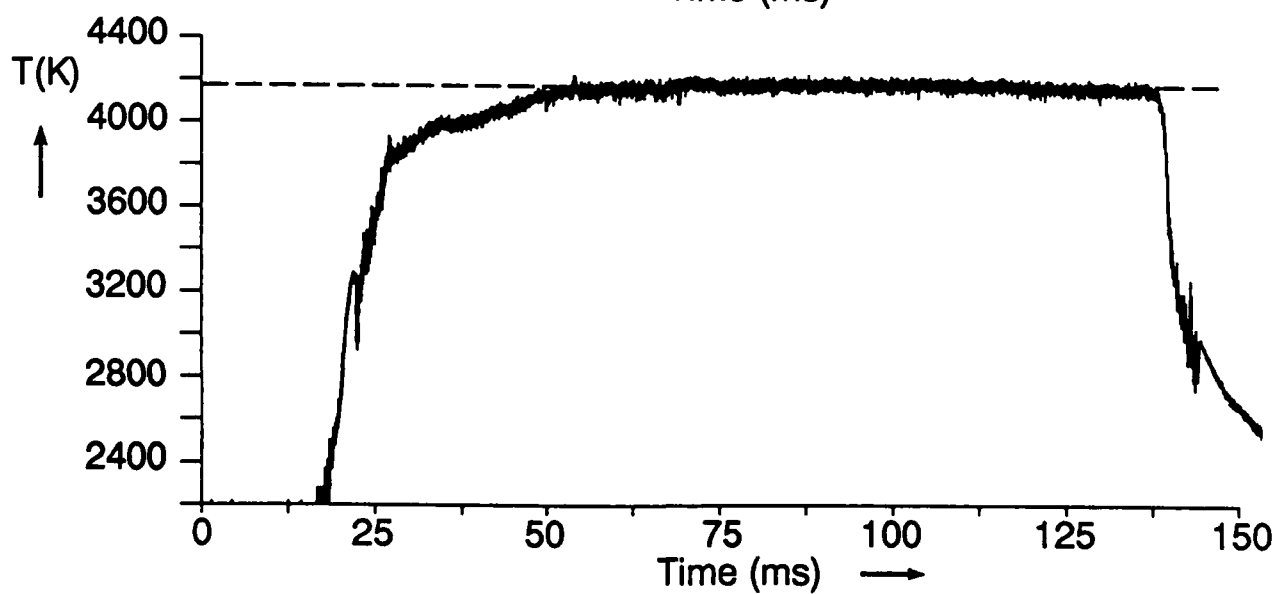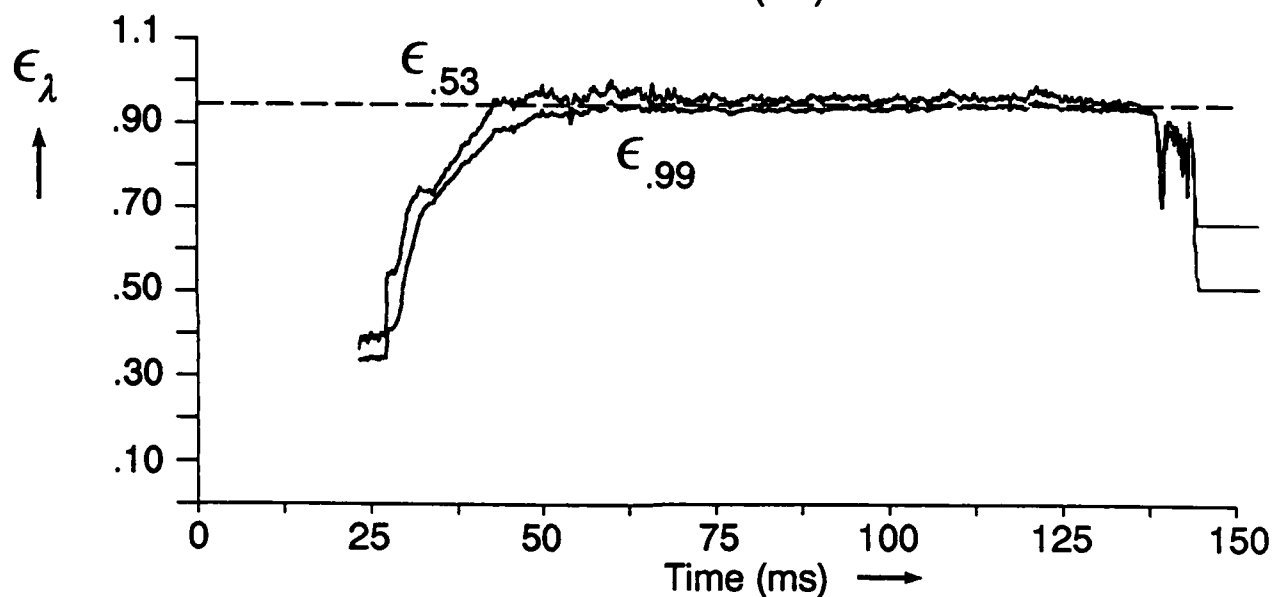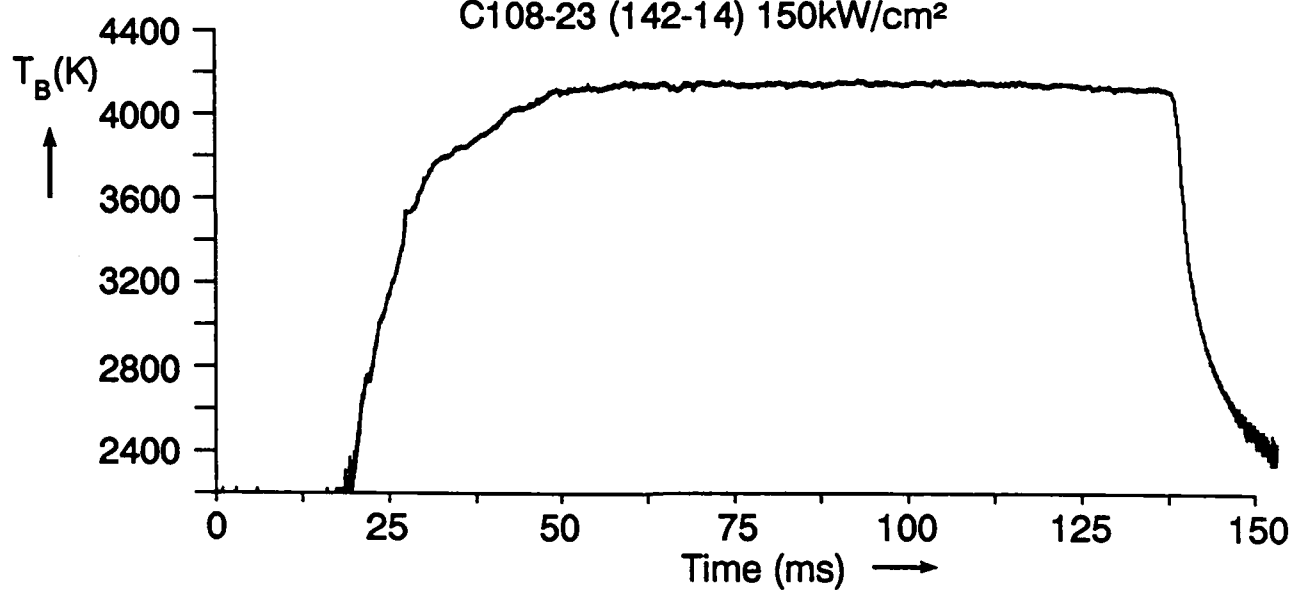
APPENDIX C

Appended are target time-resolved reflectance measurements in the format of Figures 24 and 25 for carbon barrier materials (G, C101, C102, C104, C105, C106, C107, and C108) at two irradiances (9 kW/cm^2 and 100 kW/cm^2).

GraphNOL: I_{pk} = 9 kW/cm^2
TIME RESOLVED REFLECTANCES
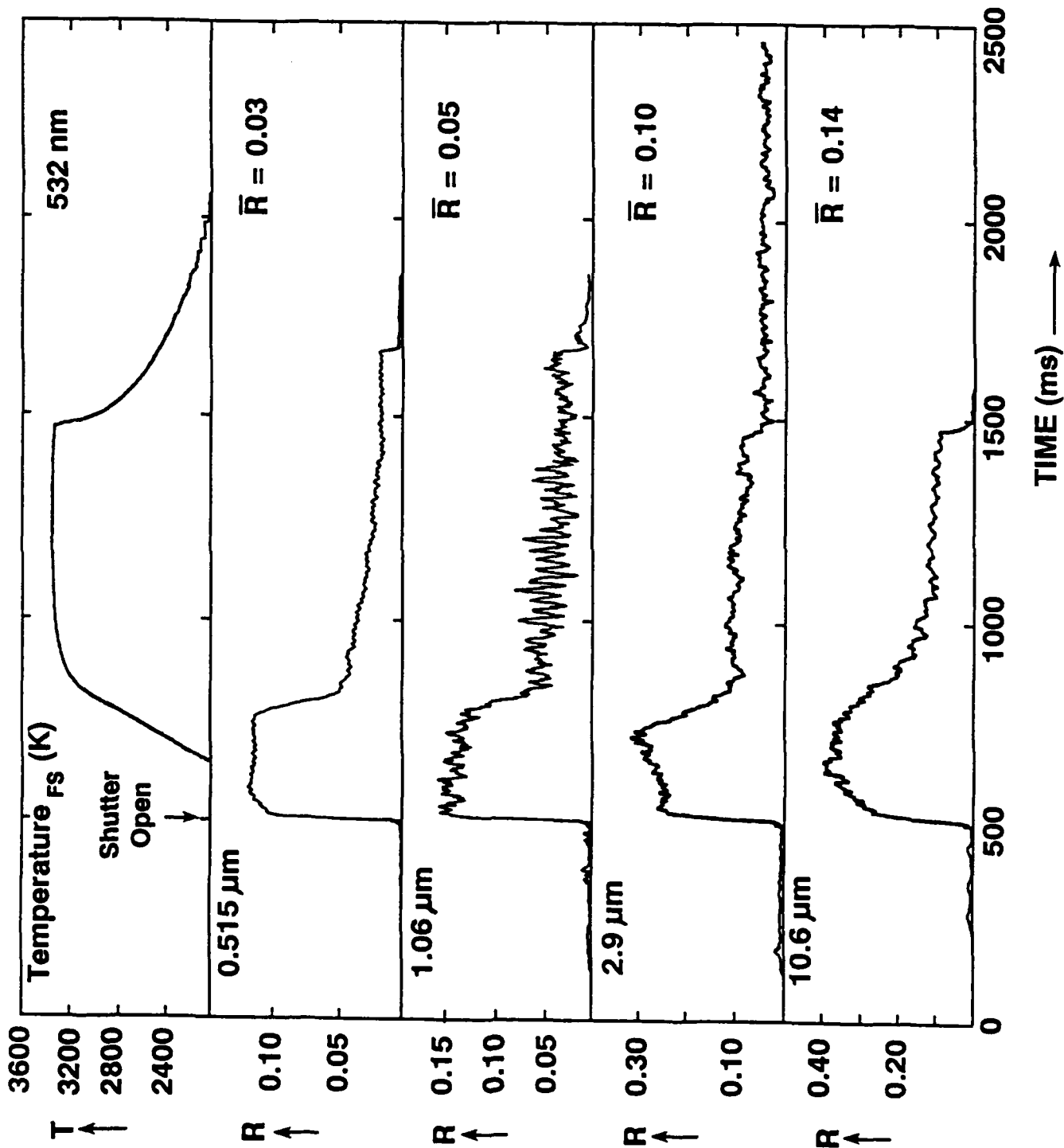
GraphNOL: I_{pk} = 100 kW/cm^2
TIME RESOLVED REFLECTANCES
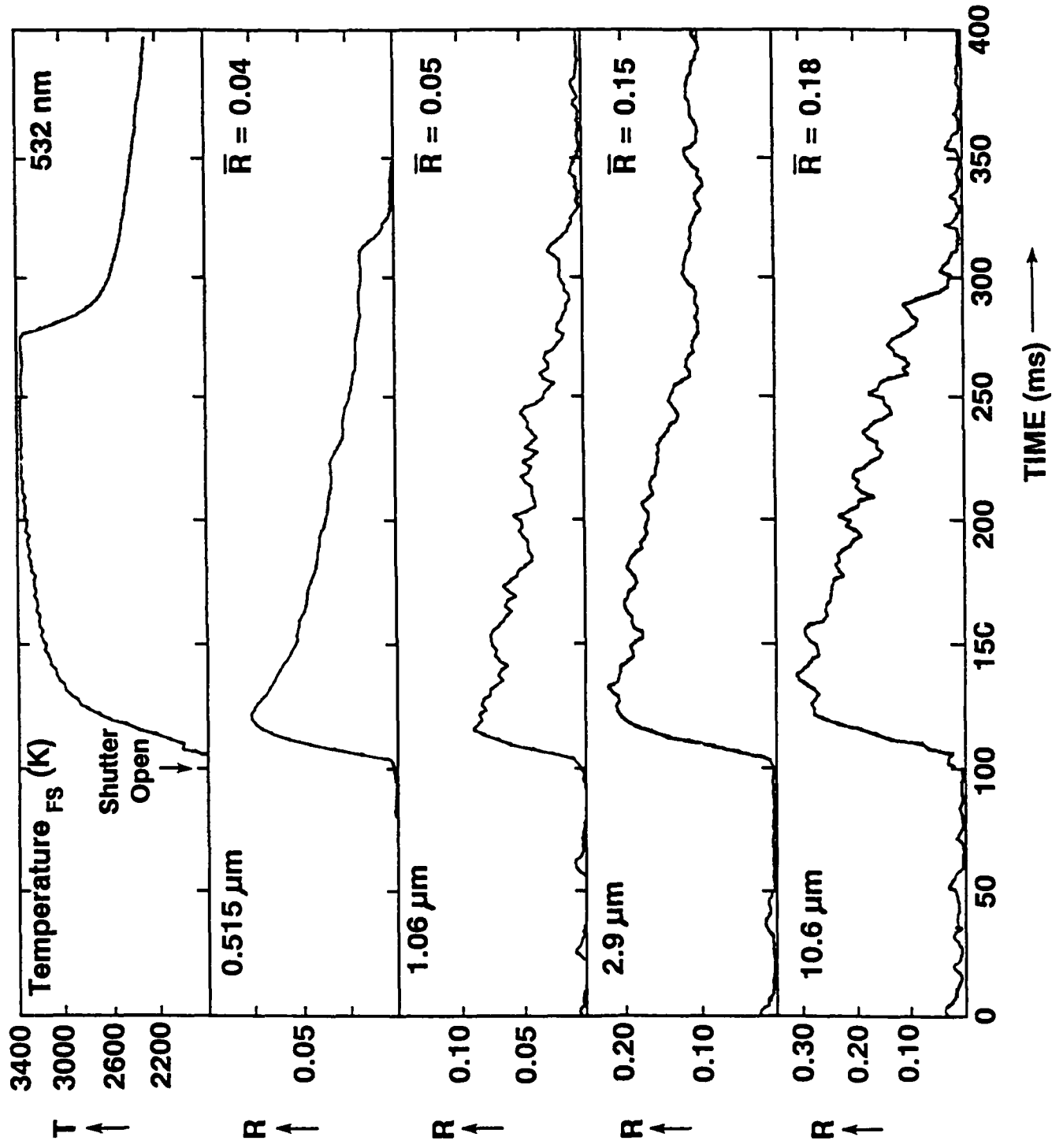
C101: I_{pk} = 9kW/cm^2
TIME RESOLVED REFLECTANCES
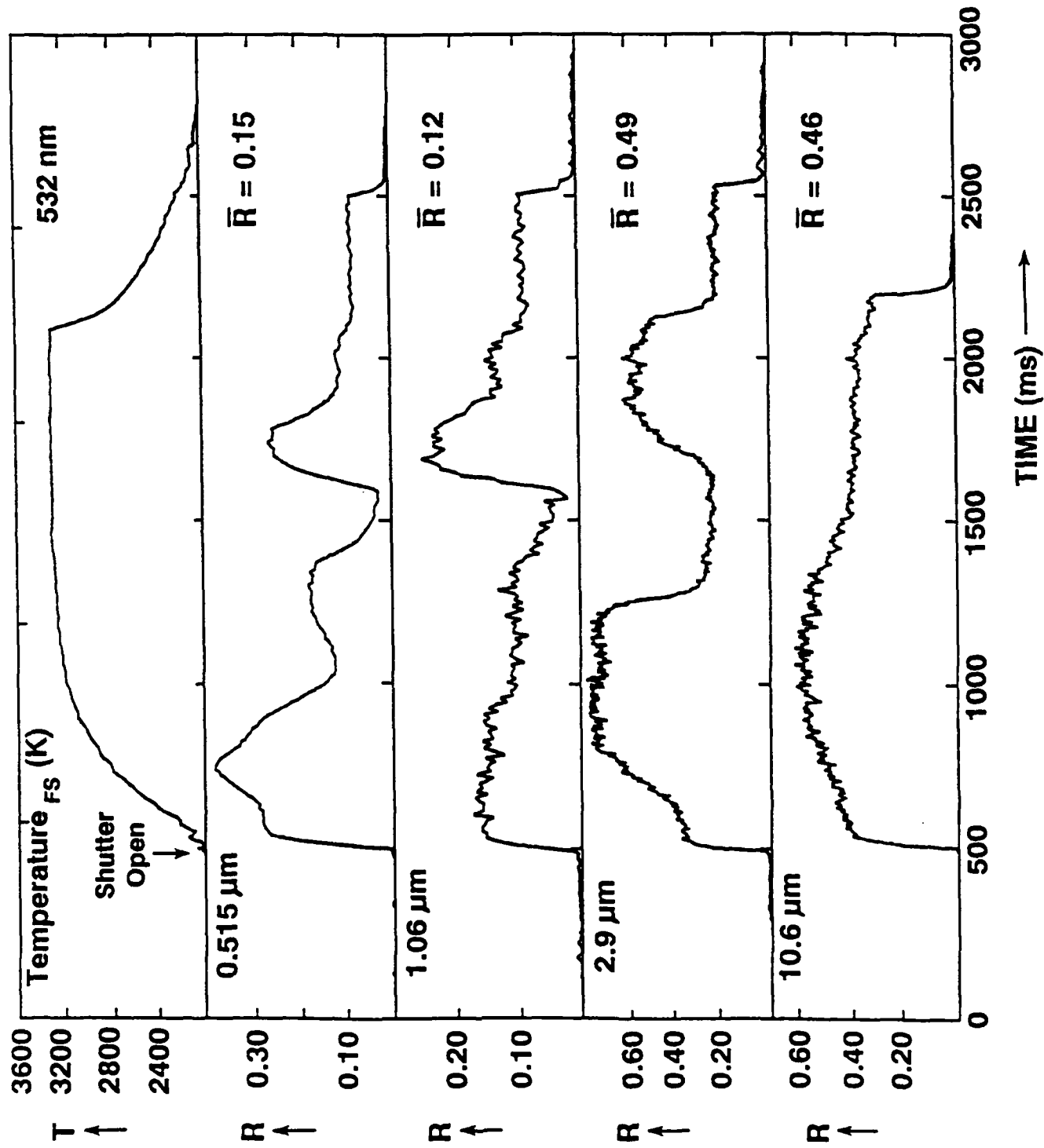
C101: I_{pk} = 100kW/cm^2
TIME RESOLVED REFLECTANCES
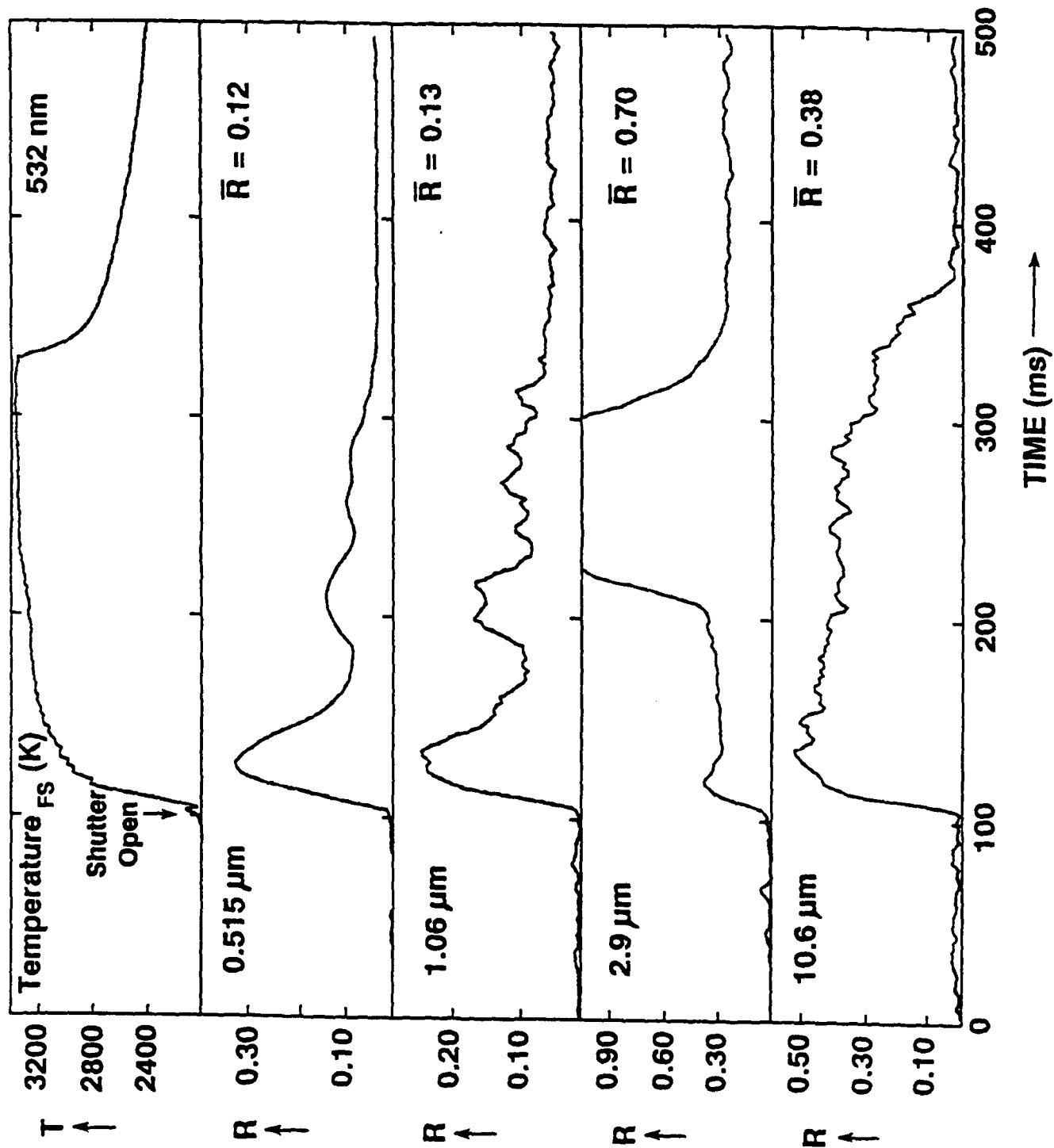
C102: I_{pk} = 9 kW/cm^2

TIME RESOLVED REFLECTANCES

C102: I_{pk} = 100 kW/cm²
TIME RESOLVED REFLECTANCES

Temperature$_{FS}$ (K) — 532 nm

Shutter Open — BT

- 0.515 µm — $\overline{R}$ = 0.10
- 1.06 µm — $\overline{R}$ = 0.13
- 2.9 µm — $\overline{R}$ = 0.60
- 10.6 µm — $\overline{R}$ = 0.59

T: 3200, 2800, 2400

R: 0.10, 0.05

R: 0.15, 0.10, 0.05

R: 0.60, 0.40, 0.20

R: 0.60, 0.40, 0.20

TIME (ms) ⟶

0   200   400   600   800

C104: $I_{pk} = 9 \text{ kW/cm}^2$
TIME RESOLVED REFLECTANCES

C104: $I_{pk} = 100$ kW/cm^2

TIME RESOLVED REFLECTANCES
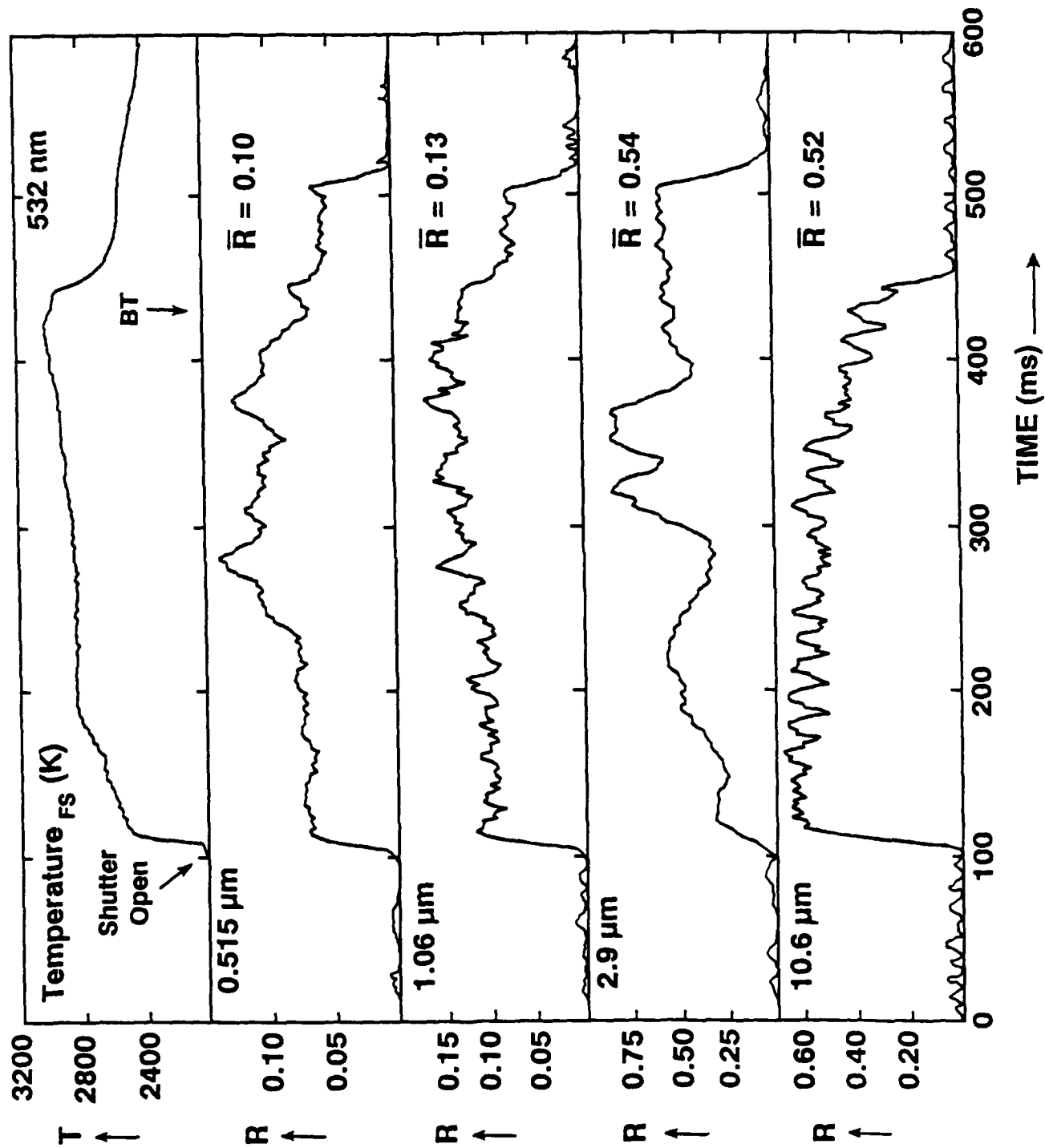
C105: I_{pk} = 9kW/cm^2

TIME RESOLVED REFLECTANCES
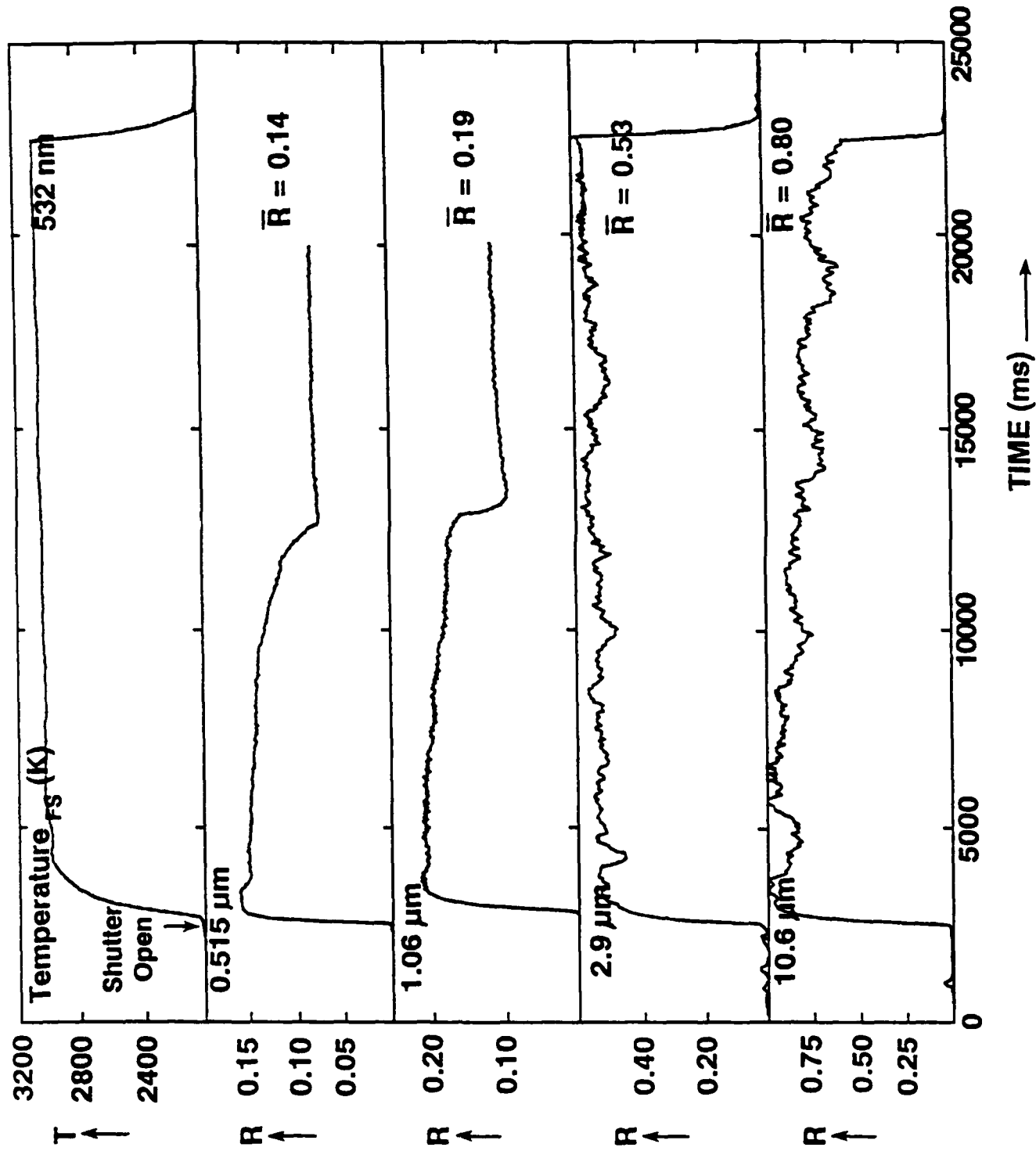
C105: $I_{pk} = 100kW/cm^2$
TIME RESOLVED REFLECTANCES
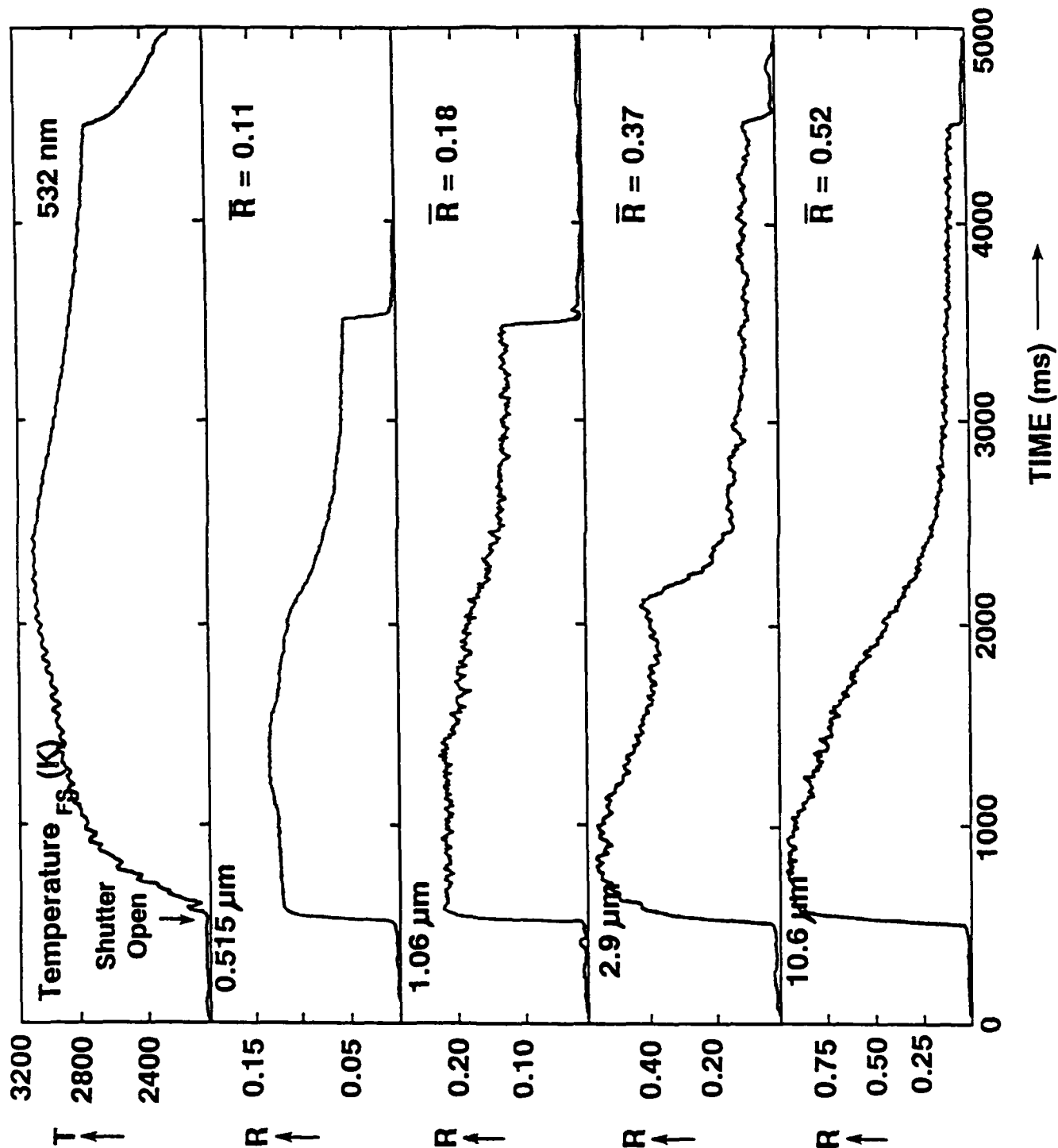
C106: I_{pk} = 9kW/cm²
TIME RESOLVED REFLECTANCES

C106: $I_{pk} = 100kW/cm^2$

TIME RESOLVED REFLECTANCES

Temperature$_{FS}$ (K)

532 nm

Shutter Open

$\bar{R} = 0.23$ — 0.515 µm

$\bar{R} = 0.29$ — 1.06 µm

$\bar{R} = 0.74$ — 2.9 µm

$\bar{R} = 0.53$ — 10.6 µm
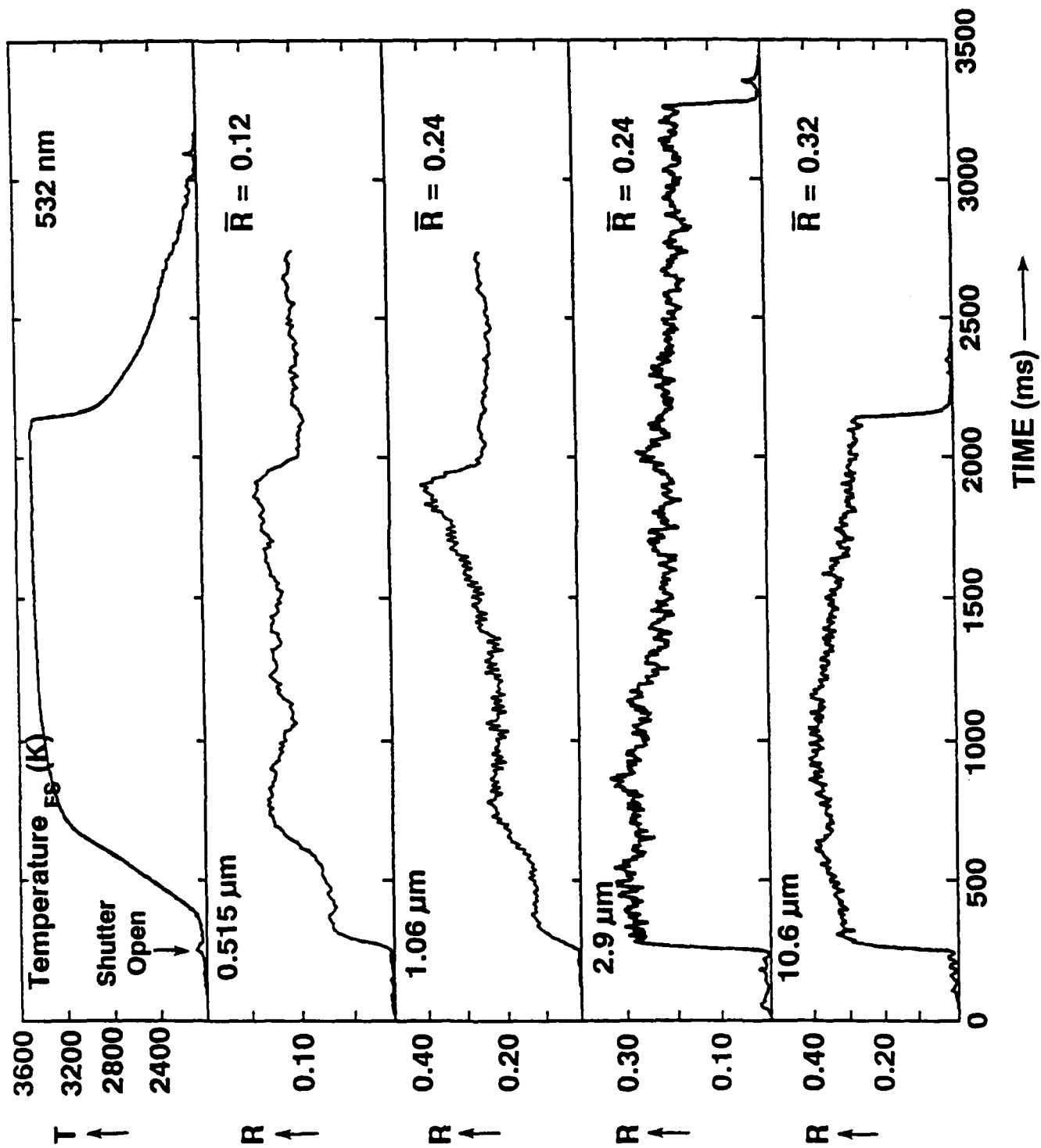
TIME (ms) →
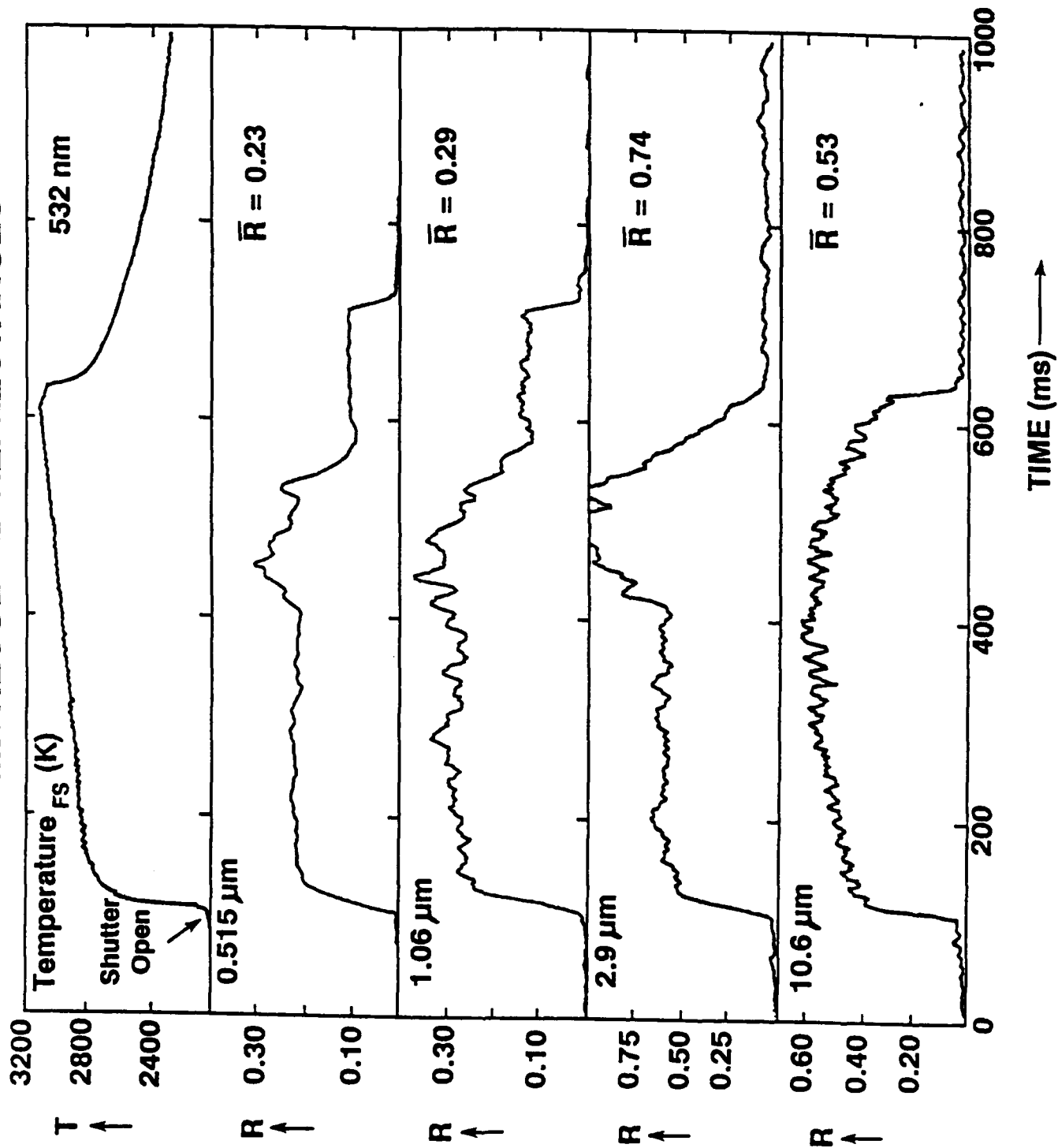
C107: I_{pk} = 9 kW/cm^2

TIME RESOLVED REFLECTANCES
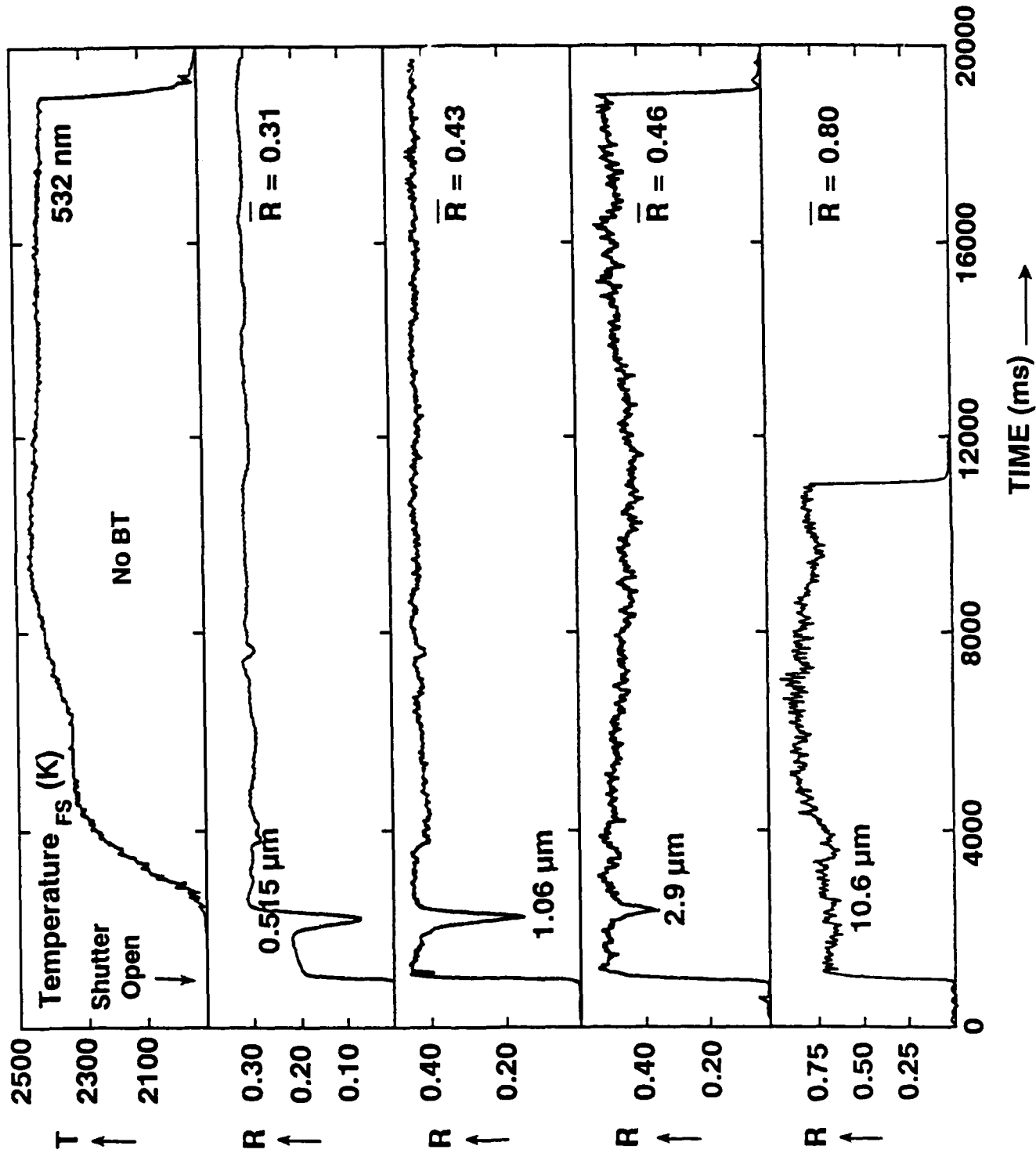
C107: I_{pk} = 100 kW/cm^2

TIME RESOLVED REFLECTANCES
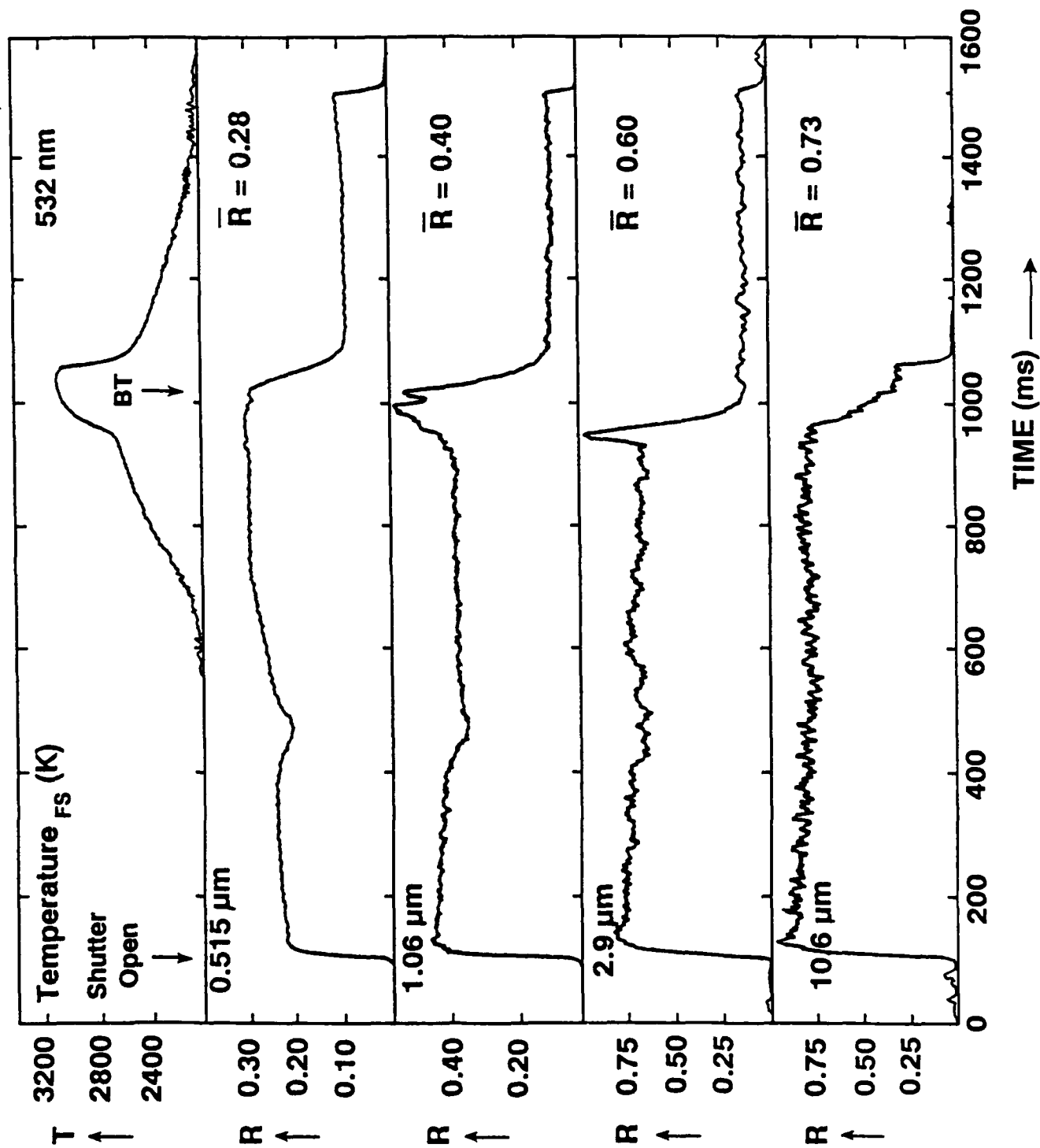
C108: I_{pk} = 9 kW/cm^2
TIME RESOLVED REFLECTANCES
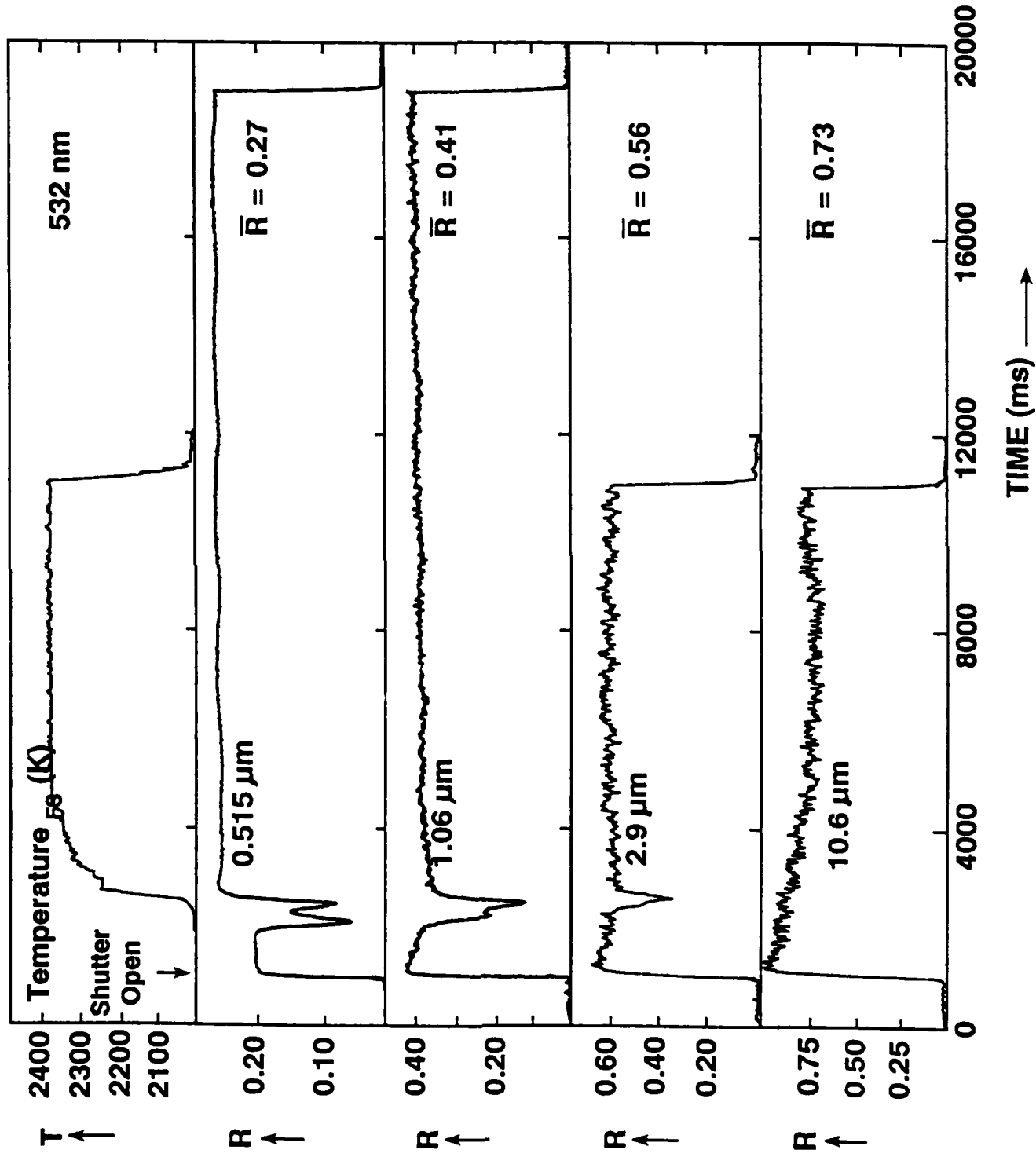
C108: I_{pk} = 100 kW/cm^2
TIME RESOLVED REFLECTANCES
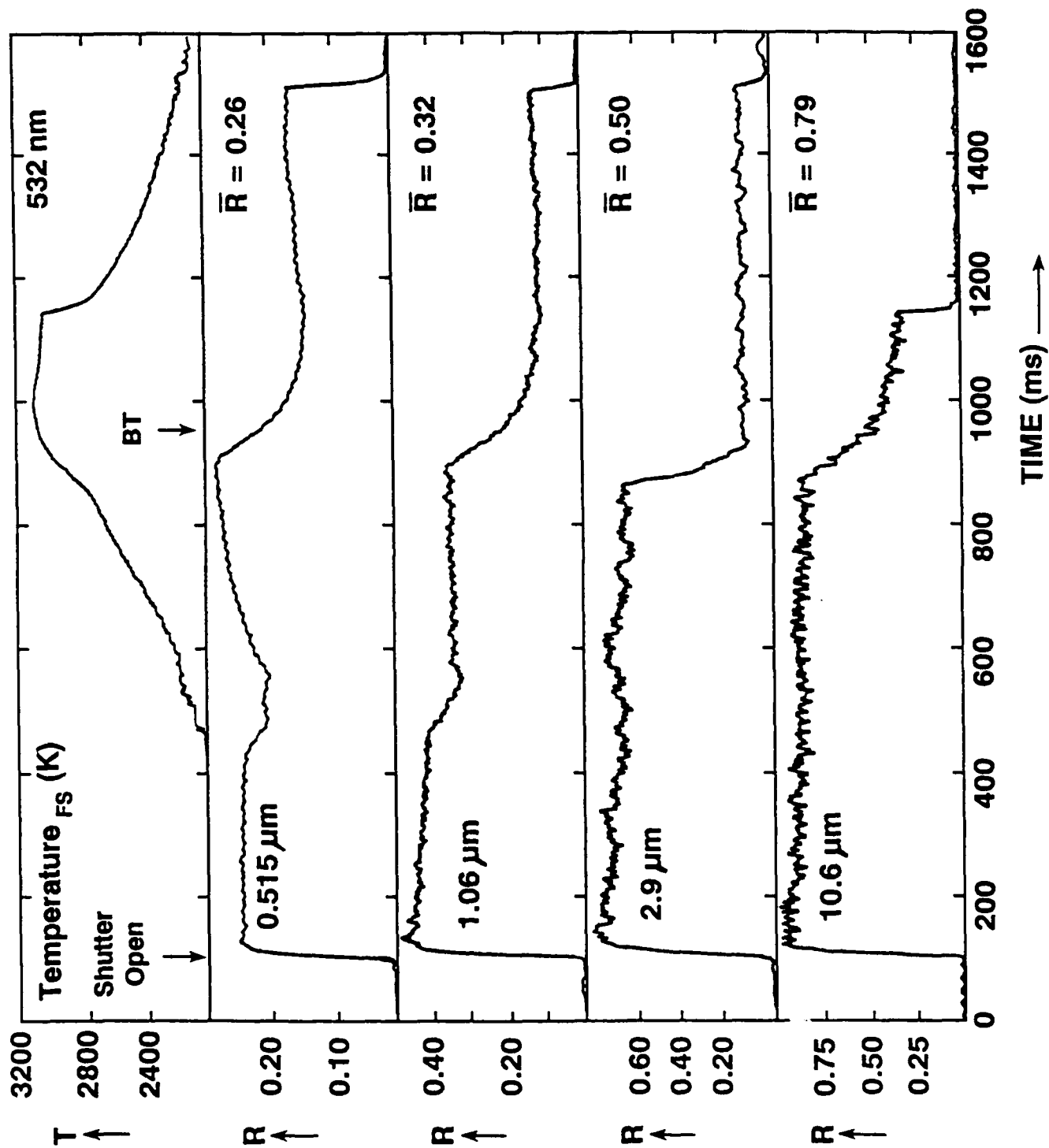
APPENDIX D: Survey Plume Emission Spectra

Plume emission spectra (relative emission intensity *vs.* wavelength) are shown for the 330 – 650 nm spectral region. Wavelengths (units: nm) and (in part) spectral assignments of prominent emission features are labelled in each panel. See the text for further discussion of individual spectra. Eleven pages of survey spectra are indicated consecutively as Pages D1 through D11.

Page D1. Plume emission spectra obtained during pulsed HF chemical laser irradiation of graphNOL (G) at 124 J/cm^2 (top panel) and 32 J/cm^2 (bottom panel) peak laser fluences.

Page D2. Plume emission spectra obtained during pulsed HF chemical laser irradiation of material GE at 128 J/cm^2 (top panel) and 32 J/cm^2 (bottom panel) peak laser fluences. These emission spectra are virtually identical to the G emission spectra shown on Page D1.

Page D3. Plume emission spectra obtained during pulsed HF chemical laser irradiation of material AF5 at 124 J/cm^2 (top panel) and 32 J/cm^2 (bottom panel) peak laser fluences. These emission spectra are virtually identical to the G emission spectra shown on Page D1.

Page D4. Plume emission spectra obtained during pulsed HF chemical laser irradiation of material A101 at 128 J/cm^2 (top panel) and 32 J/cm^2 (bottom panel) peak laser fluences. These emission spectra are virtually identical to the G emission spectra shown on Page D1.

Page D5. Plume emission spectra obtained during pulsed HF chemical laser irradiation of material A105 at 128 J/cm^2 (top panel) and 32 J/cm^2 (bottom panel) peak laser fluences. These emission spectra are virtually identical to the G emission spectra shown on Page D1.

Page D6. Plume emission spectra obtained during pulsed HF chemical laser irradiation of materials SR7 (top panel) and SR8 (bottom panel) at 128 J/cm^2 peak laser fluence. These emission spectra are virtually identical to the 128 J/cm^2 G emission spectrum shown in the top panel on Page D1.
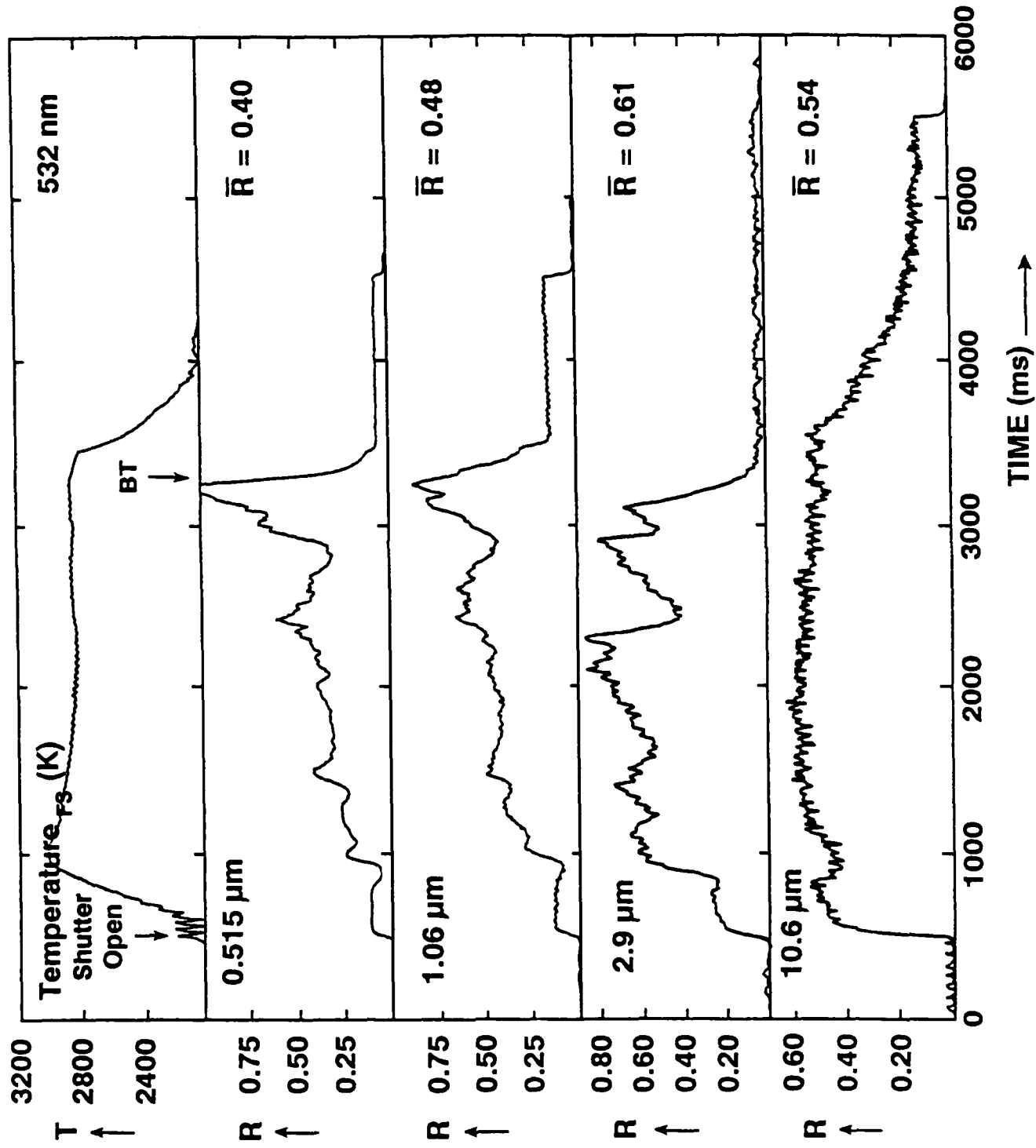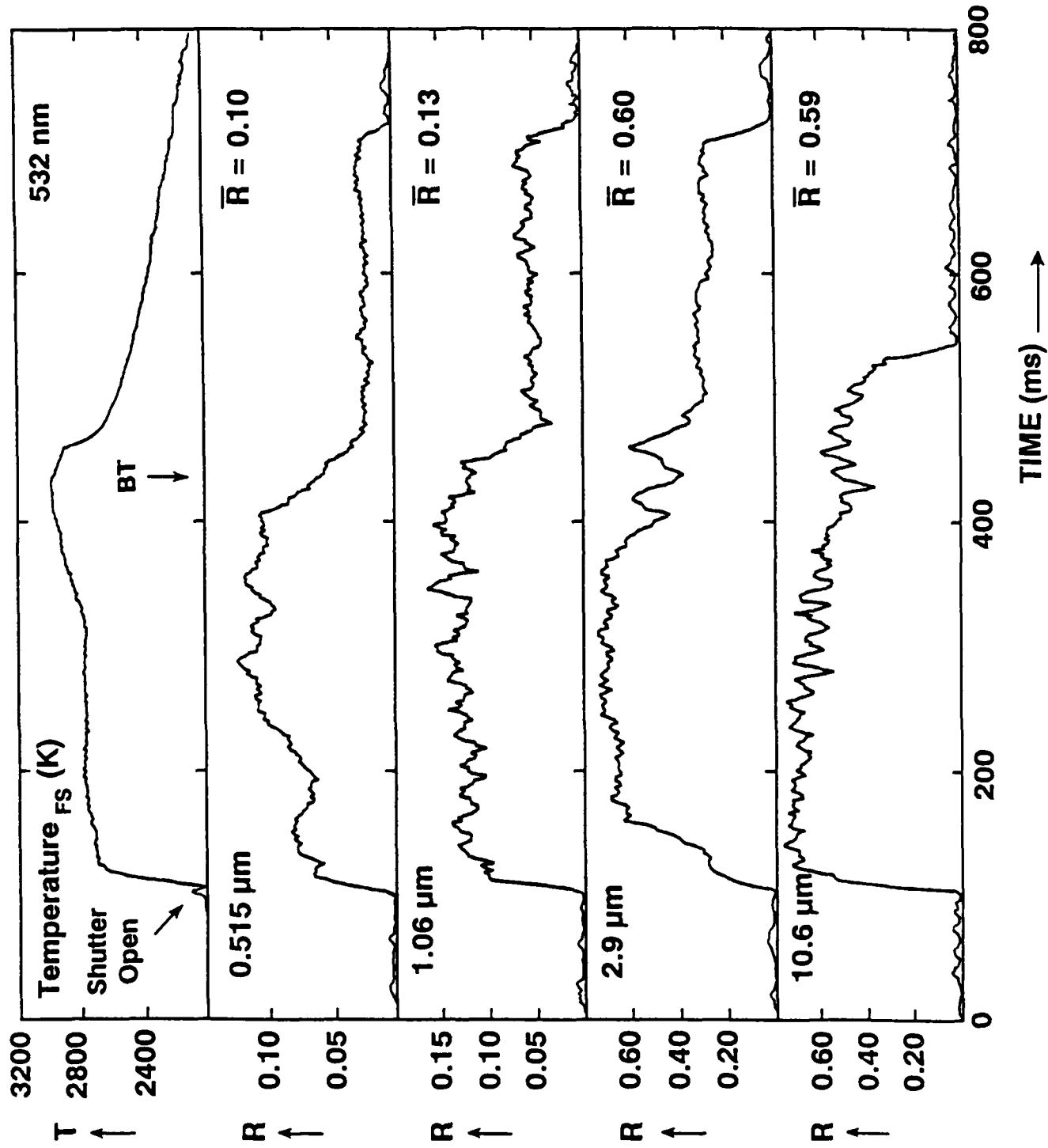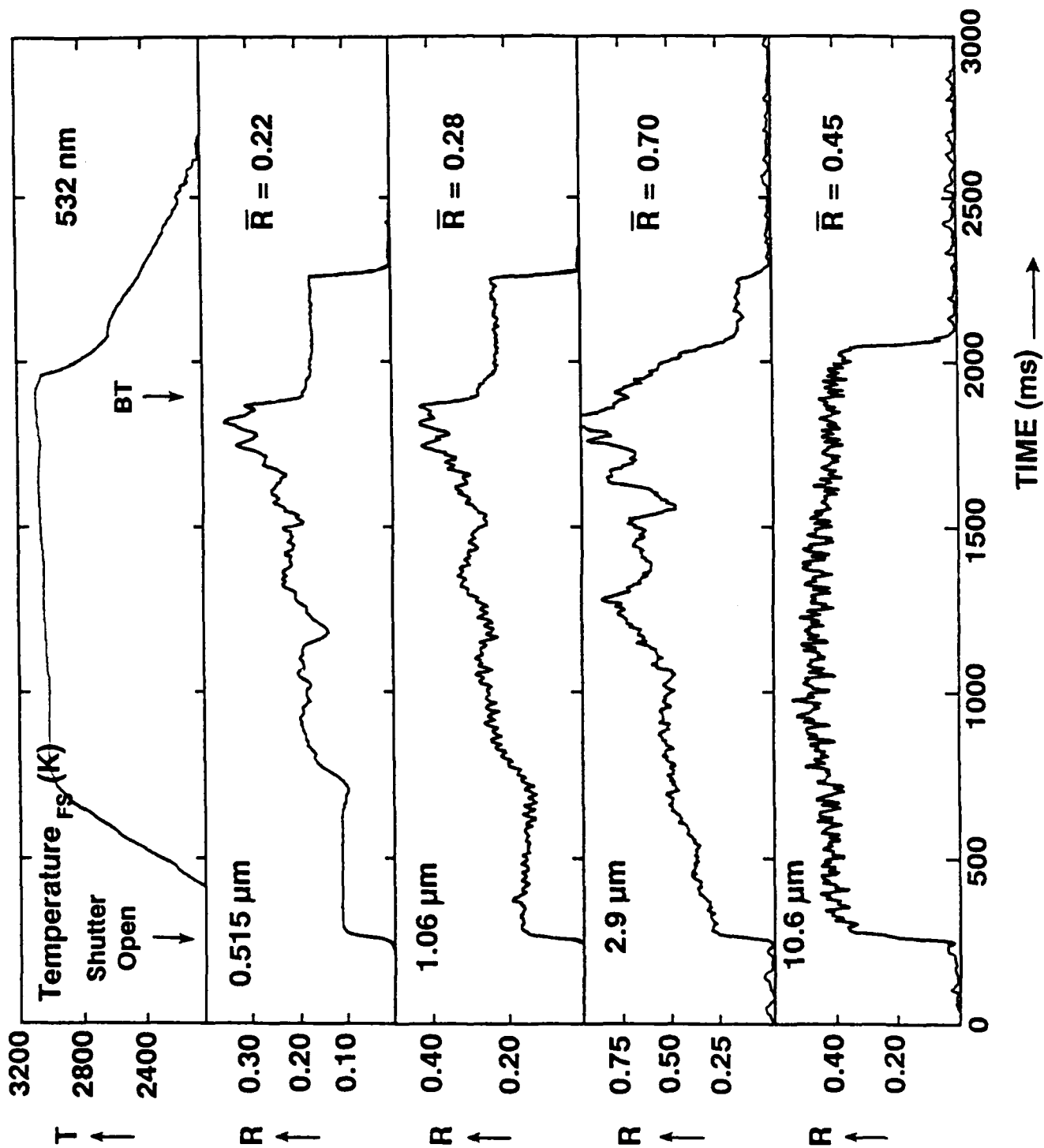
Page D7. Plume emission spectra recorded during pulsed HF laser irradiation of pure Al at 130 J/cm^2 (top panel) and 32 J/cm^2 (bottom panel) peak laser fluences. Preliminary assignments are labelled in the bottom panel.

Page D8. Plume emission spectra recorded during pulsed HF laser irradiation of material Al 6061-T6 (an aluminum alloy) at 128 J/cm^2 (top panel) and 32 J/cm^2 (bottom panel) peak laser fluences. Note that these emission spectra are virtually identical to the pure aluminum emission spectra shown on Page D7.

Page D9. Plume emission spectra recorded during pulsed HF laser irradiation of pure titanium at 132 J/cm^2 (top panel) and 32 J/cm^2 (bottom panel) peak laser fluences.

Page D10. Plume emission spectra recorded during pulsed HF laser irradiation of material TiAl6V4 (a titanium alloy) at 132 J/cm^2 (top panel) and 32 J/cm^2 (bottom panel) peak laser fluences. At the higher laser fluence, the emission spectrum appears virtually identical to the corresponding Ti spectrum; at the lower laser fluence, two additional Al III peaks are identified in the emission spectrum.

Page D11. Plume emission spectra recorded during pulsed HF laser irradiation of material A200 at 132 J/cm^2 (top panel) and 32 J/cm^2 (bottom panel) peak laser fluences. Note that both carbon (*cf.* Page D1) and titanium (*cf.* Page D9) plasma emissions are present.

GraphNOL Emission Spectra

Top panel:

$F_p = 124\ J/cm^2$
Gate = 50 ns
Delay = 60 ns
Vacuum
3 mm
38 μ Slit

14600
Emission
900

C III

465.5
459.0
406.8
505.4
580.4

Bottom panel:

$F_p = 32\ J/cm^2$
50 μ Slit

5150
Emission
800

C II
$^2F^o$ - ^2D
426.1

C III
$^1F^o$ - ^1D
406.8

C III
$^3P^o$ - ^3S
464.5

C II
^4P - $^4P^o$
514.0

C II
387.1

400   500   600

Wavelength (nm) →

GE Emission Spectra

Upper panel:
$F_p = 128$ J/cm^2
Gate = 50 ns
Delay = 60 ns
Vacuum
3 mm
40 μ Slit

Peaks labeled: 406.8, 459.0, 465.5, 505.4, 580.0

Emission axis: 15000 to 850

Lower panel:
$F_p = 32$ J/cm^2
75 μ Slit

Peaks labeled: 387.1, 406.8, 426.1, 464.0, 514.0, 566.9

Emission axis: 5400 to 800

Wavelength (nm) ⟶

x-axis: 400, 500, 600

AF5 Emission Spectra

A101 Emission Spectra

F_p = 128 J/cm²
Gate = 50 ns
Delay = 60 ns
Vacuum
3 mm
40 μ Slit

465.5

406.8

505.4

580.4

F_p = 32 J/cm²
75 μ Slit

426.1

464.5

406.8

387.1

514.0

Emission

14600

1000

14600

1000

400   500   600

Wavelength (nm) ⟶

A105 Emission Spectra

Top panel:
- 11800
- 465.5
- $F_p = 128 \text{ J/cm}^2$
- Gate = 50 ns
- Delay = 60 ns
- Vacuum
- 3 mm
- 40 μ Slit
- Emission
- 505.4
- 459.0
- 406.8
- 580.4
- 800

Bottom panel:
- 4600
- $F_p = 32 \text{ J/cm}^2$
- 75 μ Slit
- 426.1
- Emission
- 387.1
- 406.8
- 464.0
- 514.0
- 750
- 400
- 500
- 600
- Wavelength (nm) ——>
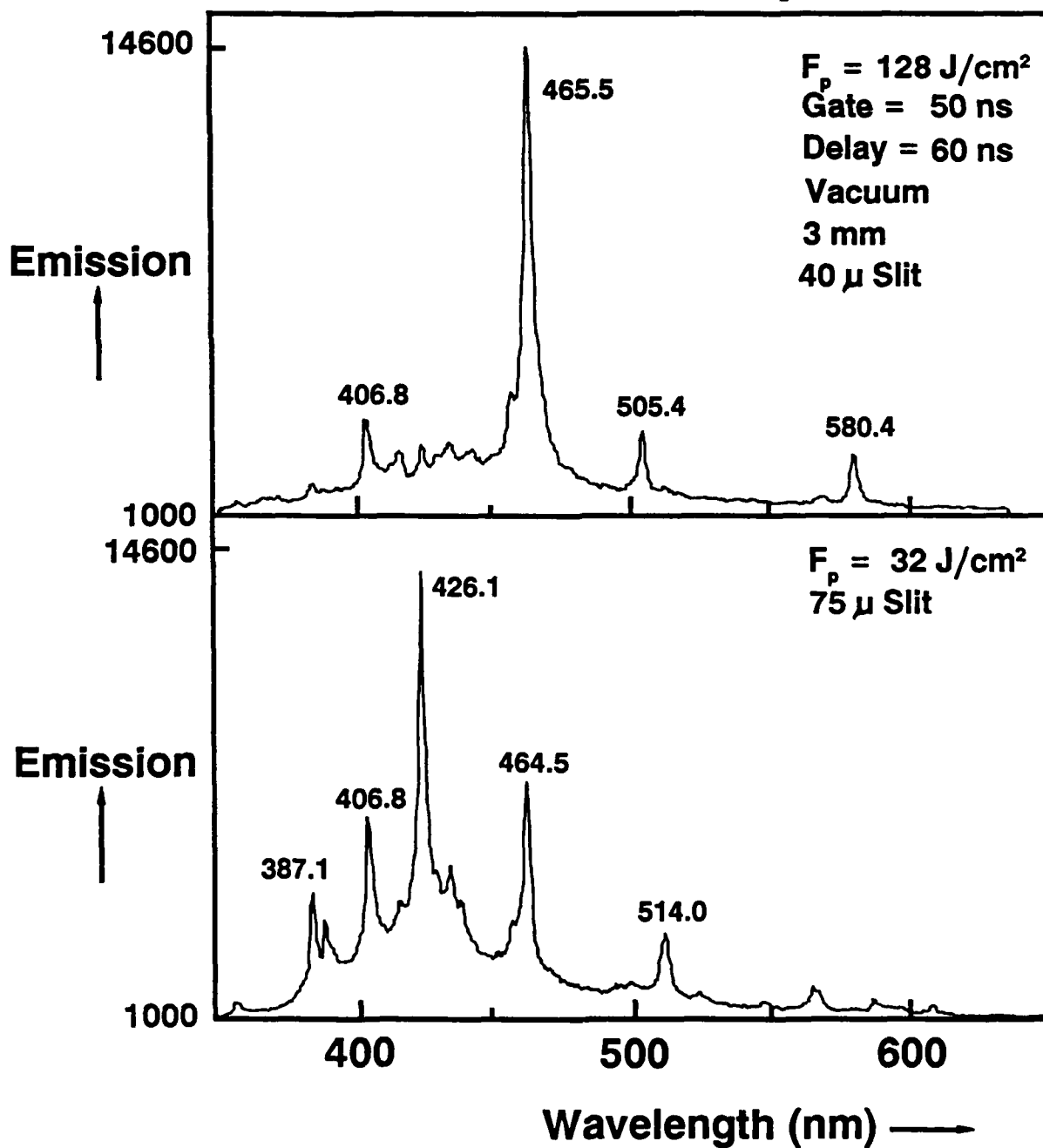
EPOXY Emission Spectra
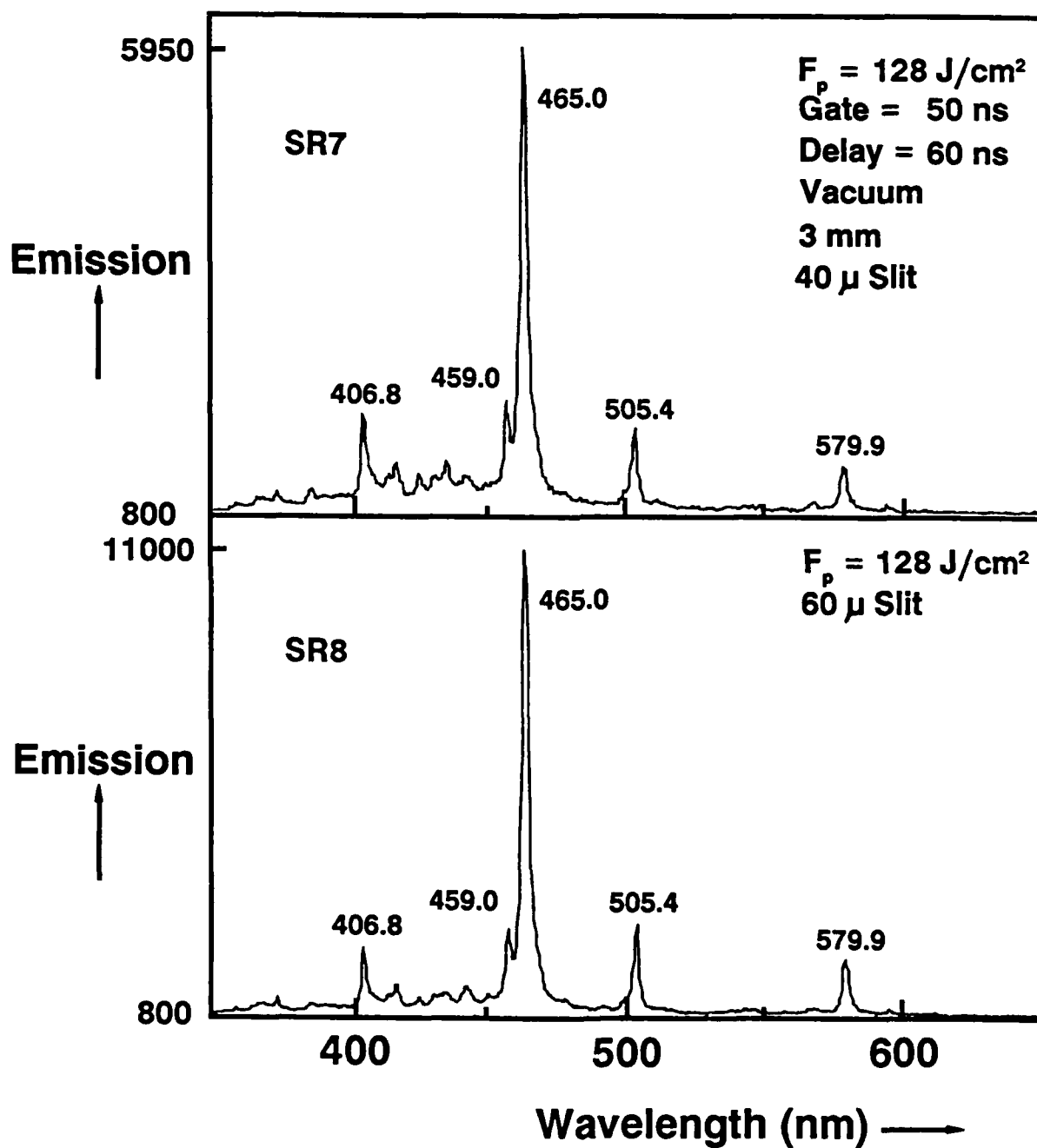
Al Emission Spectra
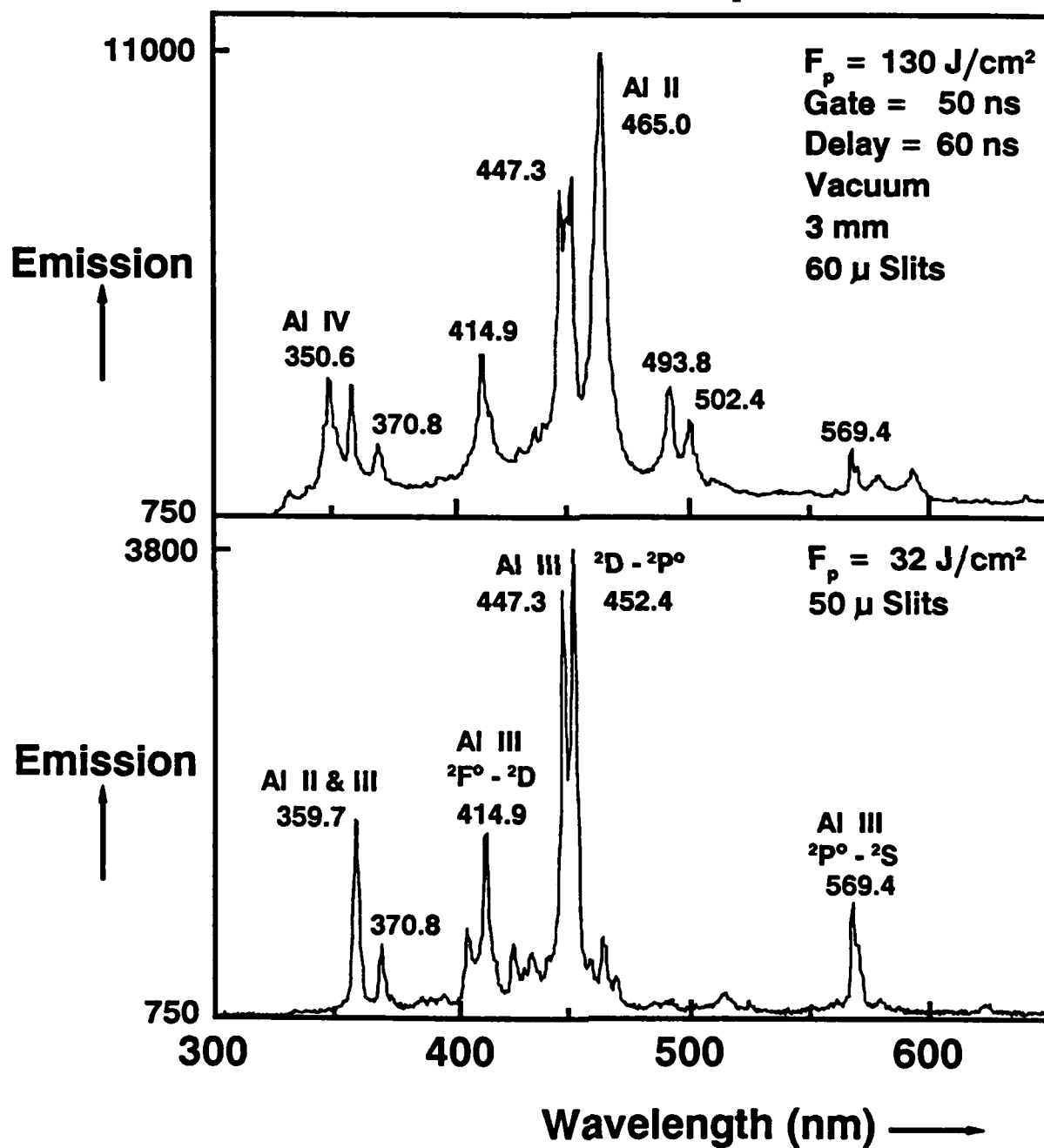
Al - 6061 Emission Spectra

Ti Emission Spectra

Top panel:
$F_p = 132 \text{ J/cm}^2$
Gate = 50 ns
Delay = 60 ns
Vacuum
3 mm
40 μ Slits

Peaks: 357.7, 413.4, 440.2, 461.5, 492.3, 509.0, 540.2, 588.5

Y-axis: Emission, 750 to 10600

Bottom panel:
$F_p = 32 \text{ J/cm}^2$
75 μ Slits

Peaks: 334.3, 357.2, 391.1, 412.9, 439.2, 461.0, 502.9, 512.5, 539.2, 588.0, 596.5

Y-axis: Emission, 750 to 4000

X-axis: Wavelength (nm) — 300, 400, 500, 600
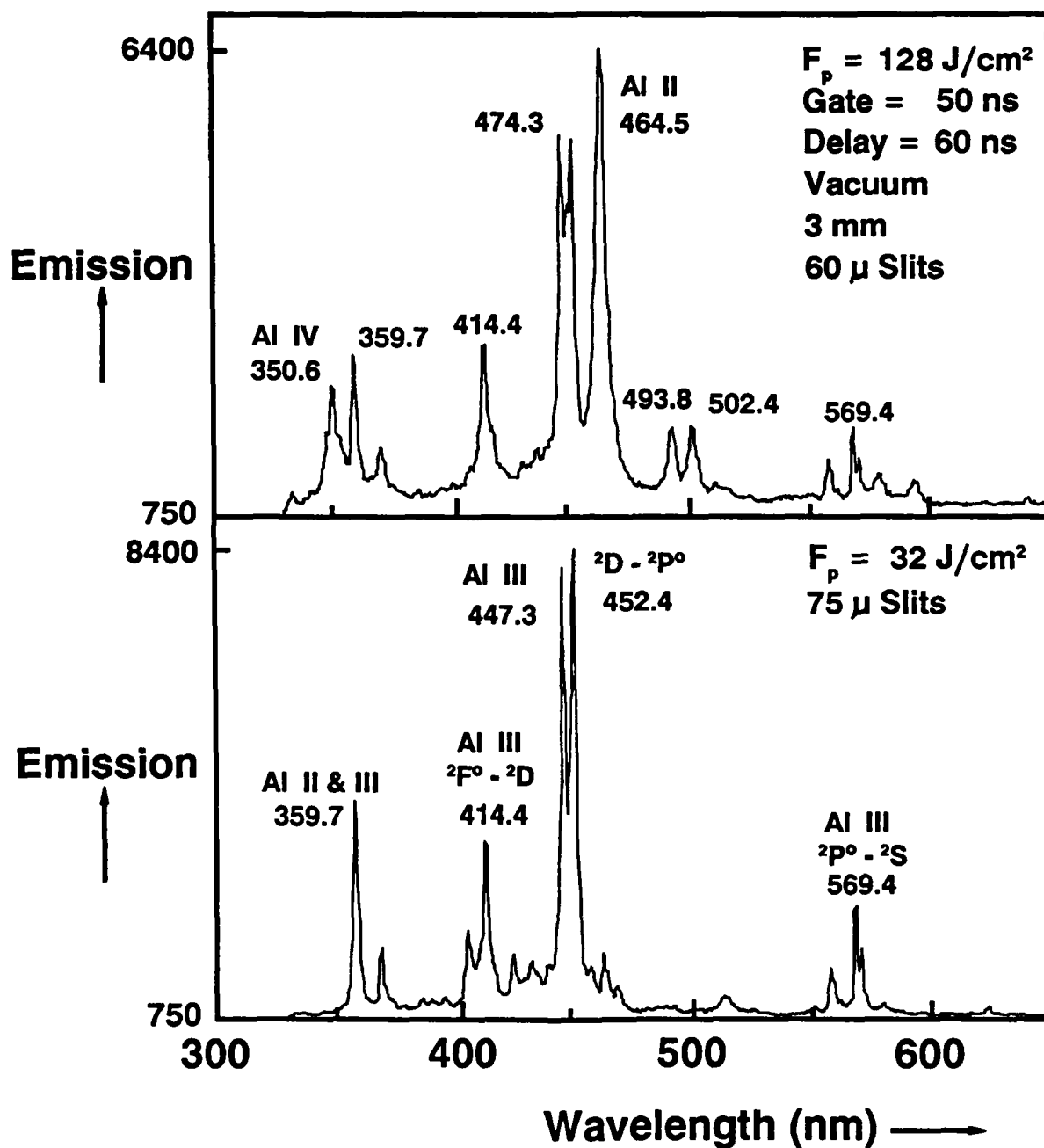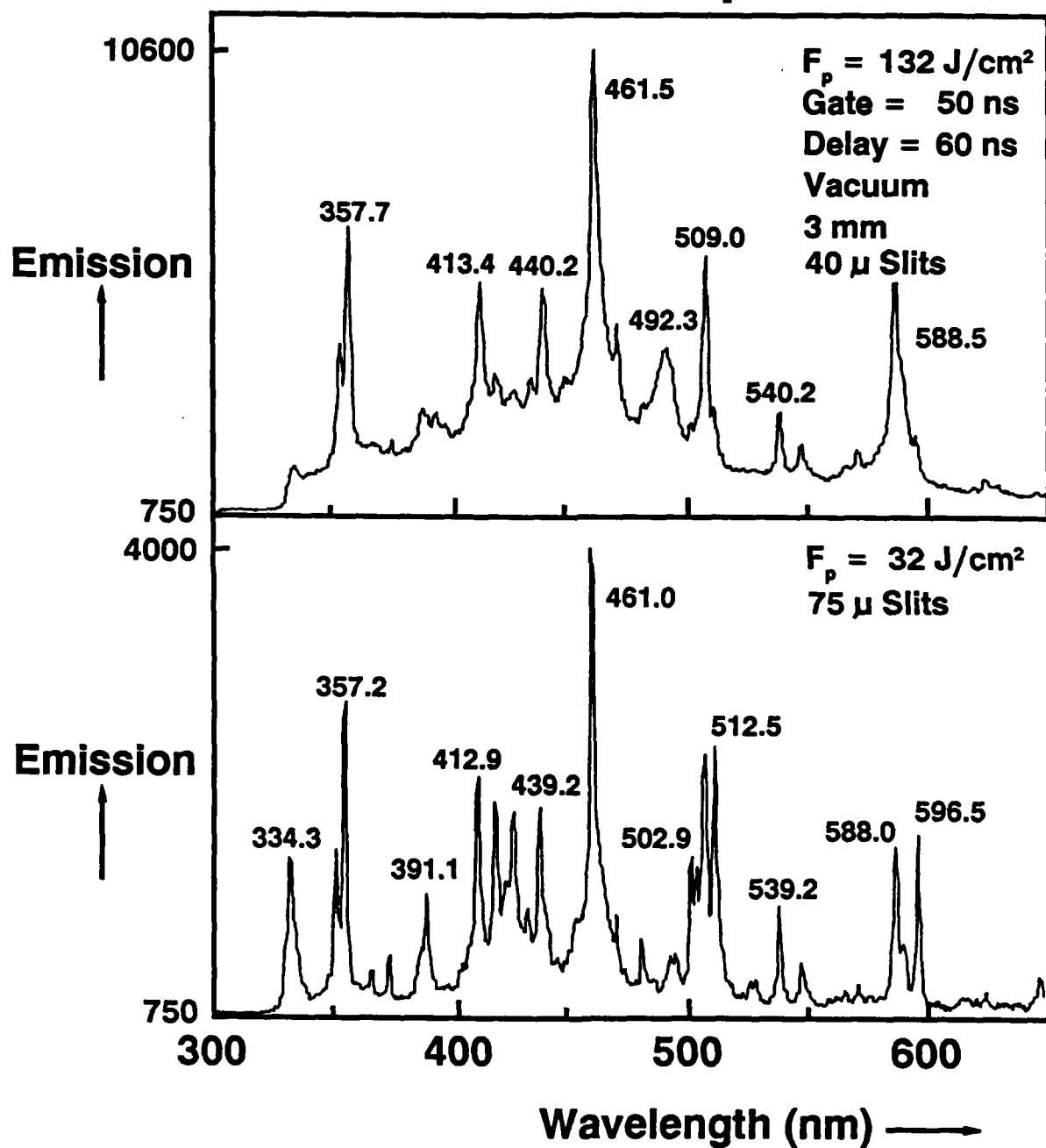
TiAl6V4 Emission Spectra

A200 Emission Spectra

Upper panel:

F_p = 132 J/cm²
Gate = 50 ns
Delay = 60 ns
Vacuum
3 mm
60 µ Slits

Emission axis: 11600 to 750

Peaks: 357.2, 412.9, 461.0, 465.0, 508.5, 539.2, 587.4

Lower panel:

F_p = 32 J/cm²
75 µ Slits

Emission axis: 2450 to 750

Peaks: 334.3, 356.6, 391.1, 406.3, 426.1, 464.0, 502.4, 512.5, 596.5

Wavelength (nm) ⟶

X-axis: 300, 400, 500, 600
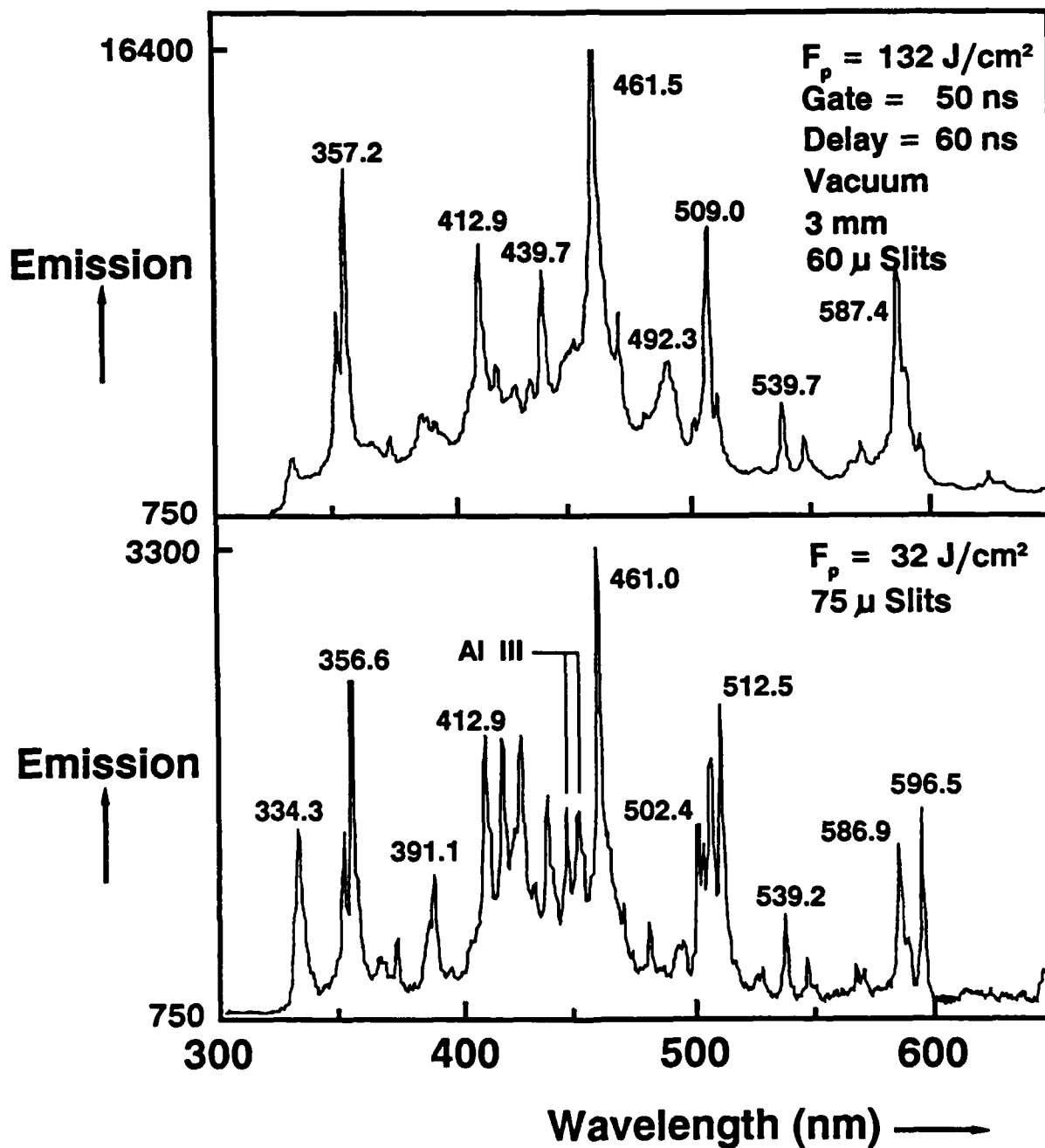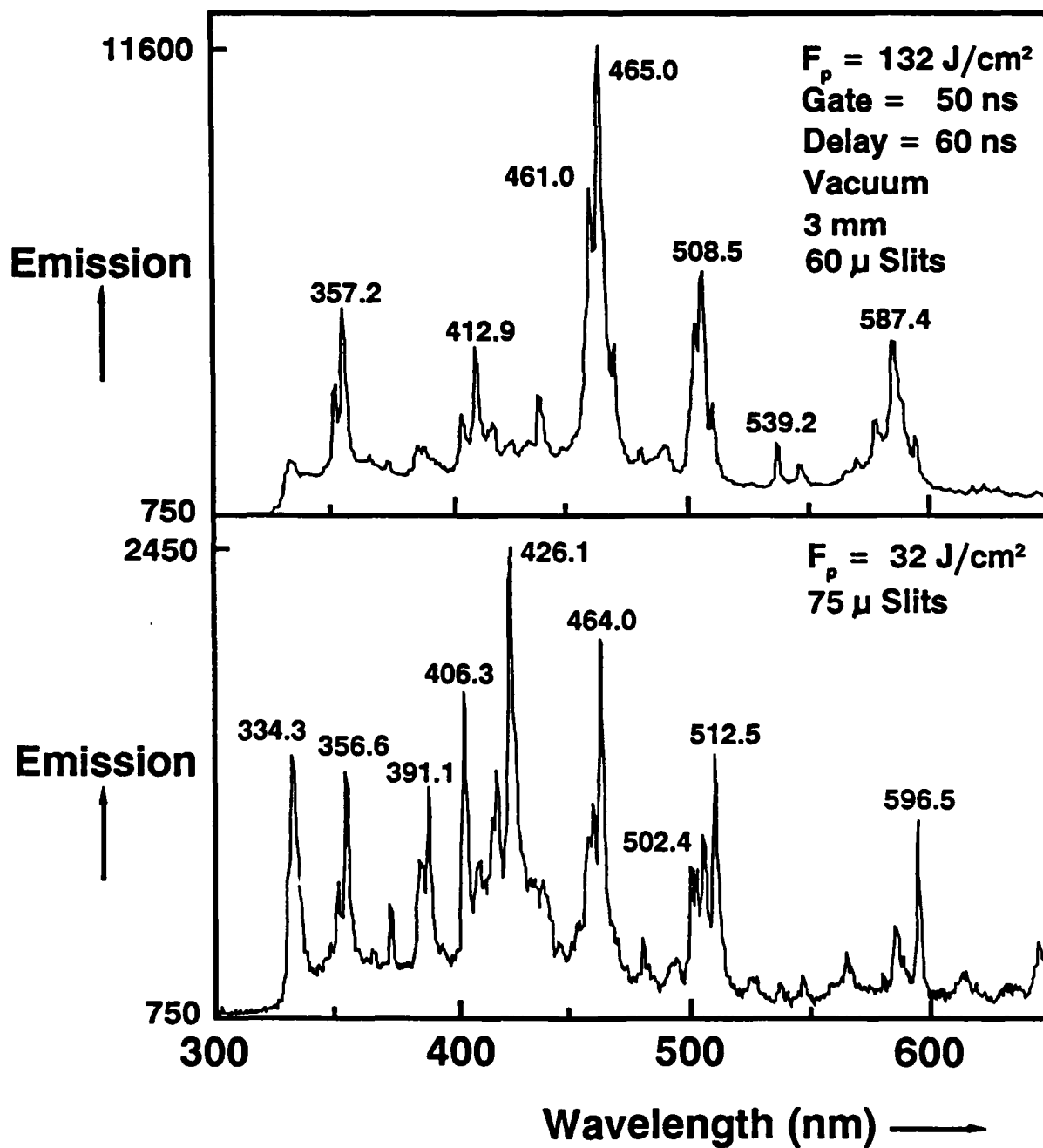
APPENDIX E: Carbon Vapor Species

The following appendix presents calculations on carbon vapor species mole fractions, total vapor pressure, and enthalpy of ablation (for all C_n with n < 7 and for monatomic carbon alone) as a function of temperature over the T = 3000 - 5000 K range.

CARBON VAPOR SPECIES

T(K)	P(atm)	Mole Fraction X_n							$H_A(kJ/g)$	
		C_1	C_2	C_3	C_4	C_5	C_6	C_7	ΣC_n	C_1 only
3000	.0006	.1032	.0613	.8223	.0044	.0086	.0001	.0001	28.989	64.388
3100	.0017	.0932	.0626	.8266	.0057	.0115	.0002	.0002	28.987	64.568
3200	.0043	.0845	.0637	.8288	.0072	.0150	.0003	.0004	28.996	64.749
3300	.0105	.0769	.0646	.8289	.0089	.0194	.0005	.0008	29.014	64.931
3400	.0243	.0702	.0653	.8269	.0108	.0245	.0008	.0014	29.034	65.113
3500	.0538	.0642	.0658	.8228	.0130	.0305	.0013	.0024	29.053	65.296
3600	.1146	.0589	.0661	.8164	.0154	.0374	.0019	.0040	29.064	65.480
3700	.2349	.0541	.0661	.8075	.0180	.0452	.0027	.0065	29.066	65.664
3800	.4657	.0496	.0658	.7959	.0208	.0538	.0038	.0101	29.050	65.848
3900	.8956	.0456	.0653	.7814	.0238	.0633	.0053	.0153	29.015	66.034
4000	1.6760	.0418	.0644	.7637	.0269	.0734	.0072	.0227	28.955	66.220
4100	2.8564	.0401	.0649	.7439	.0295	.0822	.0090	.0305	28.949	66.406
4200	4.7681	.0385	.0650	.7220	.0321	.0911	.0111	.0402	28.923	66.593
43__	7.8127	.0367	.0647	.6982	.0346	.1000	.0135	.0522	28.881	66.781
4400	12.5860	.0350	.0641	.6725	.0370	.1087	.0162	.0664	28.821	66.969
4500	19.9683	.0332	.0632	.6450	.0392	.1171	.0191	.0832	28.751	67.157
4600	31.2503	.0313	.0619	.6158	.0412	.1249	.0223	.1026	28.670	67.346
4700	48.2946	.0295	.0603	.5852	.0429	.1319	.0257	.1245	28.586	67.535
4800	73.8130	.0276	.0584	.5536	.0442	.1381	.0292	.1489	28.501	67.725
4900	111.638	.0258	.0563	.5211	.0453	.1433	.0328	.1755	28.421	67.915
5000	167.270	.0239	.0539	.4883	.0460	.1474	.0363	.2041	28.348	68.105

References:

1) M. J. Berry, "Carbon Vapor Species", Memorandum dated August 1, 1983 (Rice University, Houston, TX) - general method; carbon vapor species up to C_5 with JANAF data.

2) C. A. Klein, M. J. Berry, and P. A. Miles, "Thermochemical Heat of Ablation of Solid Carbon", J. Appl. Phys., 65, 3425-3429 (1989) - general method and comparison with experiment; carbon vapor species up to C_5 with both JANAF and LLNL data; cf. Reference 6 below.

3) H. R. Leider, O. H. Krikorian, and D. A. Young, "Thermodynamic Properties of Carbon Up To the Critical Point", Carbon, 11, 555-563 (1973) - vapor pressures of C_n (n = 1 - 7); enthalpies of formation for C_3 through C_7.

4) M. W. Chase, Jr., C. A. Davis, J. R. Downey, Jr., D. J. Frurip, R. A. McDonald, and A. N. Syverud, JANAF Thermochemical Tables, 3rd Edition (American Institute of Physics, New York, 1986), pp. 536 and 646 - thermochemical data for C_1 and C_2.

5) E. L. Lee and R. H. Sanborn, "Extended and Improved Thermal Functions for the Gaseous Carbon Species C_1 - C_7 from 298 to 10000 K", High Temp. Sci., 5, 438-453 (1973) - gas phase enthalpies for C_3 through C_7.

6) T. Risch, personal communication - general method of Reference 2 is corrected by using carbon mass fractions, rather than mole fractions, to calculate H_A.

APPENDIX F

The following appendix is an updated and extended version of Reference 66 (M. J. Berry, "Optical Properties of Metals").

OPTICAL PROPERTIES OF METALS
Updated (27 Nov 89) Report Contents

1.0 INTRODUCTION

This report summarizes data and some theoretical background on the optical properties of metals (*e.g.*, Au, W, Ta, Mo, and Ir) of interest for spacecraft survivability applications. The discussion is also pertinent to other conductive materials (*e.g.*, carbon barrier materials).

2.0 BACKGROUND

Reference 1 defines the "thermal coupling coefficient" α and its connection with basic laser, materials, and interaction parameters. For the present application, α is equal to the absorptance A of a metallic material, which is related to an "intrinsic" reflectance ($R_{intrinsic}$ - characteristic of a pure single crystal "ideal" material) and to a "defect-generated" absorptance (A_{defect} - characteristic of all defect contributions to optical absorption caused by electron scattering from impurities, voids, lattice imperfections, *etc.*) in the following way:

$$\alpha = A = 1 - R_{intrinsic} + A_{defect}. \qquad [1]$$

This report emphasizes the fundamental optical properties that determine the values of $R_{intrinsic}$ for metals as a function of wavelength, temperature, angle of incidence, and polarization of the incident laser radiation. Further emphasis is directed toward the practical limitations associated with obtaining thin film coatings of metals on particular substrates; in general, the defect-generated absorptance A_{defect} of a metallic material may be very large unless coating deposition conditions (and other variables such as surface roughness) are controlled very well.

References 2 through 4 contain general discussions about optical properties of metals. References 3 through 9 contain specific results of interest for spacecraft survivability.

3.0 IRRADIATION CONDITIONS

Figure 1 shows the irradiation geometry that must be considered. An incident beam with electric field vectors E_P and E_S polarized parallel (P) and perpendicular (S) to the plane of incidence is reflected from the surface. The angle of incidence θ is measured from a normal to the surface. For the case of a thin film of metal deposited on a substrate, the film thickness is assumed to be large enough to "mask" the substrate (*cf.* Section 4.0 below), so than only the optical properties of the metal coating (rather than the substrate and/or the coating/substrate interface) are important. The incident laser irradiance is also assumed to be sufficiently low that nonlinear effects are not important. In Section 4.0, normal incidence (*i.e.*, $\theta = 0$) irradiations by unpolarized lasers are treated first. Then, angle of incidence and polarization effects are treated.
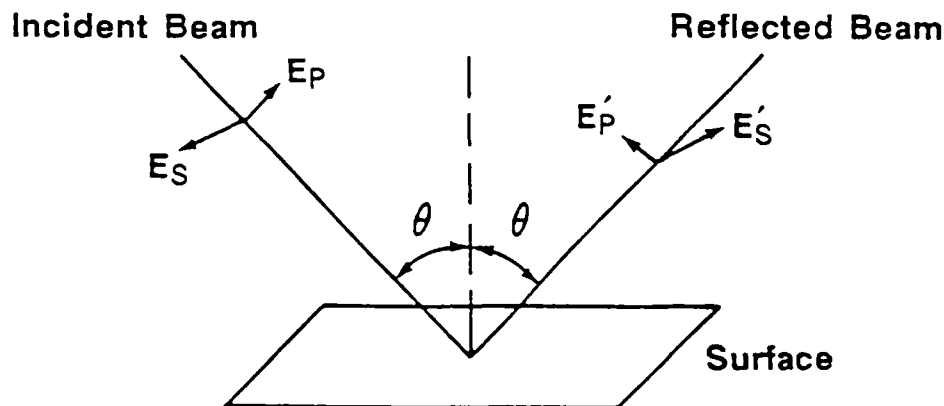
Figure 1. Incident and Reflected Beams at a Surface

4.0 OPTICAL PROPERTIES

4.1 Definitions

The optical properties (absorptance, reflectance, transmittance, *etc.* - note that these quantities are given other names such as absorptivity and reflectivity in some references) of metals and other materials are related to "optical constants" which are wavelength and temperature dependent. These optical constants are derived from experimental measurements such as spectroellipsometry, absorption calorimetry, photometric determination of reflectance, and other methods [References 2 through 4] and are usually tabulated [References 3 through 6] in one of the following ways:

1) as real and imaginary parts of the complex index of refraction N and

2) as real and imaginary parts of the complex dielectric function ϵ [note that this has the same symbol as the emittance in most references].

In this report, optical constants are given as components of N :

$$N = n + ik,\tag{2}$$

where n is the real part of the complex index of refraction (often termed simply the refractive index), i is the square root of -1, and k is the extinction coefficient. Optical constants are often tabulated as components of the complex dielectric function ϵ :

$$\epsilon = \epsilon_1 + i\epsilon_2,\tag{3}$$

where ϵ_1 and ϵ_2 are the real and imaginary parts of the complex dielectric function, respectively. The two representations of optical constants are inter-related by equations [4] through [8]:

$$\epsilon = N^2,\tag{4}$$

$$\epsilon_1 = n^2 - k^2,\tag{5}$$

$$\epsilon_2 = 2nk,\tag{6}$$

$$n = \sqrt{[\epsilon_1 + \sqrt{(\epsilon_1^2 + \epsilon_2^2)}]}/\sqrt{2},\tag{7}$$

and
$$k = \sqrt{[-\epsilon_1 + \sqrt{(\epsilon_1^2 + \epsilon_2^2)}]}/\sqrt{2}.\tag{8}$$

At normal incidence ($\theta = 0$ in Figure 1), there are no polarization effects and the reflectance R and absorptance A are given in terms of the optical constants n and k :

$$R = [(n - 1)^2 + k^2]/[(n + 1)^2 + k^2],\tag{9}$$

and
$$A = 1 - R = 4n/[(n + 1)^2 + k^2].\tag{10}$$

Metals are usually considered to be opaque solids, but their absorptions actually occur exponentially over a finite thickness of material, determined by the absorption coefficient β [note that the absorption coefficient is given the symbol α in most references, but β is used here to prevent confusion with the thermal coupling coefficient], which is related to the extinction coefficient k and the wavelength λ of the incident light:

$$\beta = 4\pi k/\lambda.\tag{11}$$

2

4.1 Definitions (continued)

The absorbed incident light (of irradiance αI) decays exponentially as it penetrates a distance z into the metal:

$$I_z = I\exp(-\beta z). \qquad [12]$$

The penetration depth (skin depth) δ is the inverse of the absorption coefficient β:

$$\delta = 1/\beta = \lambda/(4\pi k). \qquad [13]$$

The light irradiance decreases to $1/e$ (ca. 37%) of its initial value over a distance of δ, to $1/e^2$ (ca. 14%) of its initial value over a distance of 2δ, etc. A thin metallic coating generates an optical response that depends upon the substrate (and/or the coating/substrate interface) if the penetration depth δ is comparable to the coating thickness ℓ. To minimize this complication, the coating thickness ℓ should be much larger than δ. [There is less than 1% transmission for $\ell > 4.606\delta$ which corresponds to film thicknesses in the range 50 - 230 nm for metallic coatings at $\lambda = 3.8$ μm irradiation wavelength.]

The discussion given above neglects phenomena such as the anomalous skin effect (cf. Section 5.1 below) which also influence the absorptances of metallic materials. Section 5.0 treats these additional phenomena.

4.2 Sources of Optical Constants

References 3 through 6 compile sets of optical constants (typically, for low temperature crystalline metal specimens). At long wavelength, the "best" constants are usually identified by the lowest absorptance values (cf. Section 2.0 above). In this report, optical constants for gold (Au), tungsten (W), tantalum (Ta), molybdenum (Mo), and iridium (Ir) were taken from Reference 3 (which in turn selected the constants from several studies). The data reported should be near the "intrinsic limit" for pure metals and thus represent the best performance achievable with thin coatings. Practical limitations are discussed in Section 5.0 below.

4.3 Energy and Wavelength Dependence

Figure 2 shows the dependence of the low temperature (i.e., room temperature or below) absorptance of five metals on photon energy E up to 3.5 eV (energy units of electron volts). Figure 3 shows an expanded region of Figure 2 (up to 0.5 eV photon energy). Figure 4 shows Figure 2 data on a logarithmic wavelength λ scale extending to $\lambda = 165$ nm ($E = 7.5$ eV). Energy E and wavelength λ scales are interconverted using the relation:

$$\lambda \ (\mu m \ units) = 1.240/[E \ (eV \ units)]. \qquad [14]$$

Several laser wavelengths are indicated by vertical arrows on each figure; Table 1 presents a list of laser threats and characteristics. Throughout this report, laser threats at $\lambda = 3.8$ μm and 10.6 μm wavelengths are emphasized.

Figure 3 shows that Au is clearly the lowest absorptance metal (of the five metals shown - among all metals, silver is somewhat less absorptive than gold when prepared under ultrahigh vacuum conditions, but silver tarnishes rapidly upon exposure to oxygen) at long wavelength ($\lambda > 0.6$ μm) for low temperature samples. Au also exhibits very low absorptance (less than 0.01) out to ca. 1.3 eV photon energy (ca. 950 nm wavelength). At larger photon energies, an intense (high absorptance) interband transition is observed which peaks at ca. 2.6 eV photon energy - this transition gives gold its characteristic color. Well below the threshold for this interband transition, the optical properties of gold are dominated by intraband transitions (also termed free carrier or Drude transitions - cf. Reference 2).

3
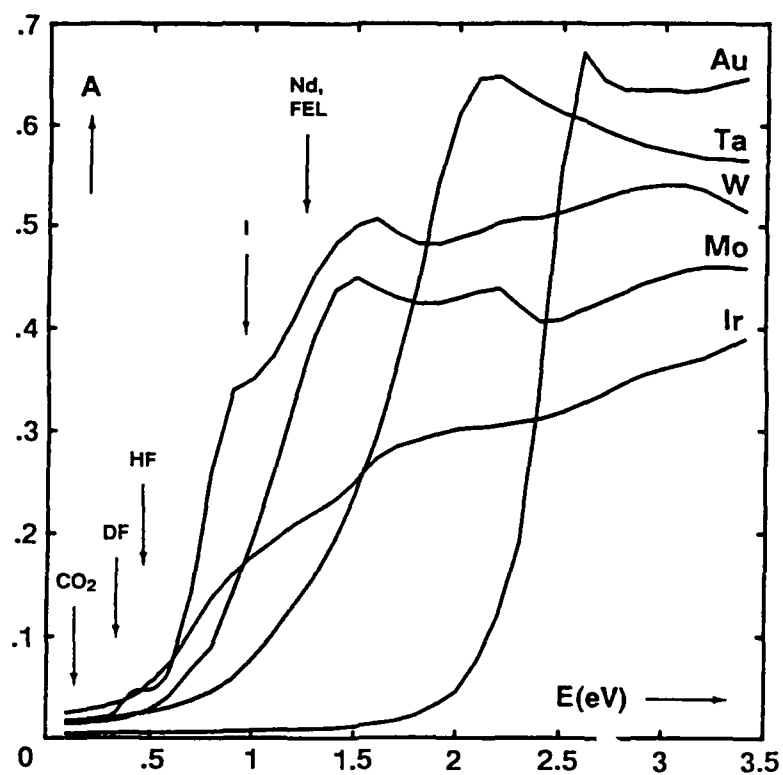
Figure 2. Low Temperature Absorptance of Several Metals *vs.* Photon Energy
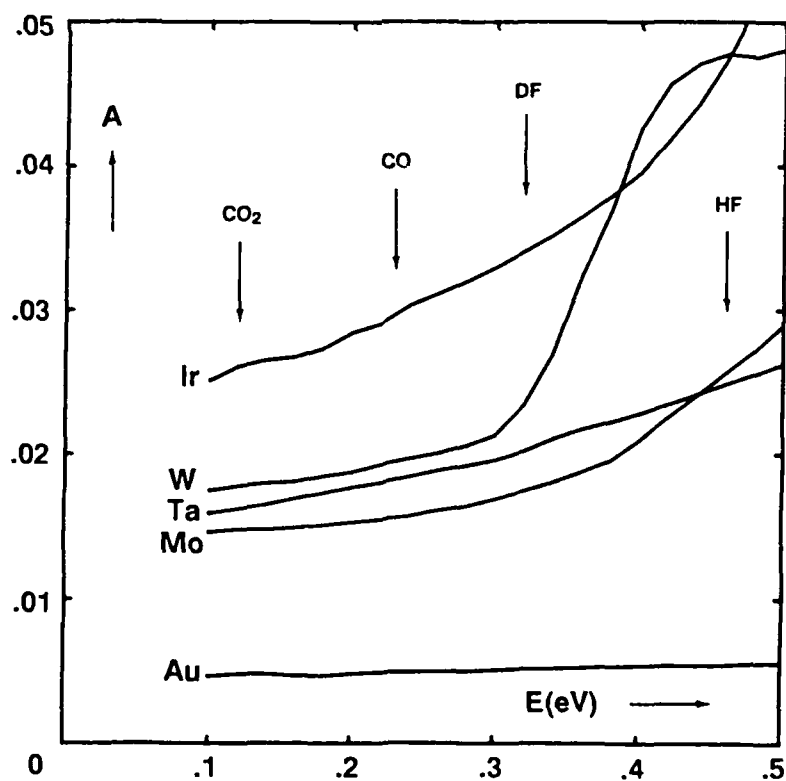
Figure 3. Expanded Version of Figure 2

4
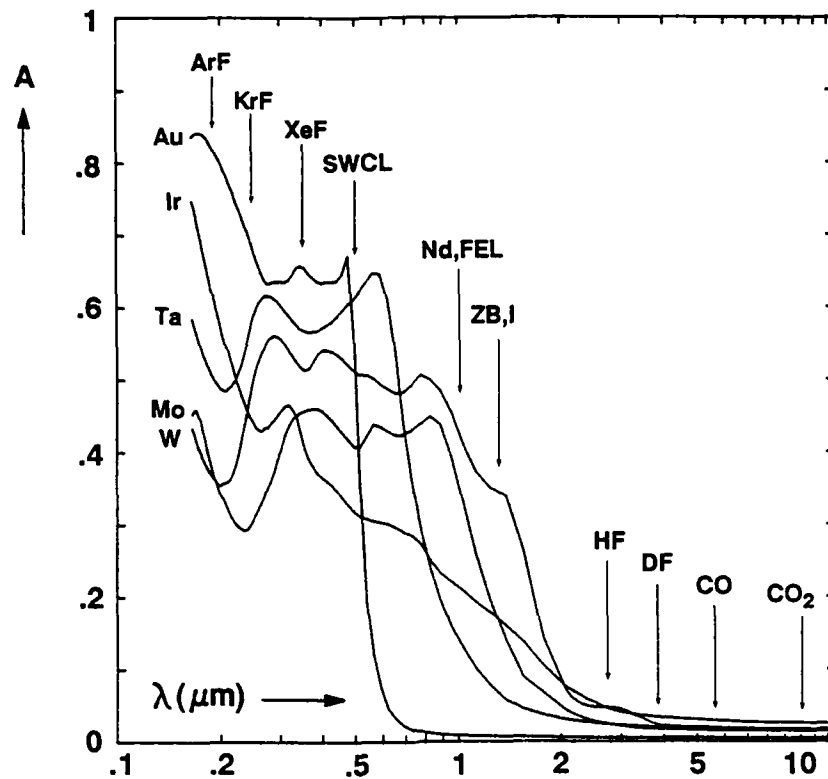
Figure 4. Low Temperature Absorptance of Several Metals *vs.* Photon Wavelength

Table 1. Laser Threats

Wavelength (μm)	Energy (eV)	Laser Type/Abbreviation	Operation[a]
10.6	0.117	Carbon Dioxide (CO_2)	GBL; cw, rp
ca. 5.5	*ca.* 0.23	Carbon Monoxide (CO)	GBL; cw, rp
ca. 3.8	*ca.* 0.33	Deuterium Fluoride (DF)	GBL; cw, rp
ca. 2.7	*ca.* 0.46	Hydrogen Fluoride (HF)	SBL; cw, rp
1.315	0.943	Iodine (I)	GBL/SBL; cw, sp
ca. 1.3	*ca.* 0.95	HF Overtone - Zenith Blue (ZB)	GBL/SBL; cw
1.06	1.17	Neodymium (Nd)	GBL/SBL; rp, sp
≤ 1	≥ 1.24	Free Electron Laser (FEL)	GBL/SBL; rp
≤ 1	≥ 1.24	Short Wavelength Chemical Laser (SWCL)	GBL/SBL; cw
0.496	2.50	Raman-Shifted Xenon Fluoride Excimer (EMRLD)	GBL/SBL; rp, sp
0.351	3.53	Xenon Fluoride Excimer (XeF)	GBL/SBL; rp, sp
0.308	4.03	Xenon Chloride Excimer (XeCl)	SBL; rp, sp
0.248	4.98	Krypton Fluoride Excimer (KrF)	SBL; rp, sp
0.193	6.42	Argon Fluoride Excimer (ArF)	SBL; rp, sp

[a] Key: GBL - ground based laser, SBL - space based laser
cw - continuous wave, rp - repetitively pulsed, sp - single pulse

5

4.3 Energy and Wavelength Dependence (continued)

Figures 2 and 3 also show that Ta has the lowest absorptance up to *ca.* 1.5 eV photon energy among the refractory metals considered. [Mo has slightly lower absorptance than Ta below *ca.* 0.44 eV photon energy, but since Ta is much more refractory, Ta coatings may be more broadly useful than corresponding Mo coatings.] Although Ta is more absorptive than Au at CO_2 (0.12 eV; 10.6 μm) and DF (0.32 eV; 3.8 μm) laser photon energies and wavelengths, Ta is undoubtedly better than Au under irradiation conditions in which Au would melt and vaporize.

At long wavelength ($\lambda > 10$ μm) [equivalent to low photon energy ($E < 0.124$ eV), four of the five metals shown in Figures 2 through 4 (*viz.*, Au, Ta, W, and Mo) have optical properties that can be treated by the free electron (Drude) model of optical properties (*cf.* Reference 2). However, iridium (Ir) has significantly larger absorptances (as shown in Figure 3) than is expected for Drude behavior; it is possible that Ir has low energy interband transitions that contribute to its absorptance even at the CO_2 laser irradiation wavelength.

At short wavelength (equivalently, at higher photon energy), the thresholds of interband transitions are readily observed for W at *ca.* 4.1 μm (0.30 eV), for Mo at *ca.* 3 μm (0.4 eV), for Ta at *ca.* 2 μm (0.6 eV), and for Au at *ca.* 0.9 μm (1.4 eV). These wavelength thresholds are imprecise, but they probably indicate the limiting wavelengths for the applicability of Drude model calculations (which are important for estimating the expected temperature dependence of the absorptance for candidate metals - *cf.* Section 4.4 below).

Note that Figures 2 through 4 show the <u>intrinsic</u> absorptances of candidate metals. The <u>actual</u> absorptances obtained in coated specimens may be considerably larger, depending upon the quality of an individual coating (and the smoothness of the substrate and/or transition coating on which it is deposited). Practical limitations are discussed in Section 5.0 below. The <u>intrinsic</u> absorptances should be considered ideal goals to be obtained by the best processing and fabrication techniques. As substrate preparation and coating deposition techniques improve, near-intrinsic performance for metallic (and other) coatings may be achieved. Near-intrinsic gold coatings (with absorptances of 0.005 at $\lambda = 10.6$ μm) on copper substrates have been developed [Reference 10]. Similar near-intrinsic performance should also be achievable for refractory metal coatings.

4.4 Temperature Dependence

There are no experimental measurements on the absorptances of any metal over a broad temperature range (extending from room temperature to the melting temperature and higher). Therefore, it is necessary to estimate temperature dependent absorptances using a theoretical model (the free electron Drude model [Reference 2]) which relates optical constants to experimentally measured properties (*i.e.*, the temperature dependent electrical resistivities) of candidate metals. The basic method is described in Reference 7; a summary of working equations is presented below.

According to Drude theory, the free electron model parameters ω_p (the electron plasma frequency) and ω_r (the electron relaxation frequency due to, primarily, electron-phonon collisions) are related to optical constants n_λ and k_λ (the real and imaginary parts of the complex index of refraction at wavelength λ) in the following way:

$$\omega_p = \omega(p_1 p_2 / p_3)^{1/2}, \tag{15}$$

and

$$\omega_r = \omega(2 n_\lambda k_\lambda / p_3), \tag{16}$$

where ω is the photon irradiation frequency (proportional to photon energy and inversely proportional to photon wavelength; in cm^{-1} units the photon frequency is found by calculating the quantity $10^4/\lambda$ where the wavelength λ is in μm units), and where the quantities p_i are related to the optical constants n_λ and k_λ as follows:

$$p_1 = n_\lambda^2 - 2n_\lambda + k_\lambda^2 + 1, \tag{17}$$

$$p_2 = n_\lambda^2 + 2n_\lambda + k_\lambda^2 + 1, \tag{18}$$

and
$$p_3 = -n_\lambda^2 + k_\lambda^2 + 1. \tag{19}$$

The temperature-dependent electron relaxation frequency $\omega_\tau(T)$ is calculated from the temperature-dependent electrical resistivity $\rho(T)$:

$$\omega_\tau(T) = \omega_\tau[\rho(T)/\rho], \tag{20}$$

where ω_τ and ρ are the corresponding values at a reference temperature (*e.g.*, room temperature). The electron plasma frequency is assumed to be constant, although it may change a few percent as a function of temperature due to the change of molar volume.

The temperature-dependent optical constants $n_\lambda(T)$ and $k_\lambda(T)$ are calculated at each wavelength from the equations:

$$n_\lambda(T) = \{[S(T) - Q(T) + 1]/2\}^{1/2}, \tag{21}$$

and
$$k_\lambda(T) = \{[S(T) + Q(T) - 1]/2\}^{1/2}, \tag{22}$$

where
$$S(T) = \{[1 - Q(T)]^2 + [Q(T)\omega_\tau(T)/\omega]^2\}^{1/2}, \tag{23}$$

and
$$Q(T) = \omega_p^2/[\omega^2 + \omega_\tau^2(T)]. \tag{24}$$

The temperature-dependent absorptance $A_\lambda(T)$ at normal incidence is then calculated from the temperature-dependent optical constants:

$$A_\lambda(T) = 1 - R_\lambda(T), \tag{25}$$

where
$$R_\lambda(T) = \{[n_\lambda(T) - 1]^2 + k_\lambda(T)^2\}/\{[n_\lambda(T) + 1]^2 + k_\lambda(T)^2\}. \tag{26}$$

Figures 5 and 6 show the temperature-dependent absorptances of four metals (Au, Ta, W, and Mo) at two wavelengths [$\lambda = 10.6$ μm (Figure 5) and 3.8 μm (Figure 6)] calculated using the above model plus temperature-dependent electrical resistivities from References 11 and 12. Each calculation shows a discontinuity at the melting temperature T_m for each metal. For convenience, the Appendix to this report contains tabulated values of the temperature-dependent optical constants and absorptances for the four metals considered. No temperature-dependent absorptances are calculated for Ir since this metal probably cannot be treated by the free electron (Drude) approximation (*cf.* Section 4.3 above). Figure 5 calculations are very good estimates for the metals considered. Figure 6 calculations are, however, expected to be lower limits for the absorptances of each of these metals due to the possible influence of interband transitions (which are not treated by the Drude model); in particular, W calculations at $\lambda = 3.8$ μm wavelength are probably inaccurate due to the onset of an interband transition in W at *ca.* $\lambda = 4.1$ μm wavelength.

Reference 7 discusses the accuracy of Drude model calculations with respect to the limited experimental information available for a few metals (Al, Cu, and Ag) over a small temperature range. Although there is good agreement between observed and calculated absorptances for this limited data base, it is necessary to obtain direct absorptance measurements for candidate metals at very high temperatures in order to confirm the calculations shown in Figures 5 and 6.
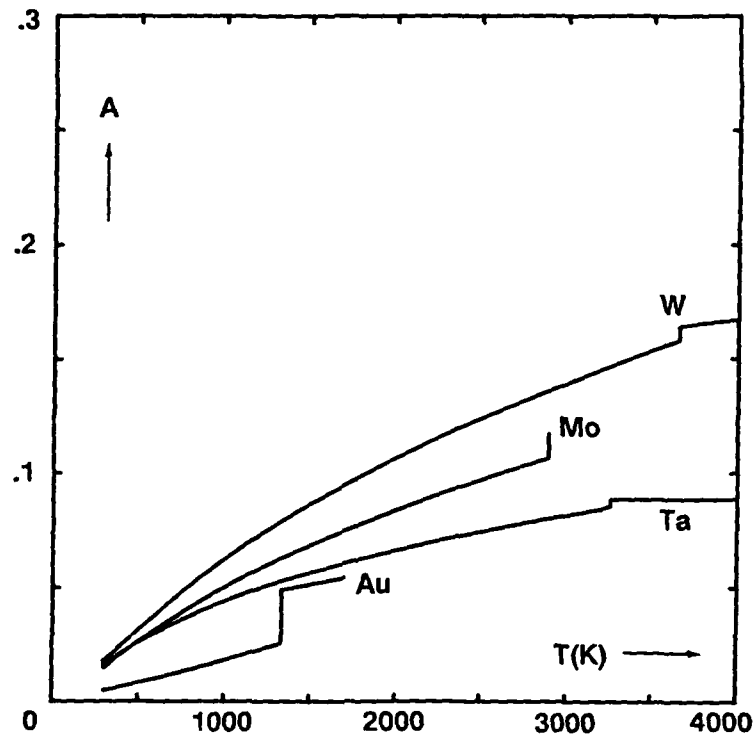
Figure 5. Absorptance of Several Metals at $\lambda = 10.6$ μm *vs.* Temperature
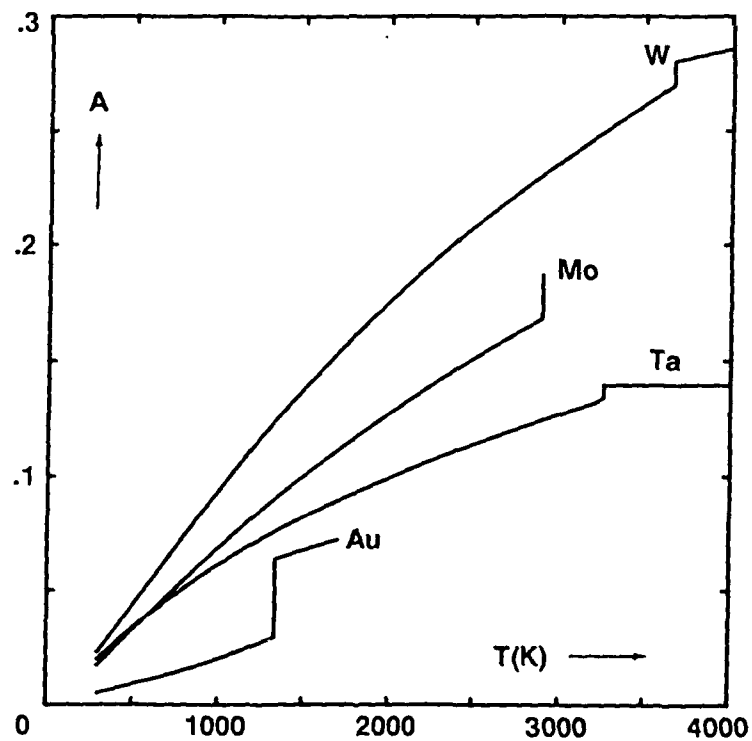
Figure 6. Absorptance of Several Metals at $\lambda = 3.8$ μm *vs.* Temperature

8

4.4 Temperature Dependence (continued)

Some conclusions based on the Drude model calculations of temperature-dependent absorptances are:

1) at each temperature, each metal is more absorptive at $\lambda = 3.8$ μm than at 10.6 μm, and

2) Ta has much lower absorptance at each wavelength and temperature than the other two refractory metals (W and Mo).

Ta offers superior potential for a coating material due to its low absorptance over an extended temperature range. It should also be superior to Au for irradiation conditions that would cause Au to melt and/or vaporize. This deduction should be tested computationally by numerical simulations of target responses and experimentally by direct laser irradiation at specified irradiance levels.

The above conclusions are only valid for intrinsic metallic coatings that are not contaminated by impurities, defects, *etc*. Section 5.0 presents a discussion on practical limitations. Another important consideration is that refractory metals such as Ta, W, and Mo will generally react with their substrates at elevated temperatures, leading to the formation of refractory carbides, borides, *etc*. that have higher absorptances than their parent metals. Hence, metallic coatings should be inhibited from reaction with their substrates by using diffusion/reaction barriers deposited between the substrate and coating layers.

If a coating as deposited does not have intrinsic optical properties due to surface roughness and other defects, it is possible that heating this coating may actually decrease the absorptance due to annealing effects. High temperature annealing may, therefore, be useful to reduce the defect concentration. Following several cycles of thermal annealing, candidate coatings may exhibit the normal temperature-dependent behavior indicated in Figures 5 and 6.

4.5 Polarization and Angle of Incidence Dependence

The above sections treat the optical properties of metals under normal incidence ($\theta = 0$; *cf*. Figure 1) irradiation conditions. At nonzero angles of incidence, there are major differences between the absorptances of photon beams that are polarized parallel (P) *vs*. perpendicular (S) to the plane of incidence (*cf*. Figure 1). The optical constants n_λ and k_λ can be used to calculate the reflectances of incident photon beams for both polarizations as a function of the angle of incidence [Reference 13]:

$$R_S = [(a - \cos\theta)^2 + b^2]/[(a + \cos\theta)^2 + b^2], \qquad [27]$$

and
$$R_P = R_S\{[(a - \sin\theta\tan\theta)^2 + b^2]/[(a + \sin\theta\tan\theta)^2 + b^2]\}, \qquad [28]$$

where
$$a^2 = \{\sqrt{[(n_\lambda^2 - k_\lambda^2 - \sin^2\theta)^2 + 4n_\lambda^2 k_\lambda^2]} + (n_\lambda^2 - k_\lambda^2 - \sin^2\theta)\}/2, \qquad [29]$$

and
$$b^2 = \{\sqrt{[n_\lambda^2 - k_\lambda^2 - \sin^2\theta)^2 + 4n_\lambda^2 k_\lambda^2]} - (n_\lambda^2 - k_\lambda^2 - \sin^2\theta)\}/2. \qquad [30]$$

The absorptance can also be calculated for a beam with an arbitrary polarization $\wp$, which is given in terms of the irradiances of the parallel (I_P) and perpendicular (I_S) components of the incident radiation:

$$\wp = (I_P - I_S)/(I_P + I_S). \qquad [31]$$

The reflectance for arbitrary polarization $\wp$ is given by:

$$R_\wp = [R_P(1 + \wp) + R_S(1 - \wp)]/2. \qquad [32]$$

9

4.5 Polarization and Angle of Incidence Dependence (continued)

For unpolarized ($\wp = 0$) radiation, the reflectance is the average of the polarized beam values:

$$R_{\wp=0} = (R_P + R_S)/2. \qquad [33]$$

For $\theta = 0$, there are no polarization effects and equations [27] and [28] reduce to equation [9].

Figure 7 shows the polarization and angle of incidence dependent absorptances of gold (Au) at $\lambda = 3.8$ μm wavelength and room temperature (300 K) calculated using equations [1], [27] through [30], and [33]. The three absorptances plotted are for light that is polarized parallel to the plane of incidence (A_P), perpendicular to the plane (A_S), and unpolarized (A). Similar calculations have been completed for Au at $\lambda = 3.8$ μm wavelength and elevated temperature (1300 K), for Au at $\lambda = 10.6$ μm wavelength at both room and elevated temperatures (300 K and 1300 K, respectively), and for other metals (Ta, W, and Mo) at $\lambda = 3.8$ μm wavelength at both room temperature (300 K) and elevated temperatures (3200 K, 3600 K, and 2800 K, respectively). All the calculations show the same trends evident in Figure 7:

1) A_P increases by more than an order of magnitude and peaks at a near grazing angle of incidence,

2) A_S decreases by several orders of magnitude as $\theta = 90$ is approached,

3) A also increases by a large factor and peaks at large angles of incidence, and

4) these effects are relatively unimportant near normal incidence, but become very significant at larger angles (*e.g.*, $\theta > 60$).

References 8 and 9 confirm these theoretical calculations for gold and other metals by direct experiments. System aspects of the polarization and angle of incidence effects shown in Figure 7 must be considered carefully for spacecraft survivability applications.

5.0 PRACTICAL LIMITATIONS

The fundamental optical constants n and k (equivalently, ϵ_1 and ϵ_2) used to prepare Figures 2 through 7 are near-intrinsic values that pertain to single photon interactions with ideal metals such as pure single crystals without defects. Several phenomena and effects contribute to degrading the performance of real materials such as engineering coatings deposited on structural substrates. In addition, high irradiance laser interactions may lead to nonlinear effects that change target responses. These practical limitations are described in the following sections. Extensive and thoughtful experimentation is required to develop materials that incorporate processing technology improvements and other advances to yield near-intrinsic performance.

5.1 Anomalous Skin Effect

An effect that is neglected in using equations [9] and [10] (which are derived by assuming that the electron mean free pathlength Λ in the metal is small compared to both the penetration depth of the radiation δ (*cf*. Section 4.1 above) and the ratio v/ω_r, where v is the electron velocity and ω_r is the frequency of the radiation in radian/sec units) is the anomalous skin effect [Reference 2 - Section 4.3]. For a metal like gold at long wavelength, the electron mean free pathlength Λ is sufficiently long that the anomalous skin effect provides a new absorption mechanism (*viz.*, inelastic scattering of electrons from the surface of the metal). Depending on the nature of the surface, the anomalous skin effect may increase the absorptance by a large factor [Reference 14]. Gold, however, can approach its near-intrinsic reflectance at $\lambda = 10.6$ μm wavelength for carefully prepared coatings and substrates [Reference 10].

The anomalous skin effect is not important at high temperatures and short wavelengths where the electron mean free pathlength Λ is small.
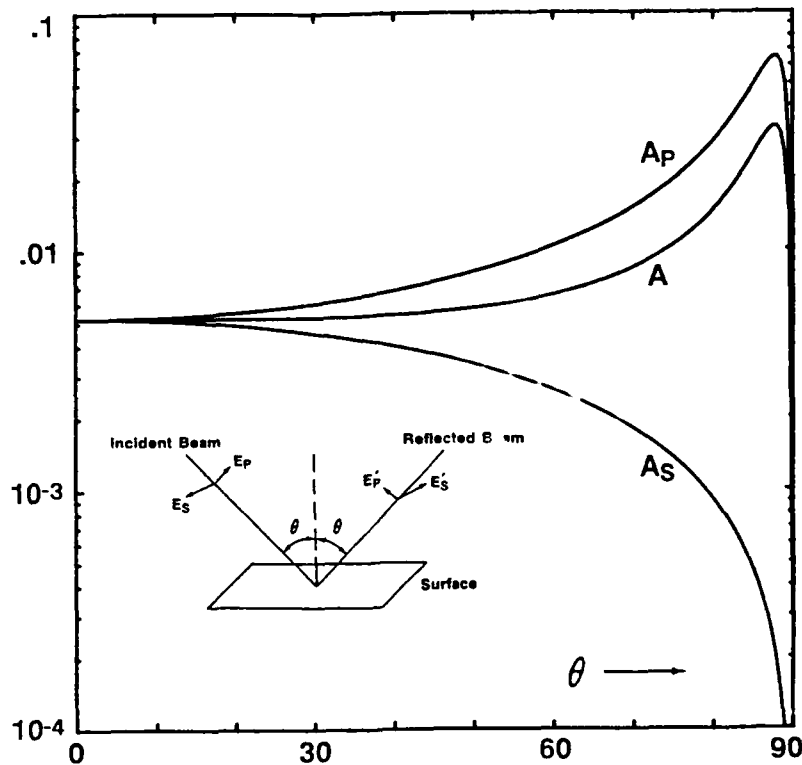
Figure 7. Absorptance of Gold at $\lambda = 3.8$ μm Wavelength and 300 K *vs.* Polarization and Angle of Incidence θ

5.2 Nonlinear Optical Absorption

The optical constants n and k pertain to <u>linear</u> optical responses of materials which are obtained under low irradiance conditions. For advanced short wavelength, high peak irradiance laser threats such as free electron lasers (FELs), strong <u>nonlinear</u> optical phenomena will be important. Depending on the metal considered (and its purity, surface roughness, defect concentration, *etc.*), nonlinear optical responses are likely to be significant contributions to the total absorptance for peak irradiances greater than *ca.* 10^4 W/cm^2. For example, gold coatings irradiated by microsecond pulse duration $\lambda = 10.6$ μm wavelength laser pulses exhibit damage thresholds as low as 2 X 10^4 W/cm^2 [Reference 10] - these damage thresholds are due to nonlinear optical absorption.

.3 Surface Roughness

Surface roughness has long been known to be a limiting factor in the optical performance of materials during laser irradiation [References 10 and 15-16]. Surface roughness can be produced by a "template effect" from a rough substrate, by poor coating procedures, and by mechanical damage in handling and/or exposure. An estimate of the magnitude of the surface roughness effect upon reflectance is provided from the relation [Reference 17]:

$$R = R_0 \exp[-(4\pi\sigma/\lambda)^2], \qquad [34]$$

where R is the observed reflectance, R_0 is the reflectance of a perfectly smooth surface of the same material, σ is the root mean square (rms) surface roughness, and λ is the wavelength of incident light. For $\lambda = 3.8$ μm wavelength irradiation, $R/R_0 = 0.99$, 0.95, 0.90, and 0.80 for values of $\sigma = 0.03$, 0.07, 0.10, and 0.14 μm, respectively, indicating that rms surface roughnesses considerably smaller than 0.07 μm are required to prevent serious degradation of coating performance.

11

5.3 Surface Roughness (continued)

Spacecraft in low earth orbit (LEO) are "sandblasted" by orbital debris, as well as "etched" by reaction with atomic oxygen (AO), over their operational lifetimes (5-10 years). It is therefore advisable to use hard reflective surfaces such as tantalum, rather than soft surfaces such as gold, as reflective coatings. As an alternative, relatively soft surfaces should be overcoated by a thin layer of a much harder material. It may also be desirable to overcoat the best reflective metals by a material that is nonreactive toward LEO AO.

5.4 Defects

Surface and bulk defects greatly limit the performance of optical materials. Surface roughness and contamination are two examples of surface defects. Bulk defects (due to substitutional impurities, lattice vacancies, interstitial atoms, dislocations, etc.) within a thickness of material comparable to the optical penetration depth δ (cf. Section 4.1 above) may severely degrade the reflectance of metallic coatings. An extensive study on defect effects has been completed on gold [Reference 18], demonstrating that the void (i.e., lattice vacancy) concentration determines the optical properties of gold coatings under a range of conditions. Such voids can possibly be annealed out of a deposited coating by thermal treatment.

5.5 Multiple Coatings

Multiple coatings of various thicknesses may be required to produce good substrate/primary coating adherence, surface smoothness, diffusion/reaction barriers, etc. Overcoatings and/or transition coatings deposited and/or formed on the primary coating by design, by reaction with energetic LEO AO, etc. will modify the optical properties of the system. In general, the Fresnel equations [Reference 19] for a multilayer set of thin films must be solved in order to predict the target response. If an overcoating thickness is much smaller than the optical penetration depth δ, it will have a very small effect on the overall reflectance - the optical properties of the primary coating will dominate. For example, if reaction of LEO AO with tantalum forms adherent Ta_2O_5 that is less than 10 nm thick, the reflectance values of pure tantalum may be retained. It is important to consider the kinetics of oxidation/passivation of candidate metallic coatings and to measure their optical properties after realistic exposures to energetic AO in order to be confident about their suitability for spacecraft survivability applications. If the AO problem cannot be solved by formation of protective oxide overcoatings, some thin inhibitor overcoatings (such as inert transition metals) should be developed and screened for thier compatibility with the primary coating.

A code that solves the Fresnel equations to calculate the expected absorptance of a multilayer (up to three layer) stack of materials for arbitrary laser polarization and angle of incidence is available for our use.

5.6 Nuclear Survivability

Thick coatings of high atomic number (high Z) materials can absorb large doses of energy from a nuclear blast with a soft X-ray spectrum, vaporize rapidly, and impart significant impulse to the spacecraft structure, leading to deleterious shock loading and damage. Therefore, thick high Z coatings may be an "Achilles' heel" in a nuclear blast environment. Thin coatings of highly reflective low Z materials are preferred to optimize survivability in a multiple (laser/nuclear/natural space) threat environment.

6.0 CONCLUSIONS and RECOMMENDATIONS

This report has summarized basic optical properties of some candidate laser armor metals for spacecraft survivability applications. Extensions to other metals and to metal carbides, borides, nitrides, and other materials are feasible, but the data base of optical constants is meager for nonmetallic materials. Spectroellipsometric measurements [Reference 20] of optical constants of coated substrates should be performed at both room and elevated temperatures over a range of wavelengths under high vacuum conditions. Priority attention should also be directed toward processing technology (optimal deposition techniques, substrate polishing techniques, *etc.*) in order to achieve near-intrinsic performance limits.

Since the temperature dependence of the absorptance is a key parameter that determines materials performance, direct experimental measurements of this quantity should be completed at pertinent laser threat wavelengths over an extended temperature range. In particular, the temperature dependence of the absorptance is practically unknown outside the Drude (free electron) model region. New models can be devised to consider interband transition effects, but these models must be validated by direct experiments.

The optical properties of metals are central to laser armor concepts for relatively low irradiance threat conditions. However, additional information is required to develop full figures-of-merit (FOMs) for actual designs. An approximate FOM has been derived for candidate mirror materials at $\lambda = 10.6$ μm irradiation wavelength, assuming that the optical and thermal properties are temperature independent and that damage is caused by melting which leads to catastrophic failure [Reference 21]. In terms of behavior relative to copper mirrors (FOM = 1), some of the candidate metals have FOMs of 0.68 (Au), 1.245 (Mo), and 7.727 (Ta) [no value is given for W]. As suggested in other sections of this report, Ta is worth priority consideration for spacecraft survivability applications.

7.0 REFERENCES

1. M. J. Berry, "Laser/Materials Interactions: CW Laser Interactions with Carbon-Based Materials", in Proceedings of the Sixth DoD Conference on DEW Vulnerability, Survivability and Effects, Volume 1 (Office of the Chief of Naval Research, Arlington, VA), pp. 333-342. CONFIDENTIAL.

2. F. Wooten, Optical Properties of Solids (Academic Press, New York, 1972).

3. J. H. Weaver, C. Krafka, D. W. Lynch, and E. E. Koch, Physics Data - Optical Properties of Metals, Parts I and II (Fachinformationszentrum, Karlsruhe, Federal Republic of Germany, 1981).

4. E. D. Palik (editor), Handbook of Optical Constants of Solids (Academic Press, New York, 1985).

5. M. A. Ordal, L. L. Long, R. J. Bell, S. E. Bell, R. R. Bell, R. W. Alexander, Jr., and C. A. Ward, "Optical Properties of the Metals Al, Co, Cu, Au, Fe, Pb, Ni, Pd, Pt, Ag, Ti, and W in the Infrared and Far Infrared", Appl. Opt., 22, 1099-1119 (1983).

6. M. A. Ordal, R. J. Bell, R. W. Alexander, Jr., L. L. Long, and M. R. Querry, "Optical Properties of Fourteen Metals in the Infrared and Far Infrared: Al, Co, Cu, Au, Fe, Pb, Mo, Ni, Pd, Pt, Ag, Ti, V, and W", Appl. Opt., 24, 4493-4499 (1985).

7. G. S. Arnold, "Absorptivity of Several Metals at 10.6 μm: Empirical Expressions for the Temperature Dependence Computed from Drude Theory", Appl. Opt., 23, 1434-1436 (1984).

8. W. D. Kimura and D. H. Ford, "Absorptance Measurements of Metal Mirrors at Glancing Incidence", Appl. Opt., 25, 3740-3750 (1986).

9. W. D. Kimura and T. T. Saito, "Glancing Incidence Measurements of Diamond Turned Copper Mirrors", Appl. Opt., 26, 723-728 (1987).

10. R. M. Wood, P. Waite, and S. K. Sharma, "The Effect of Surface Finish on the Laser-Induced Damage Thresholds of Gold-Coated Copper Mirrors", in H. E. Bennett, A. H. Guenther, D. Milam, and B. E. Newnam (editors), Laser Induced Damage in Optical Materials: 1983 (National Bureau of Standards, Washington, DC, 1985), pp. 157-163.

11. R. A. Matula, "Electrical Resistivity of Copper, Gold, Palladium, and Silver", J. Phys. Chem. Ref. Data, 8, 1147-1298 (1979).

12. P. D. Desai, T. K. Chu, H. M. James, and C. Y. Ho, "Electrical Resistivity of Selected Elements", J. Phys. Chem. Ref. Data, 13, 1069-1096 (1984).

13. Reference 4, page 70. Typographical errors in the expressions for a^2 and b^2 appearing in Reference 4 have been corrected in this report.

14. Reference 4, page 278.

15. N. Bloembergen, Appl. Opt., 12, 661 (1973).

16. R. M. Wood, Laser Damage in Optical Materials (Adam Hilger, Bristol, 1986).

17. H. E. Bennett and J. O. Porteus, J. Opt. Soc. Amer., 51, 123 (1961).

18. D. E. Aspnes, E. Kinsbron, and D. D. Bacon, "Optical Properties of Au: Sample Effects", Phys. Rev. B, 21, 3290-3299 (1980).

19. M. Born and E. Wolf, Principles of Optics, Sixth Edition (Pergamon Press, Elmsford, NY, 1980).

20. Reference 4, Chapter 5.

21. Reference 16, Section 1.3.2.

APPENDIX - ABSORPTANCE CALCULATIONS

Appended are four sets of tables of optical constants and corresponding absorptances of four metals (Au, W, Ta, and Mo) as a function of temperature for two wavelengths ($\lambda = 10.6$ μm and 3.8 μm). The absorptances are plotted in Figures 5 and 6. Sources of data and the computational method are discussed in the text.

GOLD: Optical Properties

	$\lambda = 10.6\ \mu m$			$\lambda = 3.8\ \mu m$		
T(K)	$n_{10.6}$	$k_{10.6}$	$A_{10.6}$	$n_{3.8}$	$k_{3.8}$	$A_{3.8}$
300	6.14	70.79	.0049	0.88	26.14	.0052
350	7.21	70.47	.0057	1.05	26.12	.0061
400	8.28	70.11	.0066	1.21	26.10	.0071
500	10.39	69.22	.0084	1.55	26.04	.0091
600	12.42	68.12	.0103	1.90	25.97	.0111
700	14.35	66.83	.0122	2.25	25.88	.0133
800	16.17	65.36	.0142	2.62	25.78	.0155
900	17.87	63.69	.0162	3.00	25.65	.0178
1000	19.42	61.87	.0183	3.40	25.49	.0203
1100	20.81	59.90	.0205	3.81	25.31	.0230
1200	22.02	57.81	.0227	4.23	25.09	.0258
1300	23.01	55.67	.0250	4.66	24.84	.0287
1337	23.34	54.86	.0259	4.82	24.74	.0299
1337	24.61	36.81	.0490	8.24	20.77	.0638
1400	24.49	36.24	.0499	8.34	20.57	.0654
1500	24.30	35.38	.0514	8.47	20.25	.0678
1600	24.10	34.57	.0528	8.59	19.95	.0701
1700	23.89	33.81	.0542	8.69	19.65	.0724

← Liquid   Solid →

TUNGSTEN: Optical Properties

T(K)	$n_{10.6}$	$k_{10.6}$	$A_{10.6}$	$n_{3.8}$	$k_{3.8}$	$A_{3.8}$
300	10.10	46.38	.0178	1.72	16.93	.0234
400	13.05	43.58	.0249	2.41	16.66	.0333
500	15.15	40.49	.0319	3.07	16.30	.0435
600	16.48	37.43	.0386	3.68	15.87	.0538
700	17.23	34.58	.0451	4.23	15.37	.0642
800	17.55	32.04	.0512	4.69	14.83	.0744
900	17.59	29.81	.0570	5.07	14.28	.0843
1000	17.46	27.87	.0625	5.38	13.72	.0940
1100	17.22	26.17	.0677	5.62	13.17	.1035
1200	16.92	24.69	.0727	5.80	12.64	.1126
1300	16.58	23.38	.0775	5.93	12.14	.1214
1400	16.22	22.23	.0821	6.02	11.66	.1299
1500	15.86	21.20	.0865	6.07	11.21	.1382
1600	15.51	20.27	.0907	6.10	10.79	.1462
1700	15.16	19.44	.0948	6.10	10.40	.1539
1800	14.82	18.69	.0988	6.09	10.03	.1614
1900	14.49	18.01	.1027	6.07	9.69	.1686
2000	14.18	17.39	.1064	6.03	9.37	.1757
2200	13.58	16.29	.1136	5.94	8.80	.1891
2400	13.04	15.35	.1205	5.82	8.30	.2018
2600	12.55	14.54	.1270	5.70	7.85	.2139
2800	12.09	13.83	.1333	5.57	7.46	.2254
3000	11.67	13.20	.1394	5.45	7.11	.2364
3200	11.28	12.63	.1453	5.32	6.79	.2470
3400	10.92	12.12	.1511	5.20	6.51	.2573
3600	10.58	11.65	.1567	5.07	6.24	.2673
3660	10.49	11.52	.1584	5.04	6.17	.2702
3660	10.15	11.07	.1643	4.91	5.92	.2806
4000	9.98	10.85	.1674	4.85	5.79	.2860
4500	9.49	10.22	.1769	4.65	5.44	.3024
5000	9.25	9.91	.1820	4.55	5.26	.3110

$\lambda = 10.6\ \mu m$ $\lambda = 3.8\ \mu m$

← Liquid   Solid →

TANTALUM: Optical Properties

	$\lambda = 10.6\ \mu m$			$\lambda = 3.8\ \mu m$		
T(K)	$n_{10.6}$	$k_{10.6}$	$A_{10.6}$	$n_{3.8}$	$k_{3.8}$	$A_{3.8}$
300	13.99	56.82	.0162	2.60	22.40	.0202
350	15.62	55.21	.0188	3.01	22.23	.0236
400	17.03	53.51	.0214	3.42	22.04	.0271
450	18.20	51.82	.0238	3.81	21.84	.0305
500	19.13	50.18	.0262	4.17	21.62	.0338
550	19.87	48.63	.0284	4.50	21.39	.0369
600	20.45	47.17	.0305	4.81	21.16	.0399
650	20.90	45.76	.0325	5.10	20.92	.0429
700	21.25	44.44	.0344	5.37	20.68	.0459
750	21.51	43.24	.0362	5.61	20.44	.0486
800	21.70	42.13	.0379	5.83	20.20	.0513
850	21.83	41.04	.0396	6.04	19.96	.0539
900	21.92	40.00	.0412	6.23	19.71	.0566
950	21.97	39.07	.0428	6.41	19.47	.0591
1000	21.99	38.20	.0442	6.57	19.24	.0614
1100	21.95	36.60	.0470	6.85	18.79	.0661
1200	21.85	35.19	.0496	7.09	18.35	.0705
1300	21.70	33.93	.0521	7.28	17.94	.0746
1400	21.53	32.80	.0544	7.45	17.54	.0786
1500	21.34	31.79	.0565	7.58	17.17	.0823
1600	21.13	30.86	.0586	7.70	16.81	.0859
1700	20.92	29.98	.0606	7.79	16.46	.0895
1800	20.70	29.19	.0626	7.87	16.13	.0929
1900	20.49	28.47	.0644	7.93	15.81	.0962
2000	20.27	27.80	.0662	7.98	15.51	.0993
2100	20.06	27.16	.0679	8.02	15.22	.1025
2200	19.84	26.56	.0696	8.05	14.94	.1055
2300	19.63	26.01	.0712	8.07	14.68	.1084
2400	19.43	25.50	.0728	8.09	14.43	.1112
2500	19.23	25.00	.0743	8.10	14.19	.1140
2600	19.04	24.54	.0758	8.10	13.95	.1167
2700	18.84	24.09	.0773	8.10	13.72	.1194
2800	18.65	23.68	.0788	8.09	13.51	.1220
2900	18.46	23.27	.0802	8.08	13.29	.1247
3000	18.30	22.92	.0815	8.07	13.11	.1270
3100	18.12	22.56	.0829	8.05	12.92	.1294
3200	17.95	22.22	.0842	8.03	12.73	.1318
3258	17.79	21.90	.0855	8.01	12.56	.1341
3258	17.40	21.15	.0885	7.95	12.15	.1396
4000	17.40	21.15	.0885	7.95	12.15	.1396

← Liquid Solid →

↓ Liquid

18

MOLYBDENUM: Optical Properties

	$\lambda = 10.6 \ \mu m$			$\lambda = 3.8 \ \mu m$		
T(K)	$n_{10.6}$	$k_{10.6}$	$A_{10.6}$	$n_{3.8}$	$k_{3.8}$	$A_{3.8}$
300	13.40	58.42	.0148	2.21	22.27	.0175
350	15.49	56.50	.0179	2.67	22.11	.0213
400	17.24	54.47	.0209	3.12	21.92	.0251
500	19.75	50.36	.0266	3.98	21.47	.0328
600	21.24	46.48	.0320	4.75	20.93	.0403
700	22.01	43.01	.0370	5.42	20.34	.0477
800	22.31	39.95	.0417	6.00	19.70	.0550
900	22.31	37.29	.0461	6.49	19.04	.0620
1000	22.12	34.97	.0503	6.89	18.38	.0689
1100	21.81	32.96	.0543	7.21	17.72	.0756
1200	21.43	31.18	.0581	7.46	17.09	.0821
1300	21.02	29.62	.0617	7.65	16.48	.0884
1400	20.60	28.24	.0652	7.79	15.90	.0945
1500	20.16	26.99	.0685	7.89	15.34	.1004
1600	19.73	25.88	.0718	7.96	14.82	.1061
1700	19.31	24.87	.0749	8.00	14.33	.1117
1800	18.91	23.96	.0779	8.01	13.87	.1171
1900	18.51	23.13	.0809	8.00	13.43	.1224
2000	18.13	22.37	.0837	7.98	13.02	.1275
2200	17.42	21.02	.0892	7.90	12.28	.1374
2400	16.76	19.86	.0944	7.79	11.62	.1467
2600	16.16	18.85	.0995	7.67	11.04	.1557
2800	15.60	17.96	.1043	7.53	10.51	.1642
2894	15.35	17.58	.1065	7.46	10.29	.1681
2894	14.22	15.91	.1173	7.11	9.29	.1870

← Liquid Solid →
← Liquid

APPENDIX G

The following appendix contains abstracts of the following publications sponsored under the AFOSR/HARC/Rice Program (Grant AFOSR-85-0365):

1. M. J. Berry, "Laser/Materials Interactions: CW Laser Interactions with Carbon-Based Materials", in Proceedings of the Sixth DoD Conference on DEW Vulnerability, Survivability and Effects, Volume 1 (Office of the Chief of Naval Research, Arlington, VA, 1987), pp. 333-342. CONFIDENTIAL.

2. C. A. Klein, R. F. Menefee, B. D. Krenek, and M. J. Berry, "Small Scale Laser Effects Experiments on Graphite: Coupling Coefficient, Lateral Loss, and Effective Heat of Ablation", J. Appl. Phys., 61, 1701-1712 (1987).

3. C. A. Klein, M. J. Berry, and P. A. Miles, "Thermochemical Heat of Ablation of Solid Carbon", J. Appl. Phys., 65, 3425-3429 (1989).

4. L. M. A. Levine, L. G. Fredin, and M. J. Berry, "Infrared Absorption Spectra of Cured Epoxy Resin and Human Corneal Tissue at Temperatures Up To 450 °C", SPIE Proceedings, Vol. 1064 - Thermal and Optical Interactions with Biological and Related Composite Materials, 131-134 (1989).

5. T. D. Kunz, R. F. Menefee, B. D. Krenek, L. G. Fredin, and M. J. Berry, "Laser Probe Absorption Spectroscopy Measurements on Laser Induced Plumes", High Temp. Sci., 27, xxx (1989).

LASER/MATERIALS INTERACTIONS:
CW LASER INTERACTIONS WITH CARBON-BASED MATERIALS*

Michael J. Berry

Laser Applications Research Center
Houston Area Research Center (HARC)
Woodlands, TX 77381

Department of Chemistry and Rice Quantum Institute
Rice University
Houston, TX 77251

ABSTRACT

Aspects of thermal coupling phenomenology during laser/materials interactions are reviewed, with emphasis on cw laser interactions with carbon-based materials. Fundamental physical and chemical processes that govern interactions, responses, and hardening are discussed using recent small scale laser effects experiments as examples.

Small-scale laser effects experiments on graphite: Coupling coefficient, lateral loss, and effective heat of ablation

Claude A. Klein

Research Division, Raytheon Company, Lexington, Massachusetts 02173

Richard F. Menefee, Brendan D. Krenek, and Michael J. Berry

Houston Area Research Center, 2202 Timberloch Place, The Woodlands, Texas 77380, and Department of Chemistry and Rice Quantum Institute, Rice University, P. O. Box 1892, Houston, Texas 77251

This work concerns laser-interaction experiments performed on a fine-grained, nearly isotropic synthetic graphite grade known as GraphNOL. They were carried out with a cw/DF laser of 100-W output power, at peak irradiances varying from 10 to 50 kW/cm^2 on targets of, typically, 1.5-mm diameter. One of the major objectives was to accept the difficulties associated with such small sizes and rely on analytical techniques for estimating the lateral heat loss, developing a scaling law, and formulating an improved, parametric representation of the effective heat of ablation (Q^*). The procedure rests on Breaux's formula (Ballistic Research Laboratories report no. 1834) heuristically extended to accommodate the concept of a lateral loss parameter, which relates linearly to a scaling parameter that combines target thickness, target diameter, and spot size, thus specifying how geometrical factors correlate in terms of their impact on radial losses. Our investigation demonstrates that a small-scale, low-cost laser ablation experiment can generate a rich set of well-characterized, highly accurate data, which are amenable to a comprehensive analytical evaluation. The coupling coefficient of GraphNOL to 3.8-μm radiation is 86 ± 1%, averaged over the duration of the burn, in a burnthrough experiment; this result leads to the conclusion that the intrinsic Q^* should be close to 38 kJ/g at the DF-laser wavelength.

Thermochemical heat of ablation of solid carbon

Claude A. Klein
Research Division, Raytheon Company, Lexington, Massachusetts 02173

Michael J. Berry[a]
Department of Chemistry, Rice University, Houston, Texas 77251

Perry A. Miles
R&D Associates, Marina del Rey, California 90295

The thermochemical heat of ablation of carbon, H_A, is usually set equal to 32 kJ/g as derived from the JANAF tables. There is, however, some uncertainty since JANAF-recommended values for heats of vaporization and partial vapor pressures differ from the results of a detailed analysis that was carried out at the Lawrence Livermore National Laboratory (LLNL). We find that the LLNL model yields carbon-vaporization enthalpies that are appreciably lower than the JANAF-based values. In this light, we examine experimental data generated in the course of a comprehensive investigation of laser-interaction effects in graphite and conclude that our experiments are indicative of an H_A equal to 31.0 ± 1.6 kJ/g.

[a] Also, Laser Applications Research Center, HARC, The Woodlands, TX 77381, and Antropix Corporation, The Woodlands, TX 77381.

INFRARED ABSORPTION SPECTRA OF CURED EPOXY RESIN AND HUMAN CORNEAL TISSUE AT TEMPERATURES UP TO 450 °C

L. M. A. Levine, L. G. Fredin, and M. J. Berry

Laser Applications Research Center, HARC
4802 Research Forest Drive, The Woodlands, Texas 77381
and
Department of Chemistry and Rice Quantum Institute
Rice University, P.O. Box 1892, Houston, Texas 77251

ABSTRACT

High temperature (up to 450 °C) infrared absorption spectra of a cured epoxy resin (CER) and human corneal tissue (HCT) have been measured to identify changes in absorption coefficients due to the dehydration and decomposition of polymeric materials. The observed spectral changes are analyzed and related to thermogravimetric measurements and pulsed laser ablation experiments.

LASER PROBE ABSORPTION SPECTROSCOPY MEASUREMENTS
ON LASER INDUCED PLUMES

Terry D. Kunz, Richard F. Menefee, Brendan D. Krenek, Leif G. Fredin, and
Michael J. Berry*

Antropix Corporation, 30 Meadowfair Court, The Woodlands, TX 77381;

Laser Applications Research Center, HARC,
4802 Research Forest Drive, The Woodlands, TX 77381; and

Department of Chemistry and Rice Quantum Institute,
Rice University, P. O. Box 1892, Houston, TX 77251

ABSTRACT

A computer controlled laser absorption spectroscopy (CCLAS) system has been developed to study high temperature plume species (atoms, molecules, and ions) generated by laser/materials interactions. Direct temporally/spatially resolved measurements on carbon plume/plasma species have been obtained during continuous wave (cw) and repetitively pulsed (rp) laser irradiation experiments. The measured plume characteristics (species, abundances, energy contents, and optical properties) have been interpreted to provide mechanistic understanding of laser/materials interaction phenomenology and effects.

INDEX ENTRIES

Plume; laser/materials interaction; ablation; laser probe spectroscopy; laser effects; high temperature materials; diagnostic instrumentation; optical properties; plasma generation; carbon

*Author to whom correspondence should be addressed.